



The
University
Of
Sheffield.

Magnetic Field-Induced Electronic Effects in Organic Semiconductors

Matthew Peter Philip Hodges

*Thesis submitted for the degree of
Doctor of Philosophy
October 2013*

**Department of Materials Science and Engineering
The University of Sheffield**

Abstract

Organic semiconductors have recently received increased attention as a class of functional materials due to their remarkable abilities ranging from electrical conduction to light generation. This thesis presents investigations of further novel aspects of organic semiconductors.

First, the characterisation and exploitation of the 'magnetic field effect' exhibited by some organic semiconductors is presented. Several characterisation systems were developed to facilitate the analysis of several organic semiconducting materials exhibiting a photoluminescent magnetic field effect. The largest magnetic field effect measured was of a photoluminescent intensity change of +6.5%. A morphological study of the organic thin film microstructures was performed allowing progressive optimisation to be made to the microstructures. Magnetic image contrast detection was undertaken at microscopic and macroscopic length scales by coupling the magnetic field effect material to a magnetic sample. This experiment culminated in the acquisition of the first ever magnetic field effect image of a magnetic sample. It was also found that magnetic polarity could be detected via polarisation analysis of photoluminescence, demonstrating magnetic field effect asymmetry from opposing magnetic fields.

Second, a study of electronic transport behaviour in polythiophene derivatives using the muon spin resonance spectroscopy technique is described. There is much interest in these materials and their potential use in organic spintronic applications however, deep understanding of their electronic transport properties is lacking. Several morphologies of polythiophene were analysed as a function of magnetic field and temperature. It was found that the electronic transport properties in the crystalline forms of polythiophene experience a temperature-dependent transition. It is, therefore, hypothesised that the conduction electrons begin to delocalise along the polymer chain at temperatures below room temperature.

Acknowledgements

First, and foremost, I would very much like to thank my primary supervisor, Dr Dan Allwood, and my secondary supervisor, Dr Nicola Morley, for all the support and guidance given to me throughout my three years of postgraduate research. I would also like to congratulate them on their bravery for offering me the opportunity to work with them once more after my undergraduate final year project! But, in all seriousness I would not have been able to achieve what I have without their unremitting assistance.

I would also like to thank the entire magnetics group, SCAMMD, for the additional help and assistance offered in the form of equipment training, group meetings, talks, informal chats and useful outside perspective. Special thanks go to Dr Julian Dean for help with computational modelling, and Mr James Wheelwright and Miss Ruth Bradley for allowing me to bounce ideas incessantly off them. I'd like to thank Professor John Haycock and Professor Gino Hrkac for their valuable feedback and constructive comments during my 1st and 2nd year vivas.

I'd like to thank Dr Martin Grell for the useful discussions and ideas as well as allowing me to use the thin-film cleanroom in the Department of Physics and Astronomy. I'd also like to thank his students for offering me training on some of the deposition equipment and generally making me feel welcome in their labs. I'm also grateful to Dr Linda Swanson for allowing me access to the luminescence spectroscopy laboratory in the Department of Chemistry. Many thanks go to Dr Nicola Green for all of the help with the confocal microscope in the Kroto Research Institute.

Gratitude goes out to all the departmental technical staff that have helped me with various aspects of my project including Mr Paul Hawksworth, Ms Dawn Bussey and Dr Steve Mason.

I'd like to thank my family for being so understanding of my reclusiveness during the thesis-writing months. Finally I am most thankful to my partner, Dr Megan Atkinson, for all of the lovely meals, taxi runs and generally being a pleasant distraction from some of the more stressful moments during my three years of postgraduate research.

Table of Contents

ABSTRACT	i
ACKNOWLEDGEMENTS	ii
TABLE OF CONTENTS	iii
1 INTRODUCTION	1
1.1 Magnetism	1
1.2 Organic Semiconductors	1
1.3 Thesis Outline	2
1.4 References	3
2 BACKGROUND	5
2.1 Introduction	5
2.2 Magnetic Nanostructures and Technology	5
2.3 Modern Day Magnetic Microscopy Techniques	7
2.3.1 Lorentz Microscopy	7
2.3.2 Kerr Microscopy	11
2.3.3 Scanning Electron Microscopy with Polarisation Analysis	11
2.3.4 Magnetic Transmission X-Ray Microscopy	12
2.3.5 X-Ray Photoemission Electron Microscopy	13
2.3.6 Magnetic Force Microscopy	13
2.3.7 Scanning Superconducting Quantum Interference Device Microscopy	14
2.3.8 Scanning Hall Probe Microscopy	15
2.3.9 Nitrogen Vacancy Magnetometry	16
2.3.10 Summary of Techniques	17
	iii

2.4	Photoluminescence Processes	19
2.4.1	Electronic States	19
2.4.2	Jabłoński Diagram	20
2.4.3	Franck-Condon Principle	22
2.4.4	Rate Constants, Lifetimes and Quantum Yields	25
2.4.5	Photobleaching	26
2.4.6	Heavy-Atom Effect	27
2.5	Magnetic Field Effect	29
2.5.1	Definition	29
2.5.2	MFEs in Linear Polycyclic Aromatic Hydrocarbons	30
2.5.3	MFEs in Other Systems	34
2.5.4	Current Understanding	36
2.6	Magnetic Luminescence Microscopy	42
2.6.1	Confocal Microscopy	42
2.6.2	STED Microscopy	43
2.7	References	44
3	EXPERIMENTAL TECHNIQUES	50
3.1	Introduction	50
3.2	Sample Preparation and Fabrication	50
3.2.1	Organic Materials and Solvents	50
3.2.2	Spin Coating	52
3.2.3	Electron Beam Lithography	53
3.2.4	Thermal Evaporation	58
3.3	Fluorescence Spectroscopy	60
3.4	Absorption Spectroscopy	63
3.5	Optical Microscopy	65

3.6	Confocal Microscopy	67
3.7	Atomic Force Microscopy	68
3.8	Magnetic Force Microscopy	71
3.9	Magnetic Transmission X-Ray Microscopy	72
3.10	Hall Array Magnetometry	75
3.11	Magneto-Optic Kerr Effect Magnetometry	76
3.12	Micromagnetic Modelling	79
3.13	References	81
4	SYSTEM DEVELOPMENT	84
4.1	Introduction	84
4.2	Magnetic Field Effect Magnetometry	84
4.2.1	Low Field MFE System Mk. I	85
4.2.2	Low Field MFE System Mk. II	87
4.2.3	High Field MFE System Mk. I	90
4.2.4	High Field MFE System Mk. II	95
4.2.5	High Field MFE System Mk. III	98
4.2.6	Control Software	101
4.2.7	Experimental Settings	104
4.2.8	Data Analysis Script	106
4.2.9	HF-MFE System Issues	107
4.3	Magnetic Field Effect Photography	109
4.4	Conclusion	113
4.5	References	114

5	MATERIALS CHARACTERISATION & OPTIMISATION	115
5.1	Introduction	115
5.2	Absorption, Excitation & Fluorescence Spectroscopy Measurements	115
5.2.1	TPD:BBOT:PMMA	116
5.2.2	Anthracene	118
5.2.3	Alq ₃	120
5.2.4	MEH-PPV	121
5.2.5	Tetracene	123
5.2.6	NpQ	124
5.2.7	Summary of Results	126
5.3	Magnetic Field Effect Magnetometry	126
5.4	Thin Film Morphology	138
5.4.1	Morphology of Spin-Coated Thin Films	138
5.4.2	Morphology of Thermally Evaporated Thin Films	140
5.4.3	Morphology of Thermally Evaporated Thin Films Coupled to Nanostructures	142
5.4.4	Defects in the Electron Beam Lithography Fabrication Process	144
5.5	Conclusion	148
5.6	References	149
6	MAGNETIC IMAGE CONTRAST DETECTION	151
6.1	Introduction	151
6.2	Magnetic Characterisation Using Established Techniques	151
6.2.1	Magnetic Transmission X-Ray Microscopy	152
6.2.2	Magnetic Force Microscopy	156
6.2.3	Magneto-Optic Kerr Effect Magnetometry	162
6.3	Simulation of Magnetic Luminescence Micrographs	166

6.3.1	Simulation of FePd Disc	167
6.3.2	Simulation of Ni-Fe Ring	173
6.3.3	Simulation of Ni-Fe Rectangle	177
6.4	Microscopic Regime	179
6.5	Macroscopic Regime	188
6.6	Magnetic Polarity Detection via Optical Polarisation Analysis	194
6.7	Conclusion	199
6.8	References	201
7	MUON SPIN RESONANCE SPECTROSCOPY	203
7.1	Introduction	203
7.2	Theory	204
7.2.1	Muon Production	204
7.2.2	Muon Implantation	205
7.2.3	Muon Decay	206
7.2.4	Data Acquisition	207
7.2.5	Avoided Level Crossings	209
7.3	Experimental Details	211
7.3.1	High Field Muon Spectrometer	212
7.3.2	Sample Preparation	213
7.3.3	Instrument Calibration	214
7.3.4	Data Processing	215
7.4	Experimental Results	216
7.5	Conclusion	225
7.6	References	225

1 Introduction

1.1 Magnetism

There has been a surge of interest recently in the potential to use magnetic domain phenomena to store and even process digital information, with several proof-of-concept experimental systems having already been demonstrated [1-4]. More generally the study of magnetic domains is important in enabling the creation and further development of many practical applications and technologies. Today, many important technologies exist that rely centrally on magnetic materials and magnetic domain behaviour including magnetic data storage, magnetic resonance imaging, loudspeakers, electric motors and electric generators for wind turbines.

In the last few decades several magnetic microscopy techniques have been developed [5-8] to facilitate the requirement of being able to observe magnetic phenomena at the length scales where magnetic domains exist. Although all of these techniques have their own advantages it should be acknowledged that each has shortcomings.

Therefore there is an opportunity for a new magnetic microscopy technology to diversify the range of existing techniques and potentially overcome some of their shortcomings.

1.2 Organic Semiconductors

The use of organic semiconductors in consumer technology is growing at an increasing rate [9, 10] with devices such as organic light-emitting diodes being firmly established whilst organic solar cells are being touted as the next generation of solar cell technology due to their potential low production costs and versatility [11]. Whilst much is known about them there are still many fundamental properties that remain to be explained, such as their electron dynamics and transport behaviour.

One of these is the ‘magnetic field effect’ [12] whereby a magnetic field can influence the electronic state populations in certain organic compounds giving rise to various macroscopic phenomena. One of the first descriptions of this phenomenon occurred nearly 50 years ago [13] and yet the exact mechanism of interaction between the molecule and a magnetic field has yet to be fully explained. Another example of the incomplete description of organic semiconductor transport appears with regards to their potential to be used as spintronic [14] materials. Here, several key properties such as the electron spin relaxation rate are still poorly defined for many of the promising materials being used. Therefore being able to determine some of these properties would progress research in the field.

1.3 Thesis Outline

One of the main aims of this thesis is the proposal and demonstration of a new magnetic microscopy technique that exploits an obscure photoluminescent phenomenon known as the ‘magnetic field effect’ via characterisation, optimisation and exploitation of organic semiconductors.

A second aim of this thesis is to provide greater understanding of electronic transport properties in organic semiconducting polymers using the advanced characterisation technique, muon spin resonance spectroscopy.

This thesis is divided into seven chapters (including this one). The chapters are outlined as follows:

Chapter 2 begins with a review of existing magnetic microscopy methods evaluating their advantages and disadvantages. An introduction to basic photoluminescence concepts is then discussed followed by a discussion of the ‘magnetic field effect’ including examples of where this phenomenon is manifested. This chapter is concluded with a discussion of fluorescence microscopy techniques that could be used in conjunction with the ‘magnetic field effect’ in order to visualise magnetic phenomena via photoluminescence.

Chapter 3 is devoted to a discussion of the details of the experimental methods and techniques used in this research. This includes all sample preparation methods, characterisation techniques and computer modelling undertaken.

Chapter 4 looks at the developmental evolution of several characterisation systems designed and built in order to observe photoluminescent 'magnetic field effects'.

Chapter 5 contains absorption and photoluminescent spectra from samples suspected of exhibiting 'magnetic field effect' character. Using the systems developed in chapter 4, 'magnetic field effect' magnetometry results are presented and discussed. Finally, a thin film morphological study was undertaken in order to characterise and optimise the materials for their use as candidate samples for chapter 6.

Chapter 6 is dedicated to the detection of magnetic image contrast. This begins with the use of established techniques to generate magnetic micrographs for the assessment of the magnetic behaviour of some of the test structures that were fabricated. The chapter then turns to the presentation of attempts to image magnetic structures using the 'magnetic field effect' – both at the microscopic and the macroscopic length-scale.

Chapter 7 is concerned with the study of several organic semiconducting polymers using muon spin resonance spectroscopy. The chapter begins with an introduction to the technique including the underlying theory and concepts. The experimental details are outlined followed by a presentation and discussion of the results of the experiment.

1.4 References

- [1] D. A. Allwood, *et al.*, "Magnetic domain-wall logic," *Science*, vol. 309, pp. 1688-1692, 2005.
- [2] S. S. P. Parkin, *et al.*, "Magnetic domain-wall racetrack memory," *Science*, vol. 320, pp. 190-194, Apr 2008.

- [3] I. M. Miron, *et al.*, "Fast current-induced domain-wall motion controlled by the Rashba effect," *Nature Materials*, vol. 10, pp. 419-423, Jun 2011.
- [4] S. W. Jung, *et al.*, "Current-induced domain wall motion in a nanowire with perpendicular magnetic anisotropy," *Applied Physics Letters*, vol. 92, May 2008.
- [5] D. Le Sage, *et al.*, "Optical magnetic imaging of living cells," *Nature*, vol. 496, pp. 486-U105, Apr 2013.
- [6] P. Fischer, *et al.*, "Imaging of magnetic domains with the X-ray microscope at BESSY using X-ray magnetic circular dichroism," *Zeitschrift Fur Physik B-Condensed Matter*, vol. 101, pp. 313-316, Nov 1996.
- [7] Y. Martin and H. K. Wickramasinghe, "Magnetic Imaging by Force Microscopy with 1000-Å Resolution," *Applied Physics Letters*, vol. 50, pp. 1455-1457, May 1987.
- [8] S. McVitie, *et al.*, "Quantitative imaging of magnetic domain walls in thin films using Lorentz and magnetic force microscopies," *Journal of Applied Physics*, vol. 90, pp. 5220-5227, Nov 2001.
- [9] G. Overton. (2013, 11/10/2013). *Flexible OLED market to rise 334% to nearly \$100M in 2014*. Available: <http://www.laserfocusworld.com/articles/2013/08/flexible-oled-market-to-rise-334-to-nearly-100m-in-2014.html>
- [10] V. Jakhanwal. (2009, 11/10/2013). *OLED Shipments for Primary Cell-Phone Displays to Rise Eightfold by 2015*. Available: <http://www.isuppli.com/display-materials-and-systems/news/pages/oled-shipments-for-primary-cell-phonedisplays-to-rise-two-hundred-fold-by-2015.aspx>
- [11] Z. Shahan. (2012, 11/10/2013). *Organic Photovoltaics Market to Grow 1300% by 2022*. Available: <http://cleantechnica.com/2012/05/16/organic-photovoltaics-market-to-grow-1300-by-2022/>
- [12] B. Hu, *et al.*, "Magnetic-Field Effects in Organic Semiconducting Materials and Devices," *Advanced Materials*, vol. 21, pp. 1500-1516, Apr 2009.
- [13] R. C. Johnson, *et al.*, "Effects of magnetic fields on the mutual annihilation of triplet excitations in molecular crystals," *Physical Review Letters*, vol. 19, pp. 285-287, 1967.
- [14] S. Sanvito, "Spintronics goes plastic," *Nature Materials*, vol. 6, pp. 803-804, Nov 2007.

2 Background

2.1 Introduction

This chapter contains a review of the literature describing the current state of the art of magnetic microscopy. This will be followed by an overview of basic photoluminescence (PL) concepts and processes that will be required in order to discuss the literature concerning a so-called photoluminescent ‘magnetic field effect’ (MFE) phenomenon. Finally, the potential for applying this phenomenon to a new novel magnetic luminescence microscopy (MLM) technique will also be reviewed.

2.2 Magnetic Nanostructures and Technology

In order to characterise and understand certain macroscopic magnetic phenomena it is important to study magnetic phenomena at much smaller length scales. An example of this principle can be demonstrated with the macroscopic observation of Barkhausen jumps during a magnetisation reversal event of a ferromagnetic sample. The explanation for this phenomenon originates at the microscopic level whereby an applied magnetic field propagates a boundary (domain wall) between regions of opposed magnetisation (domains). Whilst propagating, the domain wall (DW) may then encounter an imperfection in the material and become ‘pinned’. Only when the applied magnetic field has been increased above a higher threshold value will the domain wall have enough energy to overcome the pinning and ‘de-pin’ in order to continue propagating through the sample. A small but abrupt jump in bulk magnetisation with respect to applied magnetic field will be measured every time this de-pinning occurs.

Understanding such phenomena can lead to important technological breakthroughs.

Over the last few decades there has been a great drive to push technologies toward the nanoscale regime, such as the 1 Terabit/inch² milestone in hard disk drive technology [1]. This

area of research looks to be inevitably moving towards bit-patterned media [2] in which trillions of discrete ‘islands’ of magnetic material reside on a hard disk platter. Each island contains a single magnetic domain that, depending on the orientation (or chirality) of the domain, represents either a digital one or zero. Many advanced and exotic fabrication techniques such as electron beam lithography and magnetic nanoparticle self-assembly are being pursued [3-5] in order to develop this technology further.

Another area of nanoscale magnetic research includes a technology known as magnetic domain-wall logic [6]. This idea is analogous to electronic logic; however, instead of using electronic charge to drive logic operations, magnetic domain walls are used in their place. Another example involves the use of DWs in a type of non-volatile computer memory known as racetrack memory [7]. In this device, domain walls represent digital information and are stored in series in a Permalloy magnetic nanoscale wire. To address the data a spin-polarised current is used to move the DWs past a read/write head where the stored data is processed. Technologies like these could enable the realisation of lower-powered, higher-speed computing devices to become available in the future. Therefore being able to characterise the time-dependent dynamics of these systems are of real importance in understanding how these DW-circuits operate and in order to study their reliability.

In general this ‘miniaturisation’ trend, exemplified by the selection of technologies discussed above, will allow such technologies to become more capable, and hence, more useful in modern society. However, without appropriate microscopy techniques available to characterise these phenomena at ever decreasing length and temporal scales, such progress would not be able to occur.

2.3 Modern Day Magnetic Microscopy Techniques

Today there exist dozens of techniques for observing magnetic microstructure such as magnetic domains. This section will attempt to list some of the more popular methods. For a thorough review of the many existing magnetic microscopy techniques available please refer to reference [8].

2.3.1 Lorentz Microscopy

Lorentz microscopy is a broad term for a range of magnetic microscopy techniques that operate using a transmission electron microscope (TEM; see figure 2.1). In a TEM electrons are accelerated at the target sample at energies in the range 100-200 keV or 1 MeV in high voltage microscopes. When they approach the sample their trajectory is influenced by the Lorentz force:

$$\mathbf{F} = q(\mathbf{E} + \mathbf{v} \times \mathbf{B}) \quad \text{Equation 2.1}$$

where q is the charge of an electron, \mathbf{E} is the electric field, \mathbf{v} is the velocity of the electron in the electric field, and \mathbf{B} is the magnetic field generated by the sample. It is this Lorentz force generated by the magnetic field from the sample magnetisation which causes a deviation in the trajectory of the electron that is detected in order to produce an image representative of the magnetic domain structure of the sample. Lorentz microscopy is capable of producing magnetic contrast images with an extremely high spatial resolution currently ≥ 2 nm [9] and a temporal resolution of around 40 ms [8]. Several imaging modes have been developed in the last few decades as new ideas and technologies emerge and shall be discussed below.

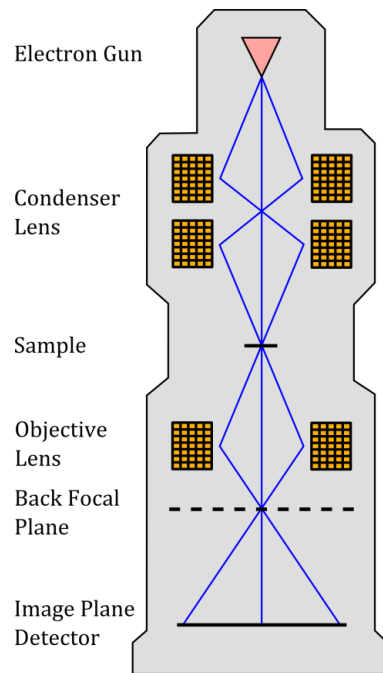


Figure 2.1: Schematic diagram of a transmission electron microscope.

The blue lines represent the electron beam path.

Fresnel-mode Lorentz microscopy operates by using a defocussed electron beam to generate image contrast (see figure 2.2). This is done so as to minimise image contrast contribution from sample topography and maximise image contrast contribution from the magnetic microstructure. The final image contrast appears in the form of bright and dark lines representing domain walls. If the electron beam is coherent then fringes aligned parallel to the walls are also present. These interference fringes become more pronounced as the microscope is further defocussed. Image interpretation is not trivial in Fresnel-mode Lorentz microscopy; comparison with micromagnetic simulations is usually required for validating observations [10].

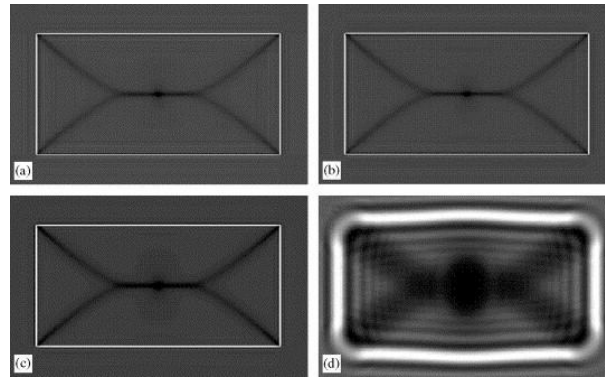


Figure 2.2: Simulated image of 20 nm thick Permalloy element with dimensions 1000×200 nm. (Contrast is the curl component of the out of plane magnetisation) (b)-(d) Calculated Fresnel TEM images for the same element at defocus values of 5, 100 and 10,000 μm [11].

Foucault-mode Lorentz microscopy operates with an electron beam that is focussed on the sample. To compensate for contrast contribution from surface topography one 'split spot' in the diffraction pattern is blocked with an aperture. The contrast that results is then from the magnetisation of the domains themselves. Foucault-mode Lorentz microscopy is a useful technique in the study of domain patterns; however, the observation of the magnetisation reversal process in magnetic materials is rather complex and requires great care as any applied magnetic field has the potential to deflect the electron beam and destroy the magnetic contrast image. One method that is used to minimise perturbation of the magnetic contrast image is via the introduction of compensating coils. These act to restore the deflection of the electron beam caused by the applied magnetic field, but only within a limited applied field range [8, 10].

Coherent Foucault-mode Lorentz microscopy is similar to Foucault-mode Lorentz microscopy, however, it utilises a highly coherent electron beam (usually a field emission gun) and a special aperture filter in order to generate quantitative image contrast (see figure 2.3). The image contrast is known as a magnetic interferogram, which is similar, but distinct, from electron holography. One limitation of the technique is that either the sample has to have a footprint smaller than the field of view of the microscope, or the operator is restricted to observations near the edge of the sample, in order to let a reference beam of electrons past that will be used for interference [8].

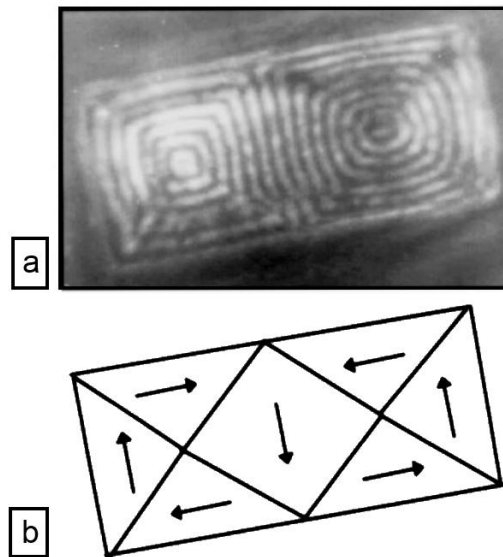


Figure 2.3: (a) Coherent Foucault micrograph of $3.0 \times 1.5 \mu\text{m}$ Ni-Fe element whilst (b) is the corresponding illustration of domain configuration [12]. © IOP Publishing. Reproduced by permission of IOP Publishing. All rights reserved.

Differential phase contrast (DPC) microscopy is a form of Lorentz microscopy that utilises a quadrant split detector to measure the diffraction of focussed electrons through the magnetic sample. Using a quadrant detector allows the technique to be sensitive to two perpendicular directions of magnetisation. This technique does, however, require the use of a scanning transmission electron microscope (STEM) in order to work [8, 10].

Electron holography Lorentz microscopy is based on the idea of capturing an interference pattern between electrons transmitted and scattered by the magnetic sample against those electrons unperturbed by the sample (known as the reference beam). Analysis of the interference pattern can then be used to reconstruct the magnetic microstructure of the sample in superior clarity compared to conventional non-holographic Lorentz microscopic modes [10].

A disadvantage common to all modes of Lorentz microscopy relates to the limits placed on the physical dimensions of the magnetic sample due to the requirement for the sample to be electron transparent. TEM Lorentz microscopy samples have to be thin enough so that electrons can emerge out of the underside of the sample in order to be detected. Therefore the combined

sample and substrate thickness is limited to a maximum of 100 nm in regular TEM and a few hundred nanometres in high voltage TEM [10].

2.3.2 Kerr Microscopy

Kerr microscopy makes use of the magneto-optic Kerr effect (MOKE) whereby a linearly polarised light beam incident on a magnetic sample surface undergoes a rotation of the polarisation by an amount that is determined by the orientation of the magnetisation of the sample of which the light is incident upon. This principle allows the magnetisation to be mapped with moderate spatial (≈ 300 nm), and very high temporal (230 fs – 200 ps [8, 13]), resolution in either a wide-field (see figure 2.4) or scanning optical microscope. The spatial resolution is ultimately limited, however, by the diffraction limit of the wavelength of light used [10].

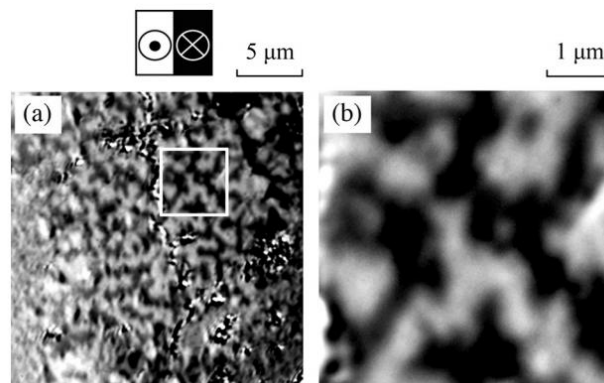


Figure 2.4: Wide-field Kerr microscopy domain images of melt-spun Nd-Fe-Al-B ribbon with a field of view measuring (a) $20 \times 20 \mu\text{m}$ and (b) $5 \times 5 \mu\text{m}$ [14].

2.3.3 Scanning Electron Microscopy with Polarisation Analysis

Scanning electron microscopy with polarisation analysis (SEMPA) operates in exactly the same manner as its parent technique scanning electron microscopy (SEM) except with the addition of a Mott detector. As an electron beam is scanned across the magnetic sample surface secondary electrons are ejected out of the sample. These secondary electrons are spin-polarised with the polarisation depending on the localised magnetisation vector of the sample from where the

electrons were ejected. The Mott detector distinguishes the electron spin allowing a high spatial resolution (≥ 5 nm [15]) quantitative vector magnetisation map to be built up as scanning progresses [10]. A point of note with SEMPA is that an ultrahigh vacuum (UHV) is required to keep the sample surface ultra-clean to prevent de-polarisation of the secondary electrons. This is disadvantageous as UHV apparatus needed for SEMPA use is very expensive due to such apparatus being rare as SEM only requires a high vacuum environment [8]. Another disadvantage of SEMPA is that image acquisition takes around 10 minutes [16] or more due to the requirement to perform the spin analysis.

2.3.4 Magnetic Transmission X-Ray Microscopy

Magnetic transmission X-ray microscopy (M-TXM) is a high resolution (spatial ≥ 25 nm [17]; temporal < 100 ps [18]) imaging technique whereby circularly polarised X-rays are directed at a magnetic sample and selectively absorbed at the surface due to an asymmetric photon-absorption cross-section of atomic core levels due to a magnetisation dependence of the circular polarisation of the incident X-rays (X-ray circular dichroism) [8, 19]. The magnetisation-dependent X-ray absorption forms the basis of the image contrast produced as the remaining X-ray light is transmitted through the sample and recorded on an imaging sensor (see figure 2.5). One unique feature of this technique is its ability to image domains in an element-specific manner allowing contributions from individual layers in a multilayered magnetic structure to be investigated [19]. This technique is typically performed on a synchrotron beamline and is discussed in more detail in §3.9.

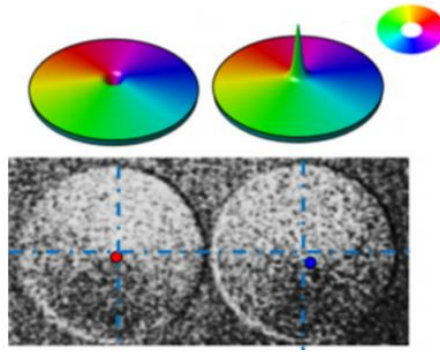


Figure 2.5: M-TXM micrographs of Permalloy discs of opposing chirality [20].

2.3.5 X-Ray Photoemission Electron Microscopy

In a similar manner to M-TXM, X-ray photoemission electron microscopy (X-PEEM) is a high resolution (spatial ≥ 20 nm [8]; temporal ≈ 100 ps [21]) technique whereby circularly polarised X-rays are directed at a magnetic sample and selectively absorbed at the surface due to an asymmetric photon-absorption cross-section of atomic core levels due to a magnetisation dependence of the circular polarisation of the incident X-rays (X-ray circular dichroism) [8, 19]. However, instead of the contrast image being formed from the remaining transmitted X-ray light, the photoelectrons emitted from the sample due to X-ray absorption are collected and form the contrast image. This means that X-PEEM does not require X-ray transparent samples in order to obtain images. However, it does mean that the samples have to be scanned in order to obtain the image and that external magnetic fields cannot be applied to the sample during image capture as this would perturb the photoelectrons and destroy the image.

2.3.6 Magnetic Force Microscopy

Magnetic force microscopy (MFM) is a scanning probe method of observing the magnetisation state of a magnetic sample. The technique is currently the most widely used magnetic imaging technique [19] and is based on the successful atomic force microscopy (AFM) technique that is predominantly used for characterising sample surface topography. In MFM, a cantilever probe is driven to oscillate at, or near, its natural resonant frequency. At the end of the cantilever is a pyramidal tip of silicon coated with a magnetic film that has been magnetised longitudinally in

order to interact with the magnetic stray field of the sample surface. As the probe is raster-scanned across the sample by piezoelectric tubes, the tip at the end of the oscillating cantilever arm experiences the gradient of the magnetic force interaction of magnetic tip and magnetic sample. This gradient is mapped to produce the magnetic image contrast (see figure 2.6) [8].

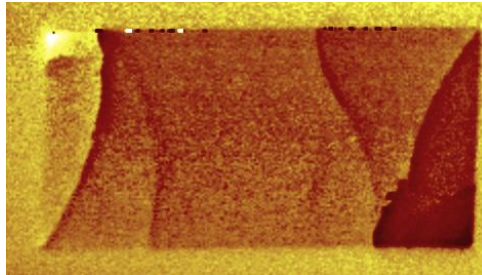


Figure 2.6: MFM image of a Permalloy rectangular element. The micrograph contains magnetic domain walls that are clearly visible.

The MFM technique is advantageous in that it has a high spatial resolution on the order of tens of nanometres [9, 22] and can scan a large sample area [19]. One of the disadvantages of the technique has been that it can suffer from poor temporal resolution with scans taking minutes to complete. However, recently several commercial systems have emerged [23] that offer much faster scanning rates (>20 Hz). Another disadvantage of the technique is that the contrast obtained is not simply a result of the sample surface magnetisation but, rather, a force gradient from the magnetic interaction of sample surface stray field and probing tip stray field. This complicates image interpretation, compared to other techniques mentioned, and makes extracting quantitative information rather difficult. Another complication of this interaction is that the tip can actually perturb the state of the magnetisation (especially in soft magnetic materials). This technique is discussed in more detail in §3.8.

2.3.7 Scanning Superconducting Quantum Interference Device Microscopy

A superconducting quantum interference device (SQUID) is a superconducting magnetometer that can measure magnetic flux densities to an extremely high sensitivity on the order of 5 aT with a few days of measurement averaging [24]. It consists of a superconducting ring separated by two Josephson tunnel junctions with each junction separated by an insulating layer. A

'supercurrent' can tunnel through the junctions with its value varying sinusoidally with the integral of the magnetic field through the ring area. Scanning SQUID microscopy (SSM), therefore, is a magnetic microscopy technique that uses SQUID to deliver images no other technique can achieve in terms of magnetic sensitivity (see figure 2.7). The first functional SSM was demonstrated in 1991 by Black, et al. [25]. The primary disadvantage of SSM is that the spatial resolution is typically on the order of $10\ \mu\text{m}$, which is predominantly limited by the area of the superconducting ring [8]. Another disadvantage is that the scan times typically take 2 – 3 hours due to measurement averaging [26].

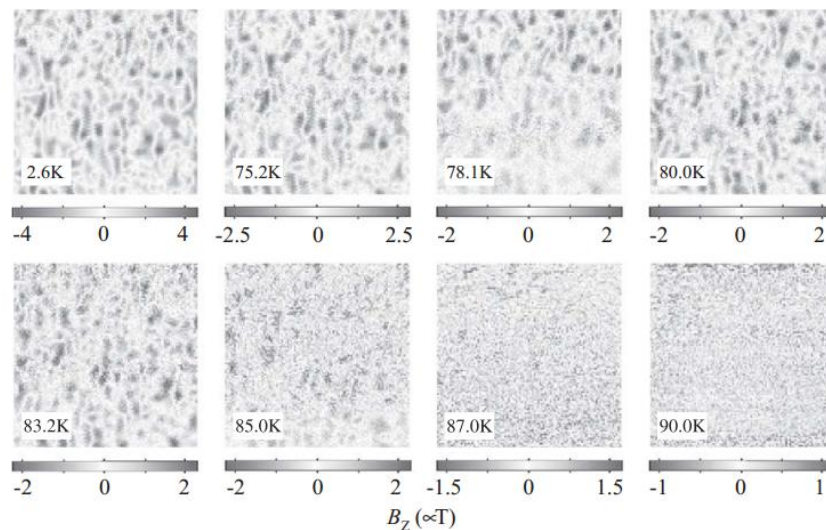


Figure 2.7: Set of scanning SQUID micrographs of a $\text{Sm}_2\text{Mo}_2\text{O}_7$ epitaxial thin film as a function of temperature. The image dimensions are $200 \times 200\ \mu\text{m}$ [27].

2.3.8 Scanning Hall Probe Microscopy

Scanning hall probe microscopy (SHPM) is a quantitative and non-invasive imaging technique for obtaining images of the magnetic field distribution on a sample surface (see figure 2.8). The technique makes use of the Hall effect which is the production of a voltage across a conducting material due to a magnetic field inducing a Lorentz force on the conduction electrons resulting in charge separation. The spatial resolution of the technique is limited by the size of the Hall sensor with probes now being fabricated at $50\ \text{nm}$ [28]. The temporal resolution of the technique is on the order of a second and can allow the instrument to be operated in real-time [29]. In terms of operation it is very similar to other scanning probe microscopy (SPM)

techniques, such as MFM, where a force-distance feedback is employed via incorporation of scanning tunnelling microscopy (STM) techniques to enable the probe to follow the sample topography. Alternatively, SHPM can operate in ‘lift-off’ mode where the probe is moved to a certain height above the sample allowing the head to be scanned extremely fast. Since the technique was first developed it has steadily been improved to operate at higher temperatures and can now operate at room temperature; however, this limits resolution and increases the time required to perform averaging as there is reduced signal-to-noise at room temperature.

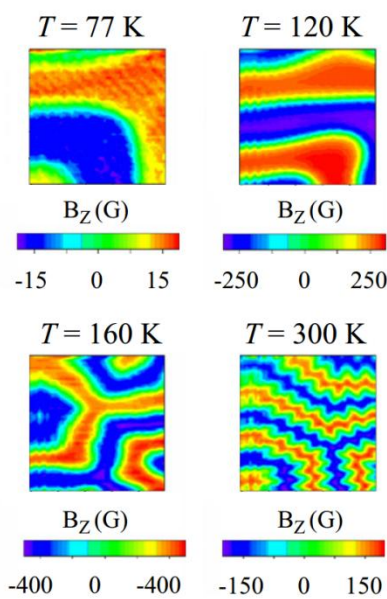


Figure 2.8: Set of SHPM micrographs of 50 μm thick iron garnet films as a function of temperature [30].

2.3.9 Nitrogen Vacancy Magnetometry

Nitrogen vacancy magnetometry (NVM) is an emerging technique [31] that relies on optically detected magnetic resonance (ODMR) to spatially resolve magnetic field. It is a scanning technique capable of imaging $> 100 \mu\text{m}$ field of view with a spatial resolution $\geq 400 \text{ nm}$ and a temporal resolution of several minutes. Central to the technique is a diamond chip that has been doped with a 10 nm thick layer of nitrogen vacancy (NV) colour centres. The electronic spin states of the NV centres are optically polarised and excited with green laser light, whilst being subjected to resonant microwave fields. The spin-state of the centres is detected via

fluorescence emission. Localised magnetic fields generate a Zeeman-shifting of the NV electronic spin resonance frequency which can be detected spectroscopically.

In figure 2.9, a NV-layered diamond chip acts as the substrate for a layer of magnetotactic bacteria. These bacteria have organelles that contain magnetite that keep the bacteria aligned to Earth's magnetic field [32]. Figure 2.9a is the wide-field optical micrograph of the bacteria whilst figure 2.9b is the NV-ODMR micrograph of the bacteria revealing dipolar magnetic contrast.

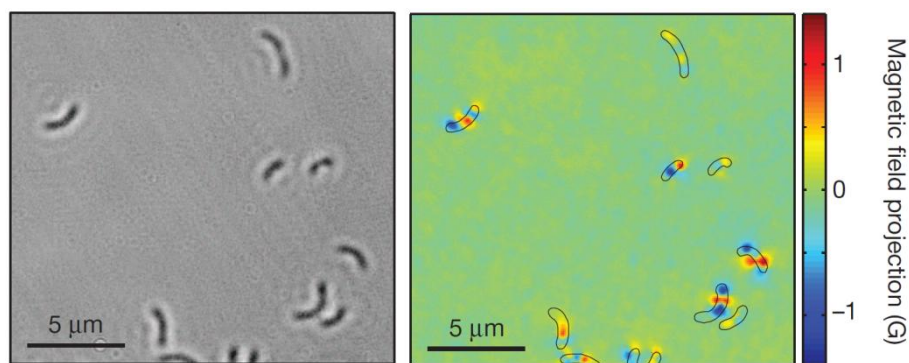


Figure 2.9: (a) Wide-field optical image of magnetotactic bacteria. (b) Nitrogen vacancy optically detected magnetic resonance image of the same region as shown in (a) [31].

2.3.10 Summary of Techniques

It has been shown, then, that there are numerous techniques available with which to observe magnetic structure at microscopic scales. However, not all techniques are suited to every situation. MFM can achieve high spatial resolution with no rigorous sample preparation but suffers from poor temporal resolution and is predominantly a qualitative technique. SSM has an extremely high sensitivity to magnetic fields but only has a spatial resolution in the order of tens of microns. Lorentz microscopy has high spatial and temporal resolution but is inherently limited to ultrathin samples. SEMPA can measure the magnetisation vector of a domain in a sample at a very high resolution without any sample thickness restraints but requires a UHV system that is very expensive and has image capture times which are quite long. Another problem common to both Lorentz microscopy and SEMPA is that external magnetic fields are difficult to apply without disturbing the electrons used for imaging. Table 2.1 contains a

summary of the various techniques discussed including the current spatio-temporal resolutions published in the literature. It must be noted, however, that these values are constantly being improved upon and therefore only represent a snapshot in time of the current state-of-the-art in magnetic microscopy.

Technique	Spatial Resolution	Temporal Resolution	Quantity Measured	Issues	Capital Investment
Lorentz Microscopy	$\geq 2 \text{ nm}$ [9]	40 ms [8]	Field	Samples need to be electron transparent.	Very high
Kerr Microscopy	$\frac{\lambda}{2(n \sin \theta)}$ $\approx 300 \text{ nm}$	230 fs – 200 ps [8, 13]	Magnetisation	Diffraction-limited spatial resolution.	Low to high
SEMPA	$\geq 5 \text{ nm}$ [15]	1 – 45 minutes [8, 16]	Magnetisation	UHV required. Poor temporal resolution.	Very high
M-TXM	$\geq 25 \text{ nm}$ [17]	$< 100 \text{ ps}$ [18]	Magnetisation	Best results obtained from synchrotron.	Extremely high
X-PEEM	$\geq 20 \text{ nm}$ [8]	$\approx 100 \text{ ps}$ [21]	Magnetisation	Best results obtained from synchrotron.	Extremely high
MFM	10-50 nm [9, 22]	26 – 300 s [23]	Field	Poor temporal resolution.	Moderate
SSM	$\geq 10 \mu\text{m}$ [8]	2 – 3 hours [26]	Field	Poor spatial resolution.	Very high
SHPM	$\geq 50 \text{ nm}$ [28]	1.4 s [29]	Field	Low temperature offers better scans.	Moderate
NVM	$\geq 400 \text{ nm}$ [31]	$\approx 1 - 5 \text{ minutes}$ [31]	Field	Sample has to be thin to interact with diamond substrate.	High

Table 2.1: Summary of magnetic microscopy techniques [10, 19].

It is therefore apparent that there is still an unfulfilled demand for a technique that can offer both high spatial and temporal resolution whilst being able to externally apply magnetic fields to a sample. It is also desirable for any new technique to work at standard laboratory environmental conditions (e.g. no vacuum system needed), to be affordable, and for the sample to not be dimensionally constrained significantly.

2.4 Photoluminescence Processes

At this stage in the literature review it is important to explain some of the basic photoluminescence processes that will be discussed in §2.5 and beyond.

2.4.1 Electronic States

In an organic semiconducting molecule (OSC) electrons exist in a configuration referred to as a molecular orbital (MO). If two electrons with anti-parallel spins ($\uparrow\downarrow$ or $\downarrow\uparrow$) occupy one MO then the multiplicity (a measure of the amount of unpaired spin) is equal to:

$$2\mathbf{S} + 1 = (2 \times (+\frac{1}{2} - \frac{1}{2})) + 1 = 1 \quad \text{Equation 2.2}$$

where \mathbf{S} = total spin angular momentum. The molecule is said to be in the singlet state (see figure 2.10). If parallel spins ($\uparrow\uparrow$ or $\downarrow\downarrow$) occupy one MO then the multiplicity equals:

$$2\mathbf{S} + 1 = (2 \times (+\frac{1}{2} + \frac{1}{2})) + 1 = 3 \quad \text{Equation 2.3}$$

The molecule is said to be in the triplet state (see figure 2.10). The electron spins forming the triplet state can arrange themselves into three different configurations, each having the same energy at zero magnetic field (referred to as being degenerate).

A multiplicity of 2 is referred to as the doublet state, but is only observed in systems with net spin of $\frac{1}{2}$, such as radicals.

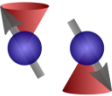
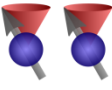
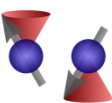
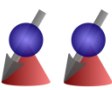
State	State Symbol	S	M _S	Spin Vector Illustration
Singlet	S	0	0	
Triplet	T ⁺	1	+1	
Triplet	T ⁰	1	0	
Triplet	T ⁻	1	-1	

Figure 2.10: List of paired exciton spin states encountered in organic semiconductors. The spin and magnetic quantum numbers are listed as well as a vector representation of the electron spins forming each state.

During absorption of a photon by a molecule, an electron is excited forming an excited quasi-particle state known as an exciton. An exciton consists of an electron-hole pair that is in a bound state such that both particles are attracted to each other via the Coulomb force. If the pair separate onto different molecules the quasi-particle is then known as a polaron [33].

2.4.2 Jabłoński Diagram

A Jabłoński diagram (see figure 2.11) is a diagrammatic representation of electronic states in a molecular system. It is a useful tool in the field of spectroscopy as it allows for the visualisation of absorptive, radiative and non-radiative transitions associated with the electronic and vibrational transitions found in these molecular systems. The energy levels depicted in figure 2.11 are the product of electronic and vibrational states (also known as vibronic levels) available to the molecule [34].

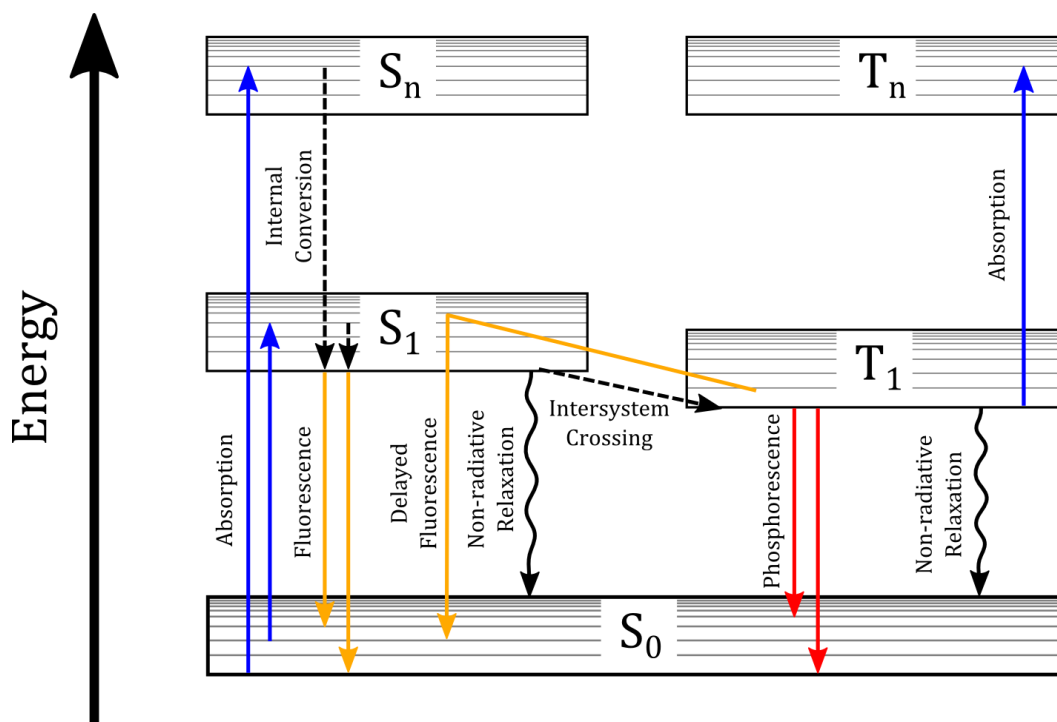


Figure 2.11: A typical Jablonski diagram illustrating the various electronic transitions that exist in an organic semiconducting molecule. S_1 = 1st singlet state; S_n = all singlet states above S_1 ; T_1 = 1st triplet state; T_n = all triplet states above T_1 ; S_0 = the electronic ground state of the molecule.

The electronic transitions that are of greatest importance are:

- Absorption. This is when a photon, absorbed by a molecule, causes a promotion of an electron into an excited state: $S_0 + h\nu \rightarrow S_1$. Intersystem absorptions are spin-forbidden due to the spin-selection rule [33]. For example, a molecule in the singlet state that absorbs a photon can only be excited to another singlet state and not a triplet state. Moreover, if the molecule is in the triplet state and absorbs a photon it can only be excited to another triplet state and not a singlet state.
- Intersystem crossing (ISC). This is the process whereby an excited molecule undergoes a ‘spin-forbidden’ non-radiative transition from a singlet state to a triplet state or vice versa: $S_1 \rightleftharpoons T_1$.
- Fluorescence. This is the process where a photon is emitted when a molecule relaxes to the ground state from the first excited singlet state: $S_1 \rightarrow S_0 + h\nu$. It can also be referred to as *prompt* fluorescence.

- Phosphorescence. This is when a molecule relaxes from the first triplet state to the singlet ground state via emission of a photon: $T_1 \rightarrow S_0 + h\nu$. This process is actually spin-forbidden, but can occur if the system has strong spin-orbit coupling [35].
- Delayed fluorescence (DF). There are three types of DF known [36]:
 - E-type DF: This is when the first excited singlet state becomes populated from the first excited triplet state via a reverse ISC. This type of DF is a thermally activated process. $T_1 \rightarrow S_1 \rightarrow S_0 + h\nu$.
 - P-type DF: This is when two molecules (a + b), both in the triplet state, collide and annihilate the triplet states to form one molecule in the first excited singlet state and one in the singlet ground state. The excited singlet will eventually relax to the ground state with the emission of a photon: $T_1^a + T_1^b \rightarrow S_1^a + S_0^b \rightarrow S_0^a + h\nu$. This mechanism of DF is also known as triplet-triplet annihilation (or fusion).
 - Recombination DF: the S_1 state becomes populated via radical ion recombination.
- Non-radiative relaxation: This is a transition between states of the same spin multiplicity: $S_1 \rightarrow S_0$. Non-radiative relaxations compete with radiative transitions, such as fluorescence or phosphorescence, and are one factor involved in determining efficiencies as shown in equation 2.7 below.

2.4.3 Franck-Condon Principle

The Franck-Condon principle [37] is a rule that is often used when trying to understand the structure of absorption and fluorescent spectra. The principle states that during a radiative transition, such as photon absorption, a molecule in the ground state, R, will undergo an electronic reconfiguration. This reconfiguration, however, occurs on a time-scale much faster than that of nuclear motions, therefore the excited molecule, R*, is only able to redistribute its nuclei into their equilibrium positions in response to the electronic reconfiguration after the electronic transition has taken place. If one then considers the equilibrium potential energy

curves of both R and R* (including vibronic levels) as a function of nuclear separation (figure 2.12) it is seen that R* will tend to have a slightly increased nuclear separation compared to R as a direct consequence of the electronic reconfiguration. Due to the fact that the radiative transitions occur practically instantaneously, they are considered to be *vertical* transitions with respect to the nuclear geometry.

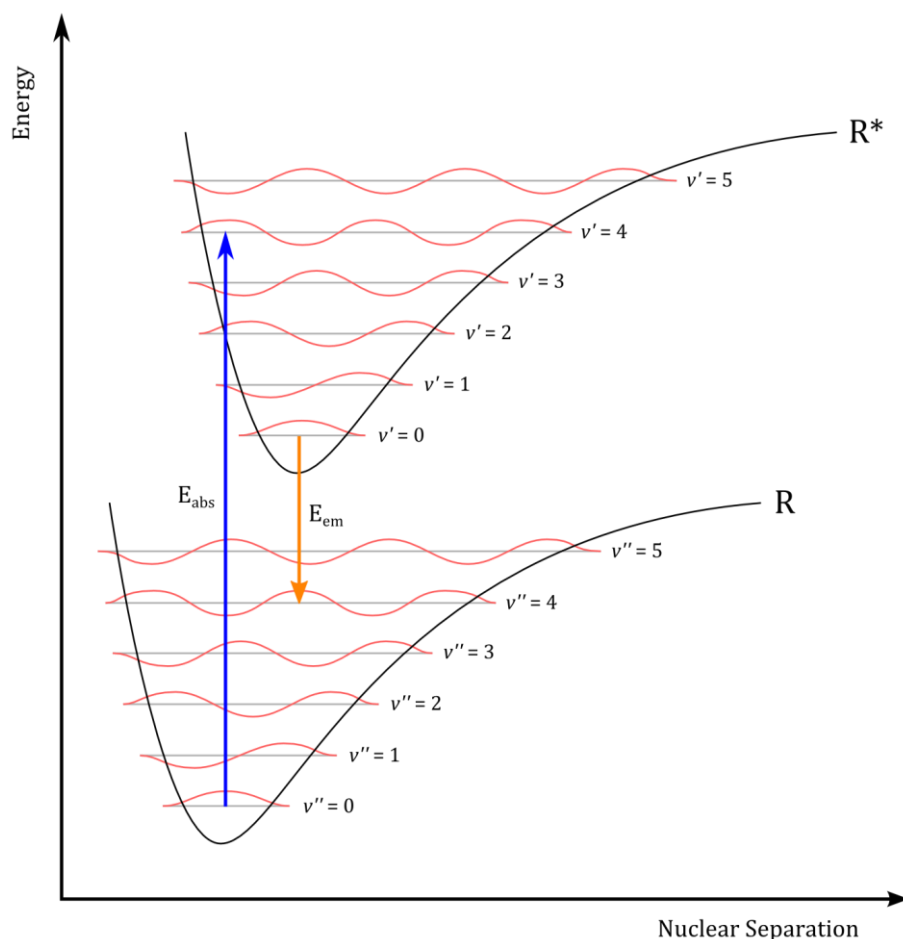


Figure 2.12: Energy level diagram demonstrating the Franck-Condon principle for radiative transitions in a diatomic molecule. Each curve is a Morse potential representing the potential energy of the molecule in the ground state, R, and the excited state, R*. E_{abs} is the energy required to excite the molecule from $v'' = 0$ to $v' = 4$, whilst E_{em} represents the energy released during a radiative transition from $v' = 0$ to $v'' = 4$.

Under this scenario, the Franck-Condon principle states that the probability for the transition to occur is directly proportional to the square of the overlap integral of the wavefunctions of the initial and final vibrational energy levels involved in the transition. This mechanism therefore explains the observed peak intensity variation seen in absorption and emission spectra as being a consequence of either good wavefunction overlap (large peak) or poor wavefunction overlap

(small peak). It also explains the mirror symmetry that is often seen between the absorption and emission bands of fluorescent molecules. As excited molecules quickly relax non-radiatively to the lowest excited state and only emit with appreciable yield from this lowest excited state (Kasha's rule) a radiative transition symmetry is formed such that absorption generally occurs from $v'' = 0$ to $v' = n$ whilst fluorescent emission generally occurs from $v' = 0$ to $v'' = n$, where n is the set of vibrational levels: 1, 2, 3, etc. This mirror symmetry is depicted in figure 2.13.

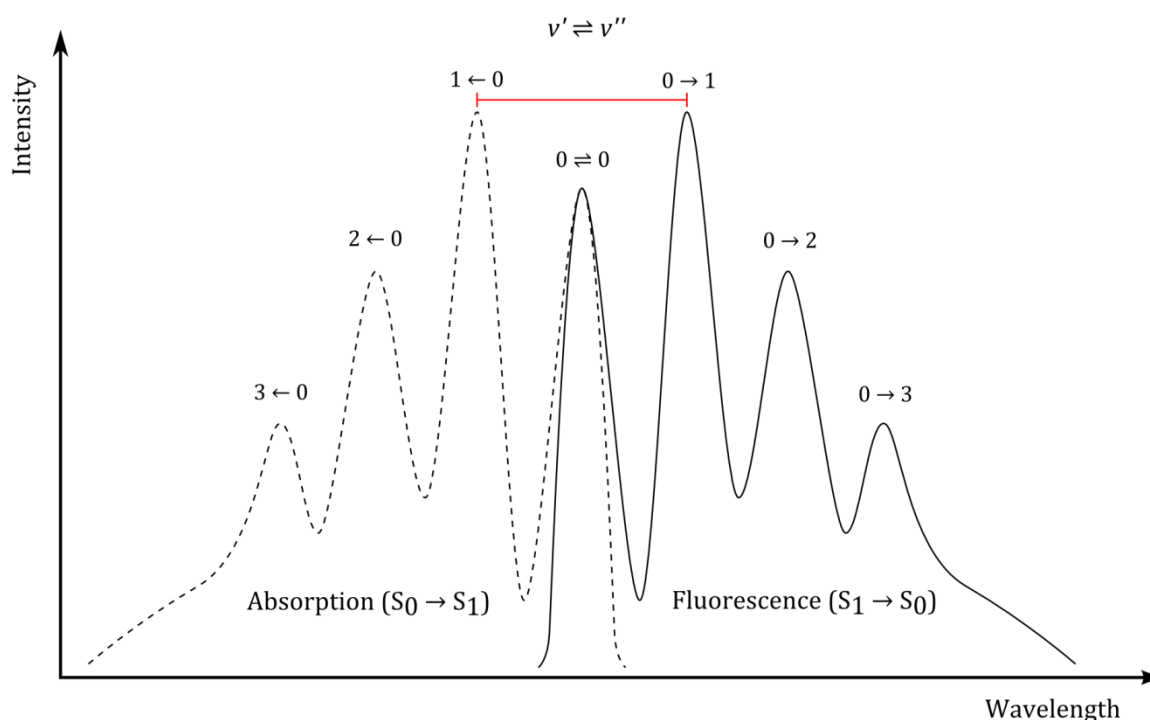


Figure 2.13: Example absorption and fluorescent spectra of a molecule demonstrating Stokes shift (red interval marker) between the largest absorption and emission peaks as well as vibronic band structure.

Another phenomenon that can be explained via mirror symmetry is known as Stokes shift [37] and is highlighted in figure 2.13 (by the red interval marker). Stokes shift is the measured difference in wavelength between the highest intensity absorption peak and the highest intensity fluorescence peak. It is explained by the fact that the energy required to excite the molecule, R, into the excited state, R^* , is larger than the energy that is released during the radiative relaxation of the molecule from R^* to R. This energy discrepancy is accounted for as thermal dissipation via an internal conversion process that the molecule undergoes when it is in the excited state (e.g. $v' = n \rightarrow v' = 0$).

The breadth of the absorption and emission bands results from the number of vibronic levels available to the molecule. For instance, atomic spectra are characterised as having sharp lines as a result of not having any vibrational modes available whilst a molecule dissolved in a solvent has broad-band spectra due to an abundance of available vibrational and rotational modes.

2.4.4 Rate Constants, Lifetimes and Quantum Yields

Transitions between electronics states occur within a fast, but finite time. These times, or lifetimes are unique for each transition. The lifetime of a state is:

$$\tau = \frac{1}{k} \quad \text{Equation 2.4}$$

where k is the rate constant (with units of seconds⁻¹). Figure 2.14 illustrates the primary rate constants whilst table 2.2 provides descriptions.

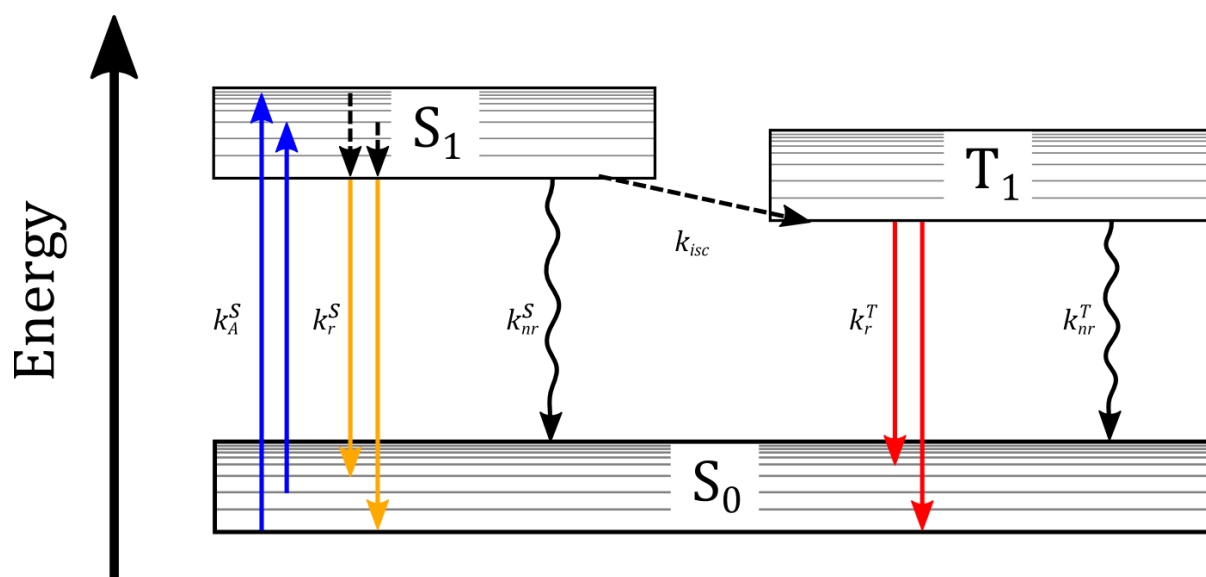


Figure 2.14: A Jablonski diagram illustrating the rate constant nomenclature for a generalised organic semiconducting molecule.

Symbol	Description
k_A^S	Rate of absorption from $S_0 \rightarrow S_1$
k_r^S	Rate constant of radiative relaxation $S_1 \rightarrow S_0$ (fluorescence)
k_{nr}^S	Rate constant of non-radiative relaxation $S_1 \rightarrow S_0$
k_{isc}	Rate constant for intersystem crossing $S_1 \rightarrow T_1$
k_r^T	Rate constant of radiative relaxation $T_1 \rightarrow S_0$ (phosphorescence)
k_{nr}^T	Rate constant of non-radiative relaxation $T_1 \rightarrow S_0$

Table 2.2: List of rate constants and their descriptions.

The rate of relaxation of the S_1 state is:

$$k_S = k_r^S + k_{nr}^S + k_{isc} \quad \text{Equation 2.5}$$

The lifetime of the first excited singlet state is therefore given by:

$$\tau_S = \frac{1}{k_S} = \frac{1}{k_r^S + k_{nr}^S + k_{isc}} \quad \text{Equation 2.6}$$

Fluorescence quantum yield, Φ_F , is defined as the fraction of molecules that relax back down from the excited singlet state to the ground singlet state with emission of fluorescent photons [35]. Written in terms of rate constants it is defined as:

$$\Phi_F = \frac{k_r^S}{k_r^S + k_{nr}^S + k_{isc}} = k_r^S \tau_S \quad \text{Equation 2.7}$$

2.4.5 Photobleaching

Photobleaching is a phenomenon that can occur when an intense light source, exciting a fluorescent sample, causes a reduction in the fluorescence intensity of the sample over a period of time. Two types of photobleaching exist: non-reversible photobleaching and reversible photobleaching.

Non-reversible photobleaching occurs when a highly energetic illumination source (such as UV radiation) acts to chemically decompose the active fluorophores comprising the sample. This

results in diminished photoluminescent intensity as individual molecules are deactivated. Certain materials are more susceptible to photobleaching than others. The fluorescence intensity of those that do degrade due to photobleaching tend to follow a time-dependent exponential decay [38].

Reversible photobleaching can occur in a fluorescent sample when the illumination source's incident irradiance is sufficiently high that a significant number of molecules can be promoted into the first excited triplet-state, T_1 , via intersystem crossing from the first excited singlet-state, S_1 . Once in this state the magnitude of the triplet lifetime, which is much larger than the singlet lifetime, effectively removes the molecule from the excitation-fluorescence cycle and puts it in a so-called 'dark state'. This can cause a depletion of molecules in the ground state, S_0 , with respect to the entire sample, meaning that the rate of fluorescence is no longer proportional to the incident irradiance but is instead limited to the triplet decay rate. This effectively causes a reduction in the fluorescence intensity as the overall number of fluorescent photons emitted is reduced per unit time. By removing the illumination source and allowing the triplet population to deplete over time the sample will be able to recover [39].

Photobleaching is usually an undesirable effect when performing fluorescence measurements, however, a technique known as FRAP (fluorescence recovery after photobleaching) utilises photobleaching in order to measure diffusion rates and other kinetic parameters in thin films and more usually biological samples such as cell membranes. A typical FRAP measurement involves exposing an area of the sample to an intense laser beam resulting in localised photobleaching. This area is then monitored with a low power excitation source to observe recovery of fluorescence which is attributed to the diffusion of unbleached molecules diffusing into the area [40].

2.4.6 Heavy-Atom Effect

Transitions between pure spin states of different spin multiplicities are forbidden by the spin selection rules due to the conservation of angular momentum. In reality, however, many

materials often exhibit these spin-forbidden transitions suggesting that there must be a mechanism to account for these observations. One of these mechanisms is referred to as the heavy-atom effect (or sometimes the heavy-ion effect). The heavy-atom effect is an enhancement of the rate of a spin-forbidden transition, such as the radiationless intersystem crossing transition $S_1 \rightarrow T_1$ (and generally any transition between the singlet and triplet states $S_n \rightleftharpoons T_n$), by the presence of an atom with a high atomic number. This phenomenon occurs due to a Z^4 -dependent strengthening of the spin-orbit coupling of the electron when in the vicinity of the “heavy atom” [41, 42] where the effects typically become apparent for elements possessing an atomic number equivalent to bromine and above. For example, reductions in the triplet lifetime (τ_T) are also observed as a result of the heavy-atom effect [43], and is expected, as the transition ($T_1 \rightarrow S_0$) is also a spin-forbidden process. The heavy-atom effect is often considered as being a quenching mechanism in fluorescent materials as the fluorescence efficiency is reduced in materials where intersystem crossing from $S_1 \rightarrow T_1$ is enhanced by the effect [44].

Generally, there are two types of heavy-atom effect that exist: internal heavy-atom (IHA) effect and external heavy-atom (EHA) effect [45]. The IHA effect describes the enhancement of spin-forbidden transitions caused by a heavy-atom that is chemically bonded to the molecule experiencing the rate enhancement. The EHA effect describes the enhancement of the spin-forbidden transitions caused by a heavy-atom that can exist in a liquid mixture such as a solvent that contains the fluorescent solute [46], as an ionic species that is weakly bonded to the fluorescent molecule [47], or as a solid mixture such as part of a polymer matrix encapsulating fluorescent molecules [48].

One example of where the heavy-atom effect can be seen is in a class of metal-organic framework materials such as the metal-tris-quinolate complexes (see figure 2.15). These complexes comprise of three organic ligands bonded to a central metal atom. By increasing the atomic number of the central atom (e.g. $Al \rightarrow Ga \rightarrow In$) it has been observed [49] that the fluorescence and electroluminescence efficiency of this series reduces due to an increase in the

rate of intersystem crossing attributed to “heavy atom quenching”. It has also been observed [50] that red-shifting of the photoluminescent emission occurs due to intramolecular charge transfer from the metal to the ligand and that the magnitude of the shift increases with the mass of the central metal atom.

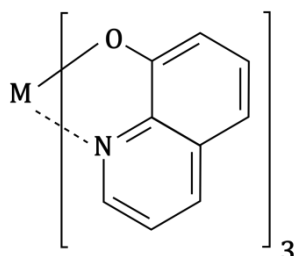


Figure 2.15: Skeletal formula of a generalised metal-tris-quinolate molecule.

The heavy-atom effect has also been exploited commercially to increase triplet efficiencies of certain phosphors [37, 51].

2.5 Magnetic Field Effect

2.5.1 Definition

In this section an area of photoluminescence research that has received sporadic attention and has had, up until now, no known technological applications realised will be discussed. Called the ‘magnetic field effect’ (MFE) in the literature, this phenomenon describes a relative change in either photoluminescence, electroluminescence, photocurrent or electrical-injection current when an external magnetic field is applied [33]. The effect is usually observed in organic semiconductors and has recently drawn new interest due to its potential to aid development in organic spintronics [33].

$$\text{MFE} = \frac{I_B - I_0}{I_0} \times 100\% \quad \text{Equation 2.8}$$

Equation 2.8 defines the MFE where I_B is the intensity of the signal when an external magnetic field is applied; and I_0 is the intensity of the signal when no field is applied.

2.5.2 MFEs in Linear Polycyclic Aromatic Hydrocarbons

One of the first observations of an MFE was by Johnson and Merrifield [52] in 1967. They noticed that when an external magnetic field is applied to a fluorescent anthracene crystal the intensity of the delayed fluorescence (DF) initially increased, then decreased, with increasing magnetic field amplitude (see figure 2.16). Sensitivity to crystal orientation was also observed. The largest observed change in DF was -20%.

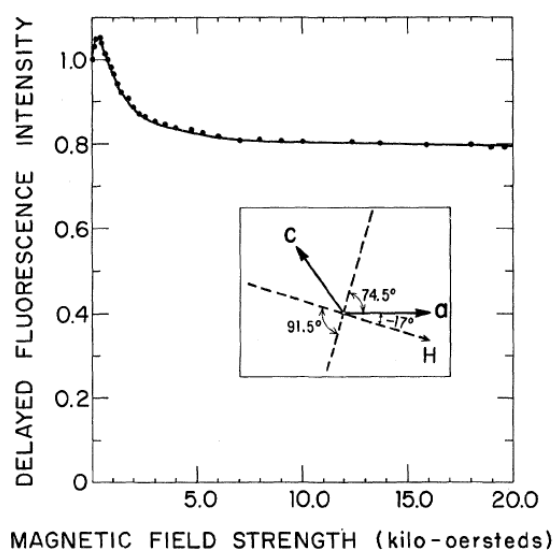


Figure 2.16: Plot of delayed fluorescence against magnetic field strength (kOe) of a single crystal of anthracene [52]. Copyright 1967 by The American Physical Society.

A year later Merrifield published a letter [53] where he theorised that the application of an external magnetic field actually alters the rate at which triplet exciton states annihilate with one another. This, he argues, explains the changes observed in Johnson and Merrifield's experiment. However, at the time of publishing no modelling was presented to elucidate the precise mechanics of this theory.

In 1972, Groff et al. [54] performed an experiment similar to Johnson's whereby an anthracene crystal was subjected to a magnetic field whilst being excited by light at 570 nm. The difference of this experiment was that a layer of Rhodamine B was adsorbed onto the surface of the anthracene crystal. The MFE now observed (see figure 2.17) was -60% DF at a magnetic field of

10 mT. This MFE was three times larger than that observed by Johnson and at one hundred times lower applied field.

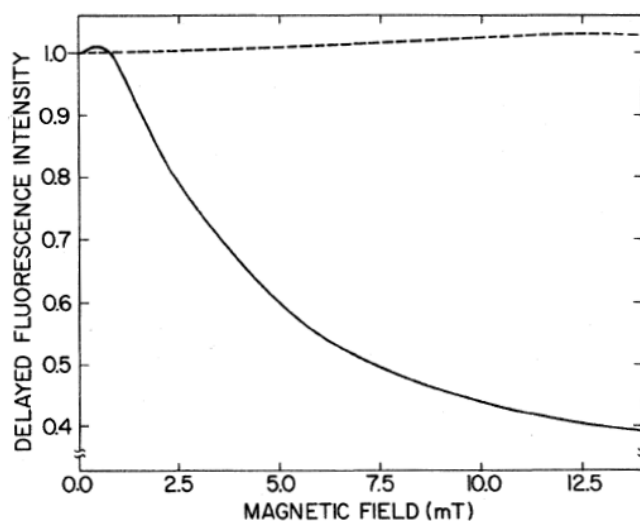


Figure 2.17: Modulation of delayed fluorescence intensity with applied magnetic field for a Rhodamine B-sensitised anthracene crystal excited at 570 nm (solid line) and 680 nm (dashed line) [54]. Copyright 1972 by The American Physical Society.

The origin of the MFE was attributed to charge injection and recombination as follows:



Using the notation ${}^aX_b^c$ where:

a = the molecular spin state (1 = singlet; 2 = doublet; 3 = triplet).

b = the molecular excitation state (1 = excited state; 0 = ground state).

c = the molecular charge.

X = the species (D = Rhodamine B dye; A = anthracene crystal).

The authors suggest that the magnetic field controls a competition between the hyperfine interaction and the Zeeman effect, such that at low fields the hyperfine interaction allows

singlet-triplet transitions to occur, but at high fields the Zeeman effect prevents the transitions from occurring. This competition manifests itself as the rate constants governing equations 2.9-12.

The authors attempted to model the system using the density matrix method by defining their own spin Hamiltonian for an electron-hole pair undergoing the singlet-triplet transition. Their result is plotted in figure 2.18.

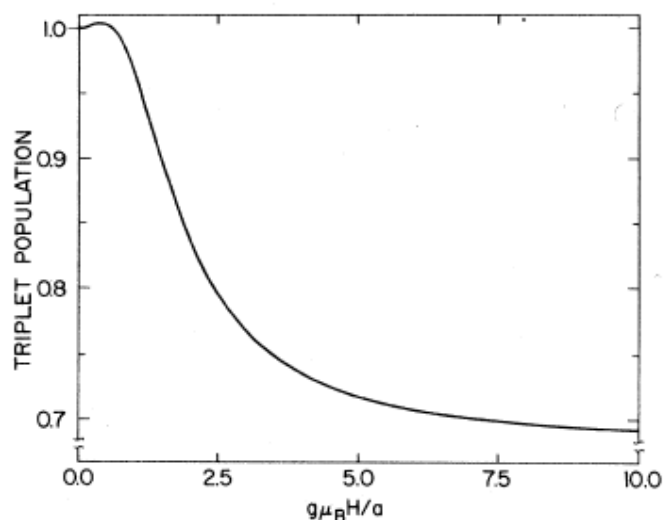


Figure 2.18: Modelled triplet population versus simulated applied field [54]. Copyright 1972 by The American Physical Society. The modelled results shown here are qualitatively similar to the experimental results shown in figure 2.17.

Although Groff's model is qualitatively correct, it is by no means quantitatively accurate. Indeed, it does not manage to replicate the magnitude of the MFE observed in the experimental results. Groff himself suggests that a more complex model involving additional protons may accomplish this.

In the same year Klein, et al. [55] observed (see figure 2.19) an MFE for *prompt* fluorescence in anthracene that had, until then, not been documented. This new MFE in anthracene was likely not observed before as it saturates at only +0.8% for 400 mT of applied magnetic field.

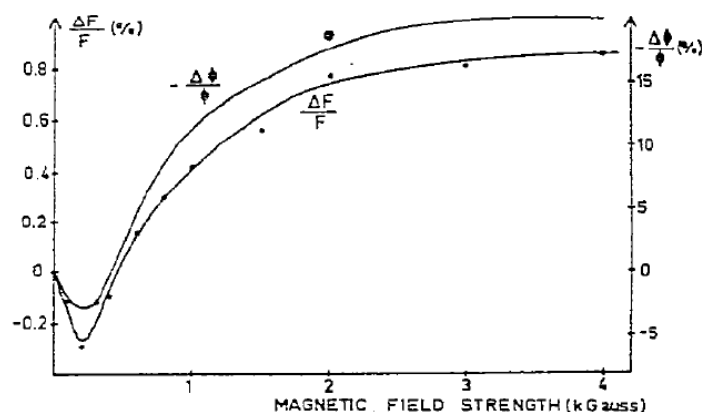


Figure 2.19: A plot of change in fluorescence intensity against applied magnetic field for the molecule anthracene [55]. The bottom line corresponds to the prompt fluorescence MFE result whilst the top line is a comparison with delayed fluorescence MFE observed by Johnson et al. [56].

An MFE on prompt fluorescence, however, had been observed before for another molecule, tetracene, which is almost identical to anthracene with the addition of one extra aromatic ring. This experiment, performed by Groff, et al. [57], explored the idea [58] that the reason tetracene has such a poor Φ_F [59] is because a dominant loss mechanism exists of the form:



where γ = rate of T-T annihilation and γ' = rate of S-S fission (see below). Groff suggests that not only does triplet-triplet annihilation occur, leading to an MFE exhibited in delayed fluorescence, but that the opposite process, *singlet fission*, may result in an MFE being exhibited in prompt fluorescence. This could be imagined in a material where singlet fission is the dominant process. In this scenario a magnetic field may act to *reduce* the rate of this process, causing a reduction in the population of molecules being converted from the singlet state into the triplet state. This would manifest macroscopically as an increase in prompt fluorescence intensity with applied magnetic field. The results of Groff's experiment, as shown in figure 2.20, appear to demonstrate that $\gamma' \propto \text{temperature}$.

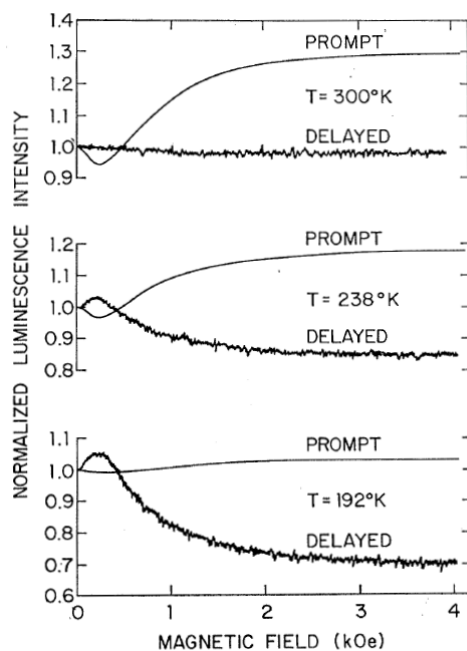


Figure 2.20: Changes in prompt and delayed fluorescence intensities measured at 300 K, 238 K, 192 K for tetracene with applied magnetic field [57]. Copyright 1970 by The American Physical Society.

This result was also seen by another group [60] as shown in figure 2.21. This group also saw the same MFE operating when the tetracene crystal was excited in an electroluminescent setup.

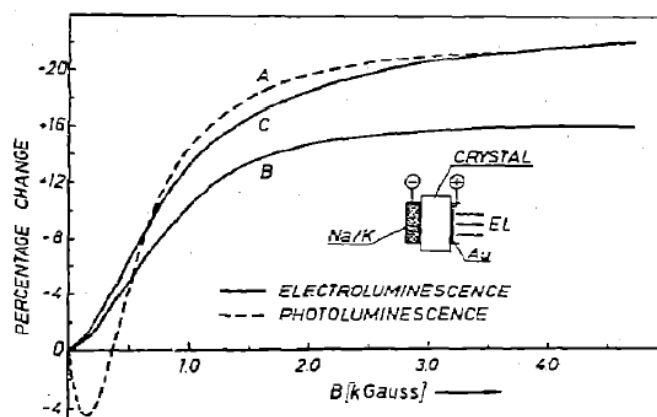


Figure 2.21: Changes in photoluminescence (line A) and electroluminescence (line B and C) from a tetracene crystal with respect to an applied magnetic field [60].

2.5.3 MFEs in Other Systems

Recently, a new wave of research has come into existence looking at MFEs in other molecular systems. An experiment performed by Garditz et al. [61] investigated MFEs in amorphous

materials. They chose to look at the photoluminescence (PL) and electroluminescence (EL) properties of tris-(8-hydroxyquinoline)aluminium(III) (Alq_3) as well as perform some MFE measurements.

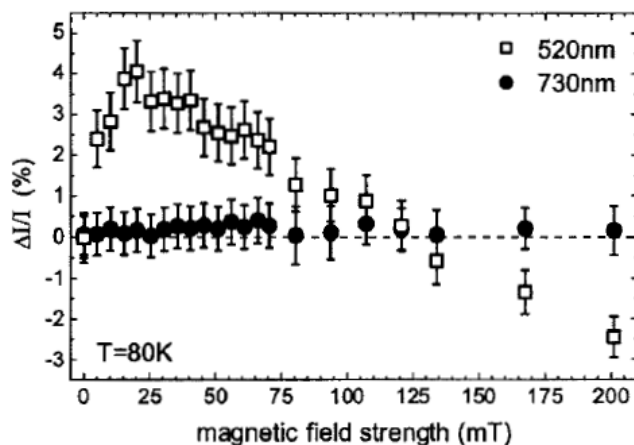


Figure 2.22: Relative change of EL intensity with respect to an applied magnetic field at 80 K. The squares represent delayed EL whilst the circles represent phosphorescent EL [61].

From their results at 80 K (figure 2.22), it can be seen that there is a marked response in the delayed EL to the externally applied magnetic field. At 20 mT the MFE reaches +4% before returning to 0% at 125 mT and continuing to beyond -3% above 200 mT. The phosphorescent EL, on the other hand, shows no obvious response at all, and is deemed to be independent of applied magnetic field.

Figure 2.23 shows the experimental results achieved at 280 K. Here the authors looked at relative changes in prompt EL (figure 2.23a), prompt PL (figure 2.23c) and voltage applied to the EL device in a constant current set-up (figure 2.23b). At these higher temperatures, it is shown that prompt EL can achieve a similar $\Delta I/I$ to delayed EL as shown in figure 2.22. It is tempting to compare this result to Groff's MFE result for tetracene (figure 2.20) [57], where, depending on temperature, the delayed and prompt fluorescence swap character. Unfortunately, one cannot make such a comparison as Garditz has not performed prompt EL measurements at 80 K and has not performed delayed EL measurements at 280 K. Perhaps these data were not published as no MFE was observed.

The prompt PL data (figure 2.23c) shows a small but clear increase in $\Delta I/I$ with applied magnetic field and appears to saturate at around +1%. This result appears similar to Klein's prompt fluorescence MFE result for anthracene (figure 2.19) [55].

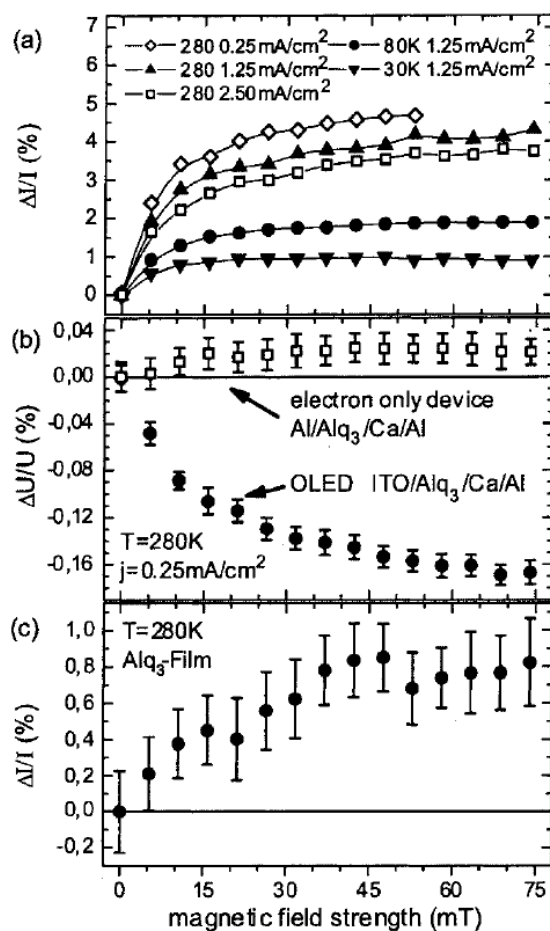


Figure 2.23: a) Relative change in prompt EL with applied magnetic field b) Relative change in voltage (at constant current) with applied magnetic field c) relative change in prompt PL with applied magnetic field [61].

2.5.4 Current Understanding

In order to explain how an external magnetic field may influence photoluminescent intensities or intersystem crossing rates, it is important to identify what conditions have to occur and what mechanisms are available in order to convert an excited molecule from a spin state of one multiplicity to another (e.g. $S_1 \rightarrow T_1$). Presented below are three mechanisms that are known to be able to provide a magnetic torque on a spin magnetic moment.

Zeeman Coupling is a spectroscopic phenomenon whereby the presence of an external magnetic field causes degenerate energy levels to split into separate levels (this result is known as Zeeman splitting). The effect originates from a coupling between the magnetic moment of an atom with an external magnetic field. The Hamiltonian is given by [62]:

$$H_{\text{zeeman}} = -\frac{\langle \boldsymbol{\mu} \cdot \mathbf{J} \rangle}{J(J+1)} \mathbf{J} \cdot \mathbf{B} = \frac{\langle \mathbf{L} \cdot \mathbf{J} \rangle + g_s \langle \mathbf{S} \cdot \mathbf{J} \rangle}{J(J+1)} \mu_B B J_z \quad \text{Equation. 2.14}$$

where $\boldsymbol{\mu}$ is the total magnetic moment of the atom, \mathbf{J} is the total angular momentum of the atom, \mathbf{B} is the external magnetic field, \mathbf{L} is the total orbital angular momentum and \mathbf{S} is the total spin angular momentum, g_s is the Landé g-factor, μ_B is the Bohr magneton and J_z is the projection of the total angular momentum of the atom onto the z-axis. As an example, if an atom is in the first excited triplet state, T_1 , a magnetic field will act to split it into three non-degenerate sub-levels T_1^{-1} , T_1^0 , and T_1^{+1} (see figure 2.10). The difference in energy between T_1^0 and $T_1^{\pm 1}$ in a magnetic field of 100 mT can be approximately calculated as:

$$\begin{aligned} E_{\text{zeeman}} &= M_S g \mu_B B \\ &= \pm 1 \times 2 \times 9.274 \times 10^{-24} \text{ J} \cdot \text{T}^{-1} \times 100 \text{ mT} \\ &= \pm 11.6 \text{ } \mu\text{eV} \end{aligned} \quad \text{Equation. 2.15}$$

The calculation yields a rather small result compared to typical singlet-triplet energy differences, ΔE_{ST} , such as 1.07 eV for tetracene [63]. Therefore it is unlikely that Zeeman coupling plays an exclusive role in MFE theories, such as those that attempt to explain experimental MFE observations on the basis of bringing the T_1^{+1} level to be isoenergetic with the S_1 energy level enabling spin-flipping.

There have been several theories published, however, that invoke Zeeman coupling as acting in combination with other mechanisms to produce MFE, and are discussed below.

Hyperfine Coupling describes an interaction between the magnetic moments of the electron spin and the nuclear spin and is given by the Hamiltonian [62]:

$$H_{\text{hyperfine}} = -\boldsymbol{\mu}_I \cdot \mathbf{B}_e \quad \text{Equation. 2.16}$$

where $\boldsymbol{\mu}_I = g_I \mu_N \mathbf{I}$ is the magnetic moment related to the nuclear spin \mathbf{I} , and \mathbf{B}_e is the magnetic flux density created by the atomic electrons. In the case of mobile conduction electrons the dominant transport mechanism in an OSC is hopping. During this process electrons encounter local hyperfine fields from nearby nuclei and precess around them. Since each hopping site has differently oriented hyperfine fields the precession axis will change and is therefore a popular explanation for the occurrence of spin relaxation in many organic spintronic devices [64]. The hyperfine interaction has been implicated in playing a role in the mixing of spin states in devices exhibiting organic magnetoresistance (OMAR) where the line-shape of the OMAR is related to the hyperfine field strength [65].

To explain the electroluminescent (EL) MFE observed in Alq₃, Kalinowski, et al. [66] described how if the applied magnetic field is greater than the hyperfine coupling, Zeeman splitting of the T₁ state will occur producing three non-degenerate levels. It is then suggested that this will remove the degeneracy between sub-levels T₁^{±1} and the S₁ state. Kalinowski then states that this will act to reduce S→T spin conversion mediated by hyperfine coupling. This analysis is based on an incorrect assumption that the singlet and triplet states are isoenergetic. In fact, the S₁ state energy of Alq₃ has been measured as 2.38 eV [67] whilst the T₁ state energy has been measured as 2.05±0.1 eV [68] giving an energy difference, E(S₁-T₁) = 0.33±0.1 eV. Odaka, et al. [69] have also cast doubt on Kalinowski's proposal on EL-MFE as any Zeeman-splitting mediated reduction in the S₁→T₁ spin conversion should also suppress the conversion from T₁→S₁ spin conversion and essentially leave the singlet population unchanged for electrically excited MFE. Odaka, instead, suggests that Zeeman splitting should cause the energy of T₁⁺¹ state to approach the S₁ state opening a channel of spin state conversion (T₁⁻¹ ↔ S₁). This seems doubtful, however, since (as has been previously stated) the Alq₃ S-T energy difference, E(S₁-T₁) = 0.33±0.1 eV whilst a magnetic field of 100 mT would only reduce this difference by approximately 11.6 µeV, effecting minimal change on the intersystem crossing rates.

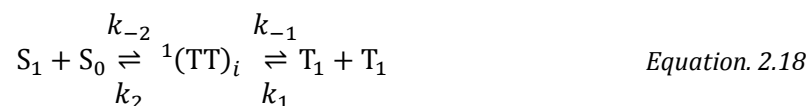
Spin-Orbit Coupling is a quantum mechanical phenomenon whereby the magnetic moment of an electron's spin couples to its orbital motion. The Hamiltonian is given as [70, 71]:

$$H_{so} = \frac{1}{2m^2c^2r} \frac{dV}{dr} \mathbf{L} \cdot \mathbf{S} = \xi \mathbf{L} \cdot \mathbf{S} \quad \text{Equation. 2.17}$$

where m is the mass of the electron, c is the speed of light, r is the orbital distance from the nucleus to the electron, V is the Coulombic potential of the electron in the field of the atom, \mathbf{S} is the total spin angular momentum and \mathbf{L} is the total orbital angular momentum. This results in an effective magnetic field that causes degenerate energy levels to split into separate levels giving rise to fine structure. This coupling also provides a source of magnetic torque that can act to increase intersystem crossing rates and is known as the heavy atom effect (as previously discussed in §2.4.6). The effect strengthens proportionally with the charge of the nucleus due to the associated increase in orbital angular momentum of the electron. Therefore, this effect is weak in organic semiconducting materials that lack the presence of heavy atoms and has been traditionally viewed as being effectively negligible relative to the spin dipole-dipole interaction between electron and hole and Zeeman coupling between exciton and an external magnetic field. Recently, however, it has been shown by Nuccio, et al. [64] using the muon spin resonance (μ SR) technique that there does appear to exist a non-negligible spin-orbit coupling in light-atom organic semiconductors, such as Alq₃, which may explain the larger than expected spin relaxation and intersystem crossing rates that have been experimentally observed in these materials.

* * *

In recent times it has generally been accepted [63] that the photoluminescent magnetic field effect (PL-MFE) phenomenon exhibited by anthracene, tetracene, and others is caused by a magnetic field-dependent bimolecular radiationless transition process referred to as singlet exciton fission, which can be expressed by the following equation:



where ${}^1(\text{TT})_i$ is a correlated triplet pair state and k_1, k_2, k_{-1}, k_{-2} are the rate constants. When $\sum_1^2 k_{-n} > \sum_1^2 k_n$ the process is referred to as singlet exciton fission (SF) and is responsible for prompt fluorescent MFE. When $\sum_1^2 k_{-n} < \sum_1^2 k_n$ the process is referred to as triplet exciton fusion (TF) and is responsible for delayed fluorescent MFE. The singlet exciton fission process is understood to be based on a spin-allowed geminate recombination mechanism whereby a molecule in the singlet ground state, S_0 , interacts with a molecule in the first excited singlet state, S_1 , to produce a correlated triplet pair state ${}^1(\text{TT})_i$. This pair state, which is commonly referred to as a “dark state”, as it is not directly accessible, is then able to dissociate into two free triplet excitons. This process is considered to be the primary reason why the fluorescence quantum yield of the acene series (0.25 for anthracene [72], 0.04 for tetracene [73], ~ 0 for pentacene [63]), reduces with an increasing number of aromatic rings as the energy difference between the first excited singlet state and the ${}^1(\text{TT})_i$ state, $E(S_1) - E(\text{TT})$, gets progressively smaller (see figure 2.24) allowing the singlet fission process to become the dominant singlet quenching channel. For anthracene, the energy difference is -0.53 eV (endoergic) and can be supplied optically; for tetracene, the energy difference is -0.18 eV (endoergic) and can be supplied thermally or optically; for pentacene the energy difference is +0.11 eV (exoergic) resulting in a very large SF rate constant.

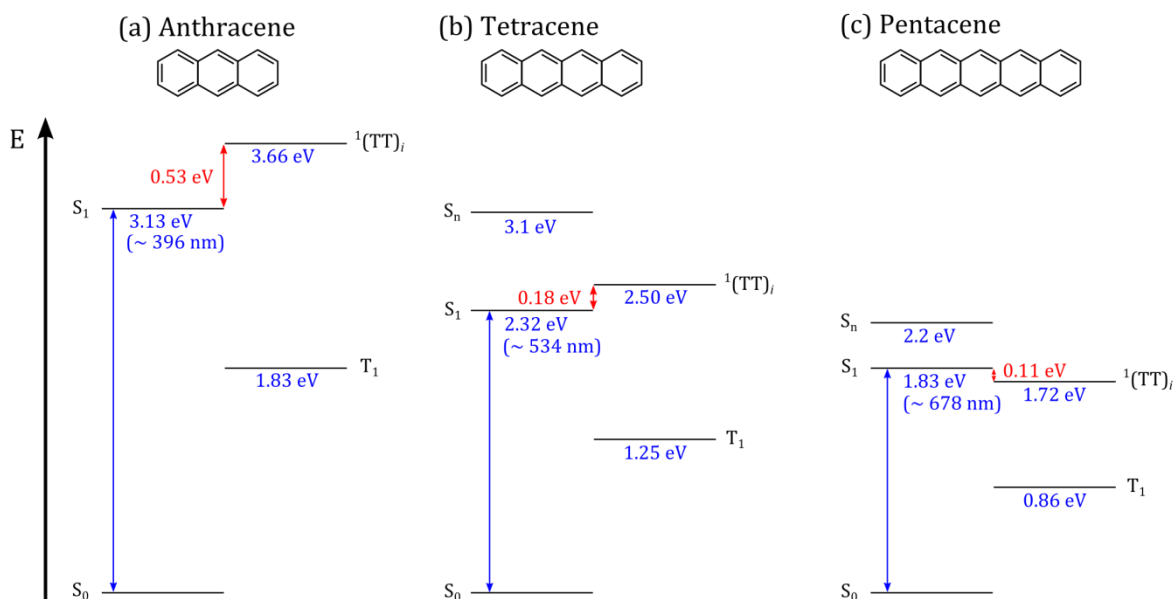


Figure 2.24: Scaled plot of spin state energies for a) anthracene, b) tetracene and c) pentacene. The energy of each of the ${}^1(TT)_i$ dark states, $E(TT) = 2E(T_1)$. Data sourced from [63, 74].

Therefore one of the prerequisites for the manifestation of singlet exciton fission is that it can occur only when $E(S_1) \approx 2 \times E(T_1)$, as this allows the ${}^1(TT)_i$ state to become isoenergetic with the S_1 state. From the onset of formation the correlated triplet pair state ${}^1(TT)_i$ can exist as one of nine possible spin states, each with varying degrees of singlet character:

$ +1, +1\rangle$	$ 0, +1\rangle$	$ -1, +1\rangle$
$ +1, 0\rangle$	$ 0, 0\rangle$	$ -1, 0\rangle$
$ +1, -1\rangle$	$ 0, -1\rangle$	$ -1, -1\rangle$

Table 2.3: The nine possible spin states of the ${}^1(TT)_i$ correlated triplet pair state where each number represents the quantum number M_S of the contributing triplet state [75].

At zero magnetic field, none of the nine pair states have a definite spin multiplicity, however, three of the nine states have singlet “character”. At low magnetic fields additional states acquire singlet character due to the field-modulated interplay between the Zeeman splitting and spin-spin interactions, whereas at high fields only two states possess singlet character (less than there was at zero magnetic field) [76]. This means that, in the presence a magnetic field, the rate of conversion of singlets to triplets will vary in accordance with the statistical likelihood of forming a pair of triplets. As a molecule excited to the triplet state cannot produce fluorescence,

any change in fission rate from the influence of a magnetic field will cause the fluorescence intensity to be modified, resulting in PL-MFE.

2.6 Magnetic Luminescence Microscopy

In order to realise a new magnetic microscopy technique, based on magnetic field effect photoluminescence, it is favourable to exploit an already established fluorescence microscopy technique. Examples of such techniques include confocal microscopy and stimulated emission depletion (STED) microscopy, which are extensively used in cell biology [38] due to their high resolving power. The following sections will discuss the basic operating principles of each technique.

2.6.1 Confocal Microscopy

Confocal microscopy is a diffraction-limited technique that differs from conventional optical microscopy in that it uses raster-scanned point-source illumination in order to obtain an image of the fluorescent sample of interest. This technique is discussed in more detail in §3.6.

This method is advantageous compared to conventional wide-field fluorescence microscopy where illumination of the entire volume of the sample makes it difficult to reject background fluorescence. With confocal microscopy the illumination spot is focussed to a plane of interest. However, regions of sample volume outside of the focal plane can still be illuminated. This extraneous source of fluorescence can be blocked by using apertures that permit greater contrast and resolution to be realised compared to conventional optical microscopy techniques.

Newer confocal laser scanning microscopes (CLSMs) are being equipped with tuneable lasers to facilitate exciting fluorochromes of different wavelengths. This is important in cell biology as it is often desirable to be able to stain different cell components simultaneously and to be able to tell them apart.

2.6.2 STED Microscopy

Stimulated emission depletion (STED) microscopy is an optical microscopy technique that can resolve beyond the diffraction limit. In STED microscopy, a normal-mode laser pulse with a circular intensity profile is focussed into a diffraction-limited spot on the fluorescent sample of interest, causing electronic excitation to occur. A few hundred picoseconds later, a second laser pulse is focussed onto the same spot as before; only this time the pulse has a ring-shaped intensity profile with an intensity of zero in the centre of the pulse. This causes the excited region of the sample to undergo relaxation via stimulated emission *except* in the centre of the excited region. After a few hundred more picoseconds the centre region, being the only region left in the excited state, undergoes spontaneous emission. Crucially, this emission area can be made to be arbitrarily smaller than the diffraction limit of the excitation laser by varying the intensity profile of the second laser pulse. The intensity profiles of each pulse are compared in figure 2.25.

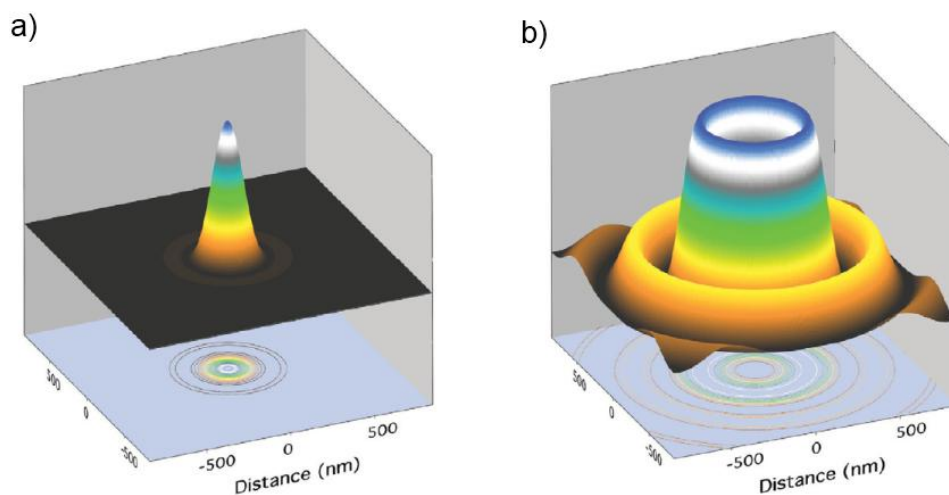


Figure 2.25: Comparison of laser pulse intensity profiles used in STED microscopy. a) Is the normal-mode Airy disk intensity profile used to initially excite the sample whilst b) is the donut-shaped intensity profile used to produce stimulated emission of the sample [77].

So far with this technique resolutions down to 16 nm have been achieved (see figure 2.26) [78].

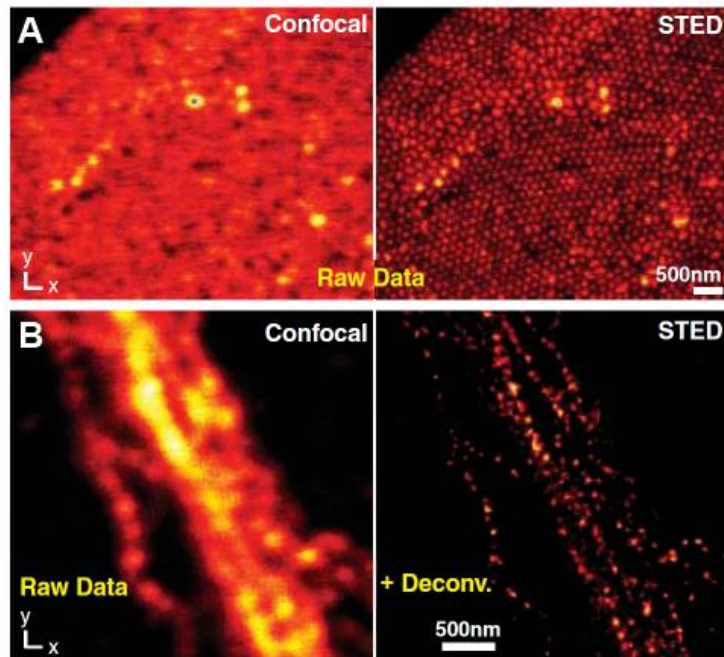


Figure 2.26: Comparison of techniques (confocal image on the left, STED image on the right). a) Is an image of fused silica beads with fluorescent cores whilst b) is an image of neurofilaments from a human neuroblastoma [78]. Reprinted with permission from AAAS.

2.7 References

- [1] R. W. Wood, *et al.*, "Recording technologies for terabit per square inch systems," *IEEE Transactions on Magnetics*, vol. 38, pp. 1711-1718, Jul 2002.
- [2] C. Ross, "Patterned magnetic recording media," *Annual Review of Materials Research*, vol. 31, pp. 203-235, 2001.
- [3] J. P. Wang, "FePt Magnetic Nanoparticles and Their Assembly for Future Magnetic Media," *Proceedings of the Ieee*, vol. 96, pp. 1847-1863, Nov 2008.
- [4] A. Kikitsu, *et al.*, "5 Tdots/in(2) Bit Patterned Media Fabricated by a Directed Self-Assembly Mask," *Ieee Transactions on Magnetics*, vol. 49, pp. 693-698, Feb 2013.
- [5] X. M. Yang, *et al.*, "Directed Block Copolymer Assembly versus Electron Beam Lithography for Bit-Patterned Media with Areal Density of 1 Terabit/inch(2) and Beyond," *Acs Nano*, vol. 3, pp. 1844-1858, Jul 2009.
- [6] D. A. Allwood, *et al.*, "Magnetic domain-wall logic," *Science*, vol. 309, pp. 1688-1692, 2005.
- [7] S. S. P. Parkin, *et al.*, "Magnetic domain-wall racetrack memory," *Science*, vol. 320, pp. 190-194, Apr 2008.

- [8] H. Hopster and H. P. Oepen, *Magnetic Microscopy of Nanostructures*: Springer, 2005.
- [9] S. Amelinckx, *et al.*, *Handbook of Microscopy, Handbook of Microscopy: Applications in Materials Science, Solid-State Physics, and Chemistry. Methods II*: Wiley, 2008.
- [10] A. Hubert and R. Schafer, *Magnetic domains: the analysis of magnetic microstructures*: Springer, 1998.
- [11] S. McVitie and M. Cushley, "Quantitative Fresnel Lorentz microscopy and the transport of intensity equation," *Ultramicroscopy*, vol. 106, pp. 423-431, Mar 2006.
- [12] A. B. Johnston, *et al.*, "In situ studies of the properties of micrometre-sized magnetic elements by coherent Foucault imaging," *Journal of Physics D-Applied Physics*, vol. 29, pp. 1419-1427, Jun 1996.
- [13] J. Li, *et al.*, "Magnetic imaging with femtosecond temporal resolution," *Review of Scientific Instruments*, vol. 80, Jul 2009.
- [14] M. Takezawa, *et al.*, "Magnetic domain observation of Nd-Fe-B magnets with submicron-sized grains by high-resolution Kerr microscopy," *Journal of Applied Physics*, vol. 109, pp. -, 2011.
- [15] T. Kohashi and K. Koike, "A spin-polarized scanning electron microscope with 5-nm resolution," *Japanese Journal of Applied Physics Part 2-Letters*, vol. 40, pp. L1264-L1266, Nov 2001.
- [16] D. T. Pierce, "Spin-Polarized Electron-Microscopy," *Physica Scripta*, vol. 38, pp. 291-296, Aug 1988.
- [17] M. Negotia, *et al.*, "Linear transport of domain walls confined to propagating 1-D potential wells," *Journal of Applied Physics*, vol. 114, pp. -, 2013.
- [18] H. Stoll, *et al.*, "High-resolution imaging of fast magnetization dynamics in magnetic nanostructures," *Applied Physics Letters*, vol. 84, pp. 3328-3330, Apr 2004.
- [19] M. R. Freeman and B. C. Choi, "Advances in magnetic microscopy," *Science*, vol. 294, pp. 1484-1488, 2001.
- [20] H. Jung, *et al.*, "Observation of coupled vortex gyrations by 70-ps-time- and 20-nm-space-resolved full-field magnetic transmission soft x-ray microscopy," *Applied Physics Letters*, vol. 97, pp. -, 2010.
- [21] K. Fukumoto, *et al.*, "Construction and development of a time-resolved x-ray magnetic circular dichroism-photoelectron emission microscopy system using femtosecond laser pulses at BL25SU SPring-8," *Review of Scientific Instruments*, vol. 79, Jun 2008.

- [22] V. Cambel, *et al.*, "High resolution switching magnetization magnetic force microscopy," *Applied Physics Letters*, vol. 102, Feb 2013.
- [23] Bruker Corporation. (2011, 23/10/2013). *FastScan - Overview*. Available: <http://www.bruker.com/fastscan>
- [24] S. K. d. Range. (2004, 01/06/2011). Gravity Probe B - Examining Einstein's Spacetime with Gyroscopes. Available: [http://einstein.stanford.edu/content/education/GP-B T-Guide4-2008.pdf](http://einstein.stanford.edu/content/education/GP-B-T-Guide4-2008.pdf)
- [25] R. C. Black, *et al.*, "Magnetic microscopy using a liquid nitrogen cooled YBa₂Cu₃O₇ superconducting quantum interference device " *Appl. Phys. Lett.*, vol. 62, pp. 2128-2130, 1993.
- [26] S. Y. Lee, "Multi-channel Scanning SQUID Microscopy," University of Maryland, 2004.
- [27] T. Y. Kim, *et al.*, "Magnetic domain structure of growth temperature-gradient Sm₂Mo₂O₇ thin film investigated by scanning SQUID microscopy," *Physica B-Condensed Matter*, vol. 329, pp. 1046-1048, May 2003.
- [28] B. Aktas, *et al.*, *Magnetic Nanostructures*: Springer, 2007.
- [29] A. Oral, *et al.*, "Real-time scanning hall probe microscopy," *Applied Physics Letters*, vol. 69, pp. 1324-1326, Aug 1996.
- [30] Z. Primadani and A. Sandhu, "Variable temperature scanning Hall probe microscopy of ferromagnetic garnet thin films," *Journal of Magnetism and Magnetic Materials*, vol. 310, pp. 2693-2695, Mar 2007.
- [31] D. Le Sage, *et al.*, "Optical magnetic imaging of living cells," *Nature*, vol. 496, pp. 486-491, Apr 2013.
- [32] D. B. Dusenbery, *Life at Small Scale: The Behaviour of Microbes*: Scientific American library, a division of HPHLP, 1996.
- [33] B. Hu, *et al.*, "Magnetic-Field Effects in Organic Semiconducting Materials and Devices," *Advanced Materials*, vol. 21, pp. 1500-1516, Apr 2009.
- [34] J. B. Birks, *Photophysics of aromatic molecules*: John Wiley & Sons Ltd., 1970.
- [35] B. Valeur, *Molecular fluorescence: principles and applications*: Wiley-VCH, 2002.
- [36] IUPAC. (2011, 03/06/2011). *IUPAC Compendium of Chemical Terminology*. Available: <http://goldbook.iupac.org/D01579.html>

- [37] N. J. Turro, *et al.*, *Modern molecular photochemistry of organic molecules*: University Science Books, 2010.
- [38] B. Matsumoto, *Cell biological applications of confocal microscopy*, 2nd ed.: Academic Press, 2002.
- [39] C. Ringemann, *et al.*, "Enhancing fluorescence brightness: Effect of reverse intersystem crossing studied by fluorescence fluctuation spectroscopy," *Chemphyschem*, vol. 9, pp. 612-624, Mar 2008.
- [40] J. B. Pawley, *Handbook of Biological Confocal Microscopy*: Springer, 2010.
- [41] A. D. McNaught and A. Wilkinson, *IUPAC. Compendium of Chemical Terminology, 2nd ed. (the "Gold Book")*: Blackwell Scientific Publications, Oxford, UK, 1997.
- [42] M. C. Zerner, *et al.*, *Advances in Quantum Chemistry*: Elsevier Science, 1996.
- [43] A. A. Mohamed, *et al.*, "External heavy-atom effect of gold in a supramolecular acid-base pi stack," *Dalton Transactions*, pp. 2597-2602, 2005.
- [44] M. Rae, *et al.*, "Fluorescence quenching with exponential distance dependence: Application to the external heavy-atom effect," *Journal of Chemical Physics*, vol. 119, pp. 2223-2231, Jul 2003.
- [45] S. P. McGlynn, *et al.*, "External Heavy-Atom Spin-Orbital Coupling Effect. I. The Nature of the Interaction," *The Journal of Chemical Physics*, vol. 37, pp. 1818-1824, 1962.
- [46] P. Suppan and R. S. o. Chemistry, *Chemistry and Light*: Royal Society of Chemistry, 1994.
- [47] N. Herron and D. R. Corbin, *Inclusion Chemistry With Zeolites: Nanoscale Materials by Design*: Kluwer Academic Publishers, 1995.
- [48] C. Baleizao and M. N. Berberan-Santos, "External heavy-atom effect on the prompt and delayed fluorescence of [70]fullerenes," *Chemphyschem*, vol. 11, pp. 3133-40, Oct 4 2010.
- [49] P. E. Burrows, *et al.*, "Metal ion dependent luminescence effects in metal tris-quinolate organic heterojunction light emitting devices," *Applied Physics Letters*, vol. 64, pp. 2718-2720, 1994.
- [50] F. J. Zhang, *et al.*, "The effect of metal electron cloud on the luminescence characteristics of organic ligands: An experimental and theoretical investigation," *Chinese Science Bulletin*, vol. 56, pp. 479-483, Feb 2011.
- [51] A. Kohler and D. Beljonne, "The singlet-triplet exchange energy in conjugated polymers," *Advanced Functional Materials*, vol. 14, pp. 11-18, 2004.

- [52] R. C. Johnson, *et al.*, "Effects of magnetic fields on the mutual annihilation of triplet excitons in molecular crystals," *Physical Review Letters*, vol. 19, pp. 285-287, 1967.
- [53] R. E. Merrifield, "Theory of Magnetic Field Effects on Mutual Annihilation of Triplet Excitons," *Journal of Chemical Physics*, vol. 48, pp. 4318-4319, 1968.
- [54] R. P. Groff, *et al.*, "Magnetic hyperfine modulation of dye-sensitized delayed fluorescence in an organic crystal," *Physical Review Letters*, vol. 29, pp. 429-&, 1972.
- [55] G. Klein, *et al.*, "Magnetic-field effect on prompt fluorescence in anthracene - evidence for singlet exciton fission," *Chemical Physics Letters*, vol. 16, pp. 340-&, 1972.
- [56] R. C. Johnson and R. E. Merrifield, "Effects of magnetic fields on the mutual annihilation of triplet excitons in anthracene crystals," *Physical Review B*, vol. 1, pp. 896-902, 1970.
- [57] R. P. Groff, *et al.*, "Coexistence of Exciton Fission and Fusion in Tetracene Crystals," *Physical Review B*, vol. 1, pp. 815-817, 1970.
- [58] C. E. Swenberg and W. T. Stacy, "Bimolecular radiationless transitions in crystalline tetracene," *Chemical Physics Letters*, vol. 2, pp. 327-328, 1968.
- [59] E. J. Bowen, *et al.*, "Resonance Transfer of Electronic Energy in Organic Crystals," *Proceedings of the Physical Society of London Section A*, vol. 62, pp. 26-31, 1949.
- [60] J. Kalinowski and J. Godlewski, "Magnetic Field Effects on Recombination Radiation in Tetracene Crystal," *Chemical Physics Letters*, vol. 36, pp. 345-348, 1975.
- [61] C. Garditz, *et al.*, "Influence of an external magnetic field on the singlet and triplet emissions of tris-(8-hydroxyquinoline)aluminum(III) (Alq(3))," *Journal of Applied Physics*, vol. 98, Nov 2005.
- [62] C. J. Foot, *Atomic physics*: Oxford university press, 2005.
- [63] M. B. Smith and J. Michl, "Recent Advances in Singlet Fission," in *Annual Review of Physical Chemistry, Vol 64*. vol. 64, M. A. Johnson and T. J. Martinez, Eds., ed Palo Alto: Annual Reviews, 2013, pp. 361-386.
- [64] L. Nuccio, *et al.*, "Importance of Spin-Orbit Interaction for the Electron Spin Relaxation in Organic Semiconductors," *Physical Review Letters*, vol. 110, May 2013.
- [65] P. Janssen, *et al.*, "Unraveling the temperature and voltage dependence of magnetic field effects in organic semiconductors," *Journal of Applied Physics*, vol. 114, Nov 2013.
- [66] J. Kalinowski, *et al.*, "Magnetic field effects on emission and current in Alq(3)-based electroluminescent diodes," *Chemical Physics Letters*, vol. 380, pp. 710-715, Oct 2003.

- [67] Y. F. Zhang and S. R. Forrest, "Existence of continuous-wave threshold for organic semiconductor lasers," *Physical Review B*, vol. 84, Dec 2011.
- [68] M. Colle and C. Garditz, "Phosphorescence of aluminum tris(quinoline-8-olate)," *Applied Physics Letters*, vol. 84, pp. 3160-3162, Apr 2004.
- [69] H. Odaka, *et al.*, "Control of magnetic-field effect on electroluminescence in Alq(3)-based organic light emitting diodes," *Applied Physics Letters*, vol. 88, Mar 2006.
- [70] V. S. Batista. (2013, 27/12/2013). *Introductory Quantum Chemistry: Spin-Orbit Interaction*. Available: <http://xbeams.chem.yale.edu/~batista/vvv/node26.html>
- [71] F. Kuemmeth, "Spin States and Spin-Orbit Coupling in Nanostructures," Cornell University, 2008.
- [72] W. H. Melhuish, "Quantum Efficiencies of Fluorescence of Organic Substances - Effect of Solvent and Concentration of Fluorescent Solute," *Journal of Physical Chemistry*, vol. 65, pp. 229-&, 1961.
- [73] A. M. Muller, *et al.*, "Evidence for exciton fission and fusion in a covalently linked tetracene dimer," *Chemical Physics Letters*, vol. 421, pp. 518-522, Apr 2006.
- [74] V. K. Thorsmolle, *et al.*, "Exciton dynamics in pentacene and tetracene studied using optical pump-probe spectroscopy," in *Ultrafast Phenomena Xiv*. vol. 79, T. Kobayashi, *et al.*, Eds., ed Berlin: Springer-Verlag Berlin, 2005, pp. 269-271.
- [75] R. E. Merrifield, "Magnetic effects on triplet exciton interactions," *Pure Appl. Chem.*, vol. 27, pp. 481-498, 1971.
- [76] Y. Zhang, *et al.*, "Thermally activated singlet exciton fission observed in rubrene doped organic films," *Organic Electronics*, vol. 15, pp. 577-581, 2014.
- [77] P. Dedecker, *et al.*, "Diffraction-unlimited optical microscopy," *Materials Today*, vol. 11, pp. 12-21, 2008.
- [78] S. W. Hell, "Far-field optical nanoscopy," *Science*, vol. 316, pp. 1153-1158, May 2007.

3 Experimental Techniques

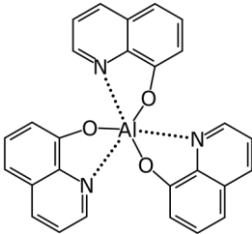
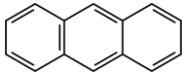
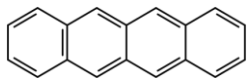
3.1 Introduction

In this chapter all materials used in the research project will be presented together with a description of all fabrication techniques and methodologies utilised. An in-depth description of all characterisation and measurement systems used will also be given with the exception of the custom-built MFE measurement systems, which will be discussed in the following chapter.

3.2 Sample Preparation and Fabrication

3.2.1 Organic Materials and Solvents

In order to investigate the magnetic field effect (see §2.5 for description) several materials were selected (table 3.1) after a thorough review of the literature based on their ability to exhibit a fluorescent MFE. The materials were purchased from the Sigma-Aldrich Corporation and were used as-is, without any further purification. Only one out of eight of the materials possessed a metal atom (Alq_3); the remaining chemicals were composed entirely of non-metallic elements. Five solvents that were used in this research are listed in table 3.2.

Short Name	IUPAC Name	Chemical Formula	Skeletal Formula	Purity	Deposition Method
Alq_3	Tris(8-hydroxyquinolino)aluminium	$C_{27}H_{18}AlN_3O_3$		99.995%	Thermal Evaporation
-	Anthracene	$C_{14}H_{10}$		99%	Thermal Evaporation / Spin Coating
-	Tetracene	$C_{18}H_{12}$		98%	Thermal Evaporation

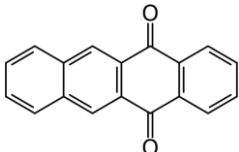
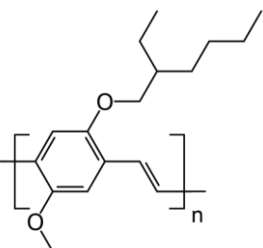
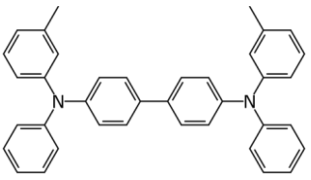
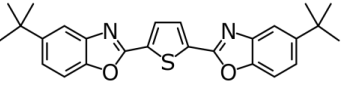
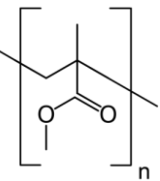
NpQ	5,12-naphthacenequinone	$C_{18}H_{10}O_2$		97%	Spin Coating
MEH-PPV	poly[2-methoxy-5-(2'-ethylhexyloxy)-p-phenylene vinylene]	$(C_{17}H_{24}O_2)_n$		Unknown	Spin Coating
TPD	N,N'-Bis(3-methylphenyl)-N,N'-diphenylbenzidine	$C_{38}H_{32}N_2$		99%	Spin Coating
BBOT	2,5-Bis(5-tert-butylbenzoxazol-2-yl)thiophene	$C_{26}H_{26}N_2O_2S$		99%	Spin Coating
PMMA	Poly(methyl methacrylate)	$(C_5O_2H_8)_n$		Unknown	Spin Coating

Table 3.1: List of chemicals used in this research. The majority of the chemicals are organic semiconductors.


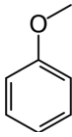
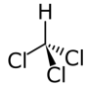
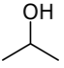
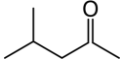
Short Name	IUPAC Name	Chemical Formula	Skeletal Formula
Acetone	Propanone	C_3H_6O	
Anisole	Methoxybenzene	C_7H_8O	
-	Chloroform	$CHCl_3$	
IPA	Propan-2-ol	C_3H_8O	
MIBK	4-Methylpentan-2-one	$C_6H_{12}O$	

Table 3.2: List of solvents used in this research.

3.2.2 Spin Coating

Spin coating is a top-down chemical deposition method used to create thin, solid, uniform polymer films from a fluidic solution deposited onto a substrate. It is most commonly used by the semiconductor industry to deposit masks, or photoresists, for photolithography [1]. All spin coating was performed in the University of Sheffield National Centre for III-V Technologies ISO 7-grade cleanroom on an EMS Model 4000 Photo Resist Spinner.

The spin coating technique works by mounting a flat substrate onto a vacuum chuck located at the centre of the spin coater. The prepared solution, containing the film-forming solute, is carefully pipetted onto the sample covering the entire surface. Surface tension causes a high contact angle between the solution and substrate surface ensuring that the solution does not flow beyond the edges of the substrate. The machine is then activated causing the vacuum chuck and sample to be mechanically rotated at 4000 rpm for 30 seconds. The solution experiences an apparent centrifugal force causing it to be uniformly spread across the sample in an equal radial distribution with excess solution flowing off the edge of the sample [1]. Most of the solvent evaporates during the spinning stage; any solvent that remains evaporates when the sample is placed on a 65 °C hotplate for two minutes.

A solid mixture comprising of BBOT, TPD and PMMA (see table 3.1) was prepared via the spin coating process. This mixture was spun onto silicon substrates and fused quartz substrates. The wafers were cut to the desired dimensions ($\approx 25 \times 25$ mm), sonicated in acetone to remove organic residue, washed with propan-2-ol to remove any remaining acetone and dried with a stream of nitrogen gas to evaporate any remaining propan-2-ol. Chloroform was used to dissolve the compounds into a homogeneous solution and allow controlled delivery to the substrate.

A typical precursor solution composition is given in table 3.3:

Compound	Quantity
BBOT	3.3 mg
TPD	3.3 mg
PMMA	13.3 mg
Chloroform	1 mL

Table 3.3: List of components that were put into solution for spin coating 'exciplex'-producing samples.

3.2.3 Electron Beam Lithography

Electron beam lithography (EBL) is an ultra-high resolution nanofabrication process that utilises an electron beam to pattern, or 'write', a set of microscopic and nanoscopic structures into a resist layer on a sample. This resist mask can then be used in combination with many physical deposition techniques, for example, thermal evaporation, in order to deposit solid structures onto the substrate.

This technique was used in order to pattern precisely designed magnetic nanostructures, which can produce predictable magnetisation configurations, onto non-magnetic substrates. By depositing a thin film of a fluorescent MFE material on top of the nanostructures it was predicted that this arrangement would provide an opportunity to optically view the magnetic configuration of the nanostructures via the fluorescent contrast pattern emitted by the MFE material in proximity to the magnetic stray field of the nanostructures.

The EBL system used in this research is a commercial Raith 150 system in the EPSRC National Centre for III-V Technologies. The technique was chosen over other patterning techniques due to its ability to write structures over a large area of up to 150×150 mm at a lateral spatial resolution ≥ 25 nm. The structures were designed in the Raith software well in advance of using the system.

Before using the EBL system a few steps of sample preparation are required. The first step of the process is to spin-coat a thin layer of resist material onto a suitably flat, defect-free substrate such as a silicon wafer. Where substrate transparency is important, i.e. in

transmission electron microscopy or magnetic transmission x-ray microscopy (M-TXM) measurements, silicon nitride membranes were used. The most frequently used resist is a solution of poly(methyl methacrylate) (PMMA) dissolved in anisole at 7% concentration. In the EBL technique PMMA acts a positive resist. This is where exposure to the electron beam causes scission of the PMMA polymer chains increasing the solubility of the exposed areas, which in turn increases the local etching rate of the developer allowing straightforward removal of the exposed material after EBL patterning has occurred [2]. The resist was pipetted onto the substrate, covering the entire surface, and then spin-coated for 30 seconds at 4000 rpm (figure 3.1a). Spin-coated samples were then transferred to a hotplate set to 180 °C and left for five minutes in order to evaporate any remaining anisole solvent.

Once the samples had been prepared they were loaded into the vacuum chamber of the EBL system. Sample alignment and electron beam focussing were performed followed by measuring the electron beam current, setting the correct beam dose (based on resist sensitivity) and calculating the dwell time (of the beam spot per unit area). Once these steps were completed the system was set to work patterning (figure 3.1b). The time taken to complete patterning depended on the total number of polygons in the design file (see figure 3.3), the desired dose, the measured electron beam current and the calculated dwell time.

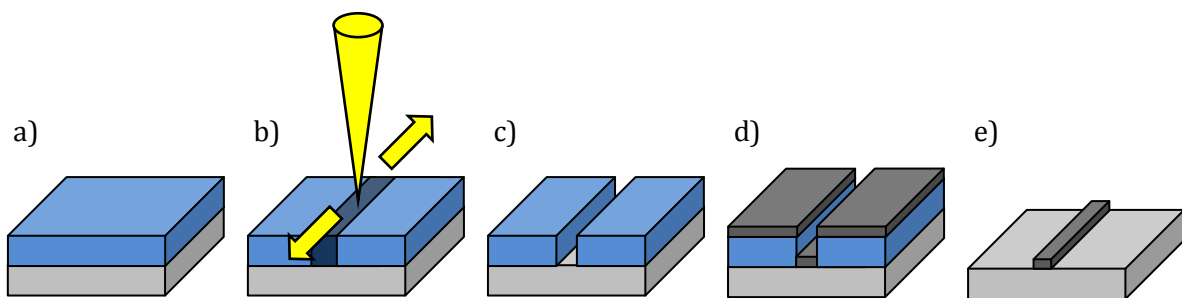


Figure 3.1: Schematic diagram of the procedure used to fabricate the EBL samples. a) Silicon substrate (light grey) is spin-coated with a thin film of PMMA (light blue); b) resist is patterned with the EBL system (dark blue); c) the resist is developed forming a PMMA mask; d) Permalloy is thermally evaporated onto the sample (dark grey); e) lift-off is performed removing the PMMA mask and the associated Permalloy.

Once the writing process had completed the samples were developed in a mixture of methyl isobutyl ketone and isopropyl alcohol (1:3 ratio) for 30 seconds. This step dissolves the portions of the PMMA resist that were exposed to the electron beam during the writing process (figure 3.1c). The samples were then deposited with a thin film of $\text{Ni}_{81}\text{Fe}_{19}$, known as Permalloy (figure 3.1d), and subjected to the 'lift-off' process (figure 3.1e). This process was performed in order to remove the PMMA mask and the evaporated Permalloy bonded on top of the mask whilst leaving the Permalloy bonded to the substrate intact. This process was achieved by placing the sample in a beaker of acetone and placing the beaker in an ultrasonic bath. The acetone acted to dissolve the PMMA whilst the ultrasonic vibrations helped to mechanically detach the weakened PMMA mask from the substrate. Once the entire mask had been removed the sample was washed in IPA removing the acetone and any residual debris.

There are several issues that one has to bear in mind when operating the EBL system. The first issue relates to how the system navigates around the sample. Purely by employing electron beam deflection the system can write to an area approximately $100 \times 100 \mu\text{m}$ in what is known as the 'write-field'. To write outside of this write-field the stage has to be moved with piezoelectric actuators, however, this increases the risk that any structures crossing the write-field boundary will contain alignment errors $\gtrsim 30 \text{ nm}$. To avoid this problem all structures were designed to remain within each write field.

Another issue one has to be aware of is known as the 'proximity effect' (see figure 3.2). The effect is capable of producing undesired resist exposure and can, in general, produce unintended structural size variation. For example, if two structures are placed too close together (figure 3.2b), an effective overlap can occur during writing whereby the intermediate space receives a cumulative electron dose large enough to be affected by the developer. When the sample is developed this area of resist would be removed along with the adjacent structures effectively merging the two structures together. The cause of the proximity effect is due to electron backscatter in the resist and at the resist/substrate interface [3]. To overcome this

effect, several things can be done. A substrate with a low atomic number, for example, will produce less electron backscatter compared to a substrate with a higher atomic number. Therefore changing the substrate to a lower atomic number can reduce the dominance of the proximity effect [4]. Another method is to reduce the resist thickness which allows the beam energy to be reduced minimising the backscatter. A final method is to design structures with proximity effect in mind; this could mean ensuring there is sufficient clearance between neighbouring structures, etc. In fact, some EBL systems have built-in algorithms that provide proximity effect correction altering the input design in order to compensate for distortions that the proximity effect can introduce. Although these algorithms are trade secrets, progress is being made in the public domain to develop robust proximity effect correction algorithms [5].

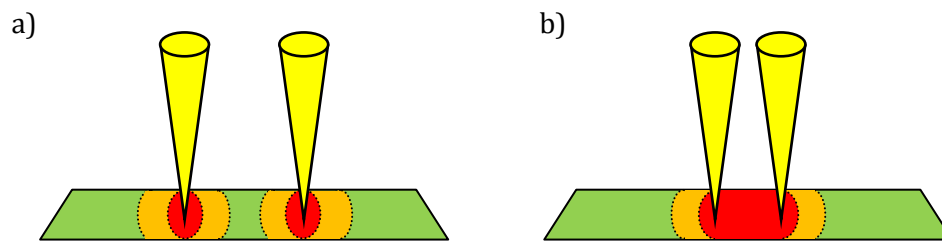


Figure 3.2: Schematic representation of the proximity effect encountered in EBL. The red zone represents an area of PMMA receiving a dose intense enough to be developed, the orange zone represents an area receiving a partial dose, the green zone represents an area where no dose was received. a) Electron beam writes to two dots with a gap between the partially dosed zones; b) The electron beam writes too close causing an area to receive a double partial dose exceeding the dose threshold above which development occurs.

As stated previously, the structures were designed in the Raith software and can be seen in figure 3.3. The structures are grouped by type each within the bounds of a $100 \times 100 \mu\text{m}$ write-field. From left to right, and top to bottom, they are referred to as the echelons; circles; squares; rings; ellipses; rectangles; sample description; notched nanowires; and serpentine wires. When fabricated from permalloy, which has a negligible magnetocrystalline anisotropy, it is the shape of the structure which plays a dominant role in determining the equilibrium magnetisation configuration. This property is referred to as shape anisotropy. The characteristic dimensions of the structures vary from approximately 200 nm up to 20 μm with each array containing many redundant copies. The largest of the objects within the arrays should allow for an upper limit to

be determined whereby, above this limit, the magnetisation configuration preferentially forms a multi-domain state. This should allow for the identification of the largest objects below this limit that can support a magnetisation configuration that is predictable, reproducible and exhibits strong domain contrast. This should prove invaluable when viewing the MFE-exhibiting thin films that are coupled to these structures.

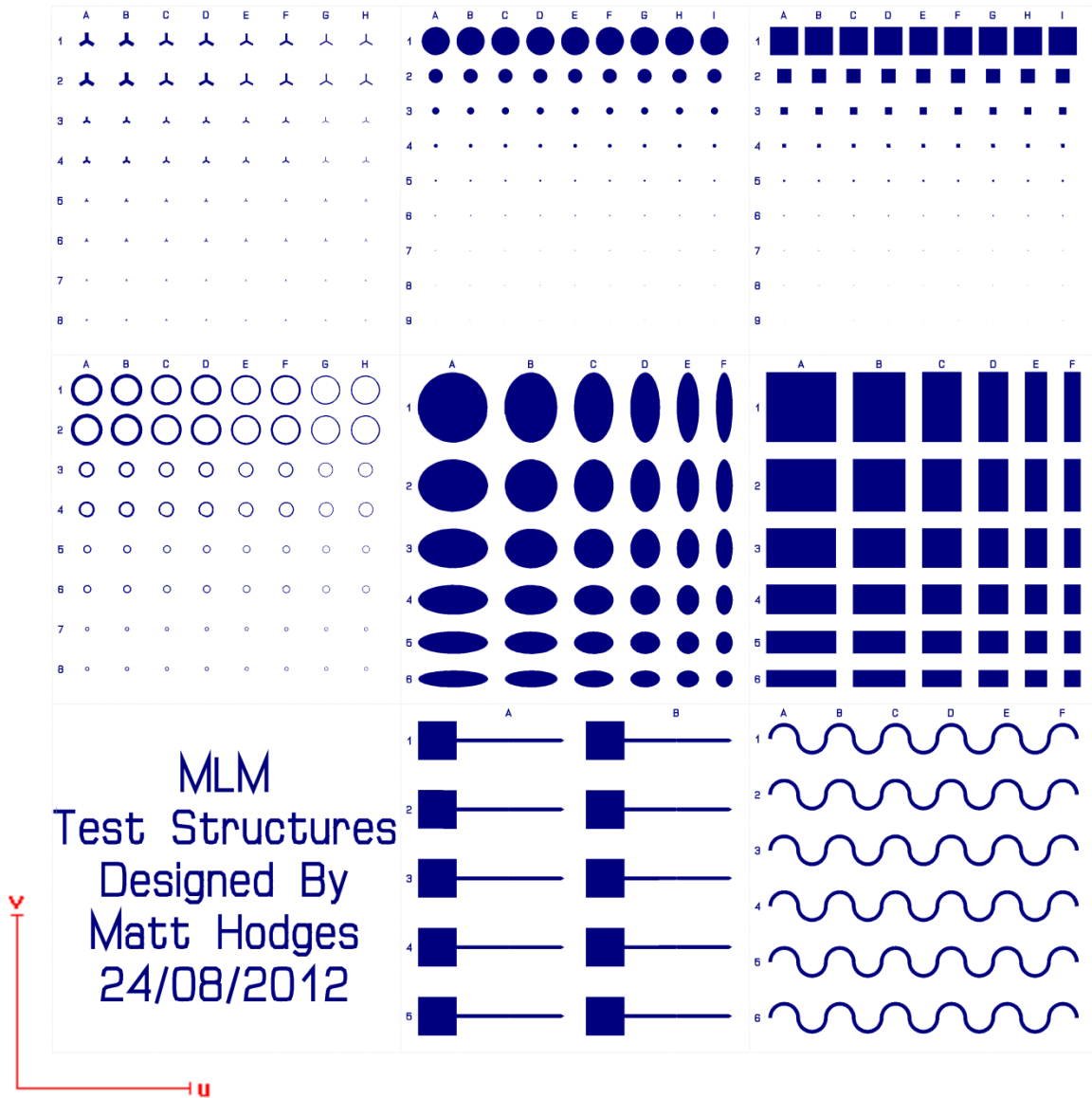


Figure 3.3: Diagram of microstructures designed and fabricated using electron beam lithography system.

3.2.4 Thermal Evaporation

Thermal evaporation is a physical deposition process used to create thin films of either organic or metallic materials. This research made use of two separate thermal evaporators: one dedicated to metallic evaporation (a Wordentec thermal evaporator shown in figure 3.4a and schematically represented in figure 3.5) and the other dedicated to organic evaporation (an Edwards E306A thermal evaporator shown in figure 3.4b). In both systems the desired evaporant material, which is usually supplied in powder form, was placed in a crucible that sits in a tungsten filament coil. The organic evaporator made use of quartz crucibles whilst the metallic evaporator used refractory ceramic crucibles. The samples were then loaded into the evaporator and were suspended directly above the crucible. They had to face downward in order for the evaporant to be deposited onto the correct side of the substrate. The systems were then pumped down over several hours to a vacuum base pressure of approximately $1\text{-}5 \times 10^{-7}$ Torr.

(a)



(b)



Figure 3.4: Photograph of (a) the metallic thermal evaporator used for the deposition of Permalloy and (b) the organic thermal evaporator used for the deposition of tetracene and other organic materials.

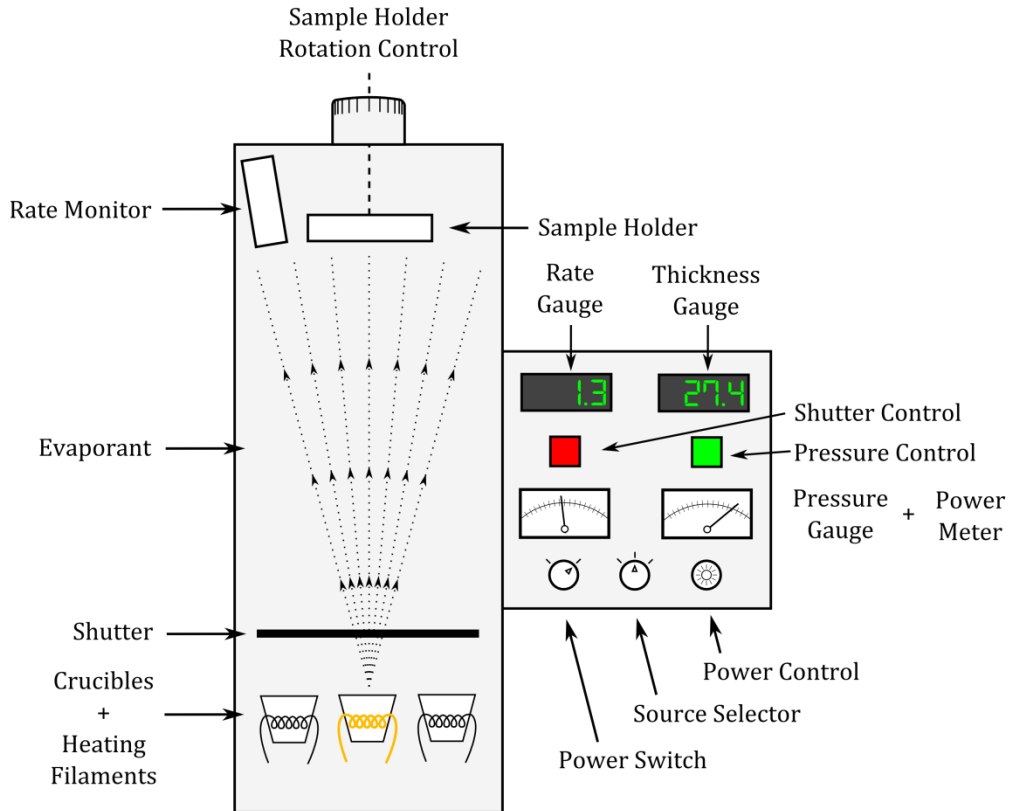


Figure 3.5: Schematic diagram of the metallic thermal evaporator used for the deposition of Permalloy.

For the metallic thermal evaporator a bake-out procedure was first performed in order to remove volatile impurities that may have collected since the last evaporation. This involved ramping the power (a system-dependent quantity) to the tungsten filament 5% every two minutes until the pre-determined evaporation rate was reached (40% for Permalloy). The power was then reduced back to zero at the same rate. After bake-out the system was left for one hour in order to return the base pressure back to the previous value. Both systems were then ready to begin the evaporation (as the organic thermal evaporator did not require a bake-out stage prior to evaporation).

Evaporation commenced in both systems with the opening of the shutter once the desired evaporation rate had been attained. For the metallic evaporator, the rate monitor is shielded by the shutter therefore the sample holder had to be rotated to the blank position in order to establish the correct evaporation rate. The typical evaporation rate used for the deposition of Permalloy was in the range 0.15-0.25 Å/s. For the organic evaporator, the rate monitor is never

obscured by the shutter so the shutter remained closed until the correct rate was reached where it was then opened to commence deposition onto the previously shielded samples. Evaporation rates used on this system are described in §5.4. The evaporation deposition geometry is described by the following equation [6]:

$$\frac{d\bar{M}_s}{dA_s} = \frac{\bar{M}_e(n+1)\cos^n\phi\cos\theta}{2\pi r^2}, \quad n \geq 0 \quad \text{Equation 3.1}$$

Where $\frac{d\bar{M}_s}{dA_s}$ = derivative of evaporated mass deposited per substrate area; \bar{M}_e = total evaporated mass; n = evaporation crucible geometry; ϕ = angle between source normal vector and the vector from source to substrate; θ = angle between vector from source to substrate and substrate normal vector; r = distance from the source to the substrate. When n is large the vapour cloud is highly directional, which can occur when the evaporation crucible is tall and narrow as n is directly scaled to the melt depth / melt surface area ratio.

As the distance between source and substrate, r , in the organic thermal evaporator is approximately 20 cm, and as the substrates cannot all be positioned so that $\theta = 0^\circ$, the film thickness uniformity diminishes with distance from the centre of the substrate support rail. This, therefore, limits the number of good quality samples that can be grown in each session. The metallic thermal evaporator, however, does not have this problem as, firstly, the distance between the source and substrate, r , is approximately 2.5 times what it is in the organic thermal evaporator at 50 cm. Secondly, each substrate can be rotated into the optimal position ($\theta = 0^\circ$) without having to break vacuum.

3.3 Fluorescence Spectroscopy

Fluorescence spectroscopy, also known as spectrofluorimetry, is a form of spectroscopy dedicated to characterising photoluminescent materials, especially those that exhibit fluorescence. The technique allows for the acquisition of an excitation spectrum and an emission spectrum of the sample of interest. The fluorescence spectrometer used in this

research was the Perkin-Elmer LS-50B and is schematically represented in figure 3.6. The acquisition of an emission spectrum typically involved exposing a fluorescent sample to, ideally, monochromatic light of known wavelength. Any fluorescence generated by the sample was then analysed by spectrally scanning through the received fluorescent light and measuring the intensity of each wavelength. To obtain an excitation spectrum the reverse is performed: the excitation light source was scanned through a wavelength range while the detector only measured the fluorescence intensity at one fixed wavelength.

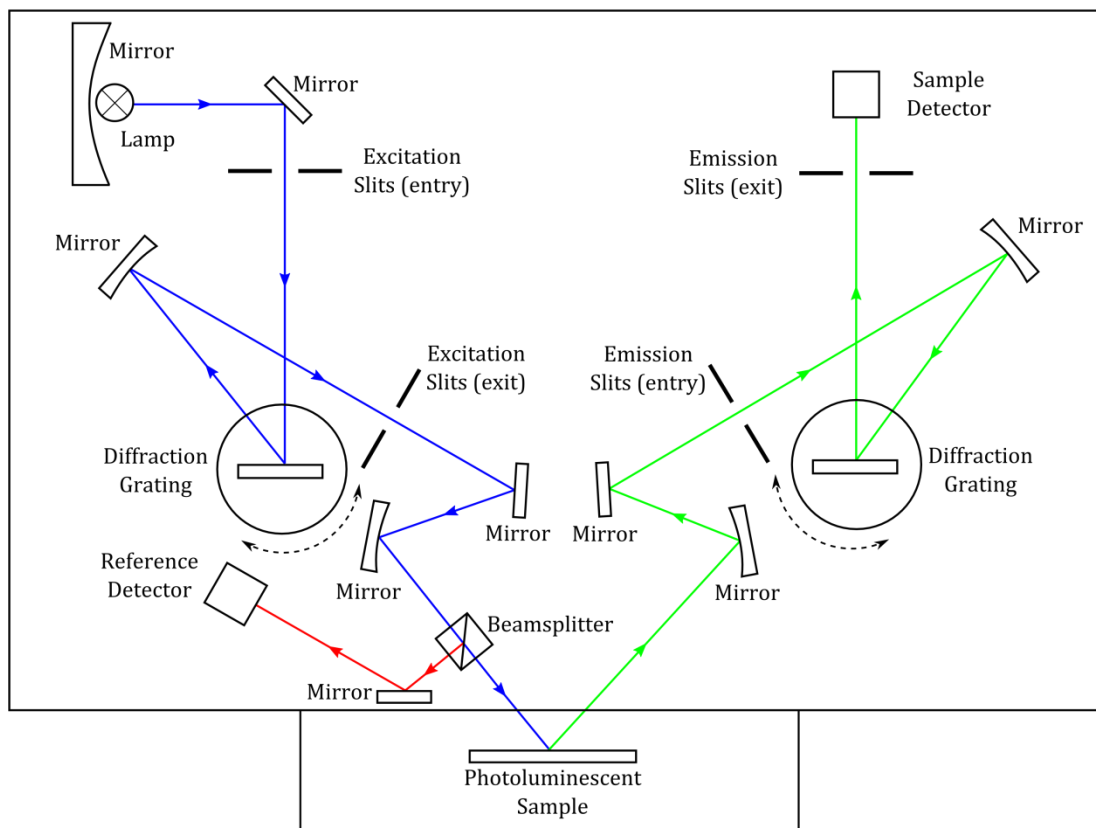


Figure 3.6: Schematic diagram of Perkin-Elmer LS-50B spectrofluorimeter.

A full description of how the LS-50B operates is as follows. A white light source in the form of a halogen lamp is collimated via a parabolic mirror and is directed into the excitation diffraction grating mounted on a goniometer. The diffraction grating disperses the light into a full spectrum of wavelengths. Depending on the goniometer angle only a very small range of wavelengths are then transmitted through the excitation slits. The light is then further collimated before it is split between a reference detector and the sample of interest. Upon absorption of the incident light

the sample will become excited, transitioning to a higher electronic state, before decaying back down to the ground state and producing fluorescent emission in the process. The fluorescent emission is then collimated via a parabolic mirror, passed through the emission entry slits and sent to the emission diffraction grating (also mounted on a goniometer). The fluorescent emission is dispersed into a polychromatic spectrum and scanned (via goniometer rotation) allowing a small wavelength range passage through the emission exit slits. A detector then measures the intensity at each wavelength, in turn, building up a complete fluorescent emission spectrum of the sample of interest (figure 3.7). A connected computer controls the whole operation of the instrument including processing of the collected data.

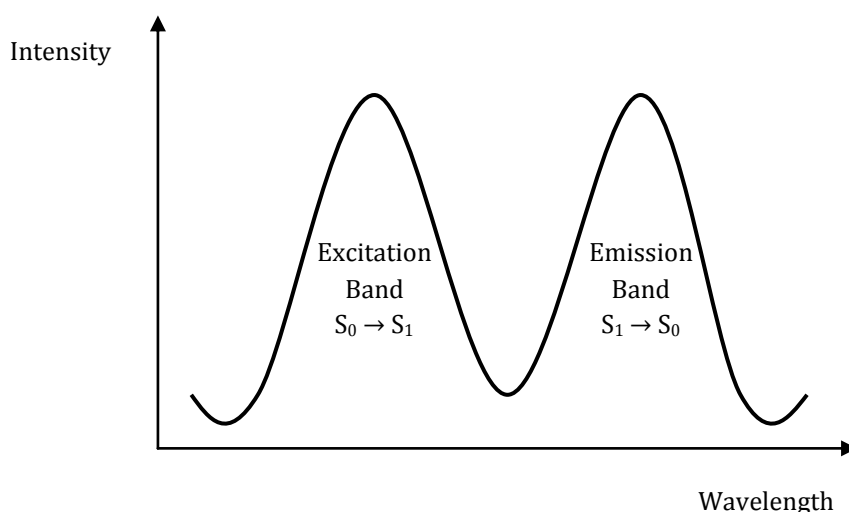


Figure 3.7: Schematic diagram of an idealised excitation/fluorescence plot as measured on a LS-50B spectrophotometer. Denoted are the typical electronics transitions that produce the spectroscopic structure observed.

Several issues can be encountered when operating the spectrofluorimeter. Firstly, if the fluorescence emissions are weak either the slits have to be widened to allow more light through or the scan rate has to be reduced allowing more time to integrate the detected emission. The former has the disadvantage that spectral resolution is lost whilst the latter means that fewer scans can be performed in a session. Another issue that can present itself is in the form of higher-order diffraction peaks. These peaks appear on the measured spectral plots and can be difficult to differentiate from genuine excitation/emission peaks, especially when measuring thin film samples deposited onto reflective substrates (such as silicon). To prevent such effects

additional optical filters may be used to attenuate them sufficiently so as not to be detected by the sample detector.

3.4 Absorption Spectroscopy

Absorption spectroscopy is a form of spectroscopy dedicated to characterising the absorption of electromagnetic radiation by matter. Absorption measurements were performed primarily to determine the most appropriate excitation source for each MFE-candidate material. All measurements made here occurred exclusively on the Perkin-Elmer Lambda 900 ultraviolet-visible spectrophotometer (shown in figure 3.8).

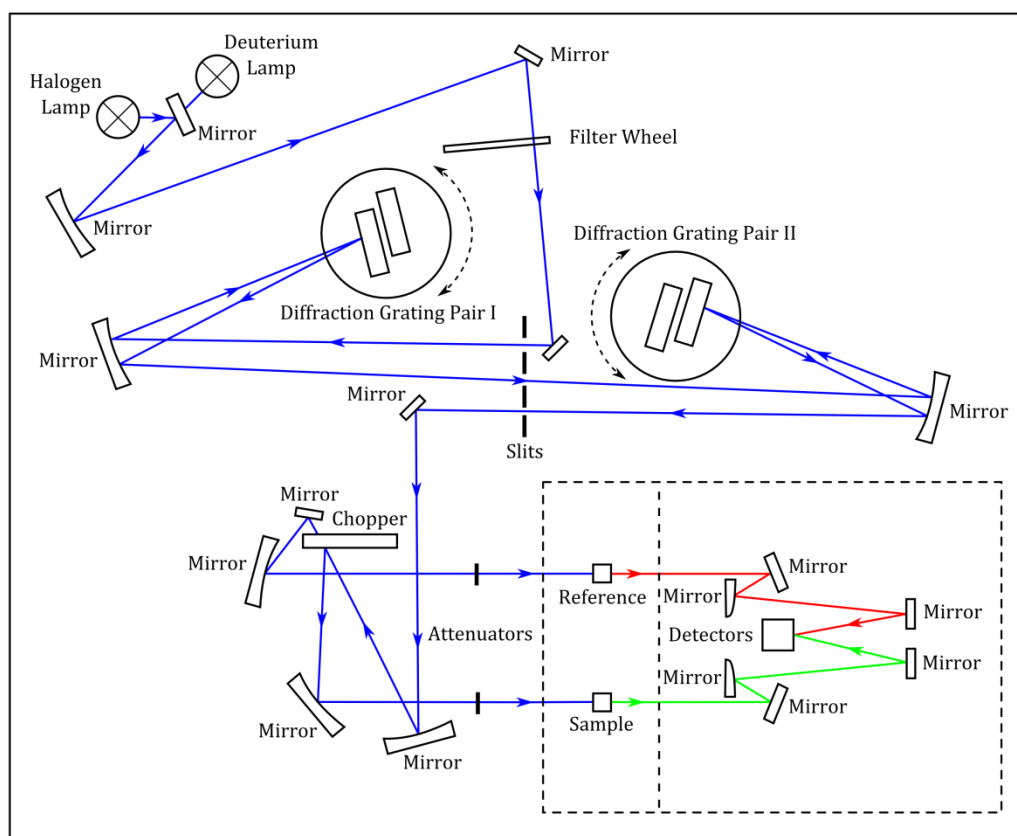


Figure 3.8: Schematic diagram of the Perkin-Elmer UV/Visible spectrophotometer.

The instrument operates in the following manner. Two lamps are used as the initial source of probing radiation. The first is a deuterium arc lamp which is a gas discharge light source that emits in the visible spectrum and especially well in the ultraviolet (UV) portion of the electromagnetic spectrum. The second light source is a halogen lamp that also emits in the

visible spectrum and especially well in the near infra-red (NIR) portion of the spectrum. Together, the two lamps cover a large range of the electromagnetic spectrum and can be selected depending on what light is needed during a measurement. The light is collimated through a series of parabolic mirrors and then filtered by a colour filter mounted on a filter wheel to begin monochromating the light. The light is then sent into the first of two diffraction gratings mounted on a goniometer where the light is then diffracted and dispersed into its constituent spectrum of wavelengths. Each goniometer hosts two diffraction gratings: one for the UV/Visible portion of the spectrum and one for the NIR portion of the spectrum (with each grating selected when required). The light is then sent through a slit where only a small range of wavelengths are permitted to be transmitted. The light is then sent to another diffraction grating and slit generating ultra-pure monochromatic light. This light is then sent to an optical chopper containing three mounted devices: a mirror to reflect the light; an aperture to transmit the light; and a beam stop to extinguish the light. The reflected beam is passed through the sample to be measured; the transmitted beam is passed through the reference sample to be measured; and the absence of beam is used to measure the “dark” quiescent signal. The transmitted light from both samples is then sent to the appropriate detector and is measured in an alternating fashion. Two detectors exist in the Lambda 900: a lead sulphide (PbS) detector which is most sensitive to NIR light and a photomultiplier tube (PMT) which is used for the UV/Visible light and are automatically selected when appropriate.

To allow unimpeded transmission of the absorption spectra the samples were deposited onto 25 × 25 mm fused quartz slides of 1 mm thickness. Fused quartz is the ideal substrate material for these measurements as it has > 90% transmission in the range 280 – 2000 nm [7]. Deposition onto the slides was performed via spin-coating or via thermal evaporation depending on the material.

A clean, unused fused quartz slide was used as the reference sample of choice in all measurements performed. This allows the fused quartz spectra to be subtracted from the

sample spectra revealing the true spectra of each sample (assuming negligible contribution from uncontrolled differences in reflectivity).

Spectra acquisition was controlled by a computer connected to the instrument allowing spectra to be processed and stored for later retrieval.

3.5 Optical Microscopy

An optical microscope is an instrument capable of visualising small features on a sample using visible light as the interaction medium. The instrument (shown in figure 3.9) includes a light source which can transmit through or reflect off a sample (for the purposes of this research the latter detection mode will be discussed). An objective lens is used to deliver light to, and collect reflected light from, the sample area of interest whilst collimating the collected light. The collimated light is then sent to a condenser lens to be recorded by a CCD camera or viewed by the user via the eyepiece. The objective lens is usually part of an interchangeable assembly of lenses that allows the user to select different magnifications. The magnifying power of a microscope is dependent on the focal length of the lenses used which, in turn, is dependent on the refractive index and geometry of each lens. Image focus is manipulated by translating the sample stage in the vertical axis.

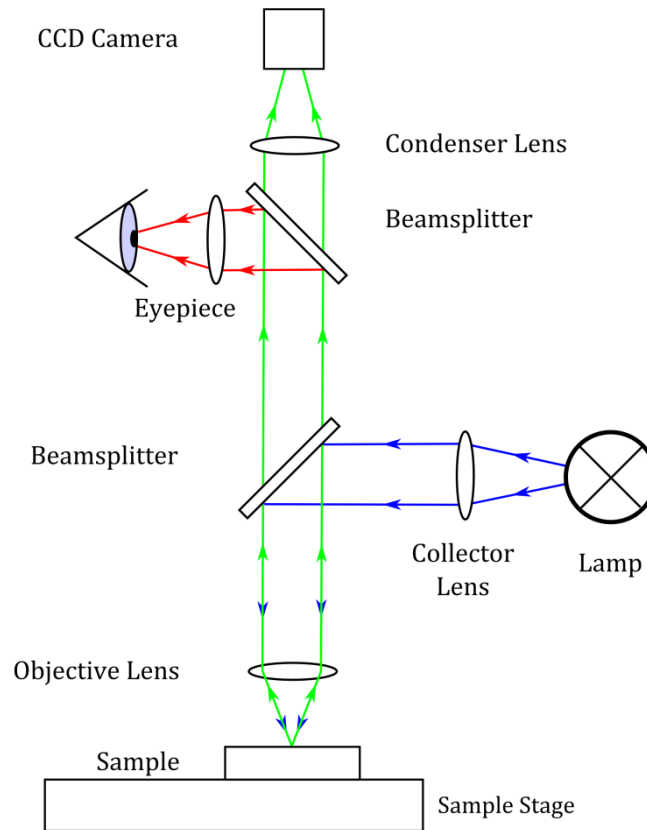


Figure 3.9: Schematic diagram of an optical microscope.

For an optical microscope operating with air as the sample/lens interface the maximum achievable spatial resolution is approximately half the wavelength of the illumination light used. This limit is referred to as the Abbe diffraction limit and is defined as [8]:

$$d = \frac{\lambda}{2(n \sin \theta)} \quad \text{Equation 3.2}$$

where d = spatial resolution; λ = wavelength of light; n = refractive index; θ = half-angle subtended by the objective lens to the sample; $n \sin \theta$ = numerical aperture.

Inputting some typical laboratory values ($\lambda = 550 \text{ nm}$; $n \sin \theta = 0.65$) into equation 3.2 yields a resolution of $\approx 420 \text{ nm}$. To increase the resolving power several techniques can be employed that modify the traditional setup. One of these includes changing the sample/lens interface from air to oil to improve the resolution since oil has a larger refractive index ($n \approx 1.5$) compared to air ($n \approx 1.0$).

An optical microscope was used in this research to assess the surface morphology of spin-coated samples in the millimetre to micrometre range.

3.6 Confocal Microscopy

A confocal microscope is an instrument capable of imaging photoluminescent material at high magnification. The particular type of confocal microscope used in this research was the Zeiss LSM 510 META upright laser scanning confocal microscope and is schematically represented in figure 3.10. The microscope was used, frequently in conjunction with a two-axis electromagnet, to attempt to capture an MFE magnetic contrast image from the fluorescent emission of a film deposited on top of magnetic microstructures.

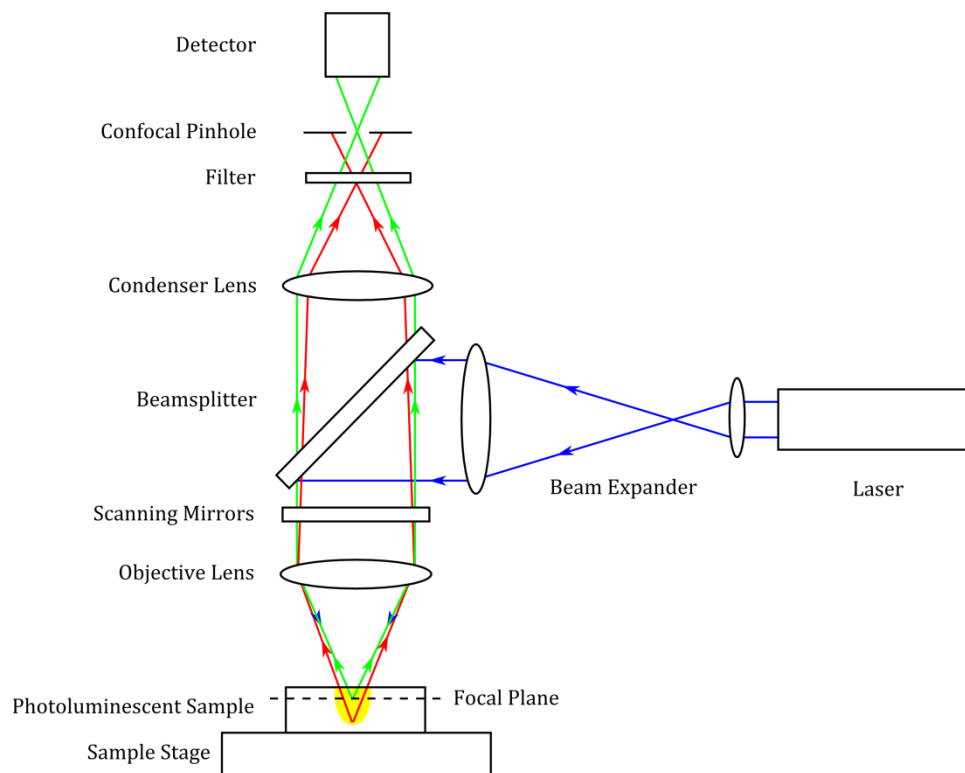


Figure 3.10: Schematic diagram of laser scanning confocal microscope.

The confocal microscope operates in the following manner. Laser light from an argon ion laser is tuned to the absorption peak of the material of interest (488 nm at 5-15% power for tetracene) and is passed through a beam expander and onto a beamsplitter where it is reflected downward towards the sample. Here it meets the scanning mirrors whose purpose is to raster scan the

laser spot over the sample line by line. This method contrasts with optical or epifluorescence microscopy where instead the whole sample is illuminated simultaneously – referred to as wide-field microscopy. Laser light is focussed by the objective lens onto a particular plane on, or in, the sample where the light is then absorbed. Upon absorption of the laser light the sample will excite, de-excite and emit photoluminescent light. This emission is captured by the objective lens, ‘de-scanned’ by the scanning mirrors and passed through the beamsplitter. The light is then passed through a suitable filter, selecting only the emission wavelength range of interest, and sent through the confocal pinhole. The pinhole is one of the key features of the confocal microscope. Its job is to block unfocussed light and transmit only focussed light. In this way, only photoluminescence from the plane of interest on, or in, the sample will be able to reach the detector. The detector, a ‘one pixel’ photodetector, measures only light intensity as image projection is not occurring - unlike in wide-field microscopes. Correlation of the time-dependent photodetector signal with the excitation laser scanning allows an image to be generated. A computer connected to the microscope coordinates the selection of the most appropriate laser source, dichroic beamsplitters, optical filters and detector settings whilst capturing and storing the scanned micrograph.

3.7 Atomic Force Microscopy

Atomic force microscopy (AFM) is a form of scanning probe microscopy whereby a mechanical probe is raster-scanned across a sample in order to determine the topography of the sample. The atomic force microscope used throughout this research was the Veeco Dimension 3100 and is schematically represented in figure 3.11.

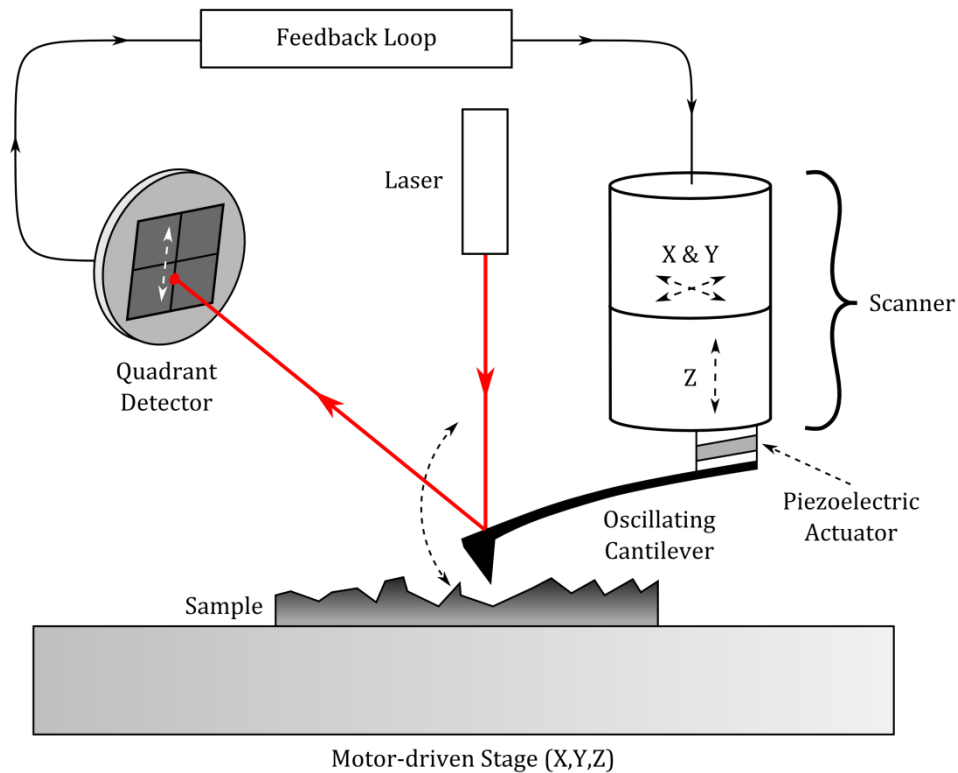


Figure 3.11: Schematic diagram of AFM operating in tapping mode.

There are three main modes that can be used with AFM: contact mode, non-contact mode and tapping mode [9].

Contact mode, the first mode to be developed for AFM, operates in the force-distance curve regime where the tip and sample experience a mutually repulsive Van der Waals force [10]. As the tip is scanned over the sample any changes in sample height encountered will cause a change in the force experienced by the tip. A laser, reflecting off the back of the tip and into a split detector, is used to measure the deflection of the tip and feedback this information to the scanner. The scanner then attempts to restore the tip to its original position by moving up or down, i.e. to maintain a constant deflection. In this manner the topography of the sample can be mapped in detail. A disadvantage of this mode is that both the tip and sample will degrade over time due to the mechanical stresses involved.

Non-contact mode operates in the force-distance curve regime where the tip and sample experience a mutually attractive Van der Waals force [10]. The cantilevered tip is forced to oscillate at or near its resonant frequency:

$$\omega_0 = c\sqrt{k} \quad \text{Equation 3.3}$$

where ω_0 = resonant frequency of cantilever; c = function of the cantilever mass; k = spring constant of the cantilever. Any perturbation in the oscillation of the cantilever is detected by a change in the resonant frequency:

$$\omega'_0 = c\sqrt{k - f'} \quad \text{Equation 3.4}$$

where ω'_0 = new resonant frequency of the cantilever; f' = derivative of the force normal to the surface. The feedback system therefore acts to maintain the oscillation frequency, keeping it near the resonant frequency by altering the height of the scanner. In this way the sample topography can be determined.

This mode of operation does not suffer from the degradation effects seen in contact mode AFM; however, problems can arise due to the formation of a liquid meniscus layer on the surface of the sample. This is caused by atmospheric water vapour and is encountered when operating under ambient conditions. Therefore the technique greatly benefits from being performed under ultra-high vacuum (UHV) conditions [10-12].

Tapping mode is similar to non-contact mode, however, where the amplitude of the oscillation for the latter is around 10 nm, the amplitude of oscillation for tapping mode is an order of magnitude larger. This allows tapping mode to operate at atmospheric pressure where it can penetrate the liquid meniscus layer that forms on the sample surface and measure the underlying changes in sample height during scanning. Tapping mode is able to achieve a lateral spatial resolution of 1-5 nm, however, this value also depends on the quality of the tip [10].

AFM operating in tapping mode requires minimal sample preparation, only that the samples are within the geometrical limits of the technique. For the Veeco Dimension 3100 the sample cannot be thicker than 12 mm and cannot contain height differences larger than 6 μm . Additionally, the maximum scan size cannot exceed 90 μm [13]. In this research the technique was predominantly used to assess sample morphology, the quality of samples fabricated using electron beam lithography and to confirm film thicknesses.

3.8 Magnetic Force Microscopy

Magnetic force microscopy (MFM) is a specialised version of AFM that is able to measure the magnetic force gradient of a demagnetising field above a magnetic sample surface whilst simultaneously measuring topographic data. A topographic data line scan is usually obtained first followed by a magnetic data line scan which is interleaved into the overall scan. This allows the magnetic data to be collected at a constant “lift height” from the sample surface. MFM makes use of a magnetic probing tip and phase detection hardware. Magnetic force microscopy was performed on the Veeco Dimension 3100 atomic force microscope. The probing tip used for MFM was the low moment magnetic etch silicon probe (MESP-LM) manufactured by Bruker. These tips are composed of antimony-doped silicon with a cobalt/chromium coating. It is the coating that allows for a magnetic interaction between the probe and the sample. MFM typically offers a spatial resolution no greater than $\approx 30\text{ nm}$ [14].

A magnetising stage (see figure 3.12), to allow the application of an external magnetic field to the sample whilst simultaneously being scanned, was designed by the author and built by the University’s Chemistry and Physics workshop. The pole pieces are composed of 1 mm diameter insulated copper wire coiled around a soft iron $5\times 5\times 100\text{ mm}$ core. Figure 3.13 contains the calibration plots for each axis.

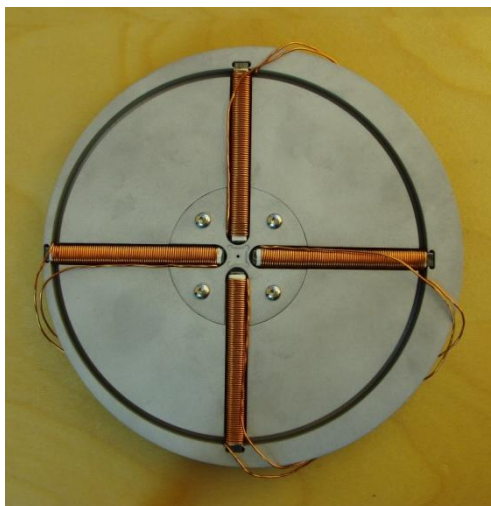


Figure 3.12: Photograph of the custom-built MFM magnetising stage.

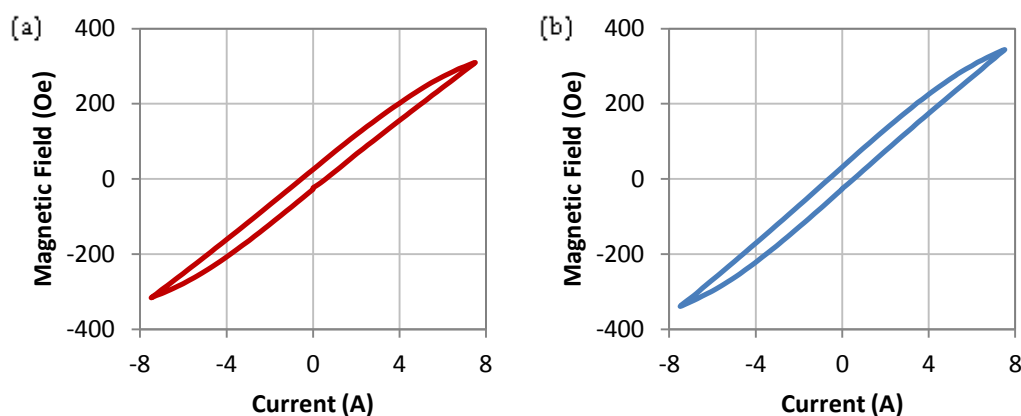


Figure 3.13: Calibration plots of the magnetising stage axes. (a) The 'red' axis is the vertical axis when stage is mounted on the AFM. (b) The 'blue' axis is the horizontal axis when stage is mounted on the AFM.

3.9 Magnetic Transmission X-Ray Microscopy

Magnetic transmission X-ray microscopy (M-TXM) is a technique used to observe micromagnetic phenomena in magnetic samples. The technique is actually a hybrid of two other techniques [15]: transmission X-ray microscopy (TXM) and X-ray magnetic circular dichroism (X-MCD), with the latter being responsible for visualising the magnetic contrast. TXM is a technique that has an inherently high resolving power due to the use of X-rays (see description of diffraction limit in §3.5). When coupled with a tuneable X-ray source the technique can also be used for chemical mapping using XANES (X-ray absorption near edge structure) [16]. X-MCD

is a phenomenon observed in ferromagnetic materials where circularly polarised soft X-rays are transmitted through a sample causing differential absorption (an example of 'circular dichroism'). This absorption is dependent on a correlation existing between the sample magnetisation and the helicity of the incident X-ray photons [17]. That is to say, if the sample is magnetic and the magnetisation direction correlates with the handedness of the incident light, then absorption will occur. If, however, there is a negative correlation, then there will be little, if any, absorption. It is these two extremes that define the contrast range observed in X-MCD.

It is obvious, then, that the use of soft X-rays generated from a synchrotron facility is vital in order for the technique to be able to resolve magnetic contrast. M-TXM micrographs presented in this research were obtained from the 6.1.2 beamline at the Advanced Light Source (ALS), University of Berkeley, California, USA (schematically represented in figure 3.14). The ALS is a third-generation synchrotron that first opened in 1993 and houses 42 operational beamlines with one more under construction [18]. Beamline 6.1.2 is a high-resolution zone-plate X-ray microscopy facility that operates from a bending magnet that generates X-rays with an energy in the range of 300-1000 eV [19]. The beamline is used for imaging various samples from biological samples and polymeric materials to magnetic samples.

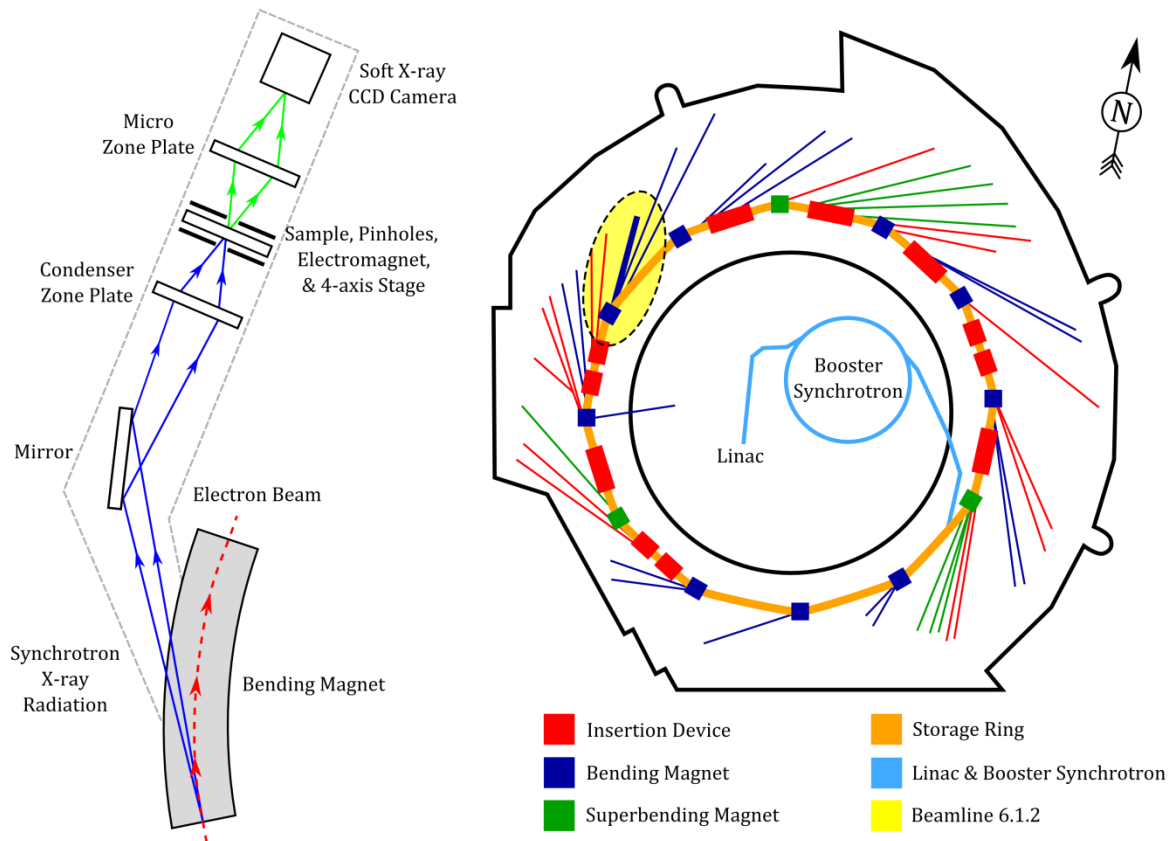


Figure 3.14: Schematic diagram of beamline 6.1.2 at the Advanced Light Source synchrotron, Berkeley. Diagram adapted from [20].

The beamline operates in the following manner. As electrons that circulate the storage ring enter the bending magnet a strong magnetic field induces a Lorentz force on the charged particles producing a curved trajectory perpendicular to the applied field and proportional to the magnitude of the field. Due to the change in momentum encountered by the relativistic electrons synchrotron radiation is released tangentially in the form of X-rays [21]. A portion of these X-rays are then directed toward beamline 6.1.2 under vacuum. In order for magnetic contrast to occur the X-ray energy has to be tuned to the absorption energy of the sample. After that the X-ray beam is focussed by a condenser Fresnel zone plate: a lens that relies on diffraction rather than refraction in order to focus light. Zone plates have to be used as traditional lenses cannot focus X-ray light. The X-rays then pass through a pair of pinholes to define the field of view and prevent stray light from entering the beam path. X-ray transparent beryllium membranes act to seal the vacuum line on each side of the sample. The sample, exposed to atmospheric pressure, is positioned between the pinholes/membranes at an angle of

30° to beam normal in order to maximise contrast contribution from *in-plane* magnetisation. The transmitted X-rays are then focussed by an objective Fresnel zone plate onto a soft X-ray sensitive LN₂-cooled CCD camera. Captured magnetic contrast images are enhanced by dividing them with a reference image (such as reversed magnetisation by applying an external magnetic field). This operation reduces the contrast contribution from non-magnetic features whilst improving the magnetic contrast. For this experiment, involving Ni-Fe samples, the X-ray energy was tuned to the L absorption edge of nickel corresponding to 854 eV.

Due to their excellent X-ray transmission properties 100 nm thick Si₃N₄ membranes were used as substrates for the Permalloy microstructures used in this experiment. The microstructures were patterned onto the membranes using electron beam lithography. As the membranes are very fragile a number of precautionary fabrication steps were undertaken. One of these steps was to avoid using the ultrasonic bath to perform the lift-off procedure as this would have delaminated the membranes from their supporting silicon frame.

3.10 Hall Array Magnetometry

Hall array magnetometry was performed using a commercial system manufactured by MagCam known as the Magnetic Field Camera [22]. This device (seen in figure 3.15) comprises of a two-dimensional array of Hall sensors that can be polled in real-time to produce two-dimensional plots of the stray magnetic field of, for example, permanent magnets. The unit consists of a 128 × 128 array of Hall sensors with a spatial resolution of 0.1 mm over an area of 13 × 13 mm. A temporal resolution ≥ 2 ms can be achieved using this system, however, longer frame averaging will produce higher signal-to-noise plots. The achievable magnetic field resolution equals 0.1 mT over a range of 0.1 mT – 5 T.

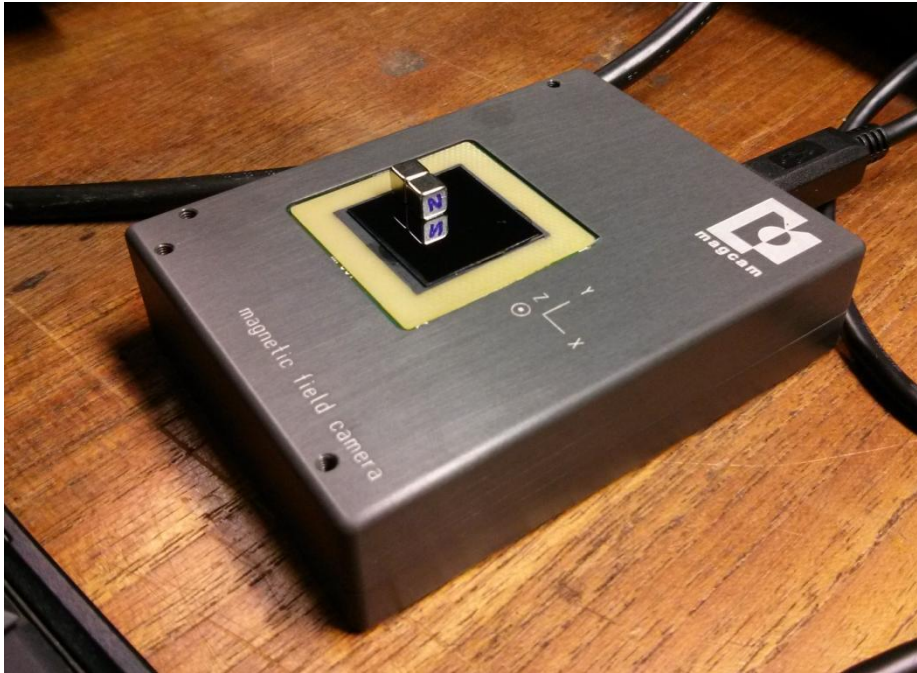


Figure 3.15: A photograph of the Hall array magnetometer with a permanent magnet positioned ready to be measured.

The device is operated at room temperature and is connected via USB to a computer running the control software. Data acquisition occurs in real-time allowing the user to make use of the live plots whilst aligning the sample to be measured. Contour plots, line plots and raw data can all be exported using the provided software.

In this research the MagCam system was used exclusively to measure the magnetic stray field of a set of NdFeB permanent magnets that were also used in the fluorescence photography experiments.

3.11 Magneto-Optic Kerr Effect Magnetometry

Magneto-optic Kerr effect (MOKE) magnetometry is a technique used to characterise the magnetic properties of materials. MOKE magnetometry exploits the magneto-optic Kerr effect [23] in order to measure the magnetisation state of a sample at a particular moment in time. The magneto-optic Kerr effect is a phenomenon whereby linearly polarised light, incident on and reflected by a magnetised sample surface, becomes elliptically polarised as well as rotated

about the plane of polarisation [24]. This change in polarisation is directly proportional to the component of the magnetisation vector of the sample which is aligned parallel to the sensitivity axis used in the measurement [24]. Knowing this, the magnetisation state of the sample can be interrogated using a quarter-wave plate (to convert the elliptically polarised light to linearly polarised light), an analyser (to analyse the polarisation state of the reflected light) and a photodetector (to measure the Kerr signal). By applying an alternating external magnetic field whilst continuously monitoring the intensity of the reflected light it is possible to produce a magnetic hysteresis loop corresponding to how the material switches its magnetisation state in response to the external field [25].

In this research MOKE magnetometry was exclusively performed using an in-house experimental focussed MOKE magnetometer (see figure 3.16).

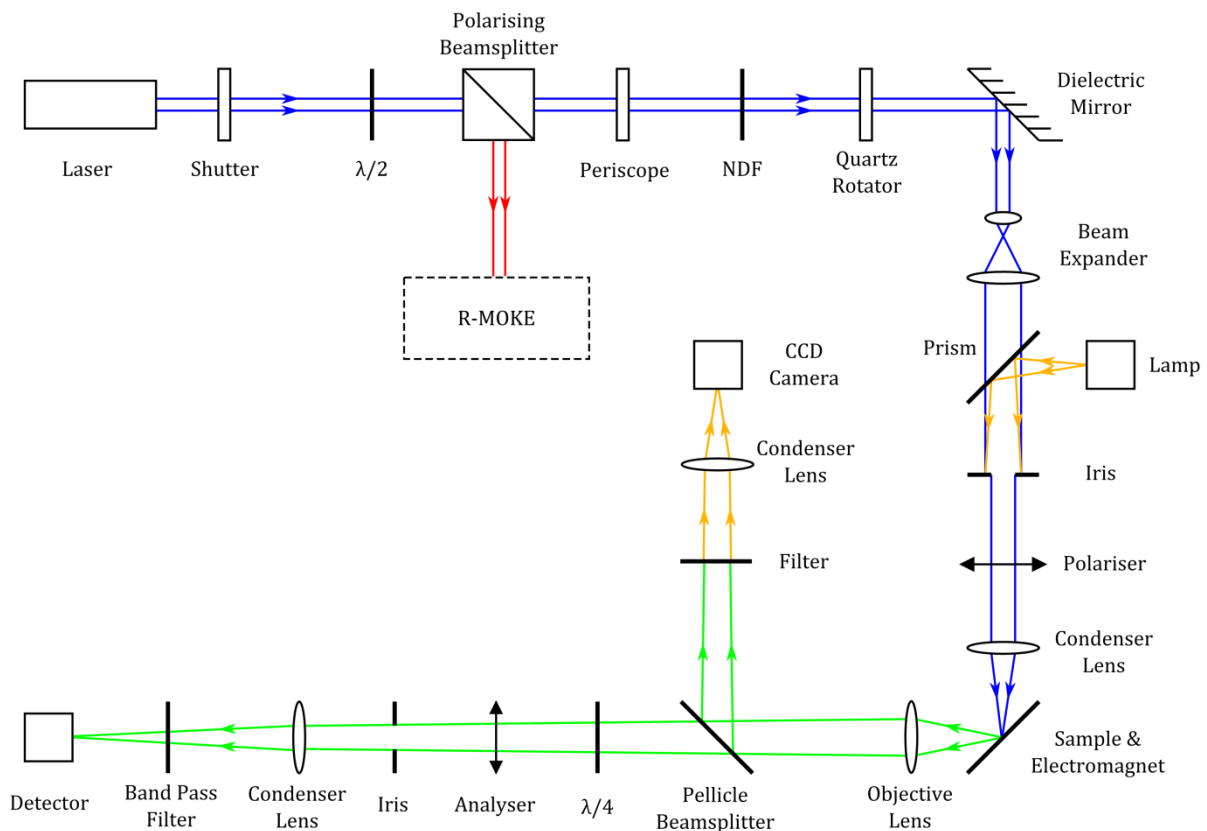


Figure 3.16: A schematic diagram of a focussed MOKE magnetometer. $\lambda/2$ refers to a half-wave plate whilst $\lambda/4$ refers to a quarter-wave plate. R-MOKE is an experimental magnetometry system currently in development that utilises radially-polarised light to detect MOKE from in-plane magnetisation.

The focussed MOKE magnetometer operates in the following manner. A continuous-wave 532 nm Coherent Verdi V2 diode-pumped laser with a maximum power of 2.2 W is sent through a half-wave plate and a polariser to reduce its intensity to minimise sample damage. The laser is intentionally operated at high power in order to provide a stable, low-noise, light source. The beam is reflected off a dielectric mirror and sent through a beam expander. White light is then introduced (for sample alignment only) and reduced in size with an iris. Both beams then pass through a linear polariser and are collimated with a condenser lens. The focal spot is aligned with the sample and reflects off towards the objective lens with the polarisation state modified. Next the beam reaches a beamsplitter where half the light is transmitted and half is reflected. The half that is reflected passes through a dichroic filter reflecting the laser light whilst transmitting everything else. This beam is then collimated by a condenser lens and is captured by a CCD (charge-coupled device) camera. The portion of beam transmitted at the beamsplitter is sent through a quarter-wave plate converting any elliptically-polarised light into linearly polarised light and then through an analyser (with the analyser angle rotated approximately 1.7° away from signal minimum which allows for transmission of the Kerr signal at the highest signal-to-noise ratio for this system [26]). The Kerr signal is then filtered through a band pass filter before being detected using a biased silicon PIN photodiode detector (EOT ET-2030).

Two Kepco bipolar power supplies are used to power the two-axis electromagnet and are controlled by a sinusoidal signal generated by a digital-to-analog converter (DAC) connected to the control computer. The sinusoidal signal is also fed to the main digital storage oscilloscope (DSO). The Kerr signal, as measured by the photodiode detector, is amplified with a current sensitive pre-amplifier and passed to the DSO. From here, the control computer polls the DSO for the time-averaged Kerr signal and plots it against the applied magnetic field producing a hysteresis loop of the magnetisation reversal process of the magnetic sample of interest.

3.12 Micromagnetic Modelling

Micromagnetic modelling was undertaken in order to determine the three-dimensional magnetic stray field profile above simulated micromagnetic objects. These objects were modelled to represent real structures that may be patterned onto samples in a practical test of the proposed magnetic microscopy technique.

The objects to be simulated were designed in a geometrical modelling software package known as GiD 7.2. Object geometries, magnetic properties and mesh structures were all defined in GiD. These definitions were then passed to a micromagnetic software package known as FEMME 4.6.5 (**F**inite **E**lement **M**icro**M**agn**E**tics), produced by SuessCo KG, which performed the time-dependent evolution of the magnetisation dynamics of the system according to the Landau-Lifshitz-Gilbert (LLG) equation until system equilibrium was reached based on energy minimisation criteria [27]:

$$\frac{\partial \mathbf{M}}{\partial t} = -\gamma \mathbf{M} \times \mathbf{H}_{\text{eff}} + \frac{\alpha}{M_s} \mathbf{M} \times \frac{\partial \mathbf{M}}{\partial t} \quad \text{Equation 3.5}$$

where \mathbf{M} = magnetisation; t = time; γ = gyromagnetic ratio; \mathbf{H}_{eff} = effective magnetic field; α = Gilbert damping constant; M_s = saturation magnetisation.

For each mesh cell the LLG equation is numerically solved before the system iterates to the next time interval and repeats the process. The effective field, \mathbf{H}_{eff} , is defined as [28, 29]:

$$\mathbf{H}_{\text{eff}} = \frac{2A}{J_s} \Delta \mathbf{J} + \frac{2K_1}{J_s} \mathbf{a}(\mathbf{J} \cdot \mathbf{a}) + \mathbf{H}_{\text{ext}} + \mathbf{H}_{\text{demag}} \quad \text{Equation 3.6}$$

where A is the exchange constant, J_s is the saturation polarisation, \mathbf{J} is the magnetic polarisation, K_1 is the first magnetocrystalline anisotropy constant and \mathbf{a} is the unit vector parallel to the easy axis. It is used as one of the primary inputs in the LLG equation (first term in equation 3.5). The effective field is a summation of the exchange interaction (first term in equation 3.6), the magnetocrystalline anisotropy (second term in equation 3.6), the externally applied magnetic

field (\mathbf{H}_{ext}) and the magnetostatic (demagnetising) field ($\mathbf{H}_{\text{demag}}$). The exchange and anisotropy energy terms are short-range interactions and depend only on the local magnetisation state whilst the external field is independent of the magnetisation of the simulated object. The magnetostatic field is a long-range interaction and is the most computationally demanding term in the LLG equation. At each iteration of the simulation the previous state of every cell is retrieved and used as an input when calculating the LLG equation (second term in equation 3.5) allowing the system to evolve with time.

In order to ensure that the micromagnetic simulation remains accurate the mesh cell size should not be any larger than the exchange length of the material – the length scale below which the magnetisation can no longer be twisted in order to minimise the dipolar interaction [24]. The exchange length can be calculated from the following equation using the magnetic material parameters used in the model:

$$l_{ex} = \min \left(\sqrt{\frac{A}{k_1}}, \sqrt{\frac{2A}{\mu_0 M_s^2}} \right) \quad \text{Equation 3.7}$$

where A = exchange constant; k_1 = first magnetocrystalline anisotropy constant; μ_0 = vacuum permeability; M_s = magnetisation saturation.

The first term in equation 3.7 determines the magnetocrystalline exchange length (for a Bloch wall) whilst the second term determines the magnetostatic exchange length (for a Néel wall).

Stray magnetic fields (the demagnetising field, generated by, but existing outside of the magnetic material) were simulated by creating a ‘dummy’ object above the object of interest and placing a ‘field box’ between the two. The dummy box was given vacuum properties and magnetostatic interactions were calculated between the two objects. The dummy and field box objects were only introduced once the main object had been evolved to energy minimum.

Simulations were executed on the MESAS computing cluster facility located in the Materials Science and Engineering department. Visualisation of the data generated by FEMME was performed by ParaView 3.1.4.1.

3.13 References

- [1] D. B. Hall, *et al.*, "Spin Coating of Thin and Ultrathin Polymer Films," *Polymer Engineering and Science*, vol. 38, pp. 2039-2045, 1998.
- [2] T. M. Hall, *et al.*, "Ion-beam exposure characteristics of resists - Experimental results," *Journal of Applied Physics*, vol. 53, pp. 3997-4010, 1982.
- [3] T. H. P. Chang, "Proximity effect in electron-beam lithography," *Journal of Vacuum Science & Technology*, vol. 12, pp. 1271-1275, 1975.
- [4] A. v. d. Kraats. (2006). *Proximity Effect in E-beam Lithography*. Available: <http://nanolithography.gatech.edu/proximity.htm>
- [5] J. J. Zarate and H. Pastoriza, *Correction Algorithm for the Proximity Effect in e-beam Lithography*. New York: IEEE, 2008.
- [6] M. Ohring, *Materials Science of Thin Films*: Elsevier Science, 2001.
- [7] UQG Optics. (2013). *Fused Quartz Data Sheet*. Available: <http://www.uqgoptics.com/pdf/Fused%20Quartz%20-%20Vit%20077.pdf>
- [8] F. G. Smith, *et al.*, *Optics and Photonics: An Introduction*: Wiley, 2007.
- [9] S. Morita, *Roadmap of Scanning Probe Microscopy*: Springer, 2006.
- [10] P. Eaton and P. West, *Atomic Force Microscopy*: OUP Oxford, 2010.
- [11] S. Rozhok, *et al.*, "AFM Study of Water Meniscus Formation between an AFM Tip and NaCl Substrate," *The Journal of Physical Chemistry B*, vol. 108, pp. 7814-7819, 2004/06/01 2004.
- [12] R. D. Piner and C. A. Mirkin, "Effect of Water on Lateral Force Microscopy in Air," *Langmuir*, vol. 13, pp. 6864-6868, 1997/12/01 1997.
- [13] National Institute of Standards and Technology, "Veeco Dimension 3100 Atomic Force Microscope Users Manual," ed, 2010.

- [14] L. Abelmann, *et al.*, "Comparing the resolution of magnetic force microscopes using the CAMST reference samples," *Journal of Magnetism and Magnetic Materials*, vol. 190, pp. 135-147, Dec 1998.
- [15] T. Eimuller, *et al.*, "Transmission X-ray microscopy using X-ray magnetic circular dichroism," *Applied Physics a-Materials Science & Processing*, vol. 73, pp. 697-701, Dec 2001.
- [16] H. Fleckenstein, *High Resolution Chemical Mapping Via Scanning Transmission X-Ray Microscopy*: BiblioBazaar, 2011.
- [17] P. Fischer, *et al.*, "Imaging of magnetic domains with the X-ray microscope at BESSY using X-ray magnetic circular dichroism," *Zeitschrift Fur Physik B-Condensed Matter*, vol. 101, pp. 313-316, Nov 1996.
- [18] Advanced Light Source. (2013). *Advanced Light Source - Quick Facts*. Available: <http://www-als.lbl.gov/index.php/about-the-als/quick-facts.html>
- [19] The Center for X-ray Optics. (2010). *Beamline 6.1.2 (XM-1)*. Available: <http://www.cxro.lbl.gov/BL612/>
- [20] Advanced Light Source. (2013). *Advanced Light Source Beamclock*. Available: <http://www-als.lbl.gov/images/stories/Beamlines/2013-05-beamclock.jpg>
- [21] D. Attwood, *Soft X-Rays and Extreme Ultraviolet Radiation: Principles and Applications*: Cambridge University Press, 2007.
- [22] MagCam. (2013). *Magnetic Field Camera*. Available: <http://www.magcam.com/Page-MagCam One-EN.htm>
- [23] H. Hopster and H. P. Oepen, *Magnetic Microscopy of Nanostructures*: Springer, 2005.
- [24] J. M. D. Coey, *Magnetism and Magnetic Materials*: Cambridge University Press, 2010.
- [25] W. Rave, *et al.*, "Quantitative observation of magnetic domains with the magneto-optical Kerr effect," *Journal of Magnetism and Magnetic Materials*, vol. 65, pp. 7-14, 1987.
- [26] D. A. Allwood, *et al.*, "Magneto-optical Kerr effect analysis of magnetic nanostructures," *Journal of Physics D-Applied Physics*, vol. 36, pp. 2175-2182, Sep 2003.
- [27] D. Wei, "Maxwell Equations and Landau-Lifshitz Equations," in *Micromagnetics and Recording Materials*, ed: Springer Berlin Heidelberg, 2012, pp. 21-52.
- [28] W. Scholz, *et al.*, "Scalable parallel micromagnetic solvers for magnetic nanostructures," *Computational Materials Science*, vol. 28, pp. 366-383, 2003.

- [29] F. Bruckner, *et al.*, "Combining micromagnetism and magnetostatic Maxwell equations for multiscale magnetic simulations," *Journal of Magnetism and Magnetic Materials*, vol. 343, pp. 163-168, 2013.

4 System Development

4.1 Introduction

In order to measure the photoluminescent magnetic field effect of several materials (§3.2.1) a custom-made system, passing through several design iterations, was designed and built. This chapter aims to describe every iteration of the system whilst explaining the design choices that were made. Results relating to the performance of each iteration will be presented and discussed.

Toward the end of the chapter another custom-built system, designed to capture macroscopic photoluminescent magnetic field effect images, will be presented describing the design and operation of the system.

4.2 Magnetic Field Effect Magnetometry

Before each iteration of the magnetic field effect magnetometer that was designed and built is discussed the operating procedure and general working principle of this system will be described.

An MFE candidate sample to be measured was placed between the poles of an electromagnet that provided a uniform quasi-static magnetic field. A high power light emitting diode (LED) that operated at constant current (continuous wave output), with the emission wavelength corresponding to the peak absorption band of the sample, was positioned to illuminate the photoluminescent sample resulting in the generation of fluorescence. Fluorescent light emitted by the sample was filtered by a long-pass filter, to block LED light whilst passing fluorescent light, and detected by a photodetector. The analogue voltage generated by the photodetector in response to detected light was converted by an analog-to-digital converter (ADC) and logged by a control program (discussed in detail in §4.2.6) running on a computer to which the ADC was connected. The program controlled the electromagnet using a digital-to-analog converter (DAC).

If it is MFE-active, the fluorescence intensity will change in the presence of the magnetic field compared to when no magnetic field is present, as described by:

$$\text{MFE} = \left(\frac{I_B - I_0}{I_0} \right) \times 100\% \quad \text{Equation 4.1}$$

where I_B and I_0 are the fluorescent intensities with and without a magnetic field, respectively.

Often the material under investigation suffers from the effects of photobleaching. This results in a fluorescent intensity that diminishes with continued exposure to light from the LED. In order to improve the confidence of the measurement the electromagnet is turned on and off repeatedly so that the change in fluorescent intensity due to the MFE can be extracted from the decaying background signal and averaged. Once the fluorescent MFE value is known for a particular magnetic field the system is set up to repeat the measurement process at another magnetic field.

For the low field MFE system, described in §4.2.1, the magnetic field is incremented manually in ~ 2.5 mT steps and, due to the electromagnet used in that build, is limited to a maximum magnetic field of ~ 30 mT. For the high field MFE systems, described in §4.2.3-4.2.5, the magnetic field is incremented automatically with minimum steps equal to 5 mT and an upper limit of 300 mT.

4.2.1 Low Field MFE System Mk. I

The first version of the LF-MFE experimental setup is shown in figure 4.1. The system consists of an electromagnet (Solentec Ltd SM Series Electromagnet [1]) positioned close to the sample, with its associated 12V DC power supply. An LED illuminating the sample is placed at a 45° angle to the sample. A collector lens, long pass filter and APD are positioned normally, with respect to the sample plane, to collect the emitted fluorescent light. An Arduino Uno microcontroller was used to control the electromagnet (output) whilst an oscilloscope is used to measure the APD voltage (input). The average voltage, as measured by the oscilloscope, is

polled by the computer every 0.5 seconds via a null modem serial cable interface using the RS-232 communication protocol.

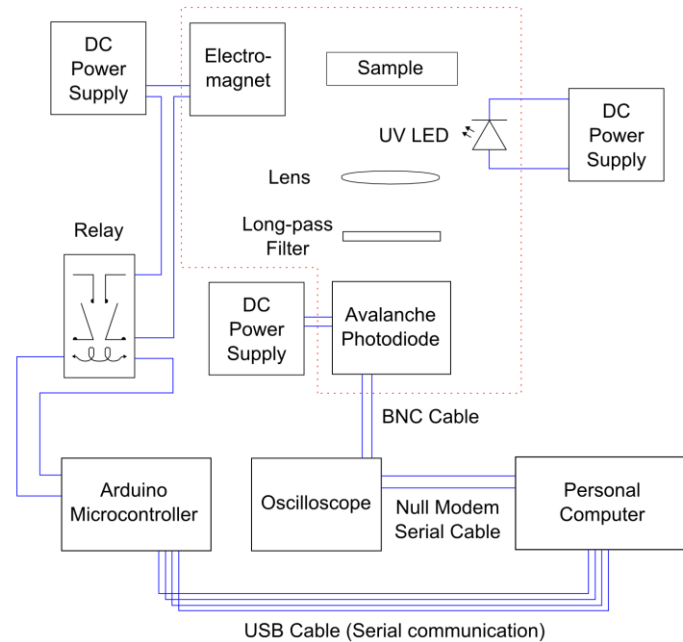


Figure 4.1: First version of the LF-MFE system. Blue lines are electrical connections; red lines denote boundaries of optical isolation.

Typical results obtained from the system are presented in figure 4.2. The first thing that can be seen is that the fluorescent signal detected by the APD decays with time. This is due to photobleaching of the sample and takes the form of an exponential decay function. What can also be seen is that when the magnet is switched on, the intensity increases, whilst when the magnet is switched off the intensity falls back to the background level – this is due to the magnetic field effect. A third point of interest is the fact that the data is very coarse in the ordinate axis. This is due to the combination of a poor 8-bit voltage resolution offered by the oscilloscope coupled to the issue that the signal background is sloped meaning that a large voltage scaling range is necessary to capture all of the data within the experimental timeframe. Normalising the data, as is shown in figure 4.3, highlights the severity of the voltage resolution issue. These results prompted the redesign of the system to include a higher resolution analog to digital converter (ADC) as well as methods to reduce the sample degradation rate caused by unnecessary photobleaching.

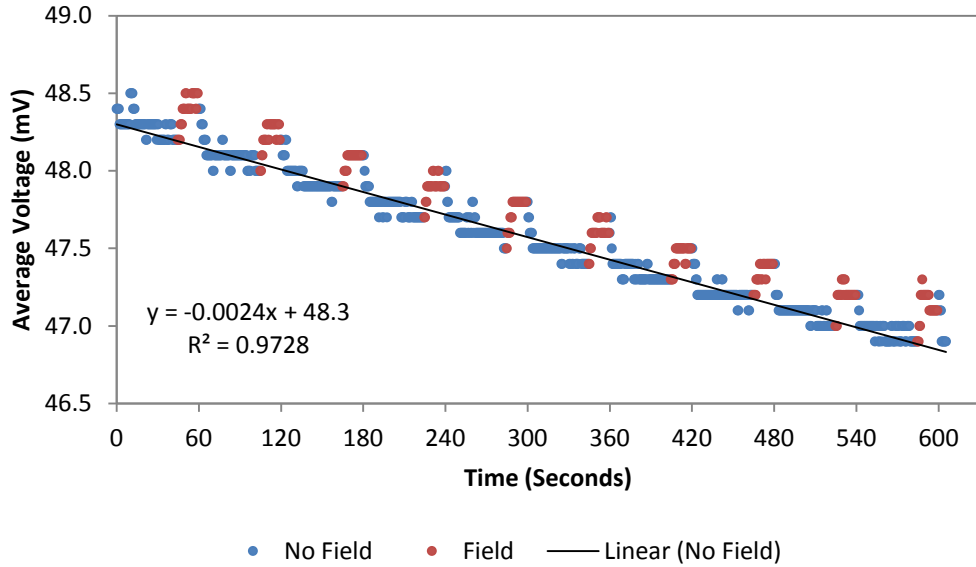


Figure 4.2: Typical result from the LF-MFE Mk I system. This particular measurement recorded the photoluminescent intensity as a function of time for the TPD:BBOT:PMMA sample.

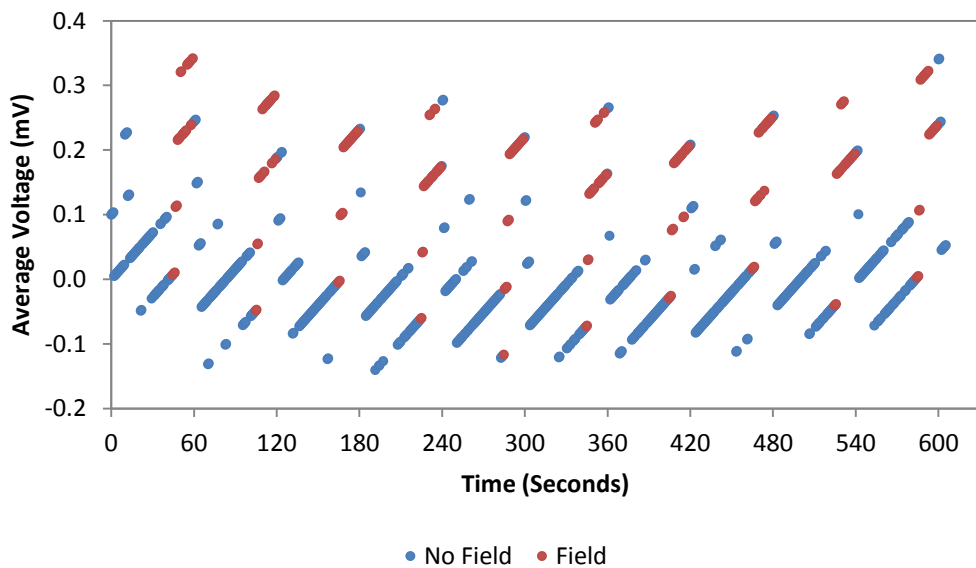


Figure 4.3: Background subtraction of MFE data using the equation of the linear fit function from figure 4.2.

4.2.2 Low Field MFE System Mk. II

The revised version of the LF-MFE experimental setup is shown in figure 4.4. The system consists of an electromagnet (Solentec Ltd SM Series Electromagnet [1]) positioned close to the sample, with its associated 12V DC power supply. An LED illuminating the sample, with a computer-controlled shutter between the two, is placed at a 45° angle to the sample. A collector lens, long pass filter and APD are positioned normally, with respect to the sample plane, to

collect the emitted fluorescent light. A National Instruments USB-6009 DAQ device with a voltage resolution of 14-bit was used to control the electromagnet (output) and measure the APD voltage (input) – replacing the oscilloscope that was used previously. As the DAQ isn't designed to directly switch the electromagnet power supply a relay was incorporated into the design. It was then found however, that the DAQ didn't have enough current available to switch the relay directly so an NPN transistor was also included into the design to solve that problem (with a 5V power supply). The shutter was created from a hard disk drive actuator arm and was included in the design in order to block LED light from reaching the sample when either the operator instructs the program to delay commencement of the experiment until the LED has stabilised or to block LED light once the experiment has finished. The shutter was controlled by the Arduino Uno microcontroller and a Sparkfun Electronics "Ardumoto" motor driver shield to provide sufficient power to actuate the shutter.

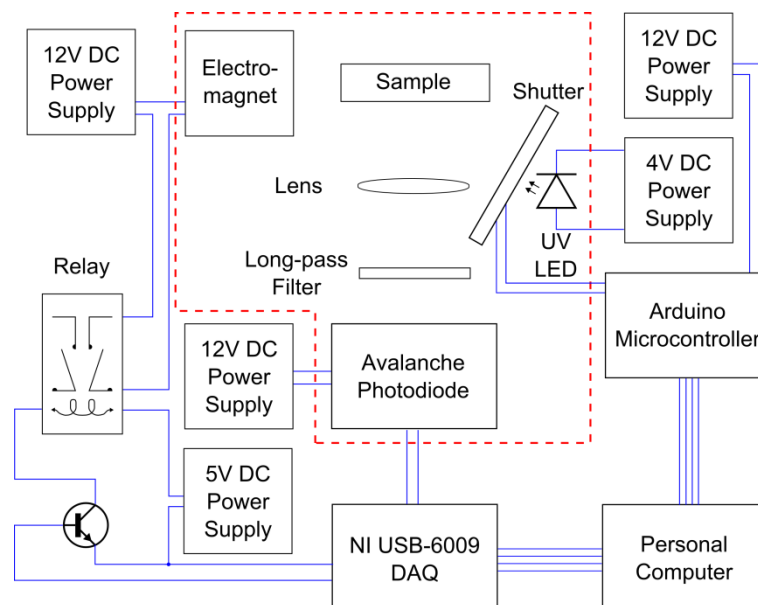


Figure 4.4: Revised version of the LF-MFE system. Blue lines are electrical connections; red lines denote boundaries of optical isolation.

The results collected from the revised version of the LF-MFE system are shown in figure 4.5a. It is immediately apparent the USB-6009 DAQ device with its improved voltage resolution has

provided the necessary resolution in order to represent the data accurately. The method of data averaging is also presented in figures 4.5b&c.

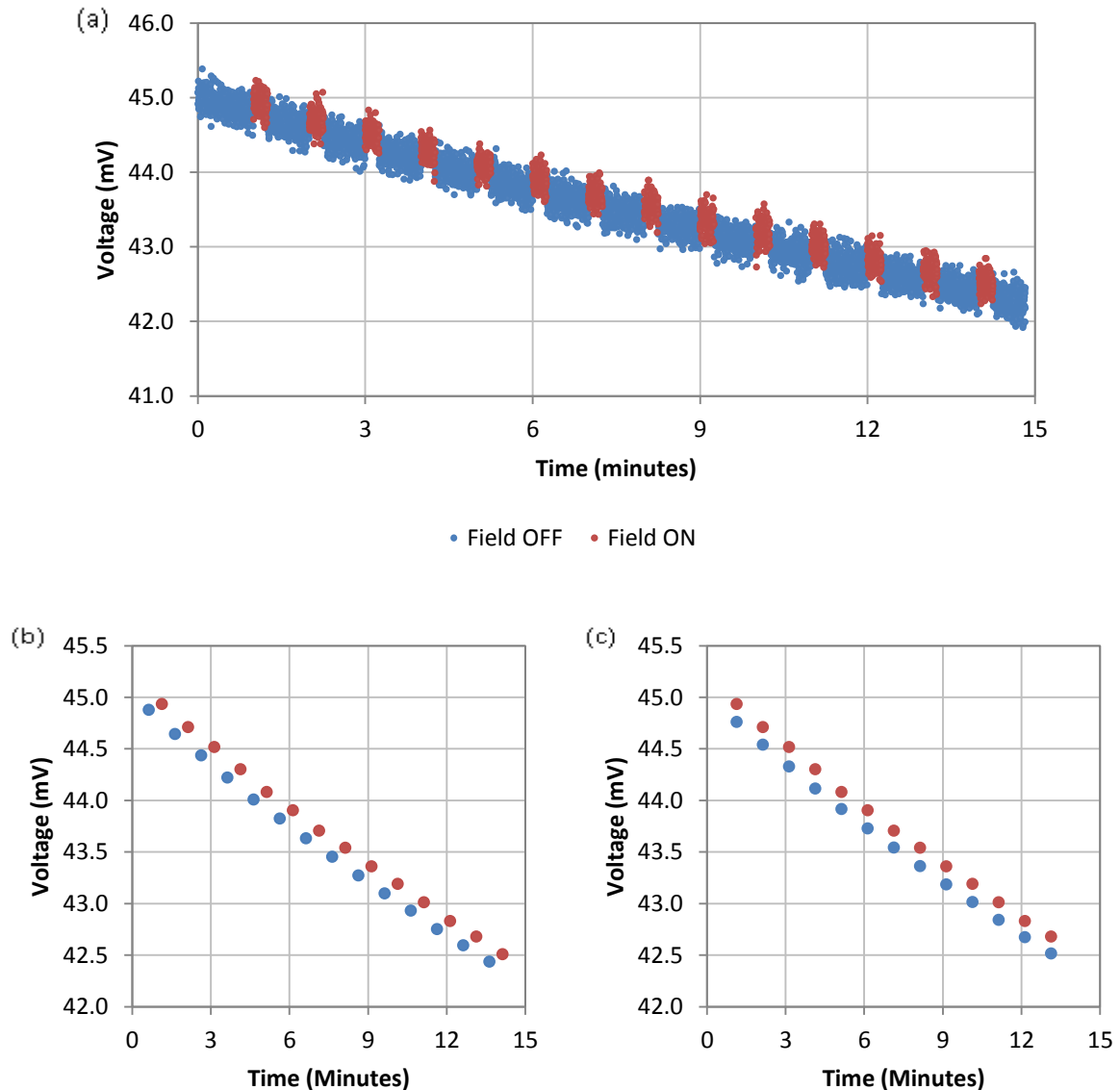


Figure 4.5: Plot of fluorescence intensity of TPD:BBOT:PMMA sample with time as measured on the revised version of the LF-MFE system. The blue data points represent the magnet in the off-state whilst the red data points represent the magnet in the on-state. (a) Raw data is plotted; (b) average value of cycle is plotted; (c) data is 'aligned' via linear interpolation of the 'field off' data set to allow calculation of the MFE for this field.

This system was designed to run the experiment autonomously; however, it was limited to running at one set magnetic field magnitude at a time. This is because the bench top power supply used to power the electromagnet was non-programmable. Other fields could be set by altering the voltage on the electromagnet power supply; however, this had to be done manually

and setting the maximum 12 volts that the electromagnet could tolerate only corresponded to a magnetic field of approximately 30 mT. There was therefore a need to move to a system that could produce stronger magnetic fields in order to explore MFE-behaviour beyond this limit and with greater autonomy.

4.2.3 High Field MFE System Mk. I

Figure 4.6 depicts the first version of the MFE system making use of the high field water-cooled electromagnet that's primarily used for high-field magneto-optic Kerr effect magnetometry. The electromagnet is a split core design offering a uniform region of magnetic field between the pole pieces with pole piece gap of 59 mm. It is powered by a Kepco bipolar amplifier and controlled by a DAC (digital to analogue converter) card in the computer. A FW Bell Model 6010 Gaussmeter was used to measure the magnitude of the magnetic field via a transverse Hall probe connected to the Gaussmeter.

When the decision was being made as to where to mount the necessary optics with which to perform the experiment, several issues were encountered. Firstly, the vicinity of the electromagnet was quite restricted which would make it difficult, but not impossible, to mount the optics around the electromagnet. Secondly, it was not known whether the magnetic field produced by the electromagnet would interfere with either the LED or the APD.

With consideration to these issues it was decided that the optics should be placed in a light-tight enclosure, connecting them to the sample via a single bifurcated optical fibre light guide (Ocean Optics BIF600-UV-VIS). The fibre, with a core diameter of 600 μm , had a wide transmission band (300-800 nm) to ensure that a variety of fluorescent MFE-candidate materials could be measured.

The DAQ that was used in this system was an upgraded version of the DAQ used in the LF-MFE system. The new NI USB-6212 BNC DAQ has 16-bit ADC conversion resolution compared to 14-bit resolution of the NI USB-6009 DAQ; a voltage range accuracy of 4.8 μV – 2.69 mV compared

to 37.5 mV – 138 mV; and a maximum sample rate of 400 kS/s compared to 48 kS/s. This improved set of specifications ensured that this component did not limit the accuracy or precision of the system significantly when measuring weakly fluorescent emissions.

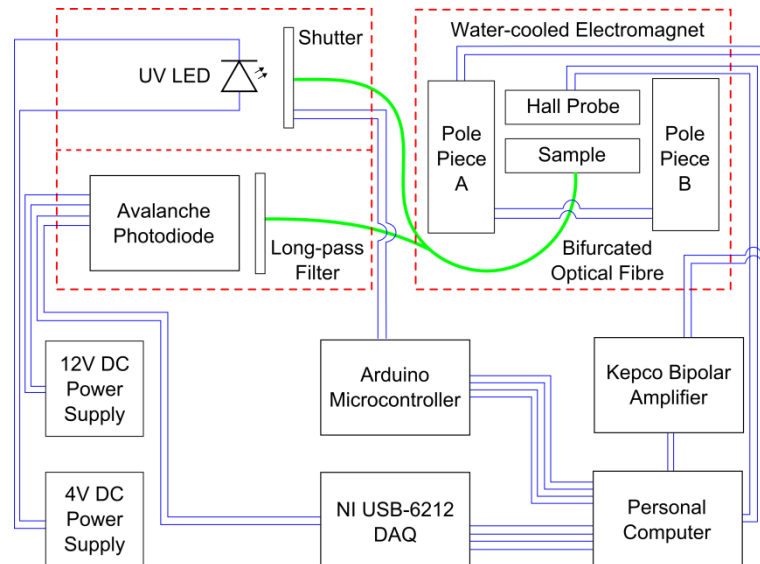


Figure 4.6: First version of HF-MFE system. Blue lines are electrical connections; red lines denote boundaries of optical isolation; whilst green lines denote optical connections.

The completion of this system also coincided with the completion of the data analysis script (discussed in detail in §4.2.8). This script provided fast, automated analysis of all of the data generated by the HF-MFE system. Figure 4.7 shows a typical output from the HF-MFE post-processing MATLAB script. One of these output figures is automatically generated for each magnetic field measured. This allows the data collected at each magnetic field to be checked for any unusual anomalies such as abrupt changes in intensity that could be indicative of LED instability, sample movement, electromagnet problems, etc.

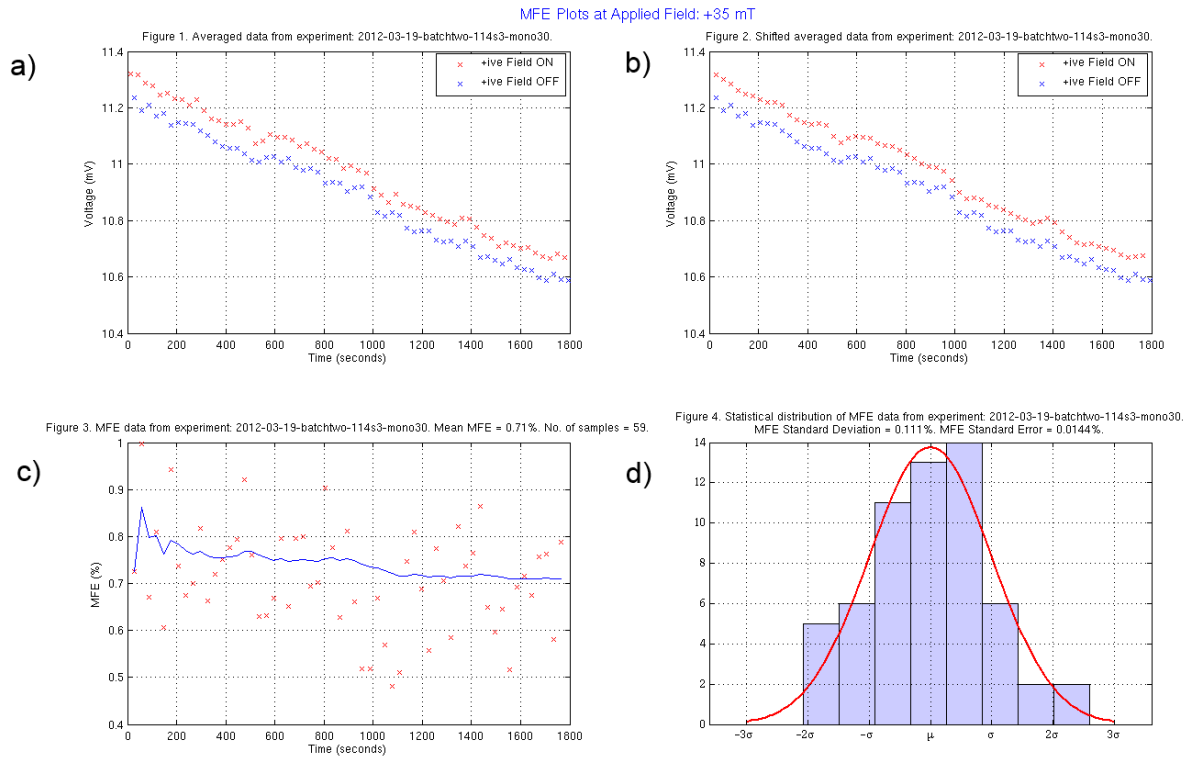


Figure 4.7: Graphical output from the HF-MFE post-processing MATLAB script of data collected at +35 mT for the TPD:BBOT:PMMA sample. (a) The raw data from 60 cycles has been averaged into 120 data points: 60 for when the field was on (red crosses) and 60 for when it was off (blue crosses). (b) The data from subplot (a) has been ‘aligned’ by interpolating one set of data points so that the MFE can be calculated. (c) The MFE values have been plotted as a function of time (red crosses) with the cumulative moving average of these data also plotted (blue line). (d) A histogram of the statistical distribution of the MFE data is shown. From these data the standard error can be calculated.

Figure 4.8 is the main output from HF-MFE post-processing MATLAB script and represents the actual MFE measured as a function of magnetic field. The error bars seen in the figure represent the standard error calculated by the script (as shown in figure 4.7d).

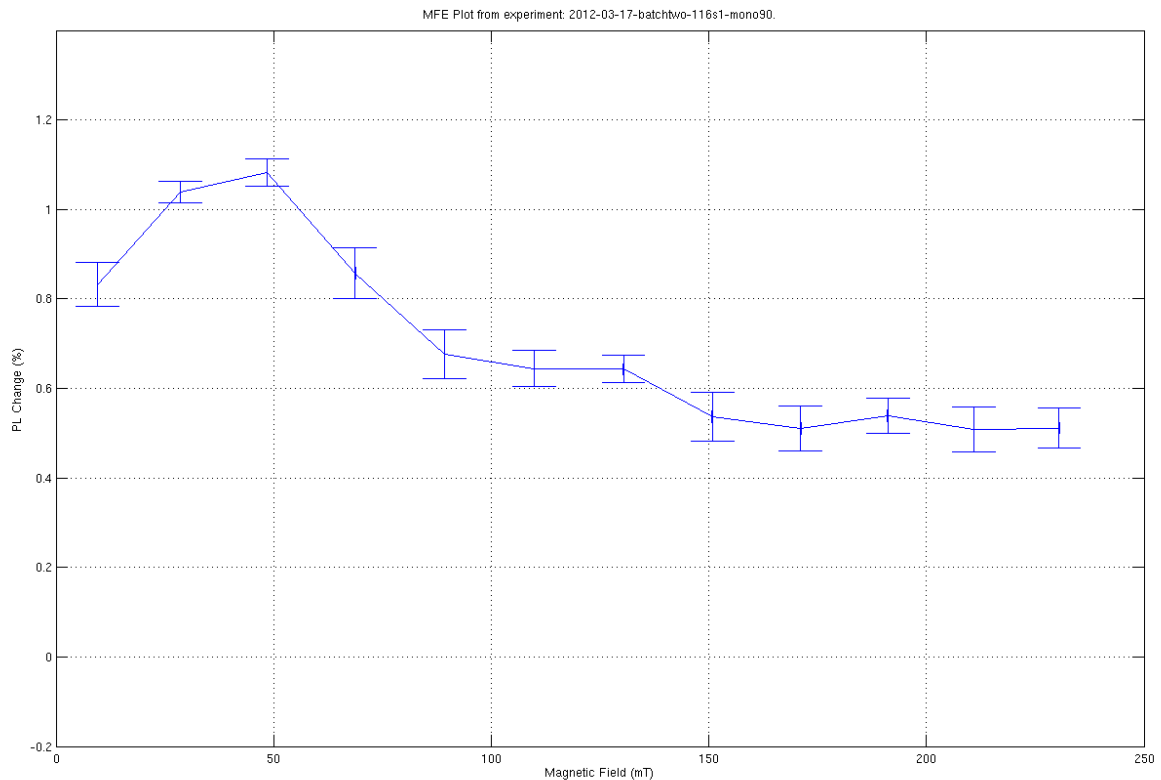


Figure 4.8: Graphical output from the HF-MFE post-processing MATLAB script demonstrating automatic generation of an MFE plot of the TPD:BBOT:PMMA sample. The measurement occurred at multiple magnetic fields and plots the associated standard error for each data point.

The system also provides an output of the raw detector voltage measured throughout the whole experiment (see figure 4.9). Again it is important to check this plot to ensure that the measurement occurred without any anomalous events. It can be seen in figure 4.9 that the signal-to-noise of the measured fluorescent intensity is quite poor when compared to the equivalent figure 4.5. It is not possible to see the fluorescent intensity variation caused by the modulation of the magnetic field in figure 4.9 whilst this is readily visible in figure 4.5 - i.e. the MFE cannot be seen as the signal-to-noise ratio is rather low. However, this demonstrates the power of the analysis script as figure 4.8 corresponds to the same data presented in figure 4.9; in figure 4.8 the MFE can clearly be seen.

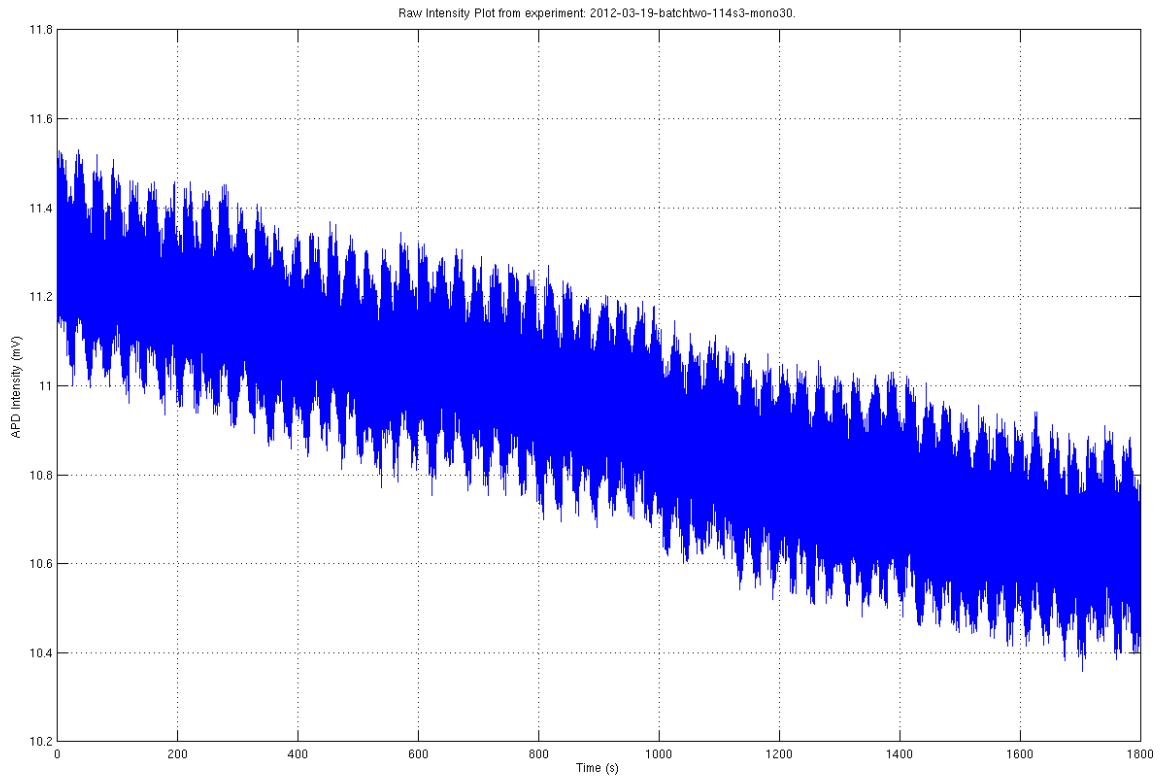


Figure 4.9: Graphical output from the HF-MFE post-processing MATLAB script demonstrating automatic generation of a plot of raw detector voltage as a function of time. It can be seen that this particular experimental run which measured the TPD:BBOT:PMMA sample suffered from poor signal-to-noise.

One of the pitfalls of this system design, it appears, is that the signal-to-noise ratio of the measured fluorescent intensity is rather low. A second version of this system was designed to address this issue.

Another drawback encountered early on in the development of this system was that the electromagnet suffered from appreciable magnetic hysteresis causing progressive error in the MFE plots (as the experiments swept from smallest to largest magnetic field). In other words, the required 'zero magnetic field' needed to measure the fluorescence intensity, I_0 (see equation 4.1), would drift further and further from true zero due to electromagnet remanence. This effect can be seen in figure 4.10. This problem was addressed in the second revision of this system.

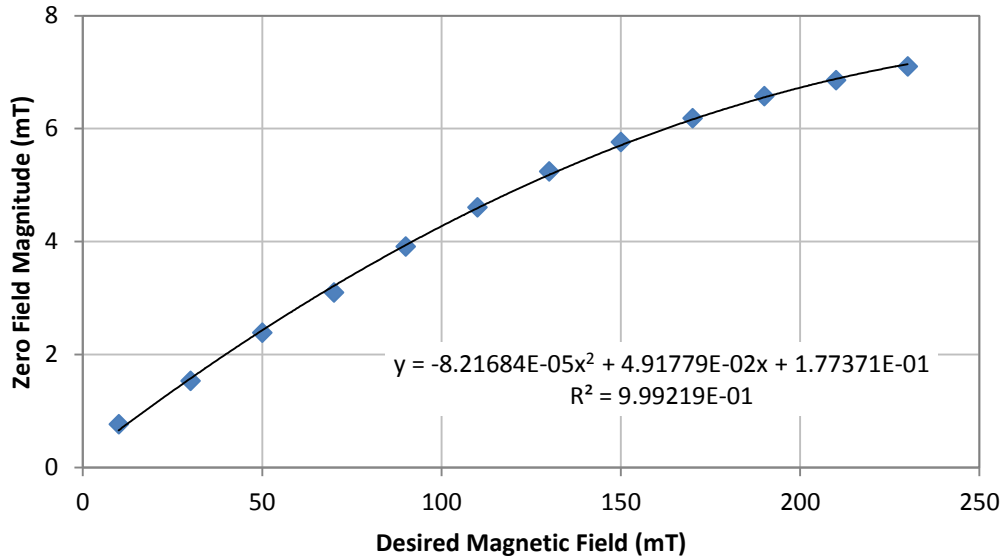


Figure 4.10: Plot of 'zero' magnetic field against the previous applied magnetic field. It can be seen that the 'zero' field diverges from 0 mT as the applied magnetic field is increased.

4.2.4 High Field MFE System Mk. II

In this version of the experimental setup, shown in figure 4.11, several changes have been made to improve the fluorescence signal to noise ratio as well as attempts to improve the detrimental electromagnet remanence effects.

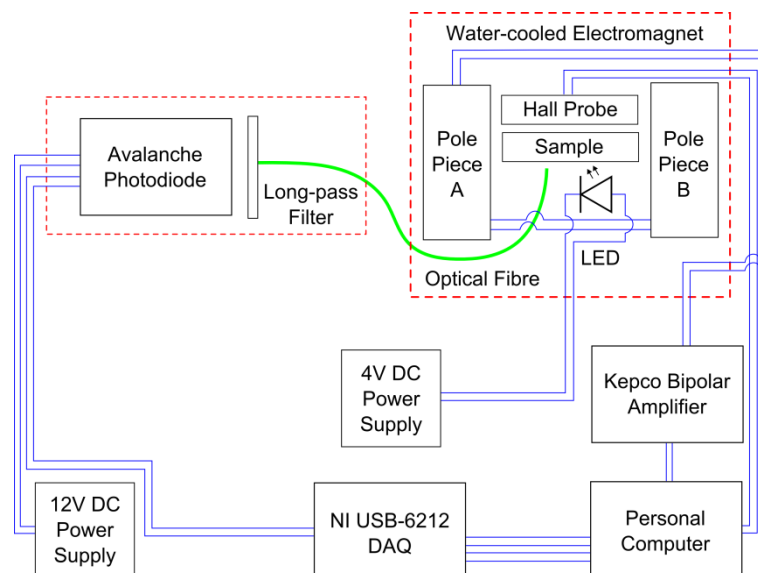


Figure 4.11: Second version of HF-MFE system. Blue lines are electrical connections; red lines denote boundaries of optical isolation; whilst green lines denote optical connections.

The first major revision involved the relocation of the LED from the separate enclosure into the main enclosure. This was undertaken in order to improve sample excitation and reduce sample photobleaching. The first improvement from this revision occurred because the fibre no longer served as a conduit for both excitation light and emission light; only the latter. This meant that the excitation light could be incident over a larger area of the sample whilst still being able to position the fibre end close enough to collect a sufficient amount of emitted fluorescent light. The second improvement (reduced sample photobleaching) occurred due to lower sample irradiance (as photobleaching is irradiance-dependent [2]). This extended the useful lifetime of each sample being measured from a few measurements to dozens of measurements.

The second revision undertaken was to change from the single-core bifurcated fibre to a regular multi-core fibre with a larger bulk diameter (3 mm). This revision enabled a greater degree of fluorescent emission capture (25 times larger capture surface area) increasing the measured fluorescence emission intensity. This had a substantial impact on the measured signal-to-noise ratio of the data.

The third revision to the system was to remove the shutter and associated microcontroller. The shutter was originally included to reduce sample photobleaching by shielding the sample from the LED during electromagnet ramping as well as to set a delayed start to the experiment until the LED stabilised. However by relocating the LED into the main enclosure it meant that the shutter no longer functioned as the mechanism would have been disrupted by the strong magnetic field produced by the electromagnet.

The final revision to the system was the introduction of a control loop feedback mechanism to correct the electromagnet's zero field remanence. This was achieved by applying a magnet control voltage proportional to the difference between the desired magnetic field and the actual magnetic field as read by the Gaussmeter. This principle was also extended to improve the magnet's ability to reach positive magnetic field targets. In order to do this an initial control voltage was set that caused the magnet to ramp toward the target field. Whilst the magnet

ramped to target field a pseudo-PID (proportional-integral-derivative) algorithm would monitor in real-time the difference between the live value and the target value as well as monitor the ramp rate. When the live-target difference approached a threshold value the ramp rate would be reduced via automatic manipulation of the control voltage by the program. If the magnet overshoot the target field a negative control voltage would be set. To prevent oscillation about the target value a rule was established that would deactivate the feedback loop if the same magnetic field value was recorded a certain number of times. The feedback loop was enabled for ramping to both zero and positive magnetic fields. As the control loop feedback mechanism was not a true implementation of a PID controller (and therefore not as versatile) the system required that the magnet was calibrated at the start of every experimental run.

The results of these system changes are apparent in the fluorescent MFE measurement of tetracene shown in figure 4.12. It can be seen that there is clear separation between the intensities where the field is on and where it is off. Not only that, but each group of field cycles can be distinguished (in this case four cycles per field). From a measurement such as this it is possible to extract the MFE signal from the drifting background.

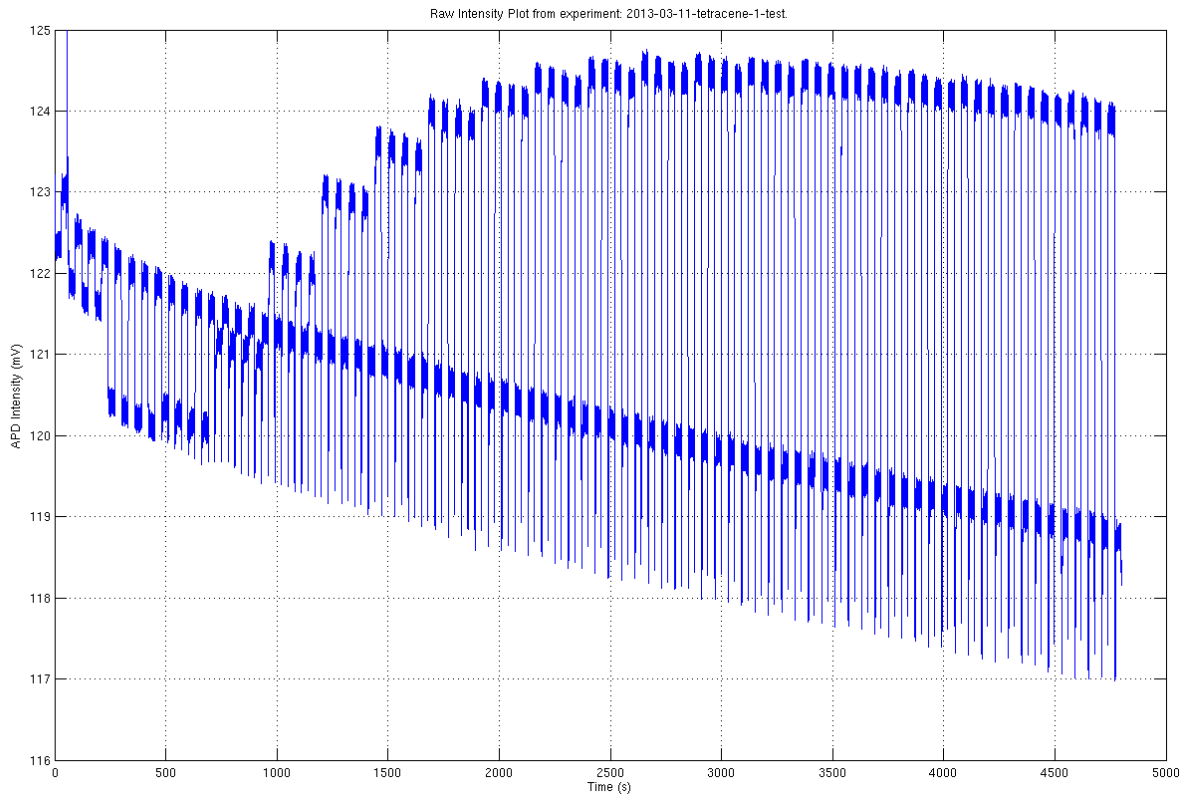


Figure 4.12: Graphical output from the HF-MFE post-processing MATLAB script plotting photodetector intensity against time. A tetracene thin film was used as the test sample.

4.2.5 High Field MFE System Mk. III

The high field MFE system went through one final revision in order to incorporate polarisation optics necessary for attempting to measure fluorescence-detected magnetic circular dichroism. As discussed in §3.9 certain materials exhibit X-ray magnetic circular dichroism (X-MCD) whereby differential absorption of incident circularly polarised light is encountered depending on the magnetic state of the sample. However, magnetic circular dichroism (MCD) can affect other wavelengths that a material naturally absorbs [3]. There have been successful attempts at detecting MCD from fluorescent emissions (FDMCD) [4] via reduced intensity of fluorescence due to reduced absorption ultimately caused by MCD. At this stage, however, it was unknown how MCD might manifest itself (if at all) in materials that also exhibit photoluminescent MFE. An experiment was devised in order to determine whether FDMCD could be observed in MFE materials.

As the clearance between the electromagnet pole pieces was a mere 59 mm a three-dimensional model of the proposed experiment system was developed in order to determine the best arrangement for the optical components under such constrained geometry (see figures 4.13 and 4.14).

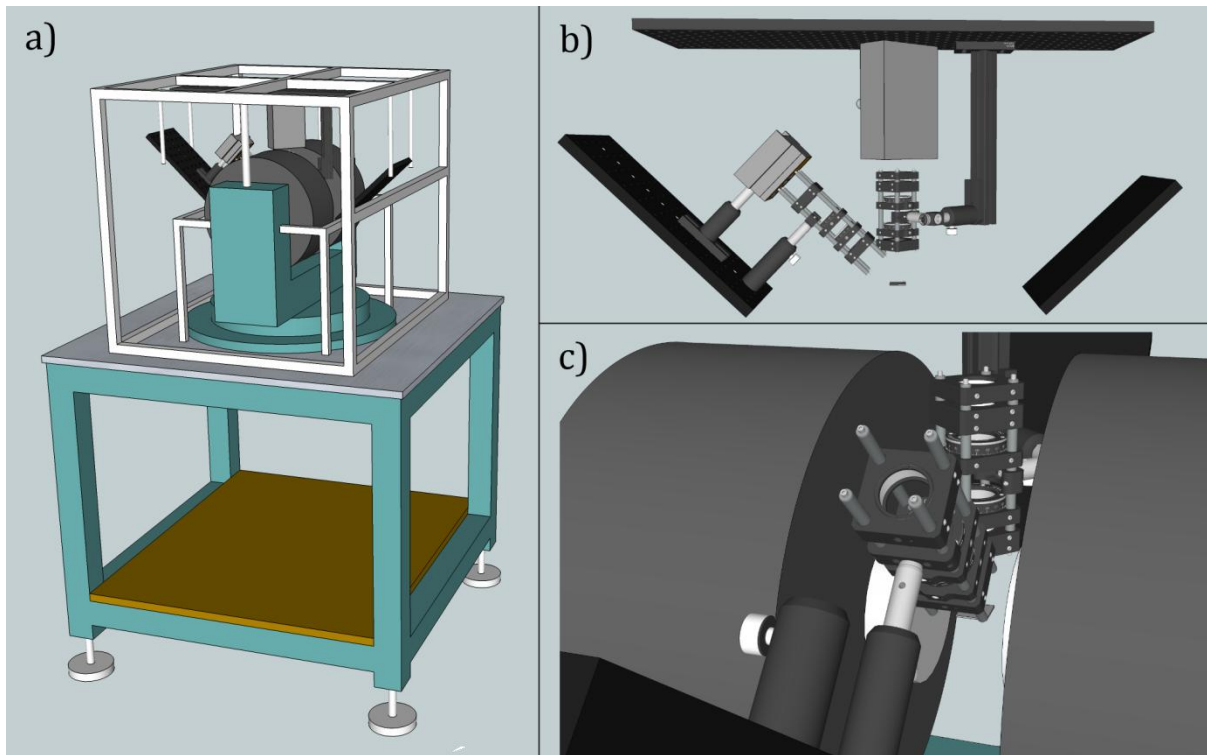


Figure 4.13: Computer rendering of the High Field MFE System Mk. III (a) rendering of the complete electromagnet and supporting frame; (b) perspective rendering of the optical equipment (expanded in figure 4.14); (c) internal rendering of the optical equipment with the excitation optics in the foreground and the emission optics in the background. This rendering illustrates the restricted nature of the system.

Figure 4.14 is a three-dimensional rendering of the HF-MFE optical polarisation measurement system. Two groups of optical components are defined: those existing between the LED excitation source and the sample are termed excitation optical components (so-called because the light is used to *excite* the fluorescent sample), whilst those existing between the sample and the photodetector are termed emission optical components (as these optical components are used to analyse the fluorescence *emission* from the sample). On the excitation side the first optical component encountered is the collector lens (CL). This lens acts to gather and collimate the light emitted by the LED onto the objective lens. The next optical component encountered is

the linear polariser (LP), which only transmits light oriented in one particular orientation – all other light is blocked. The light emitted by the LED then passes through a quarter-wave plate ($\lambda/4$), which converts the newly created linearly polarised light into circularly polarised light. Finally the objective lens (OL) focusses the excitation light onto the sample.

On the emission side of the system the first encountered optical component is a collecting lens (CL), which is used to gather and collimate the fluorescence emitted by the sample onto the condenser lens. The fluorescent emission is then passed through a quarter-wave plate ($\lambda/4$) where any light that is circularly polarised is converted to linearly polarised light. A linear polariser (LP), which is used to analyse the light, is positioned immediately after the quarter-wave plate. Only light that is oriented parallel to it is transmitted. A condenser lens is next encountered and is used to focus the analysed fluorescent emission onto the photodetector. Finally a long pass filter is used to block the excitation light and only transmit the emitted fluorescent light.

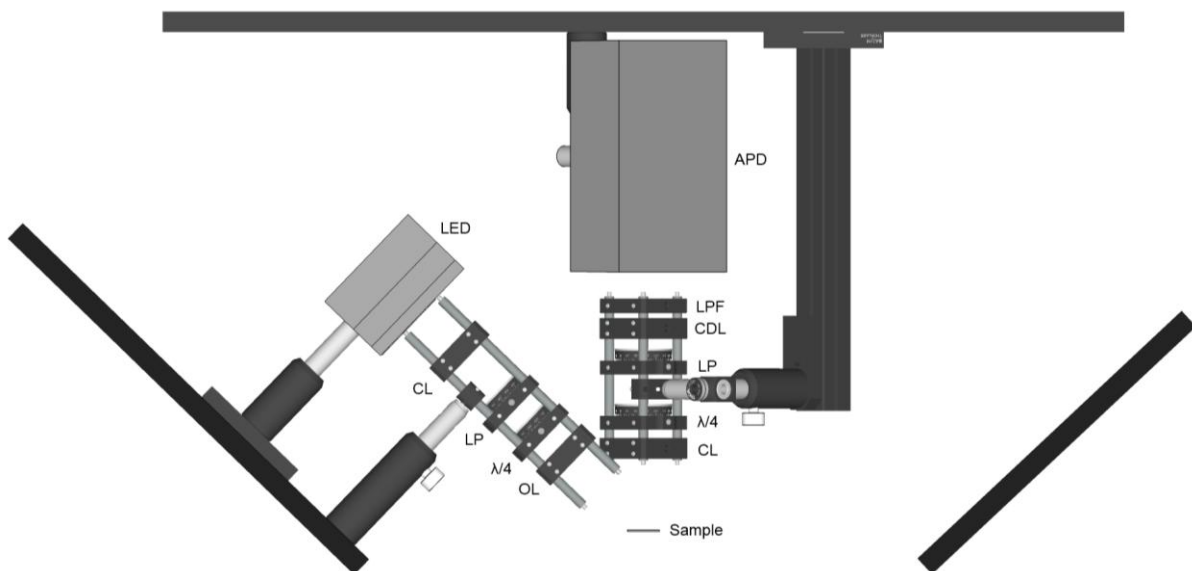


Figure 4.14: Expanded rendering of figure 4.13b in parallel projection. The excitation optical components described from left to right are: LED; collector lens (CL); linear polariser (LP); quarter-wave plate ($\lambda/4$); objective lens (OL). The sample is located centrally at the bottom of the rendering. The emission optical components described from bottom to top are: collector lens (CL); quarter-wave plate ($\lambda/4$); linear polariser (LP); condenser lens (CDL); long pass filter (LPF); APD detector.

The final version of the experiment involved only the emission polarisation optics; the excitation polarisation optics were removed from the system due to poor excitation of the sample caused by excessive attenuation by the additional optical components. Three MFE measurements were made in total. The first and third measurements were configured with the linear polariser rotated $+45^\circ$ with respect to the slow axis of the quarter-wave plate. In the second measurement the linear polariser was rotated to be -45° with respect to the slow axis of the quarter-wave plate. These two configurations should be sensitive to detecting fluorescent emission from the sample of each circularly polarised handedness should it exist. Therefore this experiment tests the hypothesis that should a magnetic field drive the generation of circularly polarised fluorescent light then the detector should be able to measure it.

4.2.6 Control Software

The software required to control the MFE experiment was developed entirely by the author in Microsoft's Visual Basic 6.0. The Visual Basic programming language was chosen above other languages (such as National Instruments' LabView) as several other systems in the laboratory were written with it as well as the author having prior experience with the language. The software coordinated the acquisition and storage of measurement data; control of the electromagnet (via the Kepco power supply) and LED shutter; the ability to store sets of 'favourite' settings; and the ability to operate autonomously once it had been initialised.

The main inputs into the system include the time (set in the operating system); APD detector analog voltage via the DAQ; and the Gauss meter magnetic field magnitude via direct RS-232 serial communication. The main outputs include control of the electromagnet via the DAQ and Kepco power supply; control of the shutter via serial communication with Arduino Uno microcontroller; file output of the measurement data with additional Boolean flags to indicate the state of various system conditions; and file output of the global settings of each experimental run.

A screenshot of the control software is shown in figure 4.15 captured at the end of an experimental run. The three main plots in the main program window corresponded to the APD voltage against time (left plot), the magnetic field against time as measured by the Gaussmeter (top right) and the magnet control voltage against time (bottom right). The program contained other useful features such as outputs of the elapsed time, remaining time and estimated finishing time of the experimental run as well as the actual system time. The status of the logging system, the shutter and the magnet were displayed in coloured boxes near the top-centre of the program window with red denoting inactive/disabled systems whilst green denoted active/enabled systems. The input settings were contained within a tabbed panel at the top-right of the program window with each setting categorised based on its function such as 'Detector Control' or 'Magnet Control'. A 'favourite settings' feature is seen on the right-hand side of the program window and allowed the user to store and retrieve successful combinations of settings for later use. An 'experimental log' pane is seen in the top-right of the program window but was never implemented. It was intended to keep a record of all users' use of the system.

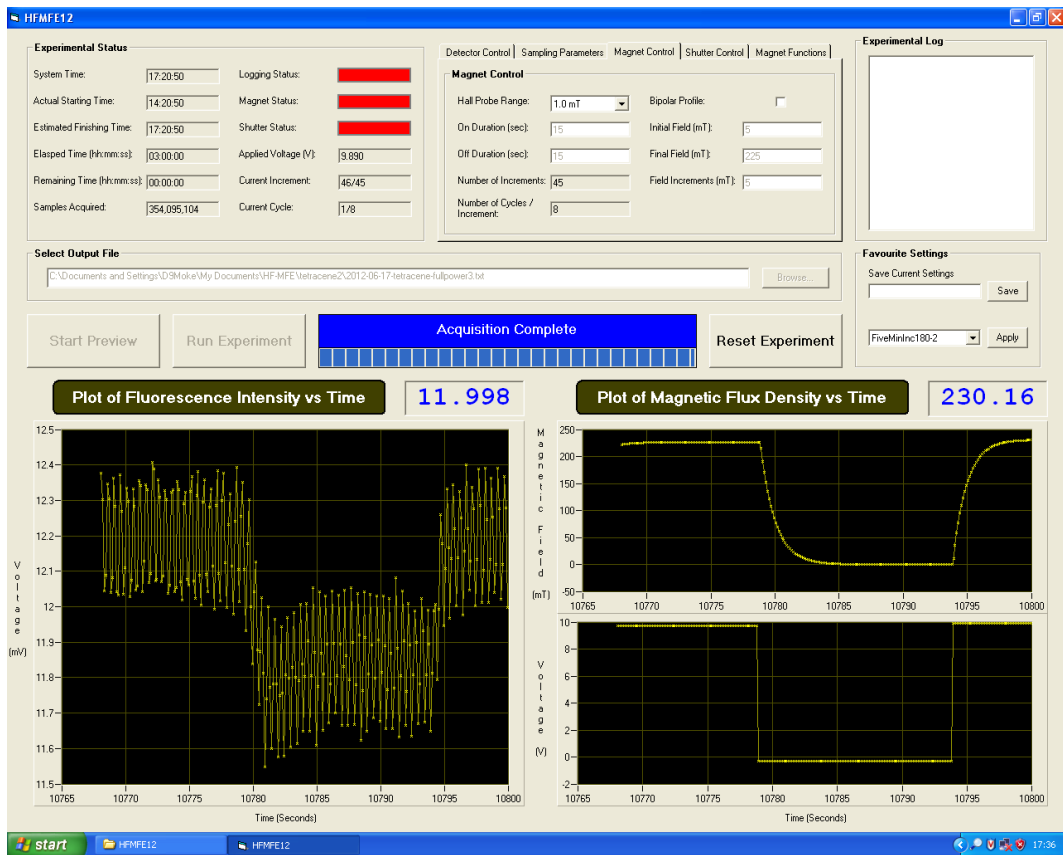


Figure 4.15: Screenshot of the software used to control the HF-MFE experiment.

An illustration and description of the electromagnet ramping and logging procedure is outlined in figure 4.16.

The calibration procedure, a pre-programmed routine that could be activated by pressing a button in the control program interface, involved applying a large, decaying sinusoidal waveform to the electromagnet. Once the waveform had reached a certain decay threshold the system would then ramp the magnet to a high field in order to determine the voltage required to attain any other magnetic field (assuming a linear response). Once this second stage of the calibration procedure had completed the decaying sinusoidal waveform was applied once more to demagnetise the electromagnet.

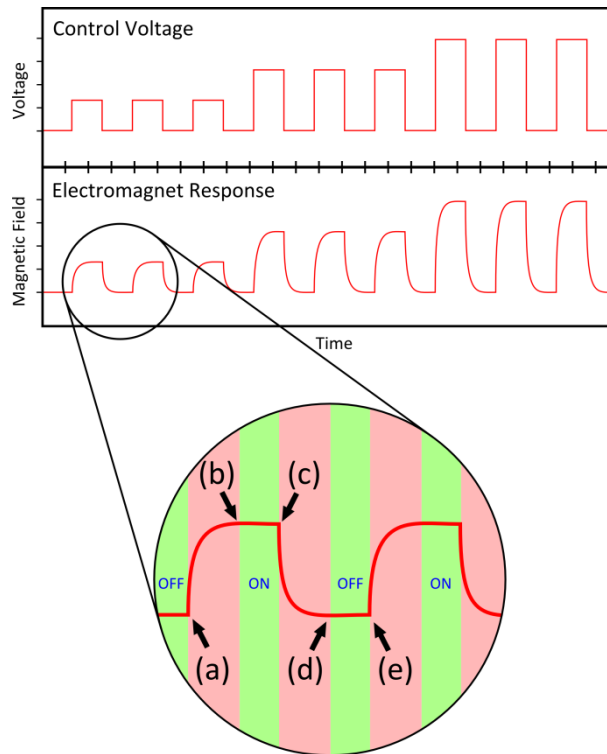


Figure 4.16: Electromagnet ramping routine. (a) Target field is set and applied; magnet begins to ramp up (b) Ramping finishes; target field is reached; logging begins (c) Logging ends; zero field set and applied; magnet begins to ramp down (d) Ramping finishes; zero field is reached; logging begins (e) Logging ends; new target field is set and applied; magnet begins to ramp up.

One disadvantage of this system results from the long ramp times which can effectively double the length of the experiment. However, these ramp times are intrinsic to the electromagnet and cannot be altered.

4.2.7 Experimental Settings

The following control program settings (tables 4.1 and 4.2) have proved to produce reliable, reproducible MFE plots and are used when a standard MFE plot is needed.

Settings	Function	Variable Symbol	Value	Unit
Experiment duration	Sets the length of the experiment.	a	120	minutes
Initial magnetic field	Sets the first magnetic field.	b	5	mT
Final magnetic field	Sets the last magnetic field.	c	290	mT
Field step size	Sets the interval between fields.	d	15	mT
'Magnet on' duration	Sets the amount of time the magnetic field is kept on.	e	30	seconds
'Magnet off' duration	Sets the amount of time the magnetic field is kept off.	f	30	seconds
Ramp time	Sets the amount of time required for the magnet to reach its target value.	g	15	seconds
Packet size	The number of samples to be measured by the DAQ before being averaged and sent to the computer program.	h	32768	samples
Packet frequency	The rate at which packets are received by the computer program.	i	8	packets / second

Table 4.1: Control program settings.

Calculated Settings	Function	Symbol	Formula	Result
Number of magnetic field steps	The final number of data points in an MFE plot.	j	$\frac{c - b}{d} + 1$	20
Number of cycles per field	The number of times the data point has been measured.	k	$\frac{60a}{j(e + f)}$	6
Number of 'magnet on' packets logged per cycle	The number of packets a data point is averaged from.	l	$i \times (e - g)$	120
Number of 'magnet off' packets logged per cycle	The number of packets a data point is averaged from.	m	$i \times (f - g)$	120
Number of lines in data file	Used by MATLAB script during post-processing of the data.	n	$a \times i \times 60$	57600

Table 4.2: Calculated program settings.

Table 4.3 contains electrical parameters used to power the LED(s). Unless otherwise stated, these values were used for all experiments. The TPD:BBOT:PMMA sample, for example, made use of the UV LED whilst the tetracene sample made use of the cyan LED based on the fluorescence spectroscopy results (§5.2.1 and §5.2.5, respectively).

Parameters	365 nm 5W UV LED	475 nm 3W Blue LED	500 nm 1W Cyan LED	Unit
Applied voltage	4.6	3.6	3.6	V
Resistor (in series)	1.0	1.0	1.0	Ω
Measured current draw	0.46	0.50	0.29	A

Table 4.3: LED electrical parameters. Current draw is measured once thermal equilibrium has been reached.

4.2.8 Data Analysis Script

As the Visual Basic program was only designed to control and record measurements for the LF-MFE and HF-MFE systems there was a need to outsource the task of data analysis to another program optimised for processing large datasets. This task was achieved in MathWorks' MATLAB R2011b via a custom script. The script began by reading the settings file generated by the Visual Basic program and calculating various experimental run statistics (using the formulae and example values from tables 4.1 and 4.2) such as the expected total number of lines in the associated data file ($n = 57600$; + 2 header lines); the expected number of fields measured ($j = 20$); the expected number of lines per cycle ($l = 120$), etc. Once this has been completed an array (named '*rundata*') was created and populated with the raw measurement data from the measurement data file. An algorithm (consisting of two nested *for loops*) then cycled through the array extracting all sample data with the exception of those measured during the magnet ramp period – these measurements were discarded (ramp time = 15 seconds, 'magnet on/off' time = 30 seconds: therefore 50% of the collected data is discarded). The extracted raw data were copied and grouped into two three-dimensional arrays – one for when the magnet was at the target field(s) (named '*plusrawon*') and another for when the magnet was at 0 mT ('*plusrawoff*'). These data were then averaged and grouped per cycle and stored in two new arrays (named '*plusavgon*' and '*plusavgoff*', respectively). The MFE per cycle was then calculated according to equation 4.1 and stored in a separate array (named '*subtractedplusresults*'). A

histogram of the standard deviation of the MFE per cycle was plotted (figure 4.7d) along with the three previously calculated arrays of data (figure 4.7a-c). A final average of the MFE per cycle was calculated and stored in a new array (named '*mfepiusresults*'). These final results were plotted (figure 4.8) along with error bars representing the standard error of the measurement in both MFE and magnetic field measurements. A final plot of the raw APD voltage against time was also plotted (figure 4.9) in order to assess the extent of photobleaching, etc.

4.2.9 HF-MFE System Issues

One unexpected issue encountered whilst operating the HF-MFE system occurred during the summer months and affected the system's ability to ramp the electromagnet to the target field(s). While this issue took some time to fault trace, it was eventually discovered that the cause of the issue was due to a faulty chiller unit that supplies water coolant to the electromagnet. Due to unusually warm weather the chiller unit was unable to maintain a constant water temperature and had allowed the water temperature to increase slightly. This warmer water caused an increase in the electromagnet's electrical impedance. This, in turn, meant that a larger than normal voltage was required to drive the electromagnet to target field. To prevent the magnet setting a magnetic field beyond the measurement range of the Gaussmeter an upper voltage limit was hardcoded into the control software. This meant that when the software tried to set a voltage to ramp the magnet to the next target field it crashed losing a small portion of the data from that run. A temporary solution of increasing the voltage limit was therefore implemented until the chiller unit was fixed.

Another issue that had been difficult to remove was unwanted, non-fluorescent, background signal. Several sources of unwanted background light were identified, including the laboratory lighting. To remove the impact of this light source the system was fitted with Velcro-attached black-out fabric. The use of Velcro allows the user to detach and reattach the fabric panels when access to the system internals is required. A second source of unwanted light identified was light directly from the excitation LED. Although a long-pass optical filter was installed to remove

this it was not completely successful. One of the reasons for this was due to the scattering of light inside the measurement system. To try to limit this effect, several focussing lenses were installed to control the spread of the light as it propagated away from the LED. This meant that essentially only the sample itself was receiving significant illumination. A piece of thick black cardboard was also placed between the LED and the detector in order to further isolate the two ends of the system.

A final issue that has been difficult to remedy was the system's high sensitivity to optical alignment. Any small misalignment of either the sample with respect to the emission optics or the detector with respect to the emission optics resulted in very large reductions in received fluorescence signal. The problem was difficult to remedy as positional adjustments to either the sample or detector had to be done by hand. However, opening the system to ambient laboratory lighting in order to manually adjust these components could very easily saturate the detector! The partial solution, therefore, had been to open the system up just enough to make the necessary adjustments whilst monitoring the detector intensity in real-time via the control software on the computer monitor.

The combination of these modifications including the use of fresh samples increased the MFE of tetracene (as an example) from early measurements of approximately 4% to over 6% in the later measurements. This occurred because the received background intensity (from unwanted light sources), as measured by the APD, is reduced minimising any 'dilution' effects stray light can have on the measured MFE. By using fresh samples, that have not been previously exposed to strong illumination and therefore have not suffered from any photobleaching, the emission intensity of the sample boosts the measured signal-to-noise ratio improving the confidence that what is being measured is close to the true MFE magnitude of the material.

4.3 Magnetic Field Effect Photography

In order to demonstrate the potential versatility of the photoluminescent magnetic field effect at being able to characterise magnetic materials an experimental system was designed and built to enable the visualisation of macroscopic magnetic structures. This system made use of a commercial digital camera (Canon EOS 20D) in order to image the fluorescence emission generated from a tetracene thin film deposited onto a silicon wafer (measuring approximately 30×30 mm). A NdFeB magnet was then placed directly behind the silicon wafer (not visible to the camera) with the idea that its external demagnetising field would generate a fluorescent MFE in the tetracene film on the silicon wafer. It was predicted that the camera should be able to detect the demagnetising field from the MFE emission in the form of a two-dimensional contrast image. Depending on the MFE material used the system should be able to produce quantitative contrast images – by mapping the emission contrast through the magnetic field-dependent relative intensity MFE plots in order to determine the magnitude of the demagnetising field in a two-dimensional plane above the magnet surface.

The new system made use of many components from the HF-MFE described above. The LED excitation source, for example, was borrowed from the HF-MFE system and together with the camera, magnet and sample were all placed in a light-tight enclosure (see figure 4.17). A collector lens was also installed in the system between the LED and the sample to focus the light optimally onto the sample and to minimise illumination of the interior of the enclosure.

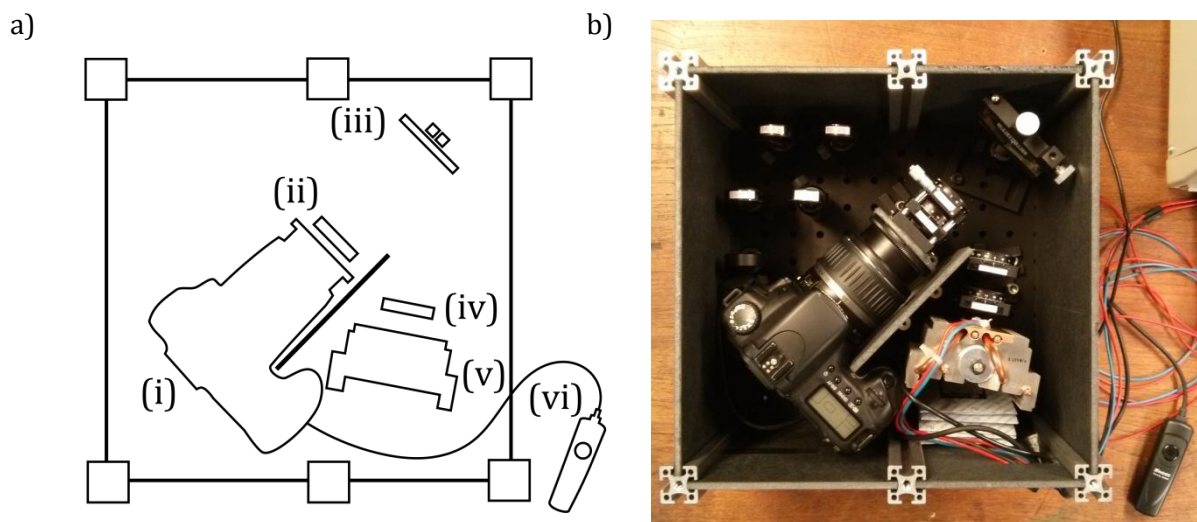


Figure 4.17: (a) Schematic of the MFE photography system. The components include (i) the photographic camera; (ii) the long pass filter; (iii) the sample with two cube NdFeB magnets placed directly behind; (iv) a collector lens; (v) the LED mounted on a heatsink; and (vi) the remote trigger release device; (b) Photograph of the MFE photography system.

The camera was put into a fully manual mode effectively disabling any automatic exposure, focussing, white balance, etc. This was done in order to control which parameters changed between photographs. The ISO setting, a feature that determines the level of gain applied to the camera's CMOS sensor, was reduced to the lowest supported value of 100 in order to suppress amplification of noise. To compensate for this the shutter speed of the camera was put into 'bulb' mode and was controlled via a shutter release cable allowing long exposure photographs to be taken. This ensured that a sufficient amount of light was collected to produce an appropriately exposed photograph. The photographs were saved in *RAW* image format to preserve the photographic data from image compression artefacts.

As the MFE candidate materials exhibit rather weak MFE (on the order of a few percent) a technique known as difference imaging was employed in order to improve image contrast. Difference imaging involves capturing two images of the subject matter and subtracting them to highlight any differences between them. Here, images of the sample were obtained with and without the NdFeB permanent magnet placed behind the sample in order to generate an MFE. By subtracting the images any differences between them (the MFE contrast pattern) could be

extracted. In order to achieve this practically it is important that the camera and sample remain in the same positions between the two photographs otherwise positional differences will contribute to the final image.

The difference imaging was performed in the ImageJ 2.0.0-beta6 software package. In order to process the propriety Canon 'CR2' RAW-formatted images into ImageJ the files were imported using the free ImageJ plugin called *DCRaw Reader* 1.4.0 with the settings shown in figure 4.18. Image misalignment was corrected with a program made by DualAlign called *i2k Align* 2.1.5 which aligned the image pairs using state-of-the-art image recognition technology. One important processing step that was vital in the image difference operation was to store the operation output to a file with a large bit depth until contrast scaling could be performed. After contrast scaling the image can be saved into a lossless 16-bit compression file format such as TIFF.

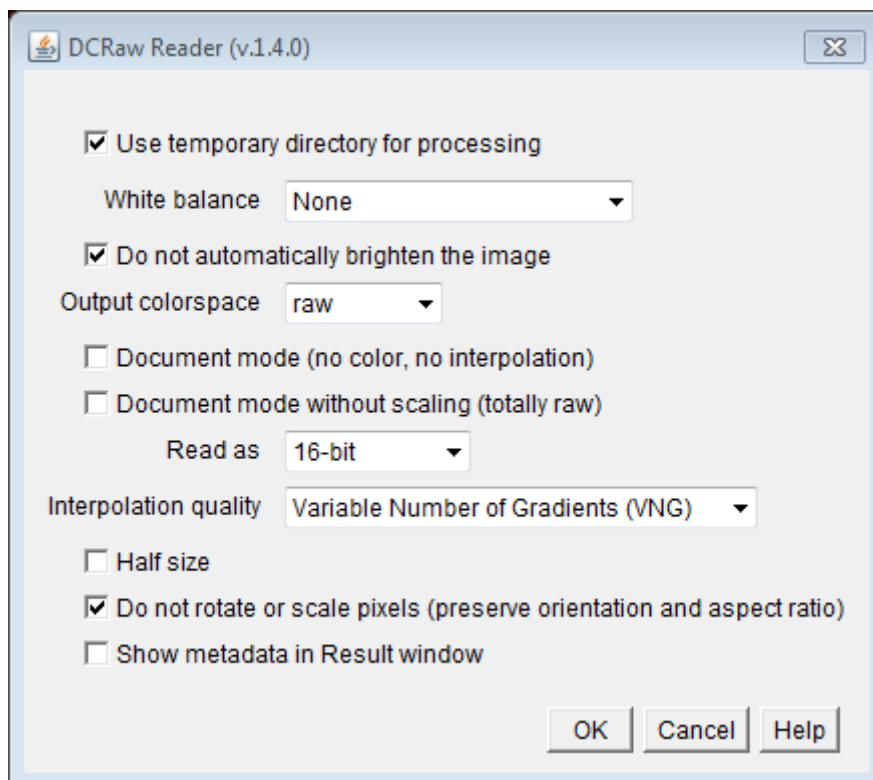


Figure 4.18: Screenshot of ImageJ plugin *DCRaw Reader* with the settings used for importing CR2 images from the camera.

Ultimately, two types of experiments were performed on this system. The first type is described above and shall be referred to as 'standard MFE photography'. The second type of experiment performed on the system involved the use of polarisation optics arranged almost identically as described in §4.2.5 and shall be referred to 'polarisation MFE photography'. However, in this experiment the polarisation optics (see figure 4.19), constituting a linear polariser (figure 4.19-i) and quarter-wave plate (figure 4.19-ii) on the emission side and a linear polariser (figure 4.19-iv) and quarter-wave plate (figure 4.19-iii) on the excitation side, were used all at the same time.

Two sets of measurements were performed on a tetracene thin film sample with two NdFeB permanent magnets placed behind the sample. The object of the experiment was to see if an MFE contrast asymmetry between the two magnets could be observed as the magnets should each produce an area of MFE contrast. The first set of measurements would occur with the excitation quarter-wave plate rotated at $+45^\circ$ whilst the second set of measurements would occur with the excitation quarter-wave plate rotated at -45° . Between them, these two sets of measurements would generate circularly polarised light of each handedness. Within each measurement set the emission linear polariser was systematically rotated through various angles (see table 4.4) in order to analyse the fluorescent emission of the tetracene sample. For each configuration of the polarisation optics a photograph of the thin film was captured. The angles listed are relative to one another whilst the angle θ refers to the independent variable that was manipulated in each experiment. As in the standard MFE photography protocol, the image contrast was enhanced through the use of difference imaging, in this case, with respect to the emission linear polariser angle set to 0° .

Set 1		Set 2	
Optical Component	Angle	Optical Component	Angle
i	θ	i	θ
ii	0°	ii	0°
iii	$+45^\circ$	iii	-45°
iv	0°	iv	0°

Table 4.4: List of optical polarisation angles used in the MFE photography polarisation experiment where (i) emission linear polariser; (ii) emission $\lambda/4$ wave plate; (iii) excitation $\lambda/4$ wave plate; (iv) excitation linear polariser.

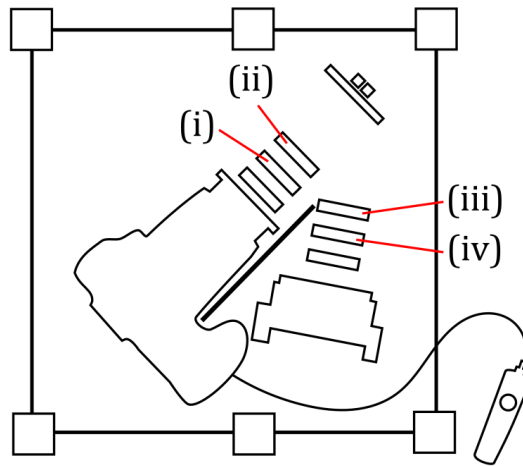


Figure 4.19: Schematic diagram of polarised light MFE photography system. (i) Emission linear polariser; (ii) emission $\lambda/4$ wave plate; (iii) excitation $\lambda/4$ wave plate; (iv) excitation linear polariser.

4.4 Conclusion

Several fluorescence magnetometry experimental systems have been designed and built in order to characterise the photoluminescent ‘magnetic field effect’ phenomenon exhibited by several organic semiconducting materials. Each system underwent several design iterations in order to improve measurement accuracy and precision, degree of automation and overall reliability. The accompanying control software and data analysis scripts were also designed and implemented from the ground-up, in tandem with each respective experimental system.

4.5 References

- [1] Solentec Ltd. *Electromagnets from Solentec Ltd.* Available: <http://www.solenoids.co.uk/electromagnets.html>
- [2] C.-P. Chang, *et al.*, "Irradiance dependence of photobleaching of resorufin," *Journal of Photochemistry and Photobiology A: Chemistry*, vol. 217, pp. 430-432, 2011.
- [3] K. Binnemans, *et al.*, "Magnetic circular-dichroism and optical absorption spectra of holmium-doped fluorozirconate (ZBLAN) glass: a prospective study," *Journal of Alloys and Compounds*, vol. 225, pp. 80-84, Jul 1995.
- [4] J. C. Sutherland and H. Low, "Fluorescence-Detected Magnetic Circular-Dichroism of Fluorescent and Nonfluorescent Molecules," *Proceedings of the National Academy of Sciences of the United States of America*, vol. 73, pp. 276-280, 1976.

5 Materials Characterisation & Optimisation

5.1 Introduction

In order to develop samples with the required properties for testing the feasibility of microscopic MFE magnetic contrast imaging a materials selection process was undertaken. This involved utilising several measurement techniques to perform characterisation as well as optimisation of the candidate materials and sample morphologies.

In this chapter absorption and fluorescence spectroscopy results will be presented in order to demonstrate what optical components were required for use with the high-field MFE magnetometer. High-field MFE magnetometry results will be presented to ensure that MFEs reported in the literature can be replicated in the laboratory. Optical microscopy as well as atomic force microscopy results will be shown that examine thin film morphology across several fabrication techniques and describe some of the drawbacks encountered from each technique.

5.2 Absorption, Excitation & Fluorescence Spectroscopy Measurements

In order to determine the appropriate excitation wavelength for each material to be examined by the MFE magnetometer it was necessary to first acquire their absorption spectra. Absorption spectroscopy measurements were performed as described in §3.4.

Since fluorescence is defined as the $S_1 \rightarrow S_0$ electronic transition only the absorption bands that represent the $S_0 \rightarrow S_1$ electronic transition will be discussed. Typically these bands exist above 300 nm and any absorption bands observed below 300 nm represent $S_0 \rightarrow S_n$ electronic transitions where $n > 1$ [1].

To be able to determine what optical equipment was necessary in order to measure the magnetic field effect of the materials listed in table 3.1 and to determine which materials were

compatible with confocal microscopy, fluorescence spectroscopy measurements were performed as described in §3.3. In most cases the excitation spectra will correlate with the respective absorption spectra. Any deviation observed, however, is due to the nature of what the absorption and excitation spectra represent. The absorption spectrum of a material represents the wavelength-dependent light attenuation due to absorption of light by the material. The excitation spectrum of a material, however, represents the absorption of light required to generate emission only at the particular wavelength being monitored. Excitation spectra are collected by monitoring emission intensity variation of a specific wavelength of the emission peak of interest. This distinction means that absorption (within the wavelength range being observed) can occur that doesn't result in fluorescent emission and, therefore, wouldn't appear on an excitation spectrum.

Major discrepancies between the absorption and excitation spectra, however, can be indicative of the existence of non-radiative transitions that occur when absorbed energy is either dissipated as thermal phonons or is transferred to a neighbouring molecule via Förster resonance energy transfer (FRET) or Dexter electron transfer [2].

In all cases presented the emission wavelength that will be monitored for generating an excitation spectrum will reside in the peak with the largest emission intensity. It should also be noted that all measurements were performed at room temperature and atmospheric pressure.

5.2.1 TPD:BBOT:PMMA

The absorption, fluorescence excitation and fluorescence emission spectra of the TPD:BBOT:PMMA sample are shown in figure 5.1. Two samples were prepared via spin coating from a chloroform solution (see table 3.3 for details) onto a fused quartz glass slide for the absorption measurements and silicon wafer for the fluorescence measurements. The absorption measurement was scanned from 250 to 500 nm and displays a rather broad absorption spectrum absorbing in the range 275-425 nm and centred at 358 nm. No significant absorption

is detected above 425 nm. The excitation measurement was scanned from 250 to 415 nm with the emission monochromator held at 420 nm – the primary peak emission wavelength of TPD:BBOT:PMMA. The emission measurement was scanned from 390 to 650 nm with the excitation monochromator held at 359 nm – the primary excitation wavelength of TPD:BBOT:PMMA.

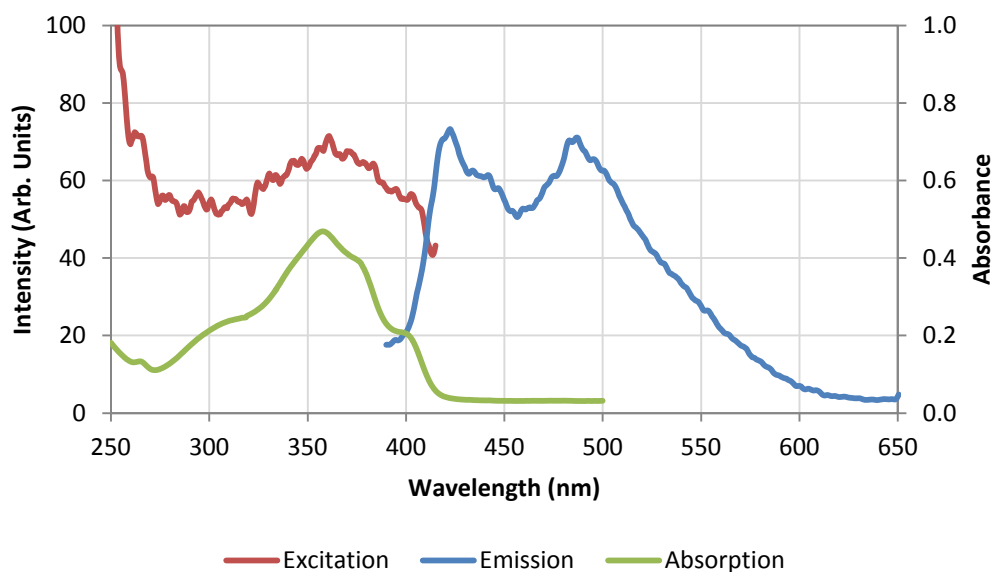


Figure 5.1: Excitation (red, left), absorption (green, left) and fluorescence spectra (blue, right) of the TPD:BBOT:PMMA sample.

From figure 5.1 it can be seen that TPD:BBOT:PMMA displays three main emission peaks centred at 420 nm, 436 nm and 485 nm. Based on the fluorescence spectra of the individual components of the mixture the first emission peak is most likely attributed to TPD [3] whilst the second emission peak is likely attributed to BBOT [4]. The third emission peak is most likely attributed to the formation of an exciplex state between TPD and BBOT [5]. These results suggest that only a fraction of the TPD and BBOT have interacted to form the exciplex. The excitation spectrum collected closely matches the absorption spectrum with an excitation peak centred at 359 nm. These measurements suggest that an ultraviolet LED emitting in the range 355-375 nm would be a suitable excitation source in order to generate fluorescent emission from the molecule at wavelengths of 420 nm and 485 nm, respectively.

5.2.2 Anthracene

The absorption, fluorescence excitation and fluorescence emission spectra of polycrystalline anthracene are shown in figure 5.2. Two samples were prepared via thermal evaporation and deposited onto a fused quartz glass slide for the absorption measurements and silicon wafer for the fluorescence measurements at a thickness of 80 nm. The absorption measurement was scanned from 280 to 500 nm where it can be seen that anthracene displays a rather broad absorption spectrum from 300 – 400 nm. A particularly striking feature is the presence of four approximately evenly spaced absorption peaks positioned at 336, 353, 373, 393 nm, respectively. This structure can be attributed to vibrational transitions between electronic energy levels according to the Frank-Condon principle [2]. No significant absorption is detected above 425 nm. The excitation measurement was scanned from 285 to 402 nm with the emission monochromator held at 419 nm – the primary peak emission wavelength of anthracene. The emission measurement was scanned from 385 to 498 nm with the excitation monochromator held at 370 nm – the secondary excitation wavelength of anthracene. This peak was chosen as it does not overlap with the emission spectrum, therefore minimising interference between the scans.

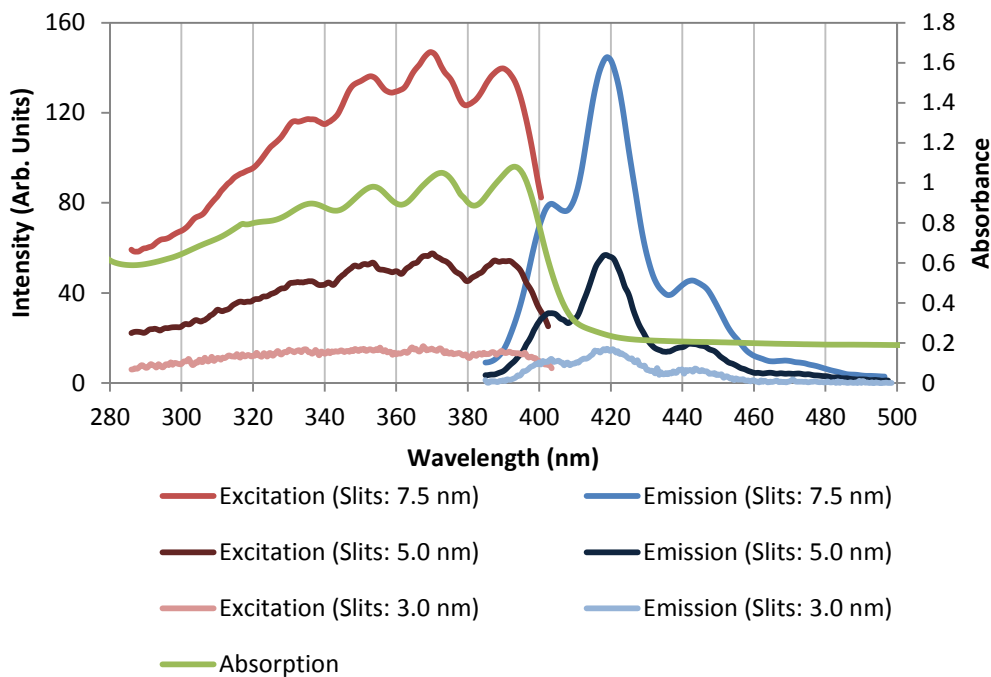


Figure 5.2: Excitation (red, left), absorption (green, left) and fluorescence spectra (blue, right) of anthracene. Slit widths (excluding absorption spectrum) from the bottom to top: 3.0 nm; 5.0 nm; 7.5 nm.

From figure 5.2 it can be seen that anthracene displays approximately four emission peaks centred at 403 nm, 419 nm, 443 nm and 469 nm with the largest peak residing at 419 nm. The excitation spectrum collected closely matches the absorption spectrum with peaks resolved at 335 nm, 352 nm, 370 nm and 390 nm. The only discrepancy visible is that the 390 nm peak is larger on the absorption spectrum compared to the excitation spectra. This is due to the intentional choice of obtaining the emission spectrum from the 370 nm peak. This means that the excitation scan will misleadingly show that the 370 nm peak is more absorbing than the 390 nm peak. However, this is only true for the *specific* emission spectrum shown in figure 5.2 where the second of the four emission peaks appears to be the largest. This is most likely caused by the choice to excite anthracene at 370 nm. If it had been excited at 390 nm it is to be expected that the largest emission peak would have been the 403 nm peak and therefore matching previous fluorescence measurements of anthracene [6]. These measurements confirm that an ultraviolet LED emitting in the range 355-375 nm would be an appropriate excitation source in order to generate fluorescent emission from the molecule primarily at 419 nm.

5.2.3 Alq₃

The absorption, fluorescence excitation and fluorescence emission spectra of Alq₃ are shown in figure 5.3. Two samples were prepared via thermal evaporation and deposited onto a fused quartz glass slide for the absorption measurements and silicon wafer for the fluorescence measurements at a thickness of 80 nm. The absorption measurement was scanned from 250 to 500 nm where it can be seen that Alq₃ displays a fairly broad and featureless absorption spectrum from 350 – 450 nm with a UV absorption peak centred at a wavelength of 384 nm. The excitation measurement was scanned from 285 to 445 nm with the emission monochromator held at 497 nm – the primary peak emission wavelength of Alq₃. The emission measurement was scanned from 450 to 597 nm with the excitation monochromator held at 383 nm – the primary excitation wavelength of Alq₃.

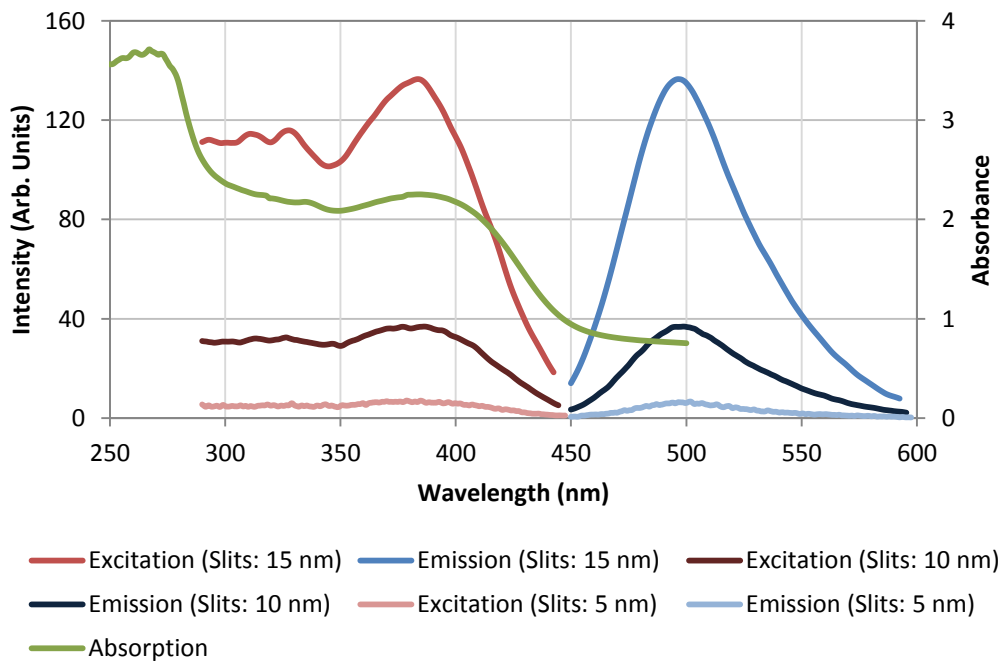


Figure 5.3: Excitation (red, left) and fluorescence spectra (blue, right) of Alq₃. Slit widths from the bottom to top: 5.0 nm; 10.0 nm; 15.0 nm.

From figure 5.3 it can be seen that Alq₃ displays one broad emission band centred at 497 nm. The excitation spectrum collected closely matches the absorption spectrum with an excitation peak centred at 383 nm. Although a slight wavelength offset exists it is most likely an

instrument calibration error. These measurements compare favourably with similar measurements made by Guo, et al. [7] and confirm that an ultraviolet LED emitting in the range 375-395 nm would be a suitable excitation source in order to generate fluorescent emission from the molecule at 497 nm. As both the excitation and emission spectra are broad, however, it would most likely be acceptable to excite the sample in the range 355-375 nm and still generate adequate fluorescent emission intensity.

5.2.4 MEH-PPV

The absorption, fluorescence excitation and fluorescence emission spectra of polymeric MEH-PPV are shown in figure 5.4. Two samples were prepared via spin coating (§3.2.2) and deposited onto a fused quartz glass slide for the absorption measurements and silicon wafer for the fluorescence measurements. The absorption measurement was scanned from 300 to 750 nm where MEH-PPV can be seen to display a very broad and featureless absorption spectrum from 400 to 600 nm with the centre of the peak residing at 504 nm. There is also a small absorption peak at 330 nm. The excitation measurement was scanned from 350 to 570 nm with the emission monochromator held at 588 nm – the primary peak emission wavelength of MEH-PPV. The emission measurement was scanned from 525 to 725 nm with the excitation monochromator held at 477 nm – the primary excitation wavelength of MEH-PPV. Both scans occurred at 300 nm per minute with all slits set to 10 nm.

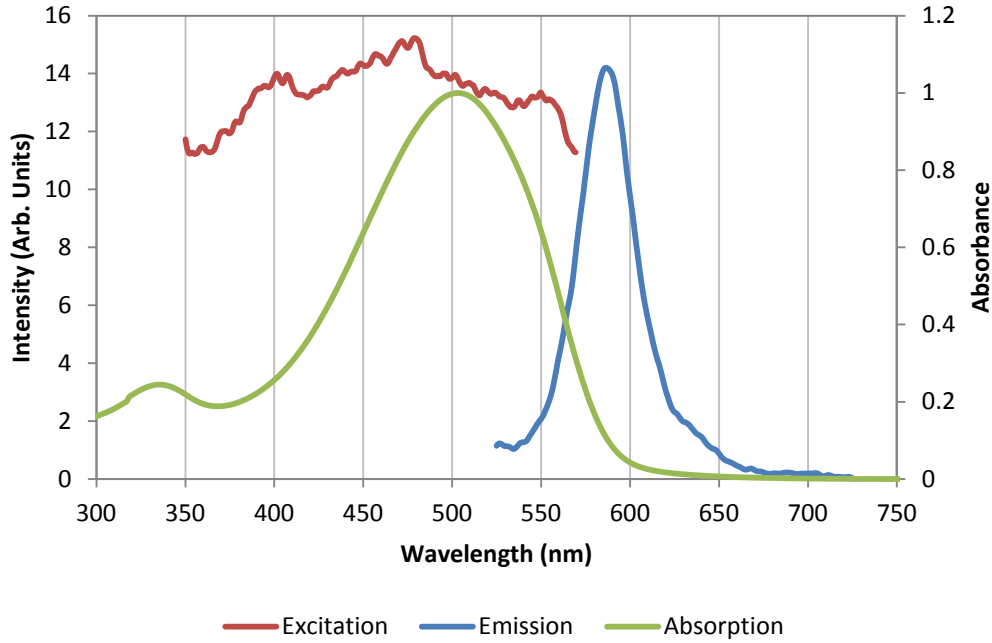


Figure 5.4: Excitation (red, left), absorption (green, left) and fluorescence spectra (blue, right) of MEH-PPV.

From figure 5.4 it can be seen that MEH-PPV displays one broad emission band centred at 588 nm. The excitation spectrum appears to display little resemblance to the absorption spectrum with an excitation peak centred at 477 nm. The main differences between the excitation spectrum of MEH-PPV and the absorption spectrum appear to be that the excitation spectrum exhibits broad, yet complex, wavelength-dependent pattern when monitoring emission specifically at 588 nm whereas the absorption spectrum presents a smooth, continuous broad-band spectrum. An explanation for this discrepancy could be found by looking at the morphology of the MEH-PPV sample. MEH-PPV is a conjugated polymer that contains a distribution of polymer chains varying in length. It has been noted by Lin, et al. [8] that certain portions of the polymer chain can behave in a “non-emissive state” whereby absorption occurs in these regions, but radiative emission (fluorescence) does not follow. In this way, these regions could, collectively, produce a significant difference between the absorption and excitation spectra not unlike what is shown in figure 5.4.

These measurements confirm that an LED emitting in the range 485-515 nm would be an appropriate excitation source in order to generate fluorescent emission from the molecule at 588 nm.

5.2.5 Tetracene

The absorption, fluorescence excitation and fluorescence emission spectra of polycrystalline tetracene are shown in figure 5.5. Two samples were prepared via thermal evaporation and deposited onto a fused quartz glass slide for the absorption measurements and silicon wafer for the fluorescence measurements at a thickness of 80 nm. The absorption measurement was scanned from 350 to 650 nm where it can be seen that tetracene absorbs readily in the visible portion of the electromagnetic spectrum from 400 – 550 nm. Similarly to anthracene five approximately evenly spaced absorption peaks are visible and are positioned at 420, 445, 476, 510, 522 nm, respectively. Due to the compromise made between obtaining good absorption intensity and detailed spectral resolution the latter two peaks are difficult to resolve; the first peak at 420 nm being barely visible. This structure, as was the case for anthracene, can also be attributed to vibrational transitions between electronic energy levels according to the Frank-Condon principle [2]. No significant absorption is detected above 550 nm. The excitation measurement was scanned from 350 to 490 nm with the emission monochromator held at 524 nm – the primary peak emission wavelength of tetracene. The emission measurement was scanned from 500 to 650 nm with the excitation monochromator held at 475 nm – the primary excitation wavelength of tetracene.

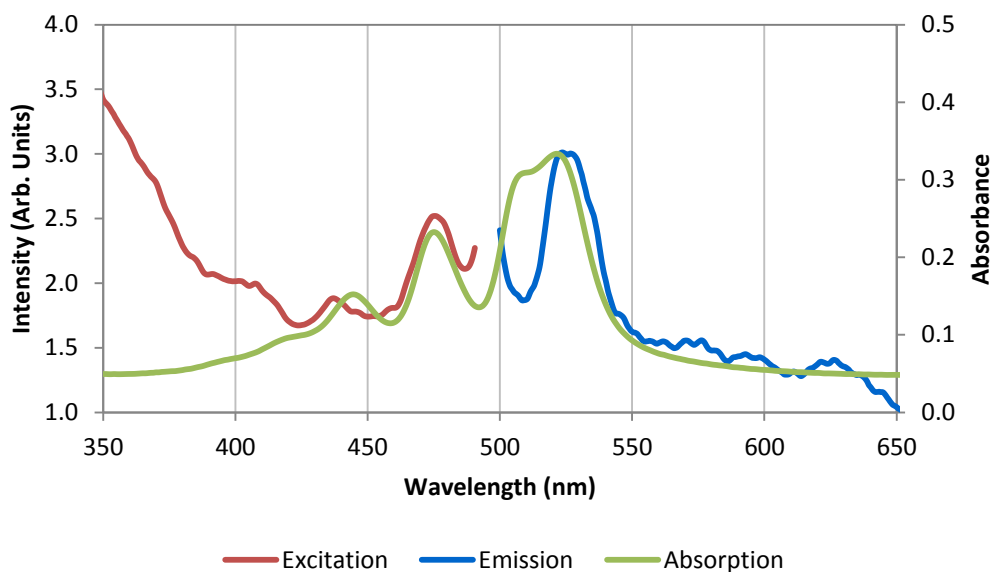


Figure 5.5: Excitation (red, left), absorption (green, left) and fluorescence spectra (blue, right) of tetracene.

From figure 5.5 it can be seen that tetracene displays essentially one emission band centred at 524 nm. The excitation spectrum collected closely matches the absorption spectrum with two excitation peaks centred at 437 nm and 475 nm, respectively. Interestingly enough, a peak from the absorption spectrum (522 nm) aligns closely with the primary peak from the emission spectrum (524 nm). This suggests that the latter peak is a 0-0 transition; an electronic transition between the lowest vibrational levels of the ground and excited states. These transitions have the same energy, and therefore wavelength, in both absorption and emission spectra [9]. From these measurements it appears that a visible wavelength LED emitting in the range 465-485 nm would be the most appropriate excitation source in order to generate fluorescent emission from the molecule at 524 nm.

5.2.6 NpQ

The absorption, fluorescence excitation and fluorescence emission spectra of polycrystalline NpQ are shown in figure 5.6. Two samples were prepared via thermal evaporation and deposited onto a fused quartz glass slide for the absorption measurements and silicon wafer for the fluorescence measurements at a thickness of 80 nm. The absorption measurement was scanned from 300 to 650 nm where it can be seen that NpQ displays a broad and featureless

absorption spectrum from 360 – 450 nm with the centre of the peak residing at 396 nm. The excitation measurement was scanned from 300 to 500 nm with the emission monochromator held at 566 nm – the primary peak emission wavelength of tetracene. The emission measurement was scanned from 450 to 650 nm with the excitation monochromator held at 362 nm – the primary excitation wavelength of NpQ.

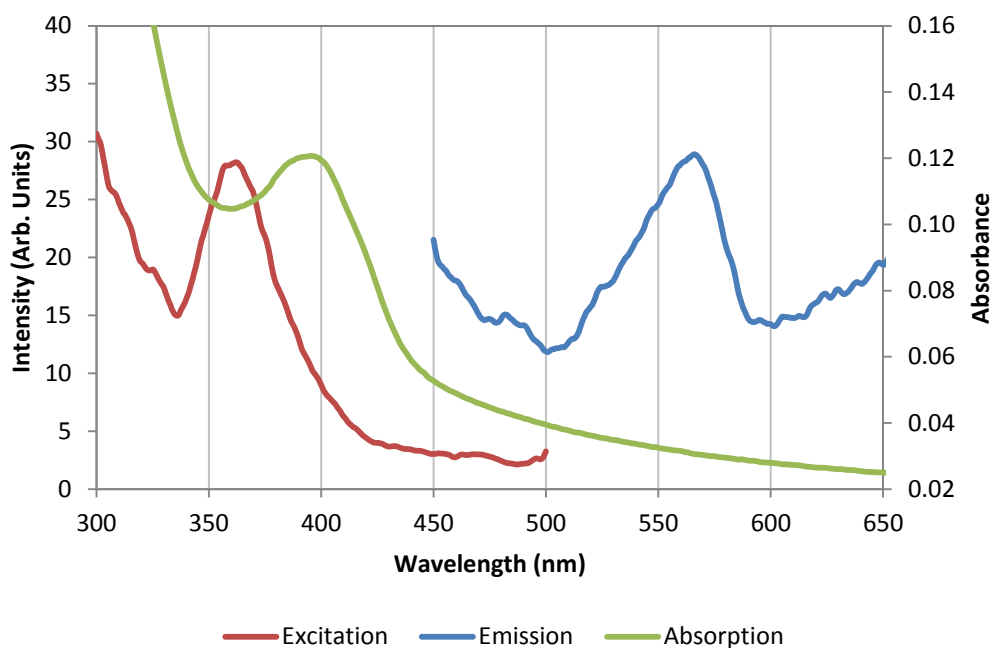


Figure 5.6: Excitation (red, left) and fluorescence spectra (blue, right) of NpQ.

From figure 5.6 it can be seen that NpQ displays essentially one main emission band centred at 566 nm. The excitation spectrum follows a shape similar to the absorption spectrum, however, the excitation peak is centred at 362 nm whilst the absorption peak is centred at 396 nm. This discrepancy is most likely due to a measurement error caused by poor calibration. However, it is possible that the discrepancy is due to a phenomenon known as photochromism. Photochromism is a reversible photochemical reaction whereby the absorption of electromagnetic radiation causes a transformation of a chemical species from one form to another. One result of this transformation is that the absorption spectra of the material can reversibly change in amplitude or position on absorption of light [10]. In a study [11] that looked at changes in absorbance as a function of irradiation exposure Malkin, et al. have shown that molecules belonging to the same class of materials as NpQ (naphthaquinones) can exhibit

photochromism. From these measurements it appears that an ultraviolet LED emitting in the range 355-375 nm would be a suitable excitation source in order to generate fluorescence emission from the molecule at 566 nm.

5.2.7 Summary of Results

The main spectroscopic results of the MFE-candidate materials presented in the previous sections have been collated and are summarised in table 5.1.

Sample	Absorption Peak(s) (nm)	Excitation Peak(s) (nm)	Emission Peak(s) (nm)	Selected LED
TPD:BBOT:PMMA	358	359	420, 485	UV (355-375 nm)
Anthracene	336, 353, 373, 393	335, 352, 370, 390	403, 419, 443, 469	UV (355-375 nm)
Alq ₃	384	383	497	UV (355-375 nm)
MEH-PPV	330, 504	477	588	Visible (485-515 nm)
Tetracene	420, 445, 476, 510, 522	437, 475	524	Visible (465-485 nm)
NpQ	396	362	566	UV (355-375 nm)

Table 5.1: Summary of spectroscopic data for the MFE-candidate materials.

5.3 Magnetic Field Effect Magnetometry

As has been discussed in §2.5 several materials are known to exhibit a photoluminescent (PL) magnetic field effect (MFE). MFE manifests itself as a change in PL intensity when the material is exposed to an external magnetic field. In order to confirm these reported observations and to determine which of the candidate materials would be most suitable for use in the development of the proposed magnetic luminescence microscopy technique it was necessary to independently measure the MFE of several materials.

The initial PL-MFE results of MEH-PPV, Alq₃, NpQ and anthracene are plotted in figure 5.7 as measured using the latest HF-MFE system (mk. III). What is immediately apparent is that the plotted data for MEH-PPV, Alq₃, and NpQ are almost identical. This is very unusual and suggests that these materials, in fact, do not exhibit PL-MFE at all. Instead it is indicative of a systematic

error that is most likely affecting all measurements. The cause of this error is most likely due to movement of the weakly ferromagnetic stainless steel optical cage assembly that is positioned between the electromagnet pole pieces. This error did not manifest in earlier builds of the HF-MFE system as they did not make use of the optical cage assembly.

In order to correct for this systematic error it is assumed that the measured MFE data for MEH-PPV, Alq₃ and NpQ all follow a background that can be removed by averaging the three curves, fitting a function to the curve and subtracting that function from all other data.

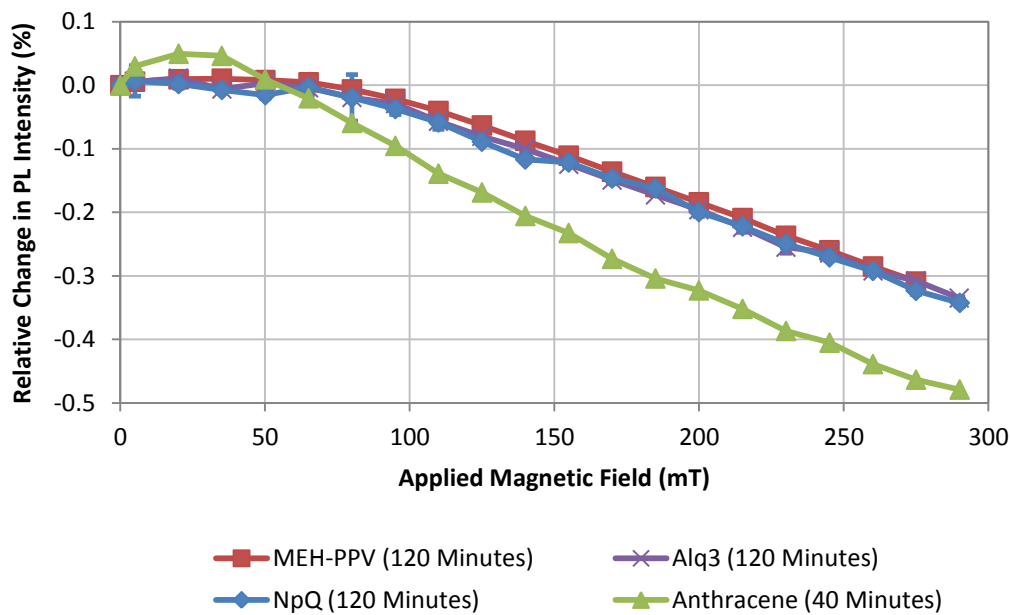


Figure 5.7: Initial PL-MFE results of MEH-PPV, Alq₃, NpQ and anthracene.

Figure 5.8 plots the average PL-MFE data of the MEH-PPV, Alq₃ and NpQ measurements as well as the cubic polynomial fit function:

$$y = 1.866 \times 10^{-8}x^3 - 1.117 \times 10^{-5}x^2 + 5.145 \times 10^{-4}x + 1.052 \times 10^{-3} \quad \text{Equation 5.1}$$

With a Pearson product-moment correlation coefficient value, R^2 , equal to 0.999. A third-order polynomial appeared an appropriate fit function for the shape of the data and is confirmed by the large R^2 value.

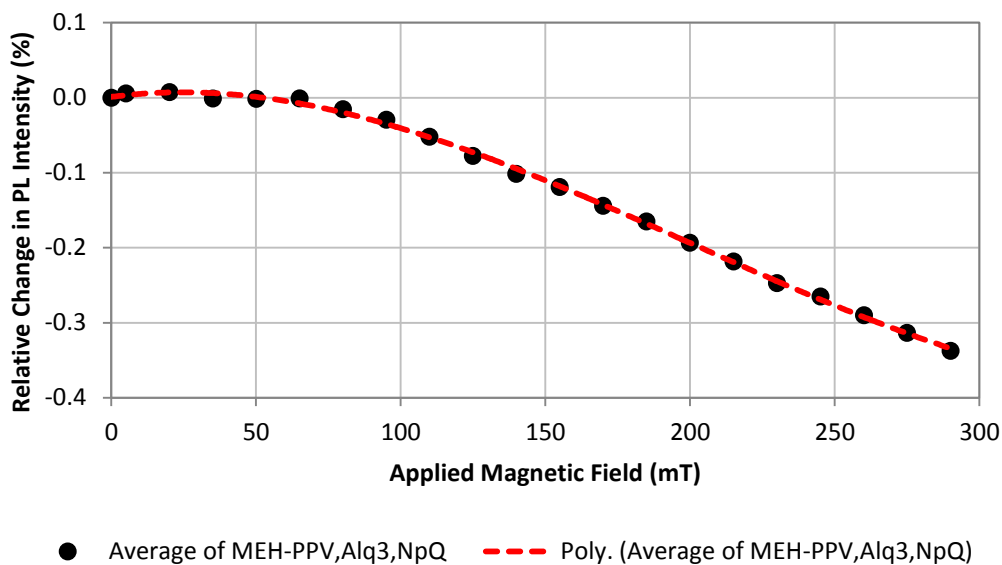


Figure 5.8: Plot of the average PL-MFE data for MEH-PPV, Alq₃ and NpQ. Also plotted is the cubic polynomial fit of the data.

The fit function was subtracted from all measured MFE data and the results are plotted in figure 5.9. It can be seen that the polycrystalline tetracene powder sample dominates the plot with an eventual positive MFE exceeding 6% at 290 mT. The next largest MFE is provided by the TPD:BBOT:PMMA sample (mixture ratio 1:1:4) with an MFE that saturates at +1% at an applied magnetic field of 50 mT (this can be seen more clearly in figure 5.10). This MFE magnitude is half that found by Hu, et al. [5] for the same mixture ratio, but follows the same profile. If we assume the exciplex, formed between interacting TPD and BBOT molecules, is responsible for the MFE observed in the TPD:BBOT:PMMA sample then the magnitude discrepancy could be due to the fact that no attempt was made to block fluorescent emissions from non-interacting TPD and BBOT fluorescent sites on the sample – only a blockage of the excitation light source from reaching the photodetector was made. Therefore non-MFE fluorescence from TPD and BBOT could have been ‘diluting’ the MFE fluorescence from the exciplex emission reducing the overall MFE measurement of the sample.

Figure 5.10, a rescaled version of figure 5.9, begins to reveal the negative MFE of anthracene which approaches -0.15% at 290 mT. Figure 5.11, an MFE plot scaled optimally for anthracene,

shows that anthracene's MFE is essentially identically inverse to tetracene's MFE with a small positive MFE at low field and a (relatively) large, negative MFE at high field.

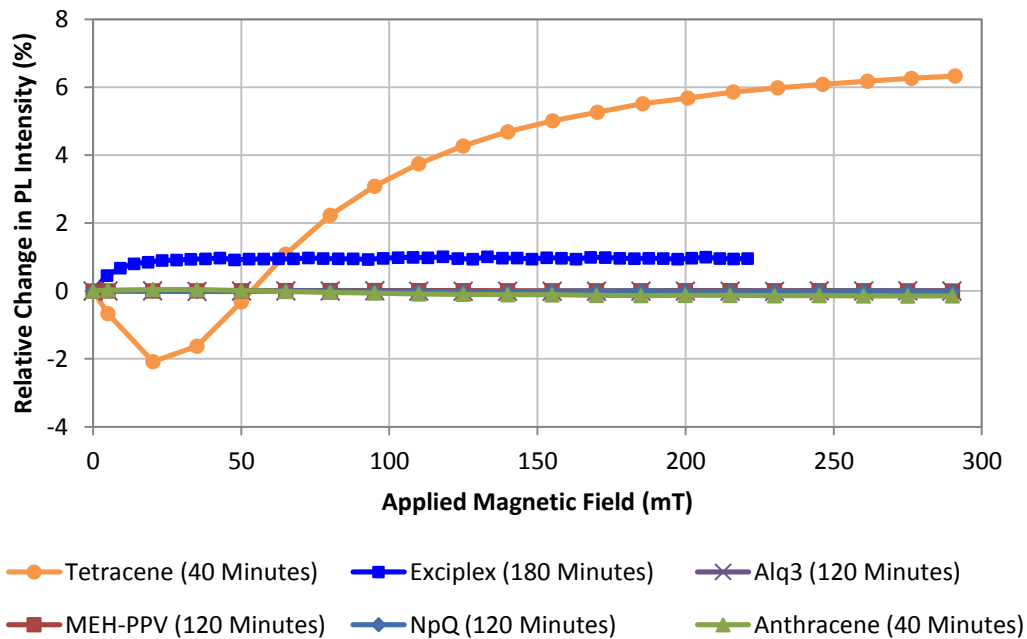


Figure 5.9: Plot of all the PL-MFE data with background subtraction applied. The plot is optimally scaled on the ordinate for tetracene. The times stated in the legend refer to the experimental durations of each scan.

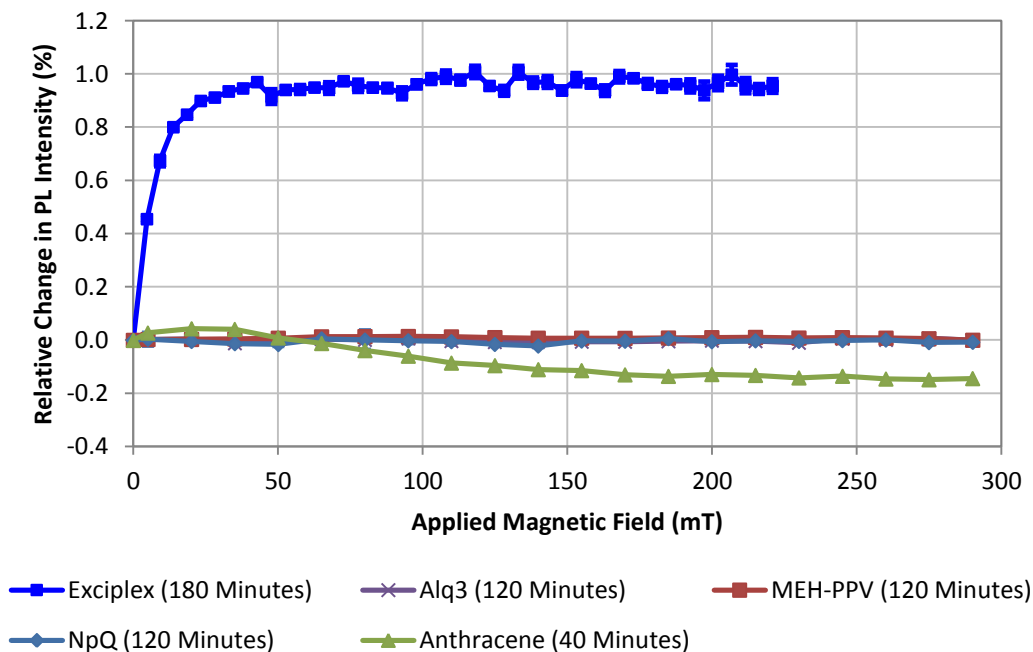


Figure 5.10: Plot of all the PL-MFE data (except tetracene) with background subtraction applied. The plot is optimally scaled on the ordinate for the BBOT:TPD:PMMA sample. The times stated in the legend refer to the experimental durations of each scan.

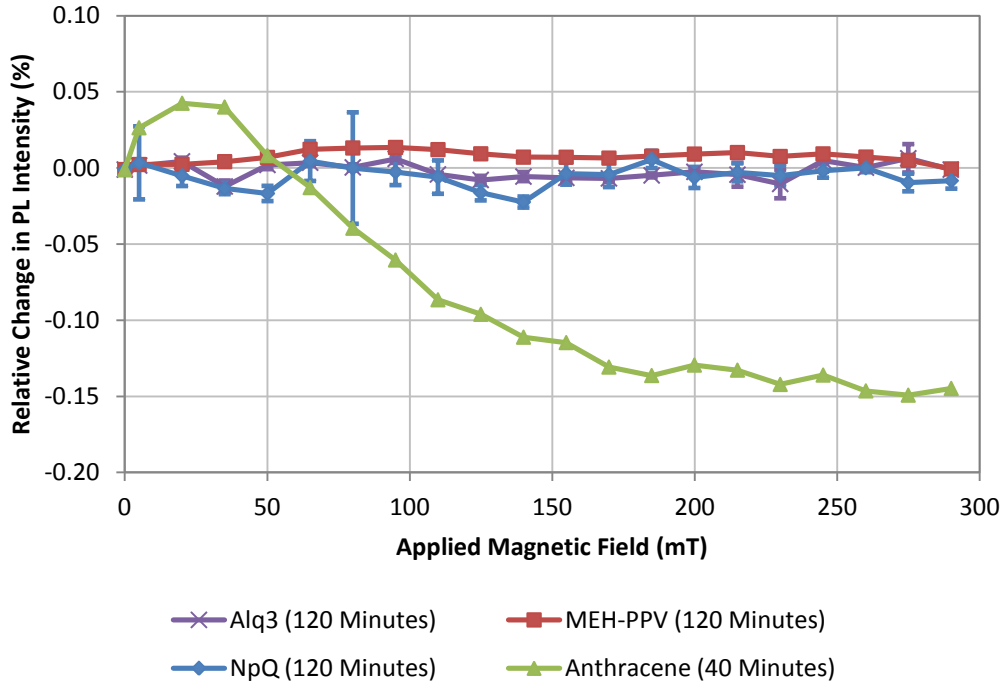


Figure 5.11: Plot of all the PL-MFE data (except tetracene and TPD:BBOT:PMMA sample data) with background subtraction applied. The plot is optimally scaled on the ordinate for anthracene. The times stated in the legend refer to the experimental durations of each scan.

Figure 5.12 compares the measured PL-MFE of anthracene with the triplet exciton annihilation rate of anthracene as measured by Johnson, et al. [12]. Triplet exciton annihilation, also known as triplet-triplet annihilation (TTA) and triplet exciton fusion, is defined as:



In their experiment they were actually measuring the delayed fluorescence intensity but verified that this intensity remained proportional to the square of the excitation light intensity. This, they say, ensured that the steady-state triplet population is independent of the triplet exciton fusion rate constant thereby establishing that the delayed fluorescence intensity is directly proportional to the triplet exciton fusion rate constant.

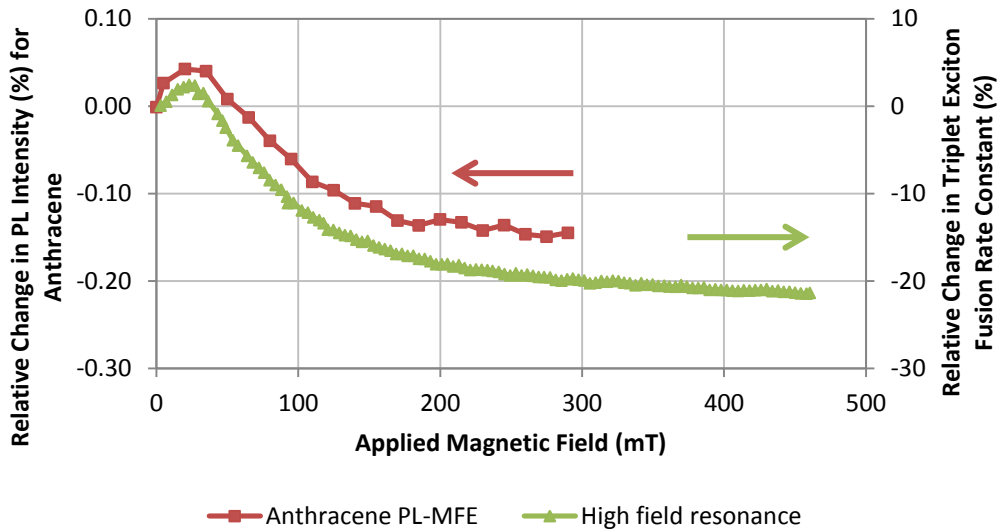


Figure 5.12: Comparison of PL-MFE data for polycrystalline anthracene against the triplet exciton fusion rate constant for high field resonance-oriented anthracene [12].

It can be seen that the PL-MFE curve closely follows the shape of the triplet exciton fusion rate constant curve. However, there is a difference in the magnitude of the change of over two orders. It can be seen that the triplet exciton fusion rate constant curve increases to +2.5% in the low field regime and surpasses -20% at 290 mT. This is in contrast to the PL-MFE anthracene curve which only reaches +0.05% change in the low field regime and -0.15% at 290 mT.

The PL-MFE measurements here did not discriminate between prompt and delayed fluorescence, meaning that both are included in the measured PL-MFE data. On this basis, two reasons are presented to explain the existence of the magnitude discrepancy between the two anthracene measurements:

1. The delayed fluorescence intensity is dwarfed by the prompt fluorescence intensity (the latter also exhibiting a weak MFE of positive character of approximately 0.8% [13, 14]). This acts to 'dilute' the delayed fluorescence MFE observed.
2. The sample that Johnson, et al. used is a single crystal of anthracene. The MFE of anthracene has a crystal orientation dependence with respect to the magnetic field direction [12]. Johnson's measurements presented in figure 5.12 are for the *ab* plane of

the monoclinic anthracene crystal oriented parallel with respect to the magnetic field direction where the optimal orientation has been found leading to large amplitude MFE. The PL-MFE measurement presented here, by comparison, is from a polycrystalline powder and therefore the MFE measured is an average of all the possible crystal orientations.

These observations suggest that the application of a magnetic field up to 50 mT on anthracene under steady-state conditions acts to increase the triplet exciton fusion rate constant causing an increase in the singlet population due to the increased annihilation rate of pairs of triplet excitons. Above 50 mT the magnetic field acts to decrease the triplet exciton fusion rate constant causing a decrease in the singlet population due to the reduced annihilation rate of pairs of triplet excitons. This process generates the delayed fluorescence MFE observed in anthracene as these population changes are compared to the initial steady-state singlet population in anthracene at zero magnetic field.

Figure 5.13 is an MFE plot of anthracene and tetracene scaled to separate ordinate axes in order to compare their shape with an applied magnetic field. It can be seen that the materials exhibit an initial increase (anthracene) or decrease (tetracene) in MFE magnitude at low magnetic field before reversing the MFE trend at higher magnetic fields. The high degree of symmetry observed between the two curves offers potential validation of the systematic error correction undertaken.

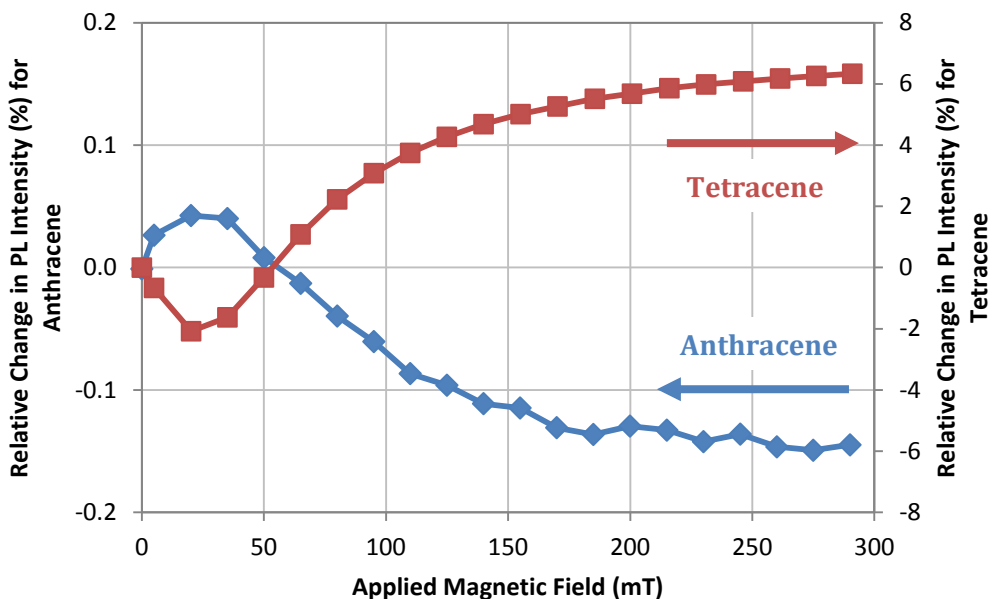
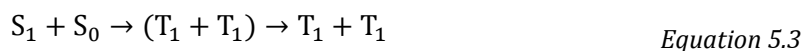


Figure 5.13: Comparison of PL-MFE data for anthracene and tetracene.

Figure 5.13 bares striking resemblance to work from a paper published by Groff et al. [15] (see figure 5.14) on tetracene that showed a temperature-dependent transition affecting which form of photoluminescence produces MFE. One discrepancy that exists between datasets is that Groff, et al. measured a maximum MFE of nearly 30% whilst the MFE, presented here, of tetracene only just exceeds 6%. This difference is explained similarly to the second explanation given for the discrepancy seen in anthracene in that this work used a polycrystalline sample whilst Groff, et al. used a single crystal aligned in the high field resonance direction. The inflection points seen in figures 5.13&14, where the MFE polarity reverses, occur at approximately 50 mT in both figures (using the relation $B = \mu_0 H$). According to Merrifield, et al. [16], who co-authored the aforementioned paper, tetracene crystals at room temperature can undergo singlet exciton fission:



This is the reverse of triplet exciton fusion (equation 5.2). They state that singlet exciton fission is highly endothermic in other materials (e.g. 4000 cm^{-1} or 496 meV for anthracene) whereas in tetracene the energy difference between the S_1 and the $(T_1 + T_1)$ state is only 1200 cm^{-1} equivalent to 149 meV where the *average* thermal molecular energy at room temperature is 29

meV ($E = k_B T$; where $T = 300$ K). Swenberg et al. [17] first proposed in 1968 that singlet exciton fission is the primary quenching mechanism explaining tetracene's low fluorescence quantum yield of 0.2% (for comparison anthracene's fluorescence quantum yield is 90%) [18].

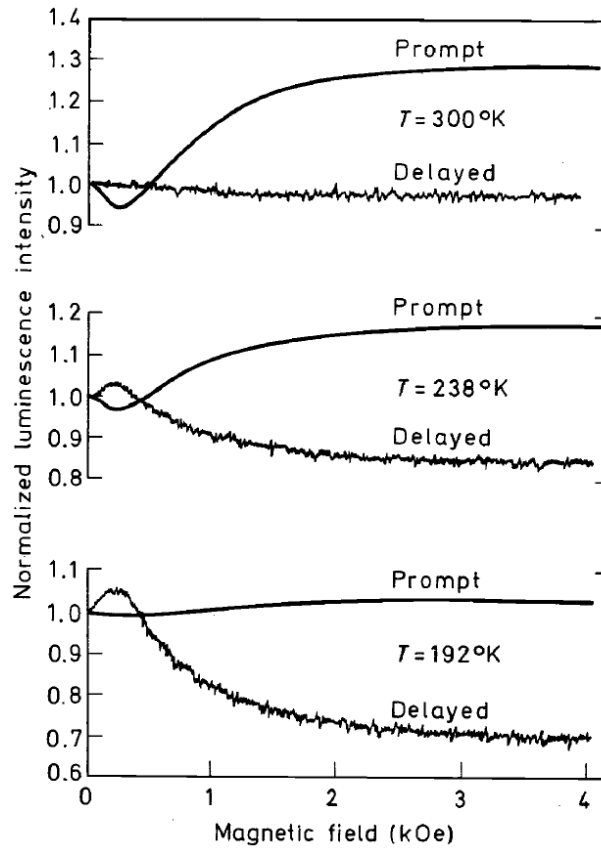


Figure 5.14: Plots of magnetic field effect transitioning between prompt fluorescence and delayed fluorescence with temperature for tetracene [15]. Copyright 1970 by The American Physical Society.

Therefore at room temperature, under steady-state conditions, there is sufficient thermal energy available for tetracene to readily convert a fraction of its singlet population into triplets via the (T_1+T_1) state. This suggests that the application of a magnetic field up to 50 mT acts to increase the singlet exciton fission causing a reduction in the steady-state singlet population which produces the negative MFE observed. Above 50 mT a magnetic field acts to decrease the singlet exciton rate causing an increase in the steady-state singlet population which produces the positive MFE observed. Since singlet exciton fission in tetracene is very efficient (95%) [19] this could explain why the magnitude of the prompt fluorescence positive MFE seen in tetracene is so large.

Since singlet exciton fission is temperature dependent a reduction in temperature below room temperature causes the singlet exciton fission rate constant to reduce proportionally at all magnetic fields – including at zero magnetic field. This results in a linear temperature-dependent reduction in tetracene's prompt fluorescence MFE. What is interesting to see from figure 5.14 is that tetracene's delayed fluorescence develops an increasingly large negative MFE with a reduction in temperature. This suggests that the triplet exciton fusion process is present in tetracene but is dominated by singlet exciton fission at room temperature. So as temperature is reduced the triplet exciton fusion process becomes dominant in tetracene and, just as is the case for anthracene, it exhibits magnetic-field dependence, which results in delayed fluorescence MFE.

If this theory is correct it is predicted that anthracene, when heated above room temperature but below its melting point (210-218 °C [20]), will undergo a similar transition as seen with tetracene whereby the prompt fluorescence MFE magnitude becomes larger than the delayed fluorescence MFE magnitude. This would be caused by a temperature-dependent transition where the singlet exciton fission process would end up dominating the triplet exciton fusion process.

An experiment was performed in order to confirm whether altering the ratio of chemicals in the TPD:BBOT:PMMA sample would indeed affect the PL-MFE as previously demonstrated by Hu, et al. [5]. Seven solutions were fabricated with differing amounts of PMMA in each such that the ratio of TPD:BBOT:PMMA ranged from 1:1:1 to 1:1:7. The results of the experiment are presented in figure 5.15.

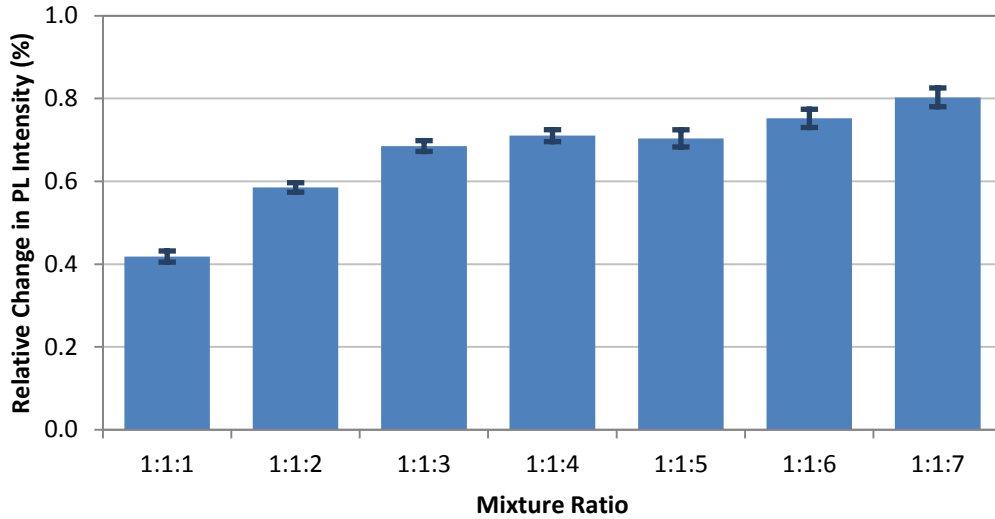


Figure 5.15: Plot of PL-MFE intensity of TPD:BBOT:PMMA at various mixing ratios all measured at 35 mT.

The results in figure 5.15 appear to show that by increasing the PMMA content of the TPD:BBOT:PMMA mixture the resultant PL-MFE (at 35 mT) increases with an apparent linear trend. Figure 5.16 contains the results of a repeat of the first experiment with new samples, this time plotting the seven mixtures at 12 different magnetic fields from 0 to 230 mT.

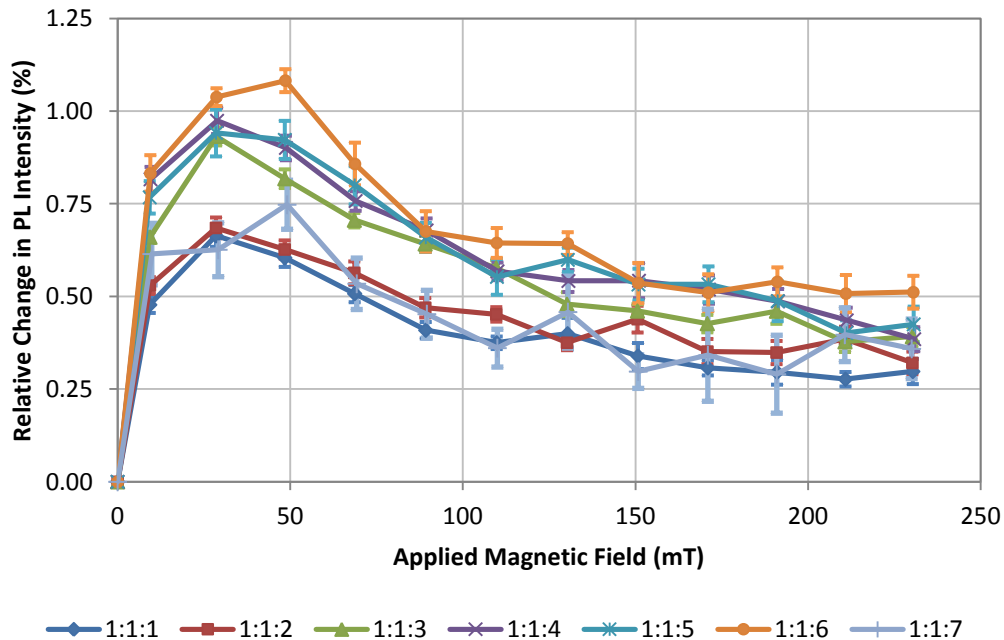


Figure 5.16: Plot of PL-MFE intensity of TPD:BBOT:PMMA at various mixing ratios as a function of applied magnetic field. These measurements were performed on new samples compared to the measurements made in figure 5.15.

It should be noted that these measurements were performed without the knowledge that the HF-MFE magnetometer contained a field-dependent background. Therefore it is not possible to subtract the background from these measurements as the background function changes with every re-build of the system (due to the system requiring disassembly in order to allow other lab users access to the high-field magnet to perform MOKE magnetometry). So although the shape of the data does not correlate with the background-corrected plot shown in figure 5.10 the relative positions of each data series still allows for the extraction of useful information (because if the background were to be subtracted it would not alter the relative positions of each data series).

The relative positions of each series appear to correlate well with the results presented in figure 5.15 and maintain the same order for all magnetic fields measured. The only exception to this, however, is the 1:1:7 ratio measurement. This measurement was predicted to exhibit the highest MFE, but it only managed an MFE between 1:1:2 and 1:1:3. The standard error of each 1:1:7 series datum is twice that of all other measurements and suggests that this particular measurement suffered from poor signal-to-noise which may have caused the low MFE due to a greater relative contribution from field-independent background intensity:

$$\text{MFE} = \left(\frac{(I_B + I_{\text{background}}) - (I_0 + I_{\text{background}})}{(I_0 + I_{\text{background}})} \right) \times 100\% \quad \text{Equation 5.4}$$

where I_B = fluorescence intensity with applied magnetic field; I_0 = fluorescence intensity without an applied magnetic field; $I_{\text{background}}$ = intensity of light not from the MFE sample. Therefore this measurement is considered erroneous and is most likely caused by an improperly fabricated sample.

It has been suggested by Hu, et al. [5] that the reason the mixing ratio alters the MFE magnitude is due to PMMA acting to increase the intermolecular distance between TPD and BBOT by physically separating them. It is these compounds that together, he argues, form an excited

complex (exciplex) that allow polarons to exhibit large e-h separation distances causing the energy difference between the singlet and triplet state, ΔE_{ST} , to become iso-energetic with the external Zeeman splitting energy, ΔE_{EZ} , when an external magnetic field is applied, which ultimately causes an increase in the intersystem crossing rate.

5.4 Thin Film Morphology

The morphology of the several of the samples created during this research was analysed using optical microscopy and atomic force microscopy and is discussed in the following sections. These analyses were performed in order to test the suitability of certain deposition methods and to optimise the deposition parameters used.

5.4.1 Morphology of Spin-Coated Thin Films

Although anthracene is traditionally deposited as a thin film onto a substrate using thermal evaporation, alternative fabrication techniques were explored to improve the resulting morphology. Presented below in figure 5.17 are the results of the attempt to spin-coat anthracene onto a silicon wafer. Figure 5.17a is an optical micrograph of anthracene spin-coated at 4000 rpm for 30 seconds onto a silicon wafer from a chloroform solution of concentration 10.6 mg/mL. At this concentration (equivalent to 43% of the saturation concentration of anthracene in chloroform at room temperature (24.5 mg/mL) [21]) it can be seen that anthracene forms clusters of crystals randomly scattered across the substrate. Figure 5.17b is from anthracene spin-coated from a solution with chloroform at a concentration of 14.9 mg/mL (60.8% of the saturation limit). At this concentration it can be seen that anthracene begins to form a two-dimensional network of 'filaments' that has most likely formed via diffusion of the anthracene to the edges of rapidly vaporising chloroform 'bubbles'. This is similar to the diffusion of inclusions in metallic grain boundary growth dynamics [22] whereby the secondary phase gets pushed to the grain boundaries. In the case of figure 5.17b, however, the primary constituent of the 'grain' (chloroform) has completely evaporated after the diffusion of

anthracene has concluded leaving only the 'grain boundary' material (anthracene) behind. Figure 5.17c shows anthracene spin-coated from a solution with chloroform at a concentration of 19.9 mg/mL (81.2% of the saturation limit). It can be seen that the filament network has now fully established with a high density of anthracene present at the 'grain boundaries' and an overall larger amount of 'grain boundaries' present compared to figure 5.17b. It appears therefore that a higher solution concentration yields smaller 'grains'.

From these results it appears that anthracene thin films fabricated via spin-coating cannot compete morphologically with anthracene thin films fabricated via thermal evaporation in terms of grain density and uniformity.

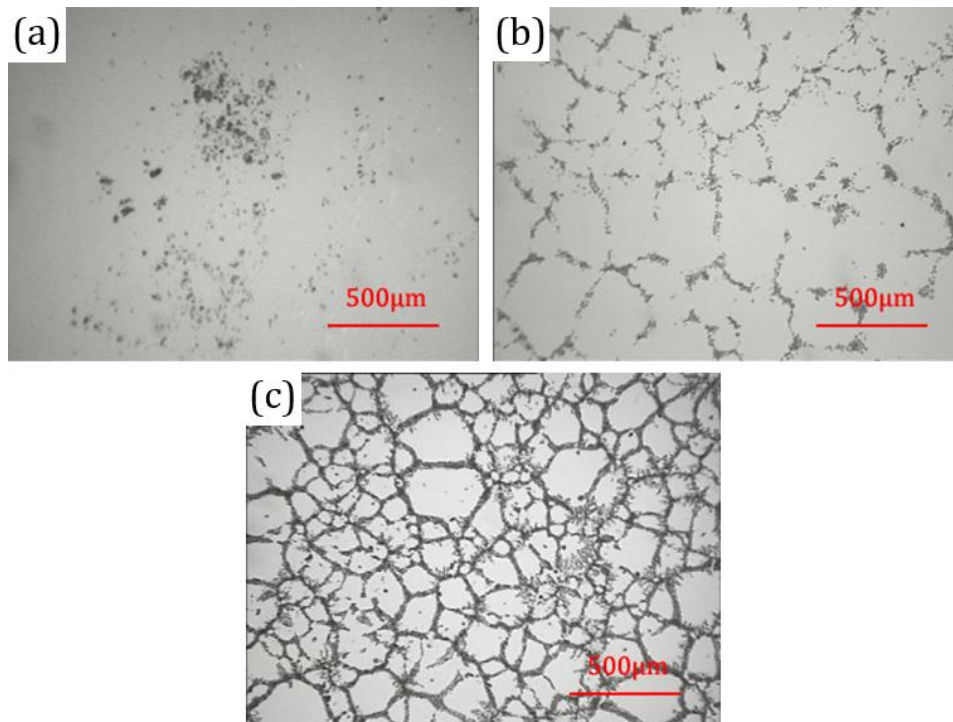


Figure 5.17: Optical micrographs of anthracene spin-coated onto silicon wafer at (a) 10.6 mg/mL; (b) 14.9 mg/mL; and 19.9 mg/mL concentration. All micrographs were captured at the same scale.

Figure 5.18 depicts an atomic force micrograph of the spin-coated TPD:BBOT:PMMA sample (of the ratio 1:1:4) and a line scan averaged over the entire micrograph. The averaged line scan allows the step height from the thin film to the underlying substrate to be measured. In this figure the step height recorded equals 79 nm. In the lower-left of figure 5.18 the micrograph reveals a rather uniform thin film with only a few defects present. These defects were probably

generated during the formation of the trench used to measure the step height and can therefore be ignored. A trench has to be scored by hand to get a thickness measurement as it is difficult to mask a spin-coating sample without damaging the entire thin film during removal of the mask.

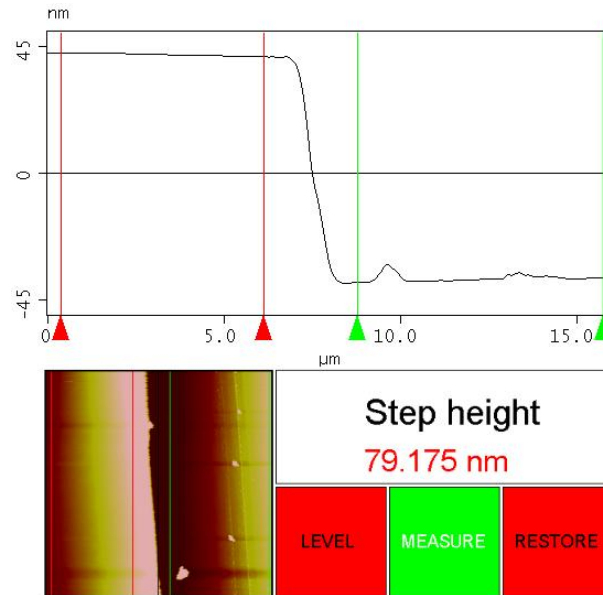


Figure 5.18: AFM micrograph of the TPD:BBOT:PMMA sample (1:1:4 ratio) spin-coated onto silicon wafer at 4000 rpm for 30 seconds. This micrograph depicts a step-height measurement of approximately 79 nm between the deposited TPD:BBOT:PMMA and the underlying silicon wafer.

5.4.2 Morphology of Thermally Evaporated Thin Films

The morphology of two samples of thermally evaporated tetracene is shown in figure 5.19. Evaporated at a rate of $1.06 \text{ nm}\cdot\text{s}^{-1}$ the film shown in figure 5.19a is composed of grains averaging around 250-300 nm in diameter whilst the film evaporated at the higher rate of $1.59 \text{ nm}\cdot\text{s}^{-1}$, shown in figure 5.19b, is composed of grains averaging around 150-200 nm in diameter. The grains visible in both micrographs appear fairly uniform and therefore exhibit a low shape distribution. The grain height appears on average to be $< 40 \text{ nm}$ according to the adjacent scale bar, however, this measurement is not a true film thickness measurement as the underlying substrates are not visible in the figure.

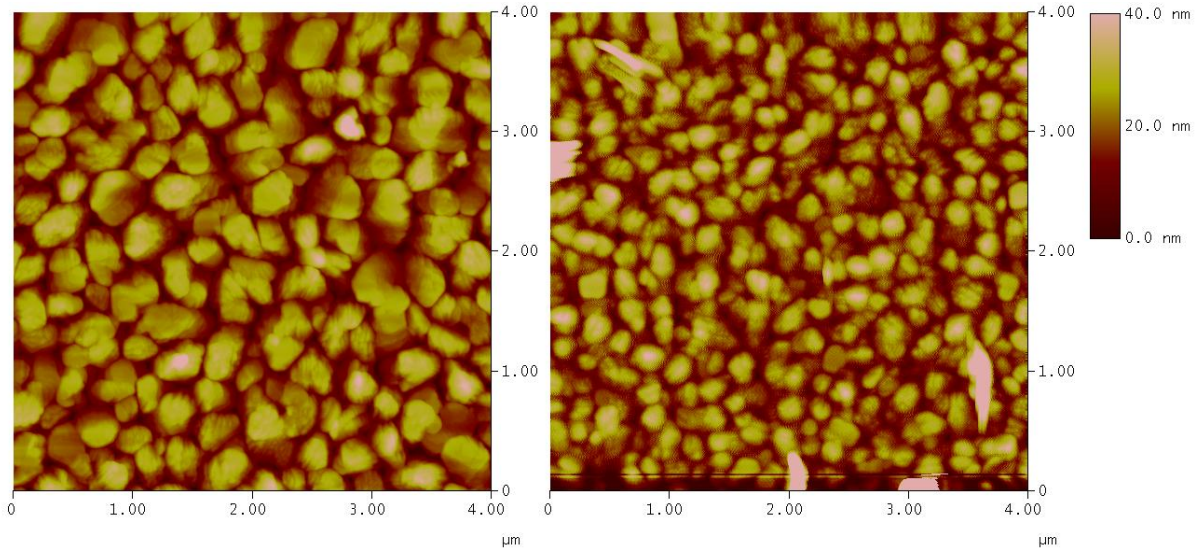


Figure 5.19: AFM micrograph of tetracene thermally evaporated onto silicon wafer at a rate of (a) $1.06 \text{ nm}\cdot\text{s}^{-1}$ and (b) $1.29 \text{ nm}\cdot\text{s}^{-1}$.

The actual thickness of the tetracene film shown in figure 5.19a is displayed in figure 5.20 and equals approximately 80 nm. This height was measured by averaging each side of the micrograph separately and subtracting them. The substrate surface was available for step height calculation by masking that portion of the substrate prior to evaporation. The large ridge aligned vertically at the centre of the micrograph is most likely a build up of evaporant caused by proximity to the side-wall of the sample mask.

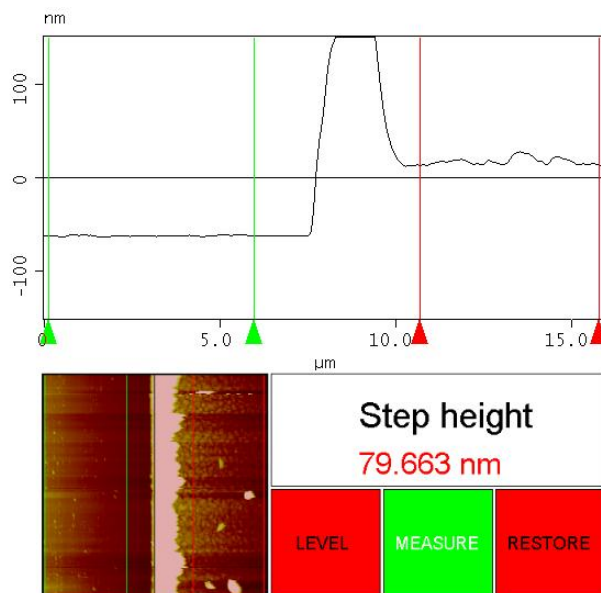


Figure 5.20: AFM micrograph of tetracene thermally evaporated onto silicon wafer at a rate of $1.06 \text{ nm}\cdot\text{s}^{-1}$. This micrograph depicts a step-height measurement of approximately 80 nm between the deposited tetracene and the underlying silicon wafer.

5.4.3 Morphology of Thermally Evaporated Thin Films Coupled to Nanostructures

In order to attempt to observe magnetic contrast via confocal microscopy it was important to create samples combining magnetic structures (Ni-Fe magnetic nanostructures) with a fluorescent MFE-active material (tetracene). 40 nm thick Ni-Fe nanostructures were fabricated using electron beam lithography and thermal evaporation onto a silicon substrate followed by the evaporation of tetracene over the entire sample. Figure 5.21 shows an atomic force micrograph of tetracene grains coupled to a rectangular Ni-Fe nanostructure. The tetracene thin film, of 80 nm in thickness, was thermally evaporated onto the nanostructure sample at a rate of $0.045 \text{ nm}\cdot\text{s}^{-1}$. This is around two orders of magnitude slower than the rates used for the tetracene thin films shown in figure 5.19 and was suggested by the operators of the equipment as it is the usual rate for depositing tetracene in organic devices. It was later realised that this rate would intentionally produce large grains as the emphasis for their research was on minimising the number of grain boundaries (as a high number of grain boundaries increases the electrical resistance of the device, therefore reducing its performance). Later deposition attempts were performed at much higher rates.

In figure 5.21 it can be seen that the tetracene grain morphology is quite different as a result of the slow deposition rate; the grains are rather acicular whilst the grains presented in figure 5.19 are more rounded. There also appears to be a morphological difference between the tetracene deposited onto the Ni-Fe nanostructures compared to the silicon substrate (see figure 5.22a also). This could be due to differences in thermal conductivity whereby silicon, with a thermal conductivity of $142.2 \text{ W}\cdot\text{K}^{-1}\cdot\text{m}^{-1}$ [23], extracted heat away from the tetracene better than Ni-Fe, with a thermal conductivity of $46.4 \text{ W}\cdot\text{K}^{-1}\cdot\text{m}^{-1}$ [24], reducing tetracene's ability to diffuse and form large grains.

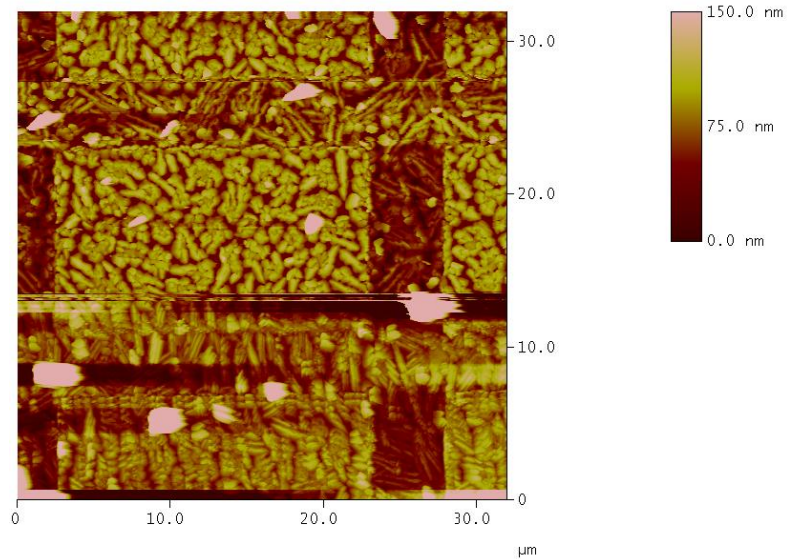


Figure 5.21: AFM micrograph of tetracene thermally evaporated onto silicon wafer and Ni-Fe nanostructures at a rate of $0.045 \text{ nm}\cdot\text{s}^{-1}$. A Ni-Fe rectangle features centrally in this figure.

Figure 5.22 contains two atomic force micrographs featuring one of the serpentine wire nanostructures. It consists of end-to-end connected semi-circular arcs each rotated 180° from the previous arc. Figure 5.22a reveals that the slow deposition rate has allowed the grains to form into an acicular morphology whereas in figure 5.22b the faster deposition rate has reduced the grain size and favoured a rounder grain morphology (if one ignores the second layer of contaminant particles). It is interesting to note that in figure 5.22a where the tetracene film couples to the Ni-Fe nanostructure there is an affinity for grains to form at the edges of the structures whilst avoiding the central region. As this would be problematic for magnetic imaging via confocal microscopy due to non-uniform film coverage it is obvious that the faster deposition rate is preferred.

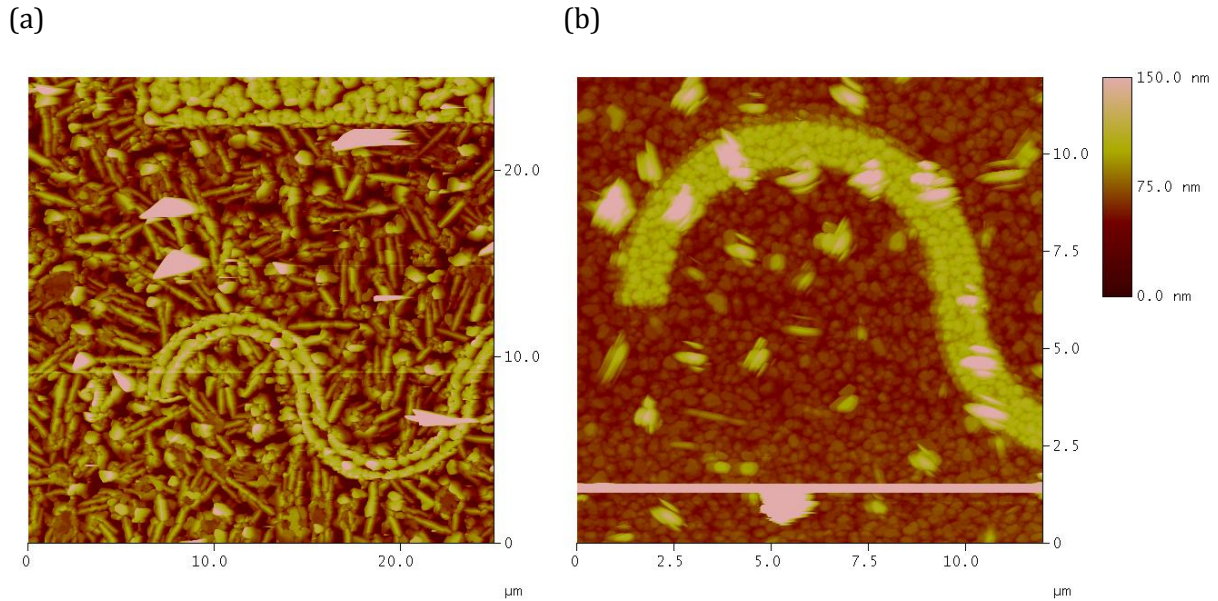


Figure 5.22: AFM micrograph of tetracene thermally evaporated onto silicon wafer and Ni-Fe nanostructures (a) at a rate of $0.045 \text{ nm}\cdot\text{s}^{-1}$ and (b) a rate of $1.29 \text{ nm}\cdot\text{s}^{-1}$.

5.4.4 Defects in the Electron Beam Lithography Fabrication Process

Although electron beam lithography is a powerful technique due to its ability to pattern complex geometries at very high spatial resolution it is still susceptible to producing fabrication defects like any other fabrication process. The main defects encountered in this work have occurred at the design translation stage where the design pattern is converted into a writing pattern by a computer algorithm. Below are examples of the defects encountered together with a discussion regarding their generation and eradication.

The first defect encountered is shown in figure 5.23. Figure 5.23a shows the atomic force micrograph of a symmetric notch in a nanowire. Figure 5.23b shows a screenshot of the same notch from the design software in its intended form. It can be seen that this structure has been separated into two discrete parts leaving an unexposed gap of PMMA between the structures. To ensure the RAITH software would write this structure properly it was necessary to create a second object (such as a rectangle with the long axis aligned horizontally) in the design that overlapped the two areas of nanowire each side of the notch.

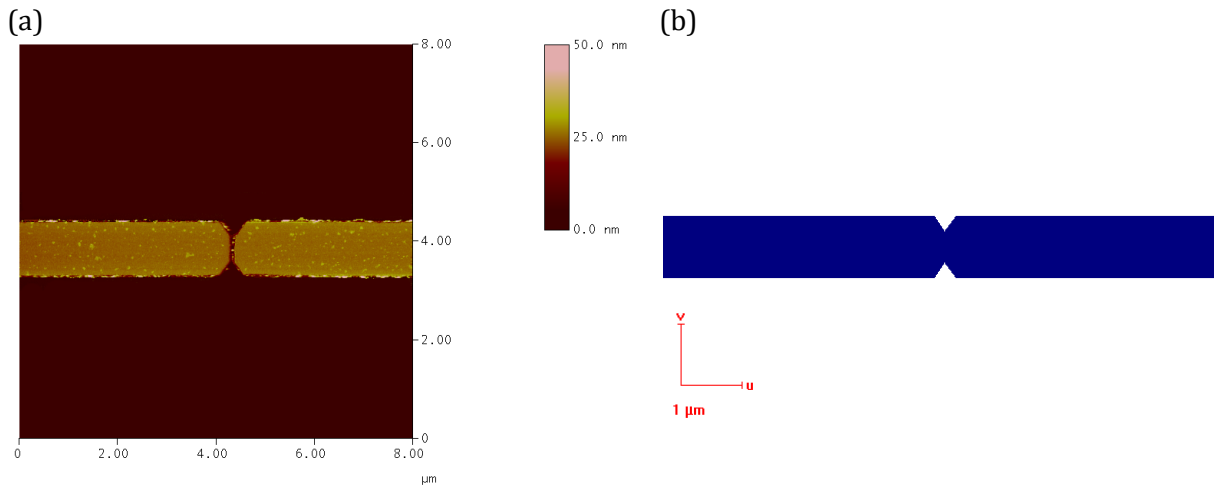


Figure 5.23: (a) AFM micrograph of a defect in a thermally evaporated Ni-Fe nanowire. (b) Schematic diagram of the intended form of the structure.

The second defect encountered is shown in figure 5.24. Figure 5.24a shows the atomic force micrograph of an incomplete ring nanostructure. Figure 5.24b shows a screenshot of the same ring from the design software in its intended form. It is clear that a failure occurred in the fabrication process that has caused this defect. It is unlikely that this is a write-error caused directly by the electron beam lithography process as the ring has a uniform wall width around the entire circumference and was able to write most of the structure. Instead the most likely explanations for the missing segment is that it was either removed during the lift-off procedure (see §3.2.3) or the sample wasn't developed for long enough.

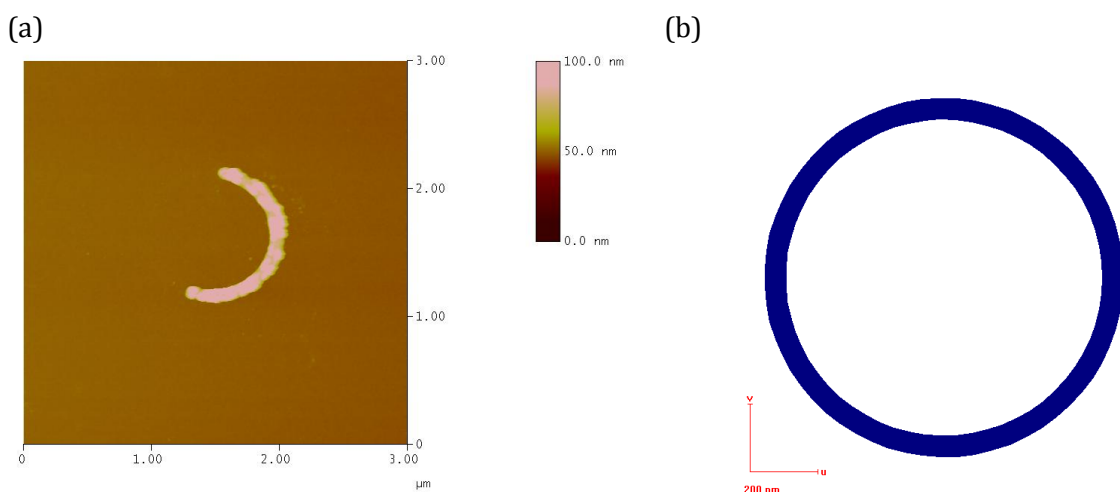


Figure 5.24: (a) AFM micrograph of a defect in a thermally evaporated Ni-Fe ring. (b) Schematic diagram of the intended form of the structure.

Figure 5.25a represents what an idealised cross-section of the sample looks like prior to lift-off with good separation between the evaporated thin film layer that will form structures and the thin film layer that will be sacrificed.

One way that structures can be lost is if the film thickness of the evaporant approaches the thickness of the spin-coated PMMA resist creating a 'bridge' between the evaporated film layers (see figure 5.25b). During lift-off, where the PMMA is being dissolved and the top layer becomes detached, the strength of the metallic bonding in the bridge can be sufficient to remove the structure layer from the substrate [25].

Figure 5.25c realistically depicts undercuts that form in the resist profile when a positive resist is used. This is caused by the 'tear-drop' shape of the electron beam volume during the EBL writing process as electrons scatter through the PMMA [26]. Also depicted within this figure is how the evaporant can get deposited on the side-walls of the resist. This latter phenomenon is less of an issue in line-of-sight deposition techniques such as thermal evaporation but can still occur nonetheless. Side-wall coating is dependent on a few factors such as source-sample distance, vacuum pressure, and undercut angle; whilst undercut angle is dependent primarily on EBL beam acceleration voltage [25]. As with the loss mechanism depicted in figure 5.25b, side-wall coating can also result in loss of material due to a strong metallic bond between the top (sacrificial) and bottom (structures) layers. To avoid side wall formation it was important, therefore, to ensure that the PMMA resist was at an appropriate thickness relative to the desired structure thickness. It was also necessary to consider whether to prioritise high spatial resolution (i.e. high acceleration voltage) or large undercut angle (i.e. low acceleration voltage) when deciding on the acceleration voltage (10 kV in this case).

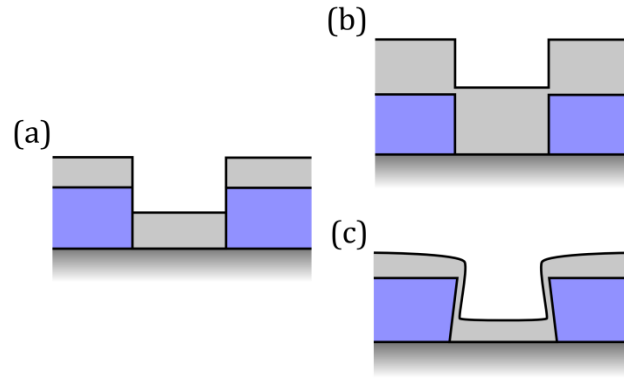


Figure 5.25: Schematic diagrams of various lift-off profiles. Blue represents the PMMA resist, whilst light grey represents the evaporated film. The dark grey bottom layer represents the silicon substrate. (a) An idealised cross-section of the sample prior to lift-off; (b) the case scenario where the resist is too thin; (c) the realistic scenario where an resist undercut forms and also where the evaporant has coated the resist side-walls.

The third defect encountered is shown in figure 5.26. Figure 5.26a shows the atomic force micrograph of a Ni-Fe nanowire leaving a nucleation pad. Figure 5.26b shows a screenshot of the same feature from the design software in its intended form. It can be seen that this structure has almost been separated into two discrete parts leaving two notch defects at the joint. As with the first defect (figure 5.23a) a second object (such as a rectangle with the long axis aligned horizontally) was inserted into the design so that an overlap is created between the two areas ensuring that the RAITH software writes this structure properly.

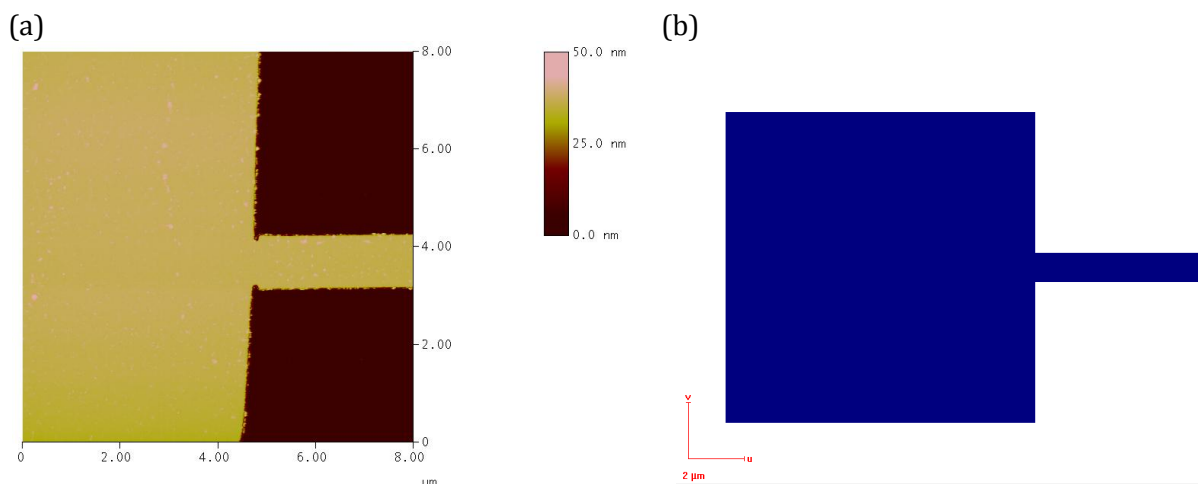


Figure 5.26: (a) AFM micrograph of a defect in a thermally evaporated Ni-Fe nanowires at the boundary with the domain wall nucleation pad. (b) Schematic diagram of the intended form of the structure.

The final defect encountered is shown in figure 5.27. Figure 5.27a shows the atomic force micrograph of the serpentine wire nanostructure. Figure 5.27b shows a screenshot of the same

feature from the design software in its intended form. It can be seen that this structure has almost been separated into two discrete parts leaving two notch defects at the joint. As with the first and third defect (figure 5.23a and 5.26a) a second object (such as a rectangle with the long axis aligned vertically) was inserted into the design so that an overlap was created between the two areas ensuring that the RAITH software writes this structure properly.

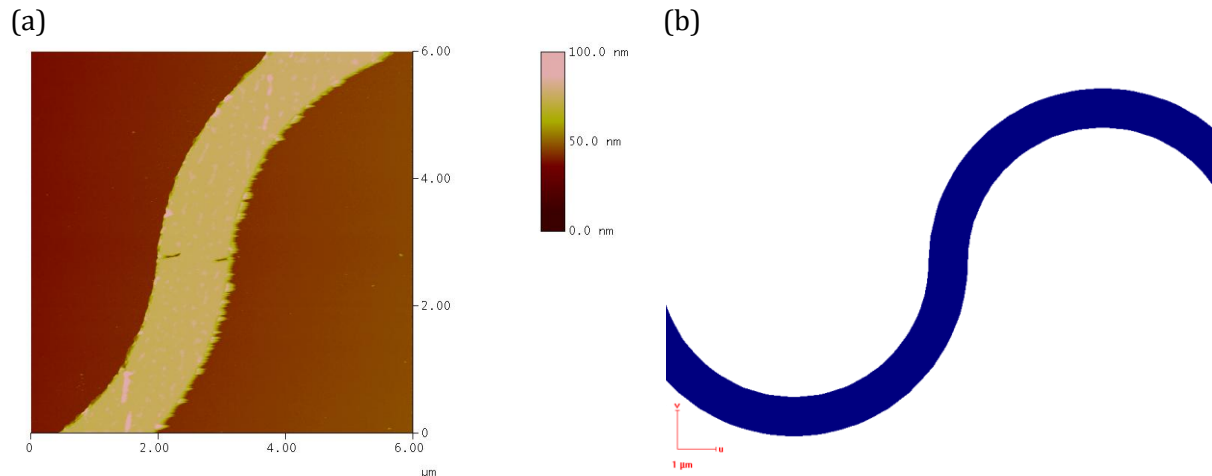


Figure 5.27: (a) AFM micrograph of a defect in a thermally evaporated Ni-Fe serpentine wire. (b) Schematic diagram of the intended form of the structure.

5.5 Conclusion

In this chapter optical absorption and fluorescence spectra of six photoluminescent magnetic field effect-candidate organic semiconducting materials were characterised. This enabled the successful selection of excitation and emission optical components necessary for measuring their photoluminescent magnetic field effect profiles.

The magnetic field effect of the selected materials was successfully measured using a custom system designed and built by the author. The MFE profiles of the six materials were analysed and corrected by subtracting a systematic background from the measurements.

Of the six materials measured only three appeared to exhibit any sizeable photoluminescent magnetic field effect. The largest PL-MFE recorded was over +6% for polycrystalline tetracene. This study allowed for the successful identification of an MFE material suitable for an attempted acquisition of MFE images that will be presented in the following chapter.

A thin film morphological study of several of the fabricated samples was undertaken with the aim to identify successful fabrication techniques and further optimise them. This served to determine which materials offered suitable thin film morphologies for use as MFE interface media for microscopic MFE imaging that will be presented in the following chapter.

Defects from the electron beam lithography fabrication process were presented and analysed with the aim to identify the cause of each defect type and provide suggestions on potential solutions.

5.6 References

- [1] B. Valeur, *Molecular fluorescence: principles and applications*: Wiley-VCH, 2002.
- [2] N. J. Turro, *et al.*, *Modern molecular photochemistry of organic molecules*: University Science Books, 2010.
- [3] T. Tsuboi, *et al.*, "Energy transfer in a thin film of TPD fluorescent molecules doped with PtOEP and Ir(ppy)(3) phosphorescent molecules," *Applied Physics B-Lasers and Optics*, vol. 81, pp. 93-99, Jul 2005.
- [4] M. A. Fourati, *et al.*, "Photophysical, Electrochemical and Crystallographic Investigations of the Fluorophore 2,5-Bis(5-tert-butyl-benzoxazol-2-yl)thiophene," *Journal of Physical Chemistry B*, vol. 115, pp. 12362-12369, Nov 2011.
- [5] B. Hu, *et al.*, "Magnetic-Field Effects in Organic Semiconducting Materials and Devices," *Advanced Materials*, vol. 21, pp. 1500-1516, Apr 2009.
- [6] I. B. Berlman, *Handbook of fluorescence spectra of aromatic molecules*: Academic Press, 1965.
- [7] Y. Guo, *et al.*, "Tris (8-Hydroxyquinoline) Aluminium Nanostructure Film and Its Fluorescence Properties," *Chinese Physics Letters*, vol. 25, pp. 4428-4430, Dec 2008.
- [8] H. Z. Lin, *et al.*, "Fate of Excitations in Conjugated Polymers: Single-Molecule Spectroscopy Reveals Nonemissive "Dark" Regions in MEH-PPV Individual Chains," *Nano Letters*, vol. 9, pp. 4456-4461, Dec 2009.
- [9] J. R. Lakowicz, *Principles of Fluorescence Spectroscopy*: Springer, 2007.
- [10] H. Bouas-Laurent and H. Durr, "Organic photochromism," *Pure and Applied Chemistry*, vol. 73, pp. 639-665, Apr 2001.

- [11] J. Malkin, *et al.*, "Photochromism and Kinetics of Naphthacenequinones," *Journal of the American Chemical Society*, vol. 116, pp. 1101-1105, Feb 1994.
- [12] R. C. Johnson and R. E. Merrifield, "Effects of magnetic fields on the mutual annihilation of triplet excitons in anthracene crystals," *Physical Review B*, vol. 1, pp. 896-902, 1970.
- [13] G. Klein, *et al.*, "Magnetic-field effect on prompt fluorescence in anthracene - evidence for singlet exciton fission," *Chemical Physics Letters*, vol. 16, pp. 340-&, 1972.
- [14] K. V. Burg and I. Zschokkegranacher, "Singlet exciton fission in pure and doped anthracene," *Journal of Chemical Physics*, vol. 70, pp. 3807-3811, 1979.
- [15] R. P. Groff, *et al.*, "Coexistence of Exciton Fission and Fusion in Tetracene Crystals," *Physical Review B*, vol. 1, pp. 815-817, 1970.
- [16] R. E. Merrifield, "Magnetic effects on triplet exciton interactions," *Pure Appl. Chem.*, vol. 27, pp. 481-498, 1971.
- [17] C. E. Swenberg and W. T. Stacy, "Bimolecular radiationless transitions in crystalline tetracene," *Chemical Physics Letters*, vol. 2, pp. 327-328, 1968.
- [18] E. J. Bowen, *et al.*, "Resonance Transfer of Electronic Energy in Organic Crystals," *Proceedings of the Physical Society of London Section A*, vol. 62, pp. 26-31, 1949.
- [19] T. P. I. Saragi and T. Reichert, "Magnetic-field effects in illuminated tetracene field-effect transistors," *Applied Physics Letters*, vol. 100, Feb 2012.
- [20] Royal Society of Chemistry. (04/10/2013). *ChemSpider - Anthracene*. Available: <http://www.chemspider.com/Chemical-Structure.8111.html>
- [21] W. E. Acree, *Thermodynamic properties of nonelectrolyte solutions*: Academic Press, 1984.
- [22] W. D. Callister and D. G. Rethwisch, *Materials Science and Engineering: An Introduction, 8th Edition*, 2009.
- [23] H. Shanks, *et al.*, "Thermal conductivity of silicon from 300 to 1400 K," *Physical Review*, vol. 130, p. 1743, 1963.
- [24] H. Fangohr, *et al.*, "Joule heating in nanowires," *Physical Review B*, vol. 84, Aug 2011.
- [25] M. J. Madou, *Fundamentals of Microfabrication: The Science of Miniaturization*: CRC Press, 2002.
- [26] M. T. Bryan, "Nucleation and propagation of domain walls in permalloy nanostructures," University of Sheffield, 2008.

6 Magnetic Image Contrast Detection

6.1 Introduction

In this chapter micromagnetic configurations and dynamics of patterned Permalloy nanostructures that have been characterised using M-TXM, MFM and MOKE will be discussed. From this study it is hoped that predictable micromagnetic configurations can be observed and reproduced when coupling these structures to a PL-MFE organic semiconducting thin film for observation via confocal microscopy.

Later, micromagnetic simulations will be presented in an effort to visually simulate what a potential PL-MFE image may look like and what level of image contrast enhancement may be required in order to make successful experimental observations.

In the third section of this chapter, confocal microscopy results will be presented of attempts to image microscopic magnetic contrast from an MFE thin film deposited on top of Permalloy nanostructures.

In the penultimate section of this chapter, results will be presented of attempts to image macroscopic magnetic contrast from an MFE thin film covering bulk sources of magnetic field.

Finally, results will be presented of experimental attempts to optically detect magnetic polarity from PL-MFE emissions.

6.2 Magnetic Characterisation Using Established Techniques

In this section experimental results from three established magnetic characterisation techniques will be presented. The first two techniques, magnetic transmission X-ray microscopy (M-TXM) and magnetic force microscopy (MFM), are described in §3.9 and §3.8, respectively. These techniques provide direct (M-TXM) and indirect (MFM) spatial imaging of the magnetisation configuration of micromagnetic structures. The third technique, magneto-optic Kerr effect (MOKE) magnetometry (described in §3.11), provides information about the magnetisation switching dynamics of micromagnetic structures. As well as providing

information on the behaviour of the magnetic microstructures and their suitability for providing predictable microscopic magnetic stray field for fluorescent MFE imaging, the capabilities of each technique will be assessed to establish how a new magnetic characterisation may compete.

6.2.1 Magnetic Transmission X-Ray Microscopy

The M-TXM sample used was comprised of permalloy nanostructures deposited onto a silicon nitride membrane via electron beam lithography and thermal evaporation (the details of this fabrication procedure are described in §3.2.3). The thin membrane was required to permit transmission of the X-ray radiation used in the M-TXM technique. The sample was analysed using the M-TXM technique on beamline 6.1.2 at the Advanced Light Source, Berkeley, California. The magnetic micrographs presented in this section have been produced by dividing one image of each microstructure taken with a saturating magnetic field applied in the +x direction, from another image taken with no magnetic field applied (i.e. at remanence). Therefore dark contrast in figures 6.1-4 represents magnetisation in the +x direction, whilst light contrast represents magnetisation in the -x direction.

Figure 6.1a shows the 'A1' circular structure from the ellipse array measuring 5 μm in diameter and 30 nm in thickness (where 'A1' is the array designation – see figure 3.3 for more details). It can be seen that the top half of the structure contains predominantly dark contrast whilst the lower half contains light contrast. At the centre of the structure a small bright dot can be seen. This contrast pattern suggests that the structure has formed an in-plane vortex state (illustrated in figure 6.1b). This state was first observed in permalloy in 2000 by Shinjo et al. [1]. It is so-called because the magnetic moments of the Ni-Fe structure are circulating clockwise around the central region minimising dipolar energy whilst slightly increasing exchange energy [1]. This configuration is most stable in very small ferromagnetic structures; structures exceeding a certain size will almost always form magnetic domains. The magnetic moments located at the central region of the structure shown in figure 6.1a actually point out-of-plane. This magnetic configuration has actually been suggested as one possible solution for magnetic random access

memory (MRAM) where the magnetic vortex chirality, clockwise or anticlockwise, represents binary number one or zero [2].

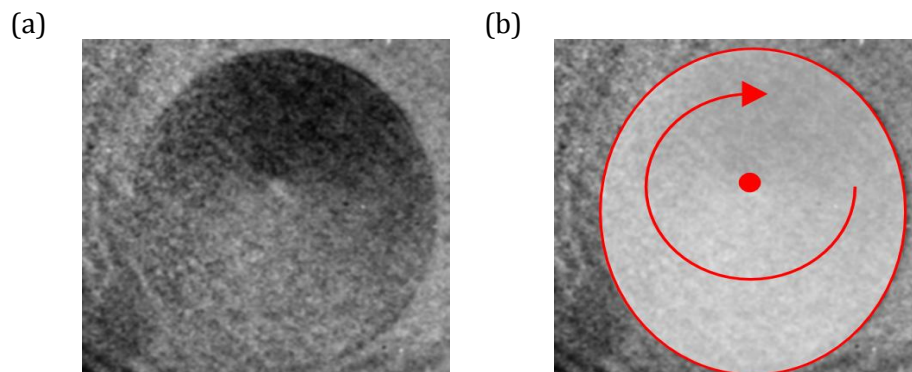


Figure 6.1: (a) M-TXM micrograph of 'A1' ellipse. The magnetic contrast was enhanced by dividing two micrographs: one with an applied saturating magnetic field in the $+x$ direction and another with the field removed. Visible near the centre of the ellipse is a vortex core. (b) Diagram illustrating the magnetisation configuration; in this case, a single clockwise vortex domain.

Figure 6.2a shows the 'B2' circular structure from the ellipse array measuring $3.75\ \mu\text{m}$ in diameter and $30\ \text{nm}$ in thickness. It can be seen that this structure exhibits three distinct magnetic domains with near uniform contrast within each domain. On closer inspection, however, the darker area appears to be separated into three discrete domains. This contrast pattern suggests that two vortex cores of opposite chirality have established themselves on opposite sides of the structure (illustrated in figure 6.2b). If the vortex cores had contacted one another during the relaxation period (after the saturating magnetic field was turned off and before the structure's magnetic moments re-aligned to reach energy minimum) they would have mutually annihilated most likely resulting in a new single vortex forming at the centre of the structure just like in figure 6.1. The mostly likely reasons the cores did not collide with one another is that either one or both of the vortices became directly pinned on a defect in the material or one of the domain walls that extends to the physical edge of the structure became pinned in place by a defect such as a rough edge. These pinning sites would have placed restrictions on the core movement effectively locking it in position and preventing annihilation [3].

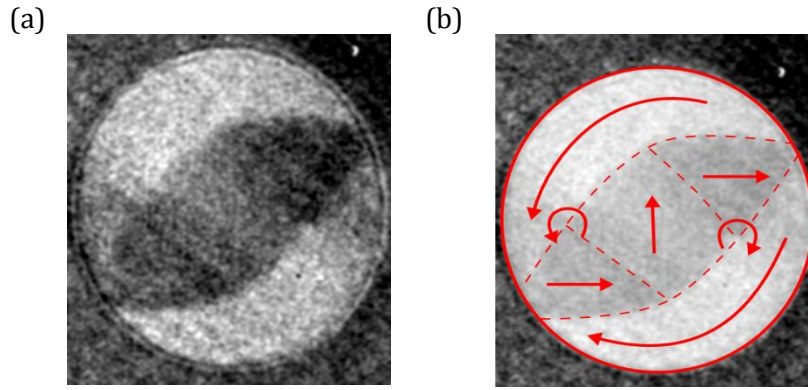


Figure 6.2: (a) M-TXM micrograph of 'B2' ellipse. The magnetic contrast was enhanced by dividing two micrographs: one with an applied saturating magnetic field in the $+x$ direction and another with the field removed. Three magnetic domains appear to exist in this structure. (b) The illustrative diagram reveals that two vortex cores of opposing chirality have created the observed magnetic domains.

Figure 6.3a shows the 'E2' elliptical structure from the ellipse array measuring $1.58 \mu\text{m}$ in the conjugate diameter, $3.75 \mu\text{m}$ in the transverse diameter and 30 nm in thickness. It can be seen that this structure adopts a contrast pattern similar to that seen in figure 6.2a. It can therefore be assumed that the structure has also formed two vortices of opposing chirality but has aligned them centrally along the long axis of the structure. This domain configuration is probably one of the lowest energy states available as suggested by the high degree of symmetry presented. This could be tested with micromagnetic modelling of the structure.

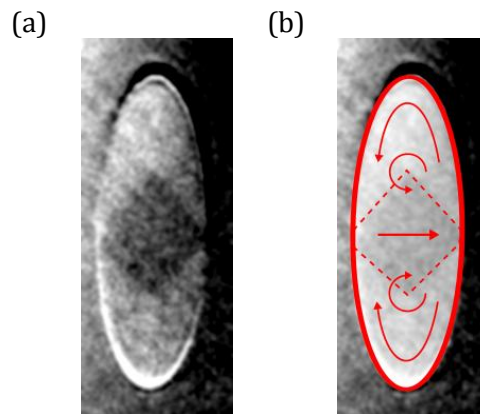


Figure 6.3: (a) M-TXM micrograph of 'E2' ellipse. The magnetic contrast was enhanced by dividing two micrographs: one with an applied saturating magnetic field in the $+x$ direction and another with the field removed. Three domains appear to exist in this structure. (b) The illustrative diagram reveals that two vortex cores of opposing chirality have created the observed magnetic domains.

Figure 6.4a shows the ‘C3’ ring structure with an outer diameter measuring $4\ \mu\text{m}$, wire width of $375\ \text{nm}$ and a thickness of $30\ \text{nm}$. It can be seen that the only contrast visible appears at two positions located at opposite sides of the ring. As the structure was saturated in the $+x$ direction and then allowed to relax, it can be assumed that the majority of the ring magnetisation is also aligned in the $+x$ direction but has relaxed to follow the geometry of the structure (since permalloy has a negligible magnetocrystalline anisotropy). It is at these points of contrast, then, where the two opposing poles meet with a ‘tail-to-tail’ domain wall on the left and a ‘head-to-head’ domain wall on the right. However, if one looks more closely it can be seen that each area of contrast is actually composed of bright and dark contrast sub-areas. This contrast pattern, therefore, suggests that vortices of identical chirality exist at these positions on the ring. Vortices are concluded because there exists bright and dark contrast at each position, whereas an alternative boundary, such as a transverse domain wall, would only exhibit one form of contrast (see figure 6.5). It can be concluded that the vortices have identical chirality because the bright contrast is consistently above the dark contrast at both positions. This state is referred to as the ‘onion state’ and is usually applied to magnetic configurations that produce transverse domain walls instead of vortices. Transverse walls are most likely to appear in rings with thinner and narrower wire widths [4].

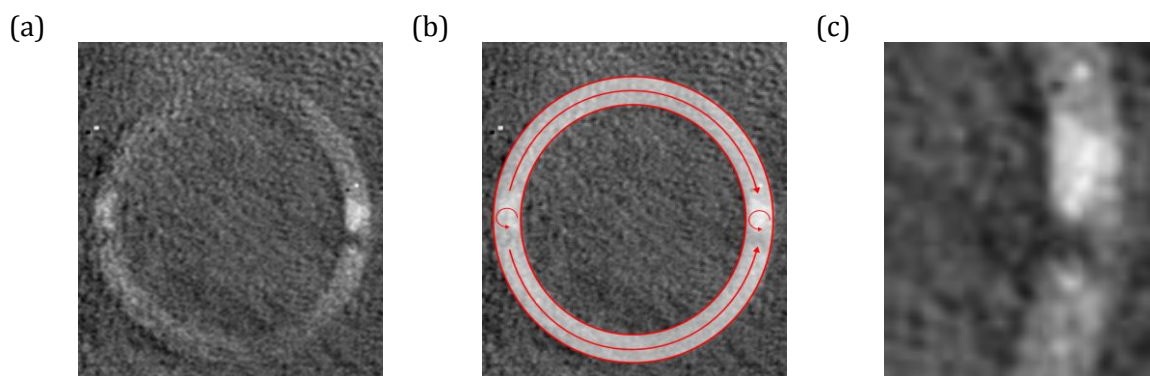


Figure 6.4: (a) M-TXM micrograph of ‘C3’ ring. The magnetic contrast was enhanced by dividing two micrographs: one with an applied saturating magnetic field in the $+x$ direction and another with the field removed. Two regions of magnetic contrast appear on opposite sides of the ring. (b) The illustrative diagram reveals that two vortex walls of identical chirality are responsible for the contrast pattern observed. (c) Magnified view of the right-hand-side vortex wall.

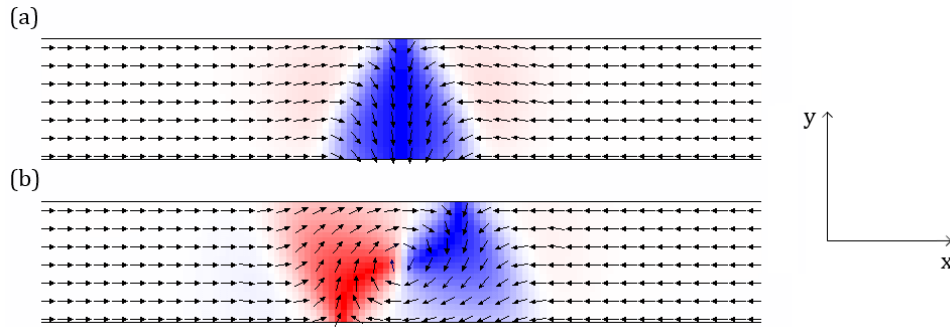


Figure 6.5: Micromagnetic simulation of a permalloy nanowire with contrast depicting the magnetisation orientation with respect to the y-axis. (a) Shows a head-to-head transverse domain wall with one triangular region of contrast whilst (b) shows a head-to-head clockwise vortex wall with two triangular regions of opposing contrast.

The magnetic micrographs presented here are the best examples of the images taken on the M-TXM instrument. Many of the other images captured did not have the contrast necessary for presentation even when dividing one image from another in order to amplify the magnetic contrast. Non-magnetic contrast gradients existing over the whole image were one of the main contributing factors preventing attainment of optimal magnetic contrast. This was caused by X-ray beam drift during the time period between the capture of the two division images. Combining that issue with the inherently weak contrast obtained from X-MCD of *in-plane* magnetised permalloy structures results in many images with indeterminable magnetic domain configurations. Although at times beam drift can be a nuisance, periods of stability do often occur and it is during these times that high spatial resolution division images can be generated (≈ 25 nm). The technique also excels in its ability to unambiguously determine magnetic domain orientation.

6.2.2 Magnetic Force Microscopy

Magnetic force microscopy (as described in §3.8) was used to characterise the magnetic permalloy microstructures patterned onto the sample described in §3.2.3. A custom-built magnetising stage was used in an attempt to apply saturating magnetic fields to the structures in-situ.

Figure 6.6 contains a set of three images of the 'A1' echelon structure. A1 consists of three connected 'arms' each measuring 2 μm in length and 1 μm in width. The structure was designed to invoke magnetic frustration as exemplified by recent efforts to generate magnetic charge defects using artificial Kagome lattice spin-ice structures [5]. In these particular geometrical structures magnetism, being an inherently dipolar phenomenon, will not be able to form a completely flux-closed state leading to the formation of a 'frustrated' magnetic domain configuration and generation of magnetic stray field. The echelon structure itself was not subject to any external magnetic fields prior to, or during, image capture. Figure 6.6a is an atomic force micrograph of the structure revealing that it has not suffered from any fabrication problems and is relatively free of particulate debris enabling the acquisition of high quality AFM/MFM scans. Figure 6.6b is the accompanying magnetic force micrograph captured in interleave mode (i.e. a topographical line scan was acquired followed by a magnetic lift-mode line scan, repeating until the image capture had completed). It can be seen that the structure has undergone energy minimisation as demonstrated by the development of magnetic domains. The top left and bottom left 'arms' of the echelon contain end domains of opposite polarity. The central right arm contains three domains with two involved in forming a 180° domain wall whilst the third domain is acting as a 'flux-closure' domain as illustrated in figure 6.6c. By minimising the arm width of the echelon it may be possible to force the magnetisation to form single magnetic domains in each arm.

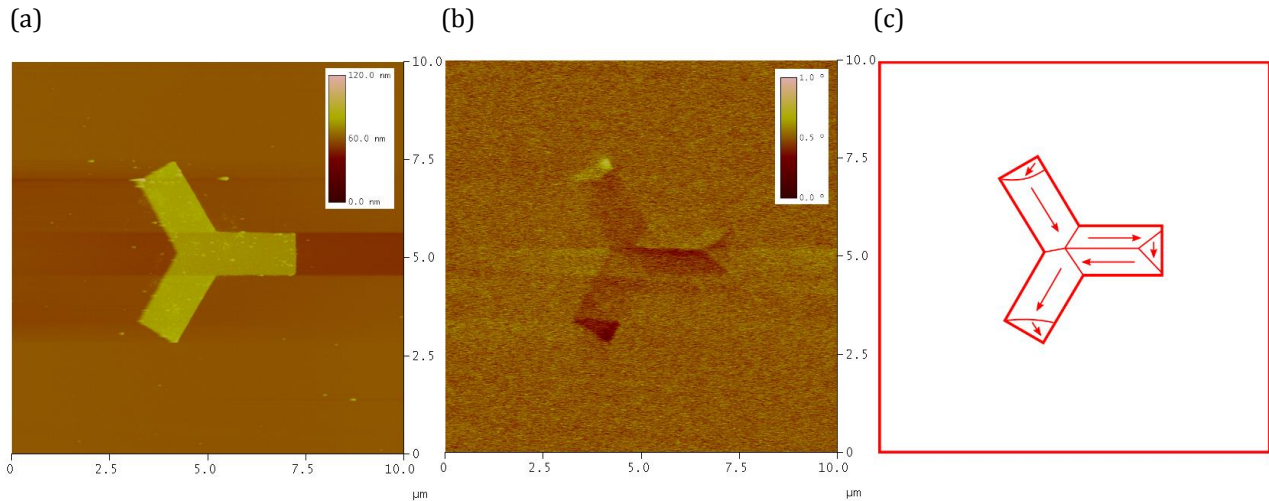


Figure 6.6: (a) Atomic force micrograph of 'A1' echelon (b) Magnetic force micrograph of 'A1' echelon revealing magnetic domain contrast; (c) illustration of magnetic domain configuration.

Figure 6.7 contains a set of three images of the 'E1' echelon. E1 consists of three connected 'arms' each measuring $2\ \mu\text{m}$ in length and $0.5\ \mu\text{m}$ in width (half the width of echelon 'A1'). Figure 6.7a shows the topographical scan of the structure, however, the scan itself is of low quality with the tip not following the topography accurately resulting in 'streaks' in the image. Despite this figure 6.7b, the magnetic image, reveals fascinating contrast with each arm hosting a region of strong contrast at its end. Two of the arms feature dark contrast whilst the lower right arm features a region of bright contrast. At the centre of the structure a region of bright contrast is present. Figure 6.7c contains the results of a micromagnetic simulation using a micromagnetic solver package known as OOMMF (Object Oriented MicroMagnetic Framework) [6]. OOMMF is similar to FEMME (described in §3.12) except it uses a *finite difference* mesh to discretise the object whereas FEMME utilises a *finite element* mesh to discretise the object. Other differences exist but shall not be discussed here. The false colour used in the simulated image plots the divergence of the magnetisation vector field. This contrast mode approximates MFM contrast closely and is used in many research papers featuring comparisons of MFM micrographs and micromagnetic simulations [7, 8]. It can be seen that the micromagnetic simulation accurately matches the contrast observed in figure 6.7b. Therefore there is confidence to suggest that the magnetic domain configuration is most likely as illustrated in figure 6.7d. Qualitatively, this structure has been unable to form any flux-closure domains

compared to the A1 echelon, which was able to form a 180° domain wall. The lack of flux-closure domains in the E1 echelon is due to the arm width being smaller than in the A1 echelon suggesting that the presence of a domain wall positioned centrally along the length of the echelon arm is energetically unfavourable. The penalty of not being able to form the 180° domain wall means that the magnetostatic energy of the E1 echelon structure is much higher than in the A1 echelon structure. This suggests that a large demagnetising field would be generated in the E1 echelon compared to the A1 echelon.

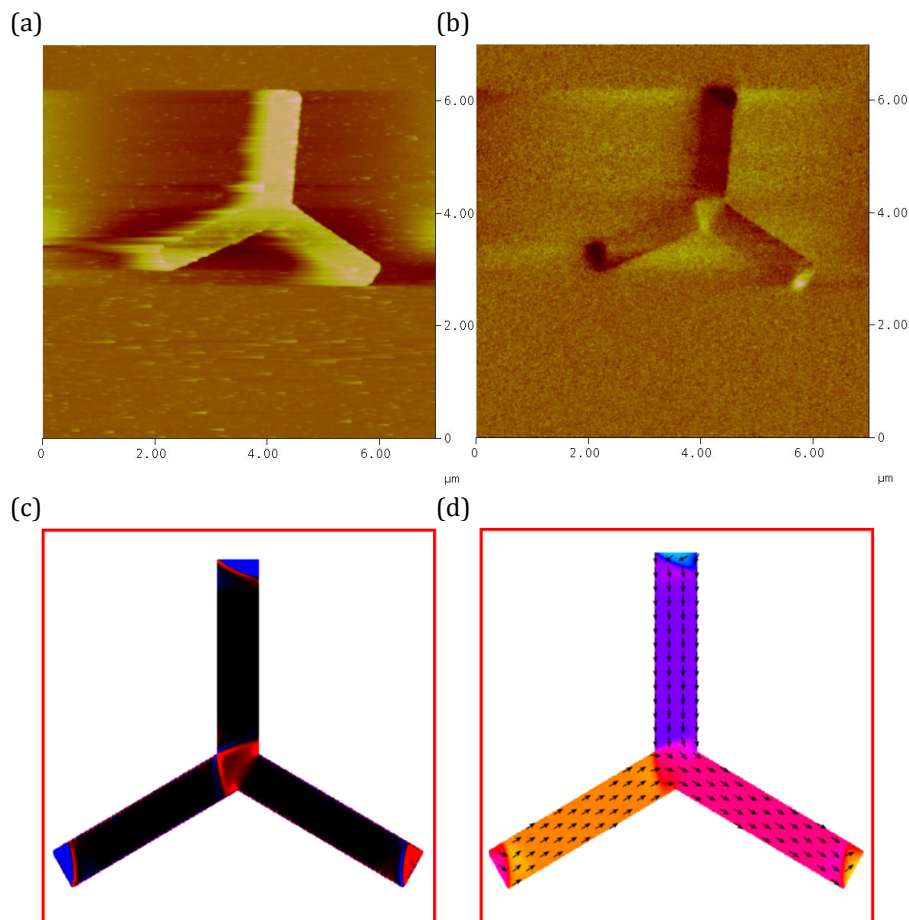


Figure 6.7: (a) Atomic force micrograph of 'E1' echelon (b) Magnetic force micrograph of 'E1' echelon revealing magnetic domain contrast; (c) OOMMF simulation result of the echelon structure with a magnetisation divergence contrast applied; (d) OOMMF simulation result of the echelon structure with a vector colour map applied.

Figure 6.8 contains a set of three images of the serpentine wires. The wires consist of end-to-end connected semi-circular arcs of $8\ \mu\text{m}$ diameter each rotated 180° from the previous arc. The wire width is $1\ \mu\text{m}$. For this set of images the magnetising stage was used to apply a magnetic field in the $+y$ direction. This field was removed before image capture commenced. Figure 6.8a

shows the topographical scan of the structures revealing some debris deposited inside some of the arcs. This is most likely PMMA that wasn't removed during the lift-off procedure and instead became trapped in the corners of the permalloy serpentine structures. It is not expected that the presence of this material would interfere with the magnetisation dynamics or the MFM imaging. Figure 6.8b shows the magnetic image corresponding to figure 6.8a. At the apices of the structures there appears to be magnetic contrast with bright contrast on the top-side of the wires and dark contrast on the bottom-side of the structures. Knowing that MFM contrast is equivalent to stray field divergence then the dark contrast represents a magnetic field source (positive divergence) and bright contrast represents a magnetic field sink (negative divergence). This means that the magnetic contrast observed represents head-to-head and tail-to-tail vortex walls as illustrated in figure 6.8c. It is also confirmed that the presence of PMMA has not interfered with the predicted behaviour of the structure and is not visible in the MFM scan (figure 6.8b).

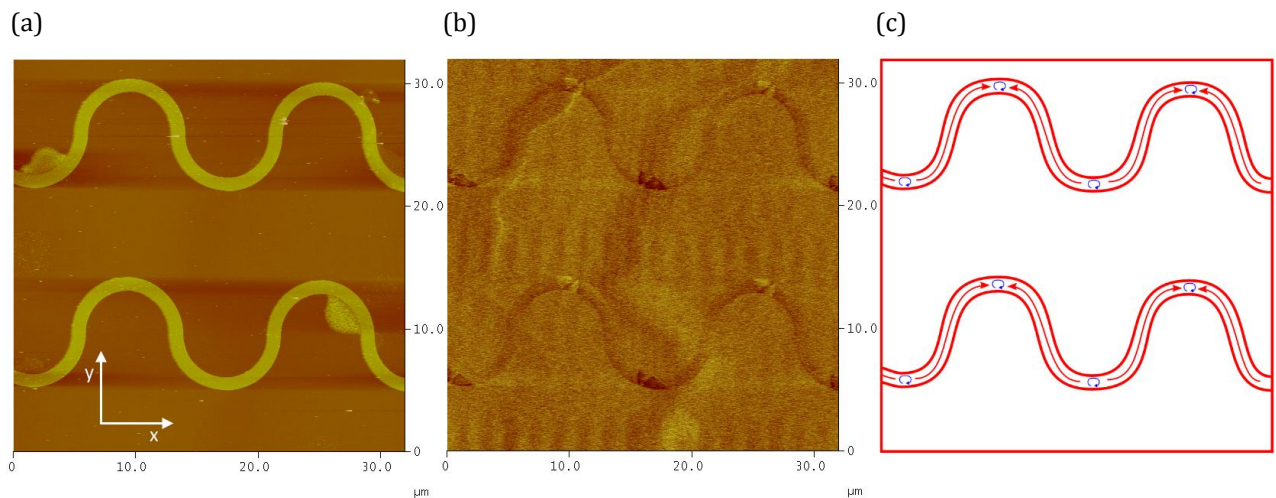


Figure 6.8: (a) Atomic force micrograph of the 'serpentine wire' structures having been saturated in $+y$ direction and allowed to relax. (b) Magnetic force micrograph of serpentine wires revealing magnetic domain contrast at the apices; (c) illustration of the magnetic domain configuration.

Figure 6.9 contains a set of three images of the serpentine wires. This time, prior to imaging the structures the magnetising stage was used to apply a magnetic field in the $+x$ direction. This field was removed before image capture commenced. Figure 6.9a shows the topographical scan of the structures revealing that scan has been translated approximately 20 μm in the $+x$

direction. Figure 6.8b shows the magnetic image corresponding to figure 6.9a. This time, it can be seen that there is little, if any, magnetic contrast present. This suggests that the magnetic field applied prior to image capture has forced the magnetisation to relax with the magnetic domains following the undulations of the wires, as illustrated in figure 6.9c. This demonstrates that it is possible to precisely control the formation of magnetic domain walls in such structures and allows one to predict where domain walls will exist. Crucially, it offers a controlled method of taking difference images where the magnetic contrast is predictably changing; a perfect test structure for the proposed magnetic field effect fluorescence microscopy technique.

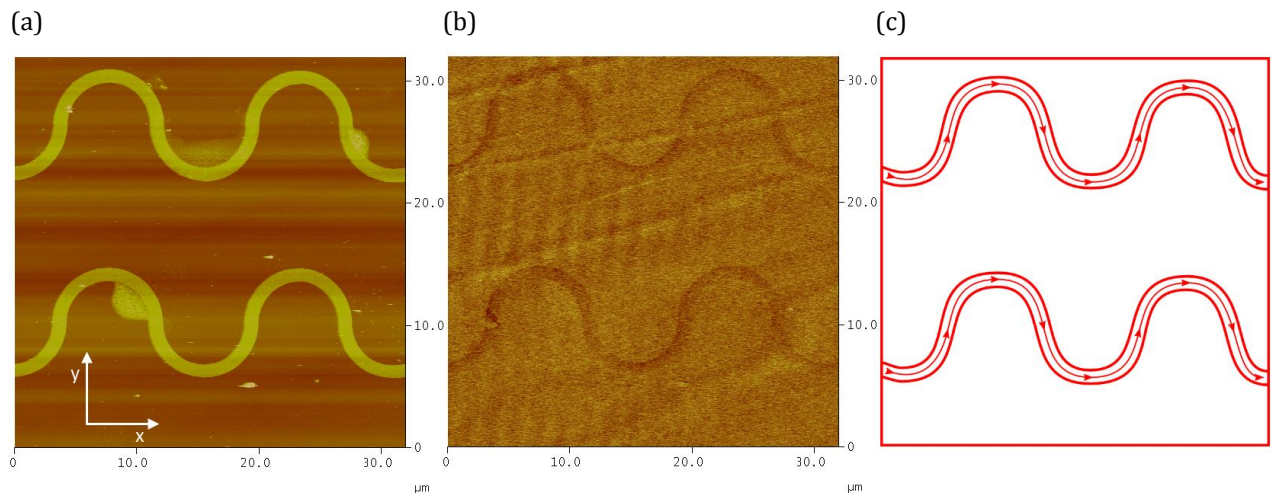


Figure 6.9: (a) Atomic force micrograph of the 'serpentine wire' structures having been saturated in the $+x$ direction and allowed to relax. (b) Magnetic force micrograph of serpentine wires revealing essentially no magnetic domain contrast; (c) illustration of magnetic domain configuration.

Figure 6.10 contains two magnetic force micrographs taken at the surface of a polished sintered NdFeB permanent magnet. The images reveal complex domain structure on the surface of the magnet. This surface structure is most likely attributed to domain branching in the bulk of the material and perpendicular to the surface. Domain branching is often observed in highly anisotropic perpendicular magnetic materials in order to minimise energy [9]. Although the magnetic stray field from this sample is much larger compared to Ni-Fe it suffers from rather complex, irregular, domain structure therefore reducing its suitability as an MFE substrate candidate.

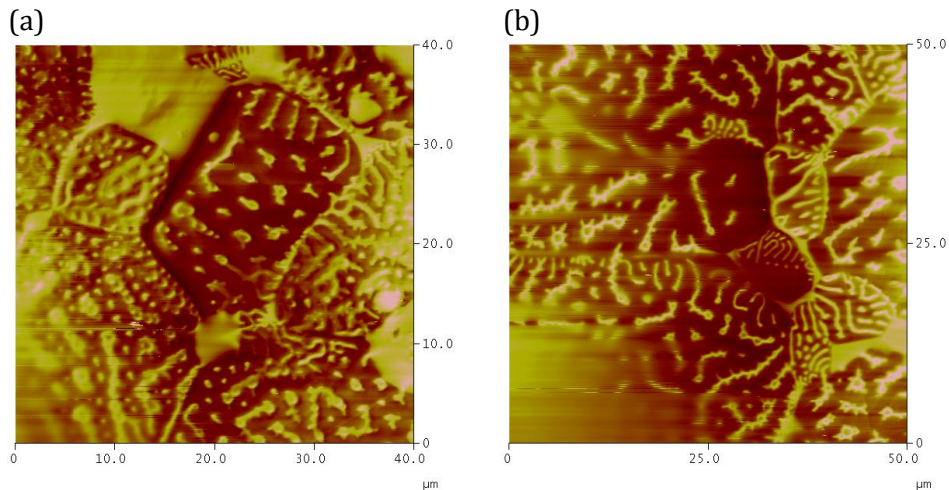


Figure 6.10: Magnetic force micrographs of a polished sintered NdFeB permanent magnet.

(a) $40 \times 40 \mu\text{m}$ scan size (b) $50 \times 50 \mu\text{m}$ scan size.

6.2.3 Magneto-Optic Kerr Effect Magnetometry

In this section focussed magneto-optic Kerr effect magnetometry was used to measure the magnetic switching behaviour of several of the permalloy ring structures patterned onto the microstructures sample described in §3.2.3. The measurement system used is described in §3.11. Of particular interest was being able to determine the magnetic field required to reproducibly generate head-to-head domain walls in the rings (a magnetisation configuration known as the onion state) as well as being able to determine which rings are most suited at performing this function. Figure 6.11 contains a grid of MOKE hysteresis loops captured for three different ring geometries. The second column in figure 6.11 contains hysteresis loops that each represent an average of approximately 810 individual hysteresis loops ($27 \text{ Hz} \times 30 \text{ seconds}$). The third and fourth columns show example ‘single-shot’ measurements of one hysteresis loop, offering the opportunity to witness any stochasticity in the switching behaviour.

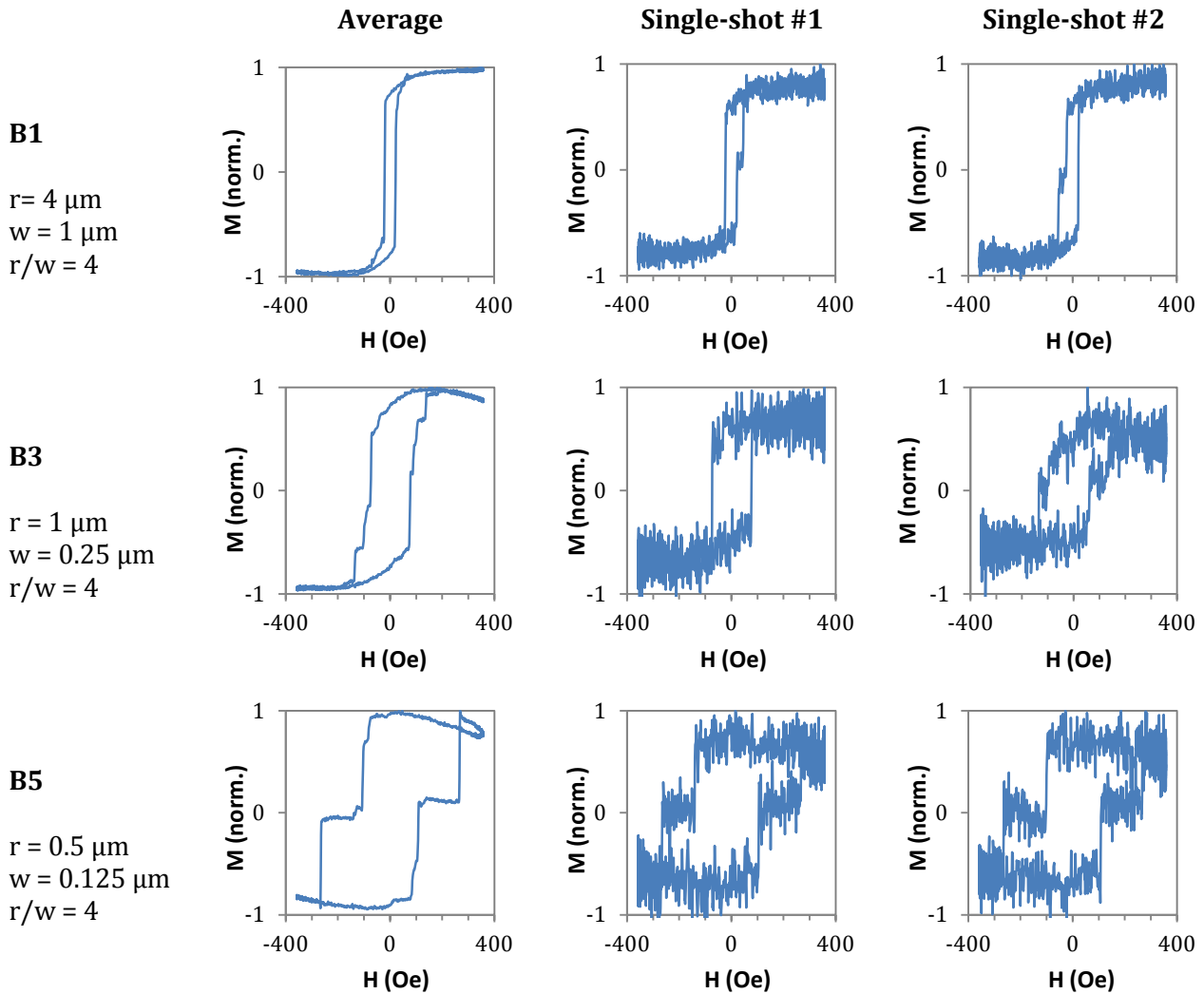


Figure 6.11: MOKE magnetometry results showing hysteresis loops of the switching behaviour of a selection of Ni-Fe ring structures. The first column identifies the ring designation and geometrical parameters where r = radius and w = ring wire width; the second column contains averages of 810 hysteresis loops whilst the third and fourth columns represent 'single-shot' measurements containing exactly one hysteresis loop.

Abscissa is applied magnetic field (Oe) and ordinate is normalised magnetisation.

From figure 6.11 it can be seen that the loops from the 'B1' ring (radius: $4 \mu\text{m}$, wire width: $1 \mu\text{m}$) displays evidence of two switching events occurring in the single-shot measurements at magnetic field magnitudes of 24 and 46 Oe, respectively. However, it does not occur frequently enough to be reflected in the average measurement. This 'double-switching' is best explained by an onion-to-vortex transition (illustrated in figure 6.12). This is a reversal mechanism in which the magnetisation transitions from an onion-state, a two-domain state with a pair of head-to-head domain walls forming along the field direction axis, to a vortex state, where the magnetisation circulates continuously around the entire ring with no domain walls present.

When the MOKE laser spot is centred on and covers the entire ring the vortex state is detected as having net zero magnetisation. This is why on a MOKE hysteresis loop the transition representing the formation of the vortex state occurs at zero magnetisation.

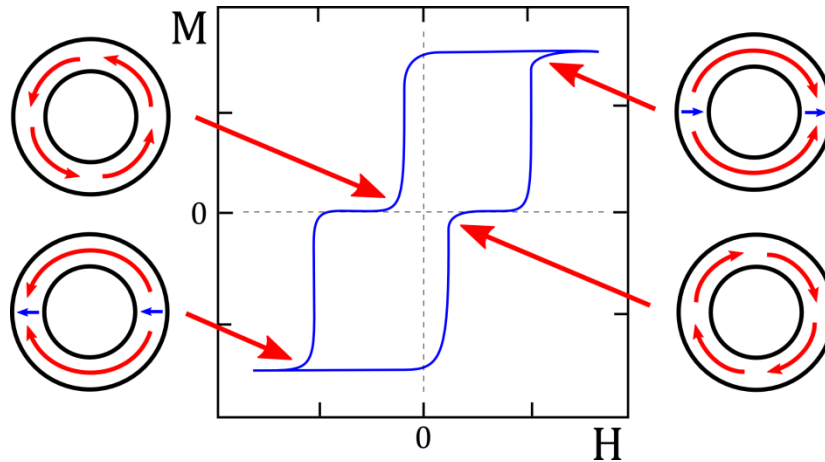


Figure 6.12: Schematic diagram of a MOKE hysteresis loop obtained from a ring exhibiting double-switching.

The 'B3' ring (radius: 1 μm , wire width: 0.25 μm) shows further evidence of the double-switching mode in the second single-shot measurement with switching values of 66 and 130 Oe, respectively. The first single-shot measurement, meanwhile, clearly demonstrates single-switching. The vortex formation transitions can just about be made out in the average loop for 'B3', but they exist at approximately ± 0.8 normalised magnetisation, reflecting their relative infrequency.

The 'B5' ring (radius: 0.5 μm , wire width: 0.125 μm), however, provides the best evidence that onion-to-vortex switching is occurring in these structures as both single-shot measurements clearly demonstrate the two transitions at an applied magnetic field of 110 and 263 Oe, respectively. Moreover, the average measurement has the transitions positioned very near zero magnetisation suggesting the switching mode dominates the reversal process for this ring size.

Figure 6.13 contains a single-shot MOKE hysteresis loop of the 'C3' ring that was also imaged using M-TXM (see figure 6.4). The ring has an outer radius of 2 μm and a ring wire width of 375 nm ($r/w = 5.33$). Just like 'B5' ring, this ring also consistently transitions through the vortex

state during magnetisation reversal as indicated by the existence of double-switching events at applied magnetic fields of 52 and 180 Oe.

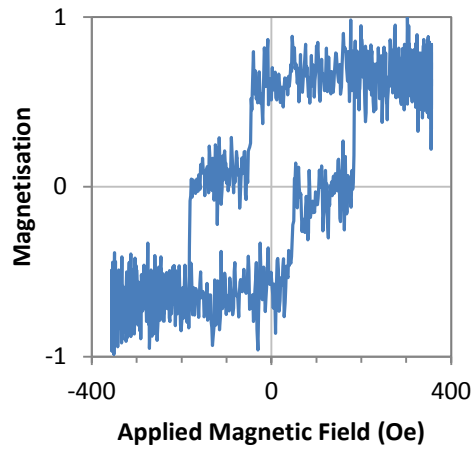


Figure 6.13: Single-shot MOKE hysteresis loop obtained from 'C3' ring. See figure 6.4 for M-TXM image of this ring at remanence.

Figure 6.14 contains a plot of the measured switching fields against the ring radius. Power law fit functions have been applied to the data, although more data would be needed to assess how well these functions model the observed trend. Generally, though, it can be seen that as the ring is reduced in size the switching field increases. Similar behaviour has been observed in the switching dynamics of Co and Ni-Fe nanoscale elements by Kirk, et al. [10].

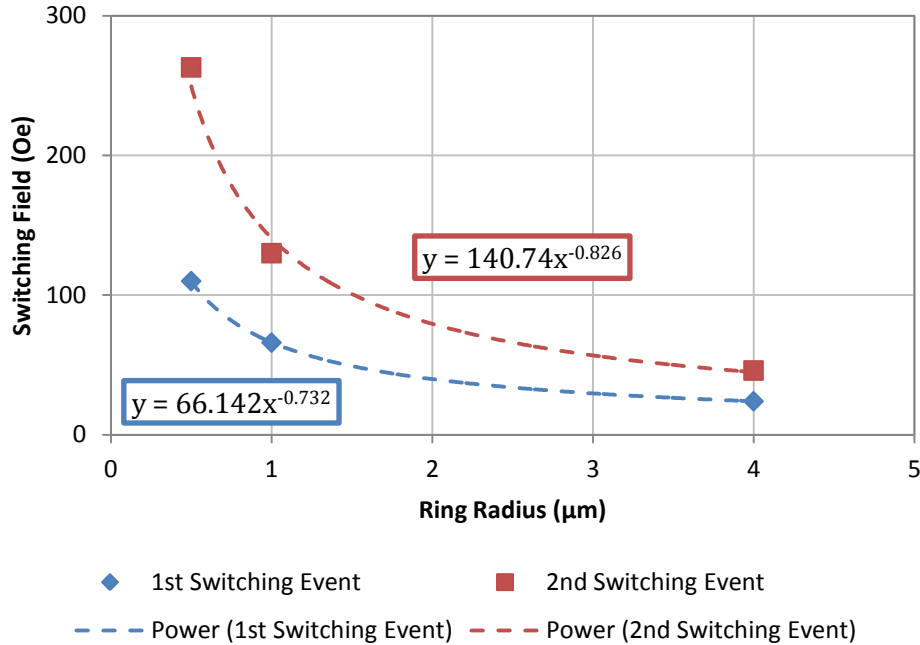


Figure 6.14: Plot of switching fields for the 'r/w = 4' ratio Permalloy rings.

It is also observed that as the rings are reduced in size the stability of the vortex-state increases and forms more readily during magnetisation reversal as evidenced by the increased frequency of the zero magnetisation transitions. The increasing stability of this single domain state with reduction in size is analogous to how small magnetic structures favour single magnetic domain configurations due to the competition between exchange energy, demagnetising energy and the energy 'cost' associated with the formation of a domain wall [9]. The switching behaviour of these structures has been successfully described by the Stoner-Wohlfarth model [11].

6.3 Simulation of Magnetic Luminescence Micrographs

This section presents calculations which are based on micromagnetic models developed to determine the likely appearance of fluorescent micrographs of organic MFE materials coated onto magnetic structures and thin films. By simulating both a micromagnetic object and the stray magnetic field in a volume above the surface of the object it will be shown that the MFE experimental data presented in §5.3 can be mapped onto the magnetic stray field magnitudes. By taking xy-plane sections spaced 10 nm apart up to a height of 50 nm above the object's surface different MFE material film thicknesses can be simulated.

The micromagnetic models were executed using the FEMME code (§3.12) and interpreted with scripts in MATLAB R2011b. The first script was used specifically to read the contents of the magnetic stray field ‘fieldbox’ file and store each xy-plane of interest into separate matrices. These matrices were then read by the second script, which mapped the MFE magnitudes to the magnetic stray field magnitudes, scaled the data to optimally maximise contrast and generated the final images.

6.3.1 Simulation of FePd Disc

A simulation of a FePd disc (figure 6.15) measuring 600 nm in diameter, 30 nm in thickness with a tetrahedral mesh size of 5 nm was made along with a simulation of the magnetic stray field volume above the disc which measured 720 x 720 x 60 nm with a cubic mesh size of 5 nm. The FePd disc was initialized with randomly oriented domains so that it could form a realistic magnetic domain pattern unperturbed by any initial magnetisation orientation. Table 6.1 contains the magnetic material parameters used to represent FePd (obtained from Seemann, et al. [12]).

Property	Symbol	Value
Direction Of The Uniaxial Magnetocrystalline Anisotropy Axis In Spherical Coordinates Measured From The Z-Axis	θ	0 rad
Direction Of The Uniaxial Magnetocrystalline Anisotropy Axis In Spherical Coordinates Measured From The X-Axis In The XY-Plane	φ	0 rad
First Magnetocrystalline Anisotropy Constant	K_1	1.5×10^6 J/m ³
Second Magnetocrystalline Anisotropy Constant	K_2	0 J/m ³
Saturation Magnetisation	J_s	1.88 T
Exchange Constant	A	1.6×10^{-11} J/m
Gilbert Damping Constant	α	0.1

Table 6.1: Magnetic material parameters of FePd used in the simulation of the disc. Parameters obtained from Seemann et al. [12].

In figure 6.15 it can be seen that the structure has relaxed to a low energy state, with respect to the initial state, forming a combination of out-of-plane maze and bubble domains, which is typical of materials that exhibit perpendicular anisotropy, such as FePd. The observed average

domain width of 50 nm is on the same order as found experimentally by Seemann, et al. for L1₀-ordered FePd [12].

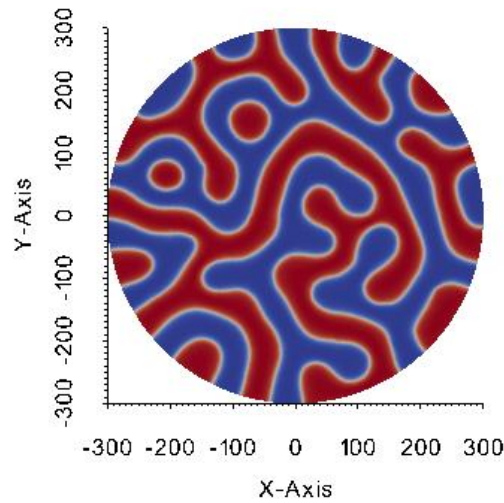


Figure 6.15: Plot of the simulated FePd disc. Axis units are in nanometres whilst the colour map represents the magnetisation magnitude in the z-axis (perpendicular to plane of page) with red denoting positive magnetisation and blue denoting negative magnetisation.

Figure 6.16 contains plots of the FePd disc's magnetic stray field at various plane sections normal to the disc surface at distances from 0 to 50 nm in steps of 10 nm. The contrast used here represents the sum of the x, y and z magnetic field magnitudes. It can be seen that despite this field summation the contrast pattern hasn't significantly altered from that seen in figure 6.15, which is rendered with only z-axis magnetisation contrast. The only contribution from x and y axes is the appearance of a slight "embossing" effect on the domains. This demonstrates that the z-axis magnetic field dominates the other two axes.

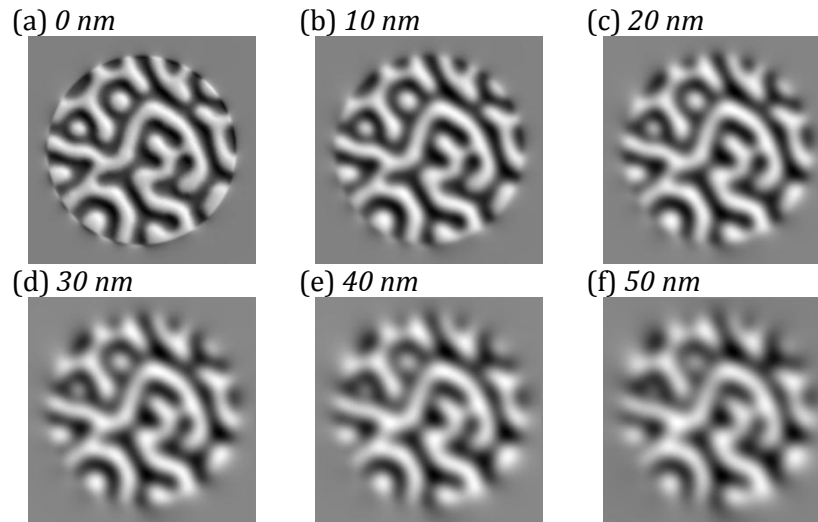


Figure 6.16: Plot of FePd disc's magnetic stray field ($x+y+z$) with normalised contrast at increasing z -distance (a-f) from sample surface.

Figure 6.17 shows simulated MFE micrographs for each of the images in figure 6.16. The MFE of the TPD:BBOT:PMMA sample (figure 5.10) has been mapped through the magnetic stray field generated by the FePd disc. It is immediately apparent that there is no magnetic field orientation sensitivity as demonstrated by the lack of contrast between domains of opposing magnetisation polarity. This is due to the assumed independence of the TPD:BBOT:PMMA sample fluorescence to magnetic field orientation based on the amorphous nature of the spin-coated polymeric thin film. Figure 6.17a shows limited contrast with only “speckling” at the domain walls. This speckling is most likely an aliasing artefact due to the coarse discretisation employed. As the section height increases (figures 6.17b-d) the speckling disappears due to an effective field averaging caused by the increased distance from the field source. At the largest heights shown (figures 6.17e-f) the field lines have diverged sufficiently to clearly reveal the domain walls. It can be seen through the set of images that the projection of the domains suffers from distortion as the field sampling height is increased. This is due to the magnetic flux lines diverging with respect to distance in the z -axis and not remaining parallel with the axis. Therefore the domains are represented most accurately at the smallest distance from the disc's surface.

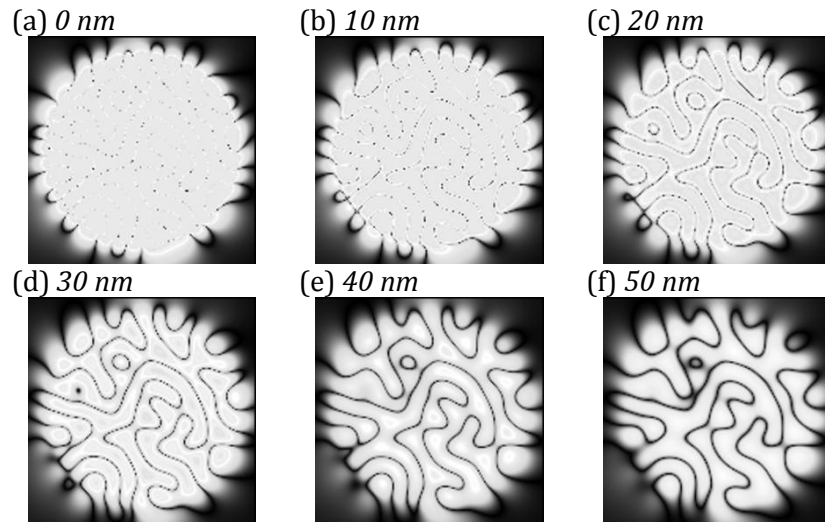


Figure 6.17: Plot of FePd disc's magnetic stray field ($x+y+z$) mapped through TPD:BBOT:PMMA MFE with normalised contrast.

Figure 6.18 contains a set of simulated MFE micrographs in which the tetracene MFE (figure 5.9) has been mapped through the magnetic stray field generated by the FePd disc (figure 6.16). The images are similar to the images seen in figure 6.17, however, due to tetracene's bipolar MFE the domain walls are visibly clearer at smaller distances from the disc with speckling only visible in figure 6.18a. This is different to figure 6.17 as the TPD:BBOT:PMMA MFE profile has only monopolar character. It can be seen that as the plane section distance from the disc is increased in the z-axis the image switches from having domains of bright contrast to domains of dark contrast. The reason behind this transition (illustrated in figure 6.19) is due to a gradual reduction in the average magnetic stray field as the height is increased. This alters the normalised contrast scaling according to the tetracene MFE profile. Therefore small magnetic fields begin to invoke dark contrast correlating to the negative MFE portion on tetracene's MFE plot.

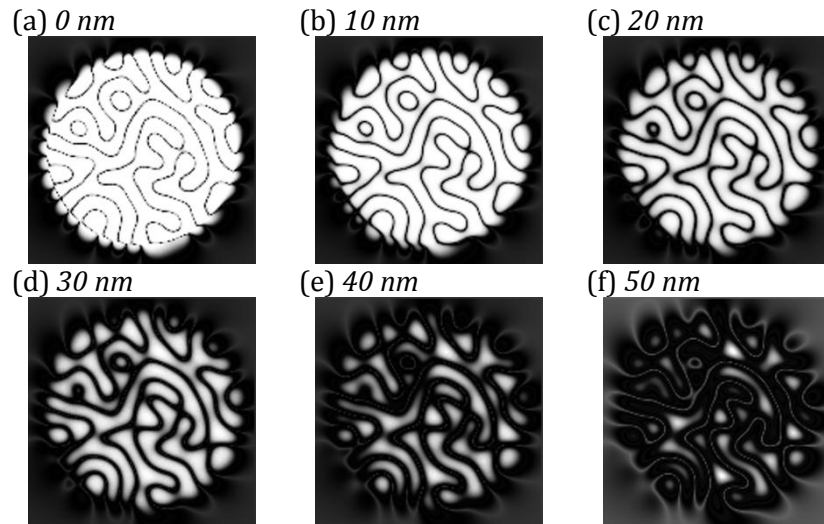


Figure 6.18: Plot of FePd disc's magnetic stray field ($x+y+z$) mapped through tetracene MFE with normalised contrast.

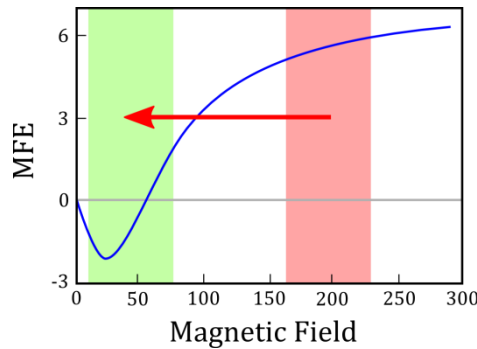


Figure 6.19: Schematic diagram illustrating the cause of the contrast transition seen in figure 6.18. The red band represents the domain contrast range as seen at low sample height. The green band represents the domain contrast range at a large sample height.

Figure 6.20 plots the scaling factor used to normalise the image contrast in the TPD:BBOT:PMMA and tetracene simulated MFE micrographs shown in figures 6.17 and 6.18. The first thing to notice is that the TPD:BBOT:PMMA images require approximately 200 \times scaling whereas the tetracene images require only around 30 \times scaling. The second thing to notice is that the scaling factor is initially independent of the distance from the object surface until about 40 nm where the scaling factor begins to increase for both curves. This region of uniform scaling is caused by both the TPD:BBOT:PMMA and tetracene MFE's exhibiting a plateau at high magnetic field. Because the scaling is governed by the largest contrast value in the image (see figure 6.21), which is dependent on the largest magnitude of stray field present in the xy -plane sampled, the scaling remains static until the magnetic field is sufficiently weak to begin moving

away from the plateau region on the MFE curve. This reduces the contrast observed and therefore triggers the scaling normalisation process.

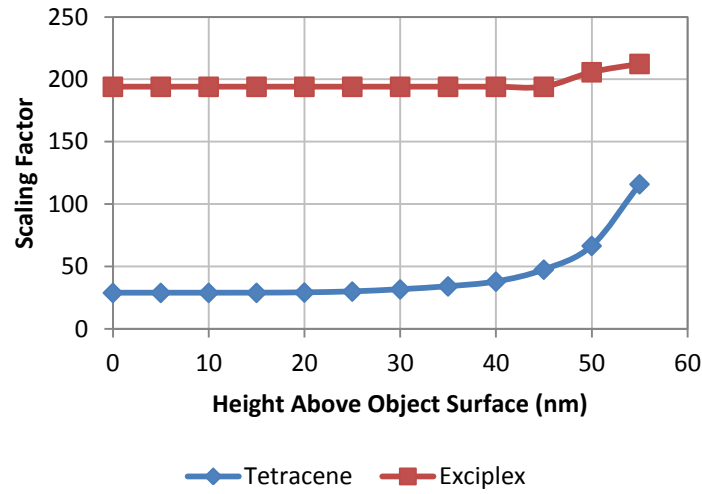


Figure 6.20: Plot of scaling factor required to normalise FePd disc contrast plots shown in figures 6.17 & 6.18.

Figure 6.21 is a schematic diagram illustrating how the contrast normalisation process operates. First the experimental MFE data is mapped onto the summed $x+y+z$ stray field values for each xy -plane. This occupies a small portion of the available bit-depth representing the “brightness space” (a). MATLAB utilises a double-precision floating point number format by default which is equivalent to a 64-bit depth delivering 15-17 significant decimal digits of precision. The minimum pixel brightness from the entire image is determined and subtracted from all pixels effectively moving the un-scaled contrast to the bottom of the brightness space (b). The new maximum pixel brightness is then determined and used to expand the contrast to occupy the full brightness space (c) whilst the scaling factor used is recorded.

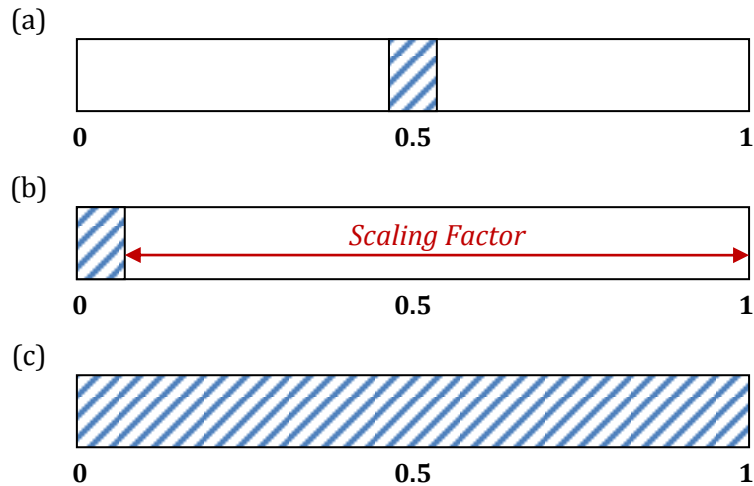


Figure 6.21: Schematic diagram representing the contrast normalisation process. The horizontal axis represents contrast where 0 = black, 0.5 = grey and 1 = white. (a) Original image contrast occupies a small portion of available bit-depth. (b) The minimum pixel brightness is subtracted from all data effectively darkening the image. (c) The maximum pixel brightness is used as the scaling factor to normalise the image contrast.

6.3.2 Simulation of Ni-Fe Ring

A simulation of a Ni-Fe ring (figure 6.22) of 1 μm outer diameter, 900 nm inner diameter, 15 nm thickness and a tetrahedral mesh size of 5 nm was made along with a simulation of the magnetic stray field volume above a portion of the ring which measured $200 \times 200 \times 80$ nm with a cuboidal mesh size of 2 nm in x and y and 5 nm in z. The Ni-Fe ring was initially saturated in the +y direction with an external magnetic field before removal of the field allowing the magnetisation to relax to a low energy configuration. In this case the relaxation was via the formation of an onion-state with a head-to-head and tail-to-tail domain wall aligned to the y-axis. Table 6.2 contains the magnetic material parameters used to represent $\text{Ni}_{80}\text{Fe}_{20}$.

Property	Symbol	Value
Direction Of The Uniaxial Magnetocrystalline Anisotropy Axis In Spherical Coordinates Measured From The Z-Axis	θ	0 rad
Direction Of The Uniaxial Magnetocrystalline Anisotropy Axis In Spherical Coordinates Measured From The X-Axis In The XY-Plane	φ	0 rad
First Magnetocrystalline Anisotropy Constant	K_1	0 J/m ³
Second Magnetocrystalline Anisotropy Constant	K_2	0 J/m ³
Saturation Magnetisation	J_s	1.00 T
Exchange Constant	A	1.3x10 ⁻¹¹ J/m
Gilbert Damping Constant	α	0.1

Table 6.2: Magnetic materials parameters of Ni-Fe used in the simulation of the ring.

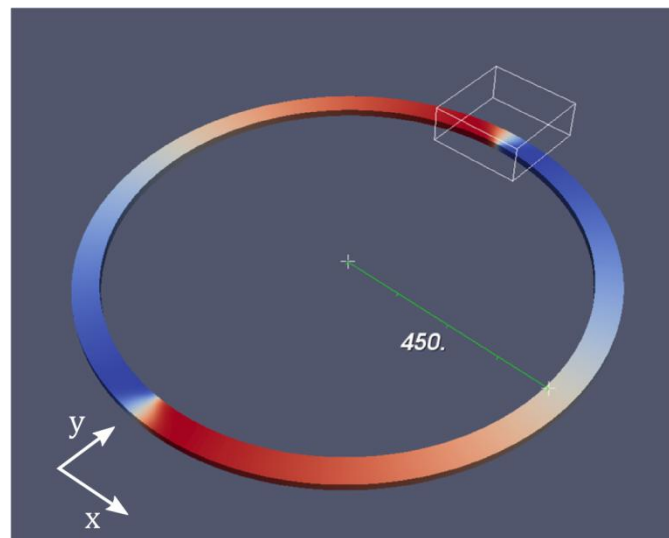


Figure 6.22: Plot of the simulated Ni-Fe ring with the fieldbox outlined in white. The ruler, featured in the figure indicating the distance from the centre to the inside of the ring, is aligned along the x-axis whilst the transverse domain walls are aligned along the y-axis. Red denotes magnetisation aligned in the +x direction whilst blue denotes magnetisation aligned to the -x direction.

Figure 6.23 contains plots of the Ni-Fe ring's magnetic stray field at various plane sections from within the fieldbox shown in figure 6.22. This box is centred above the transverse head-to-head domain wall. As was the case in figure 6.16 the contrast used here represents the sum of the x, y and z magnetic field magnitudes. Of immediate note is that the transverse head-to-head domain wall can clearly be seen with strong contrast at the top of the image. As the plane is elevated these contrast regions expand before ultimately consuming the finer structure of the ring section.

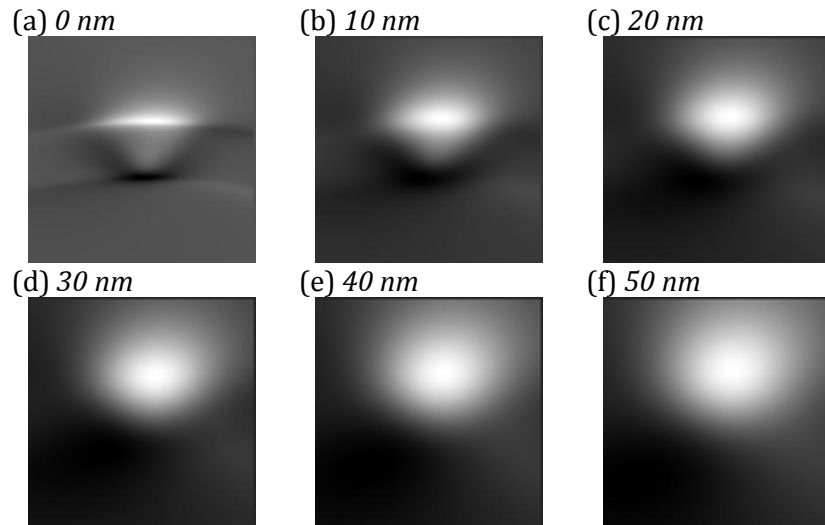


Figure 6.23: Plot of section of Permalloy ring's magnetic stray field ($x+y+z$) with normalised contrast at increasing z-distance (a-f) from sample surface.

Figure 6.24 contains a set of the Ni-Fe ring simulated MFE micrographs using the TPD:BBOT:PMMA MFE profile. On first appearances the contrast obtained is rather complex suggesting that all three axes have contributed strong magnetic field equally. This is unlike what was obtained from the FePd disc in figure 6.17 where the z-axis dominated the magnetic field contributions. As the plane is elevated the landscape begins to simplify as fine detail is averaged together and domain features become distorted. At a height of 50 nm the contrast has reduced to two areas of contrast with little retention of the original domain wall geometry.

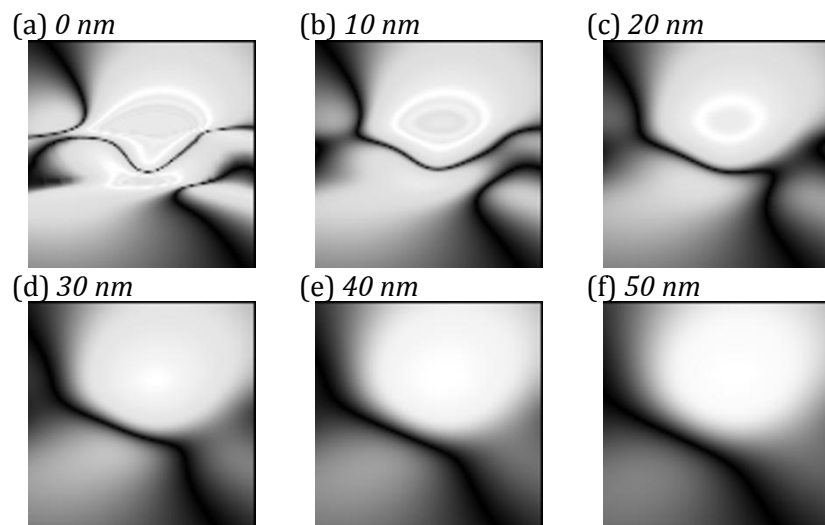


Figure 6.24: Plot of section of Ni-Fe ring's magnetic stray field ($z+y+z$) mapped through TPD:BBOT:PMMA MFE with normalised contrast.

Figure 6.25 contains the set of Ni-Fe ring simulated MFE micrographs using the tetracene MFE profile. This set of images is obviously similar to figure 6.24. However, this time the bipolar character of tetracene's MFE profile has produced interesting bands of contrast in figures 6.25e-f representing magnetic field magnitudes being mapped through the negative region of tetracene's MFE profile. This idea is reinforced by the fact that figure 6.26 reveals that the scaling factor jumps and reaches a second plateau just at the elevations where band formation appears in figures 6.25e-f. This means that the maximum stray field magnitudes in these two figures correspond with the negative region of tetracene's MFE profile.

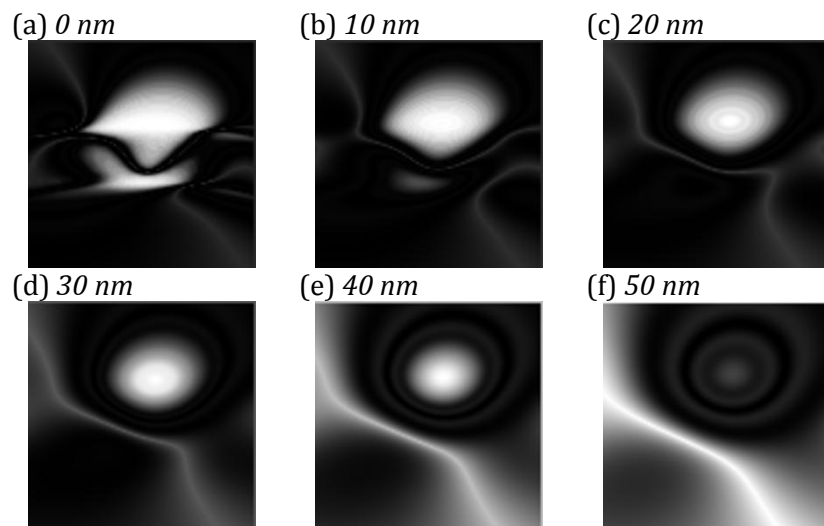


Figure 6.25: Plot of section of Ni-Fe ring's magnetic stray field ($x+y+z$) mapped through tetracene MFE with normalised contrast.

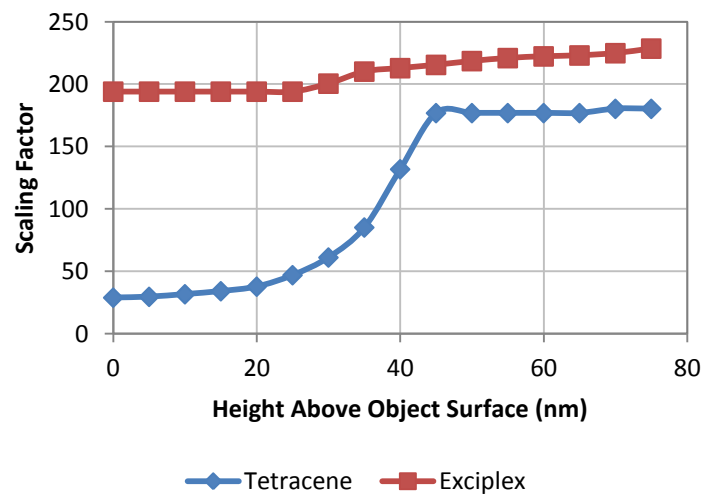


Figure 6.26: Plot of scaling factor required to normalise Ni-Fe ring section contrast plots shown in figures 6.24 & 6.25.

6.3.3 Simulation of Ni-Fe Rectangle

A simulation of a Ni-Fe rectangle (figure 6.27) measuring $500 \times 200 \times 50$ nm with a tetrahedral mesh size of 7 nm was made along with a simulation of the magnetic stray field volume above the rectangle which measured $1005 \times 405 \times 105$ nm with a cubic mesh size of 5 nm. The Ni-Fe rectangle was initialised with the magnetisation aligned in the +z direction but was then allowed to relax the magnetisation to a low energy configuration; in this case via the formation of the in-plane “flux-closed” diamond structure [13]. Table 6.2 contains the magnetic material parameters used to represent $\text{Ni}_{80}\text{Fe}_{20}$.

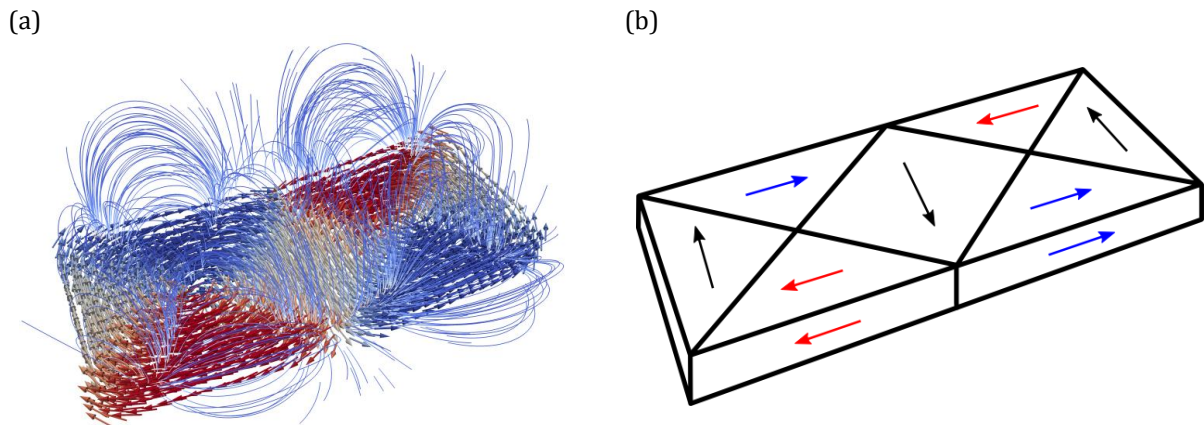


Figure 6.27: (a) Screenshot of micromagnetic simulation of Ni-Fe cuboidal nanostructure. The lines emanating from the cuboid represent contour lines of magnetic stray field. (b) Schematic diagram of simulated nanostructure.

Figure 6.28 contains plots of the Ni-Fe rectangle’s magnetic stray field at various plane sections above the structure. As stated previously the contrast used here represents the sum of the x, y and z magnetic field magnitudes. It can be seen that although the object has minimised its energy by forming a flux closed structure there is still sufficient flux “leaking” from the structure in order to form magnetic stray field images of the domain structure. The domain walls offer the strongest contrast in the figure suggesting that the flux is being dispelled at these locations and not from the centres of the domains. As the plane elevation is increased the domain wall contrast begins to dominate forming a pattern of two interlocking chevrons of opposing contrast.

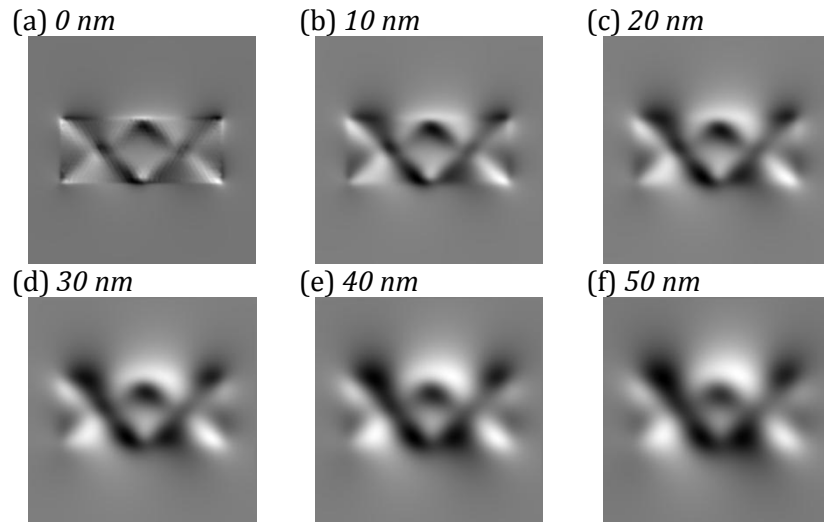


Figure 6.28: Plot of section of Ni-Fe rectangle's magnetic stray field ($x+y+z$) with normalised contrast at increasing z -distance (a-f) from sample surface.

Figure 6.29 contains a set of simulated MFE micrographs of the Ni-Fe rectangle using the TPD:BBOT:PMMA MFE profile. It can be seen that these images appear as convoluted forms of the original diamond structured magnetisation pattern of the Ni-Fe rectangle. It is also observed that, compared with the equivalent images in figure 6.28, the MFE images extend well beyond the in-plane limits of the rectangle to form a “halo” around the object.

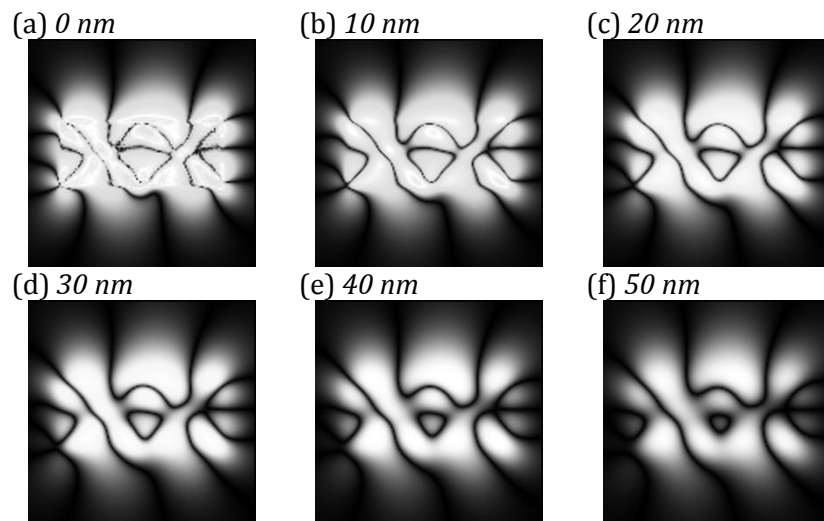


Figure 6.29: Plot of section of Ni-Fe rectangle's magnetic stray field ($x+y+z$) mapped through TPD:BBOT:PMMA MFE with normalised contrast.

Figure 6.30 contains a set of simulated MFE micrographs of the Ni-Fe rectangle using the tetracene MFE profile. As has been already seen in figure 6.25 at a certain elevation the contrast effectively inverts due to the average magnetic stray field in the plane reaching the negative

region of tetracene's MFE profile. In both cases this is accompanied with the second plateauing in each respective scaling factor plot (figure 6.31).

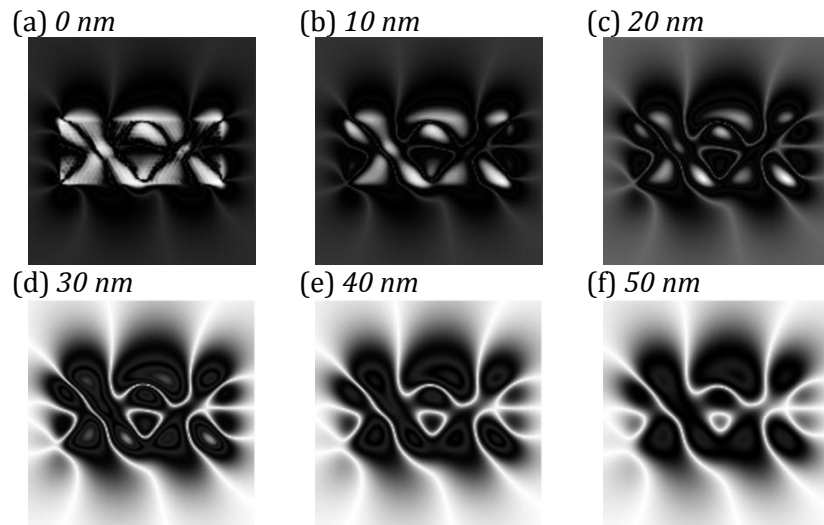


Figure 6.30: Plot of section of Ni-Fe rectangle's magnetic stray field ($x+y+z$) mapped through tetracene MFE with normalised contrast.

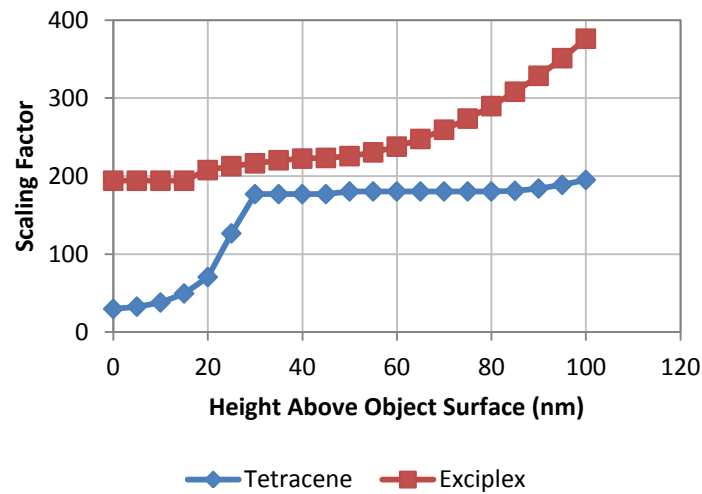


Figure 6.31: Plot of scaling factor required to normalise Ni-Fe rectangle contrast plots shown in figures 6.29 & 6.30.

6.4 Microscopic Regime

This section presents images obtained using confocal microscopy. These results form an attempt to image MFE-derived magnetic stray field contrast from organic thin films deposited onto various magnetic substrates. Some images were obtained by supplementing the usual confocal microscopy arrangement discussed in §3.6 with an in-situ in-plane magnetising stage.

This stage allowed control of the patterned magnetic nanostructures' magnetisation configuration offering the opportunity to perform difference imaging whereby the magnetic contrast could be filtered from other sources of image contrast.

The polished sintered NdFeB permanent magnet discussed in §6.2.2 was the first sample to be imaged using confocal microscopy. This substrate was considered to be a good candidate for capturing an MFE image as the magnetic stray field generated is large due to the out-of-plane magnetisation and exists on an optically resolvable length-scale. The TPD:BBOT:PMMA chemical mixture was dissolved into chloroform and the solution was spin-coated onto the magnet at 4000 rpm for 30 seconds. Due to the absorption peak existing in the ultraviolet region of the electromagnetic spectrum (§5.2.1) the microscope had to excite the sample using the class 4 tuneable Ti-Sapphire two-photon laser as the microscope was not equipped with a UV laser. Two-photon microscopy utilises a femtosecond laser which operates at double the wavelength of the molecule's absorption wavelength (e.g. 700 nm for a peak absorption wavelength of 350 nm). By operating the laser at high power the probability that the molecule will absorb two photons simultaneously increases resulting in excitation of the molecule [14]. Figure 6.32 shows two confocal micrographs of the thin film surface. It can be seen in both images that there exists a lot of surface detritus most likely resulting from polishing the NdFeB magnet. Figure 6.32a displays a subtle undulating background contrast. This is actually the result of contrast originating from two separate bandpass channels (405-501 nm and 435-485 nm) and therefore may represent segregation of the fluorescent components TPD and BBOT. Figure 6.32b is a micrograph taken at a single bandpass channel (435-485 nm) but is dominated by sample topographical contrast. Clearly, cleaner substrates were needed in order to minimise this topographical contrast. Another issue with this sample is that the magnetisation state could not be altered as NdFeB has a large magnetic coercivity. Opting to use magnetic samples that could be switched between different magnetisation configurations and coupling this with difference imaging to improve the magnetic contrast would be greatly desired.

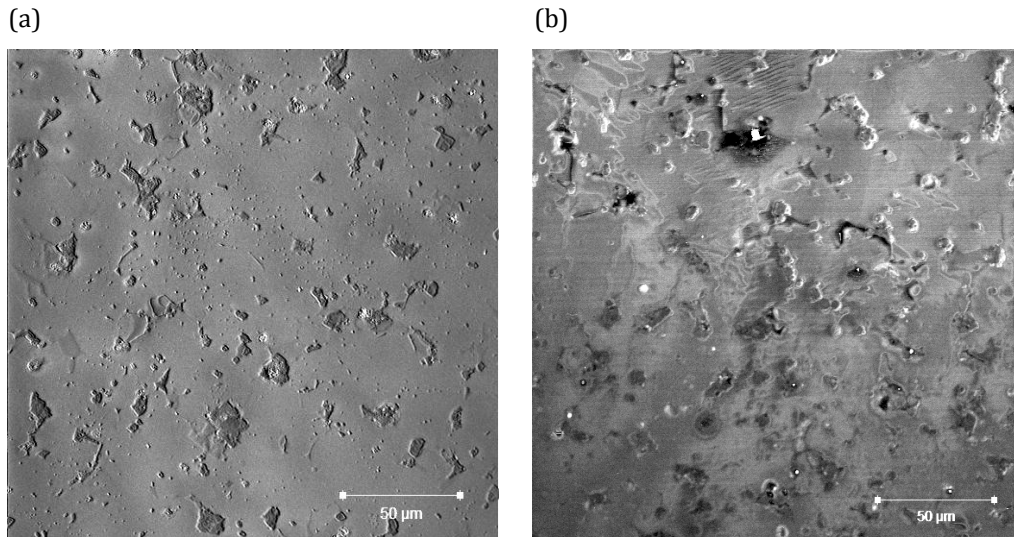


Figure 6.32: Confocal micrographs of TPD:BBOT:PMMA thin film spin coated onto a polished sintered NdFeB permanent magnet.

In response to the previous results new samples consisting of tetracene thermally evaporated onto Ni-Fe nanostructures were prepared and are presented in figure 6.33. The tetracene film was excited using an argon ion laser operating at a wavelength of 488 nm at 15% relative power whilst the emission was collected using a 505 nm long pass filter. The objective lens used was an oil immersion lens as this provided the highest spatial resolution due to the higher numerical aperture of oil compared to air. To protect the thin film from contacting the oil a thin cover slip was placed on top of the sample. Due to the precariousness of this arrangement it was important to secure the cover slip relative to the sample and stage so that the objective lens didn't displace it and damage the tetracene film. It can be seen that the Ni-Fe nanostructures are clearly visible in the micrograph. This is attributed to a difference in reflectivity of the tetracene fluorescence emission between the silicon substrate and the nanostructure. A second thing to notice is that the individual tetracene grains can be seen using this technique. Morphology similar to this is seen in AFM micrographs shown in figures 5.21 and 5.22. A final feature worth mentioning is that inter-grain contrast variation is observed, i.e. a variation in the fluorescence intensity of the tetracene grains. Cicoira, et al. attribute this phenomenon to variation in crystalline grain orientation after having observed it for themselves in tetracene thin films deposited onto SiO₂ [15]. They suggest that brighter grains correspond to orientations more

favourable for laser excitation and that films grown at higher deposition rates do not suffer from this phenomenon.

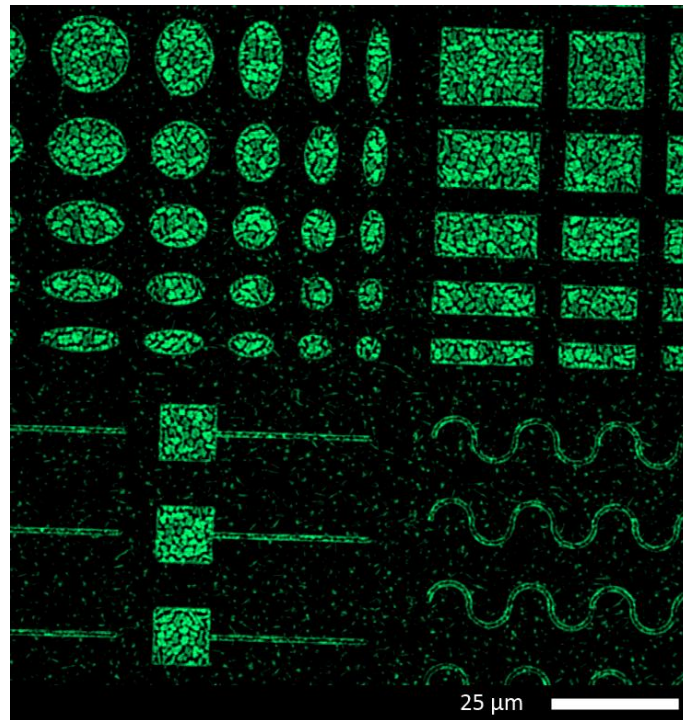


Figure 6.33: Confocal micrograph of the first attempt at thermally evaporating a thin film of tetracene onto Ni-Fe nanostructures samples (deposition rate = $0.045 \text{ nm}\cdot\text{s}^{-1}$). The green hue is a false colour added to the micrograph. Presented area measures $133.6 \times 133.6 \mu\text{m}$.

Refinement to the tetracene thin film via reduction of the average grain size was made by increasing the evaporation rate from $0.045 \text{ nm}\cdot\text{s}^{-1}$ (figure 6.34a) to $1.29 \text{ nm}\cdot\text{s}^{-1}$ (figure 6.34b) and finally $1.51 \text{ nm}\cdot\text{s}^{-1}$ (figure 6.34c). From these figures it can be observed quite clearly that the morphology exhibits greater uniformity and homogeneity as the evaporation rate is increased.

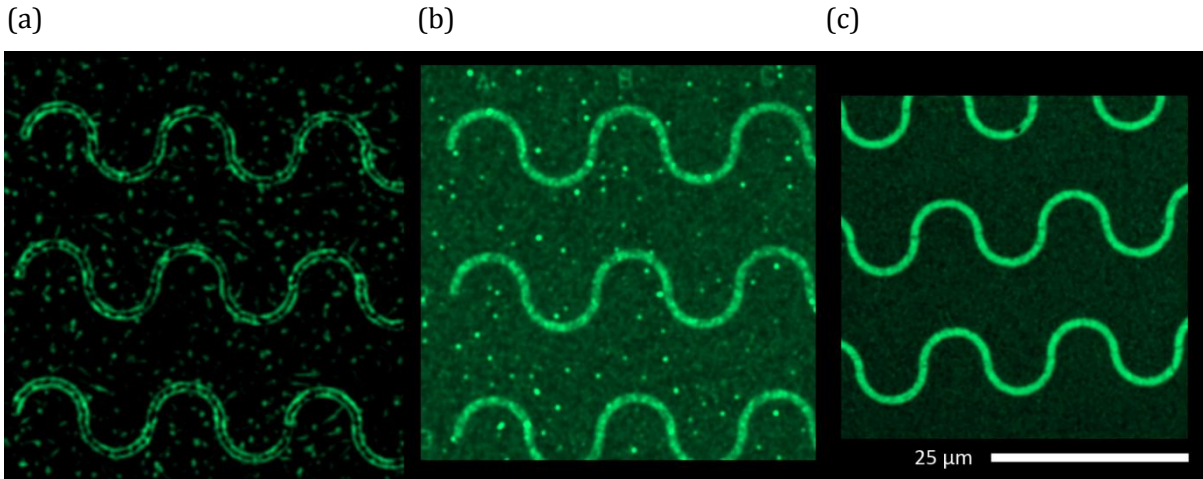


Figure 6.34: Confocal micrographs demonstrating the refinement of the tetracene thin film morphology. (a) Tetracene was deposited at a rate of $0.045 \text{ nm}\cdot\text{s}^{-1}$. This micrograph is the fluorescence analogue of figure 5.22a. Presented area measures $46.9 \times 51.4 \mu\text{m}$. (b) Tetracene was deposited at $1.29 \text{ nm}\cdot\text{s}^{-1}$. This micrograph is the fluorescence analog of figure 5.22b. Presented area measures $44.5 \times 44.5 \mu\text{m}$. (c) Tetracene was deposited at $1.51 \text{ nm}\cdot\text{s}^{-1}$. Presented area measures $44.1 \times 42.8 \mu\text{m}$.

Once the film morphology had been improved sufficiently attempts were made to produce magnetic contrast-enhancing difference images by subtracting one image, where magnetic domain contrast would appear strongest, from another image, where magnetic domain contrast would appear weakest. A magnetising stage would provide the ability to manipulate the magnetic domain configurations within the nanostructures.

Figure 6.35 contains three micrographs of the serpentine wire structures demonstrating the first use of difference imaging to select magnetic contrast on the confocal microscope. Figure 6.35a is a micrograph of the serpentine wire structures where a saturating magnetic field in excess of 100 Oe has been applied in the +x direction and then removed producing a magnetisation configuration described in figure 6.9 in which no domain walls should be present in the wires. Figure 6.35b is a micrograph of the serpentine wire structures with the saturating magnetic field also in excess of 100 Oe applied orthogonally in the +y direction and then removed. The magnetisation configuration should now be aligned as described in figure 6.8 with domain walls formed at the apices. Figure 6.35c is the difference image resulting from subtracting figure 6.35a from figure 6.35b using ImageJ 2.0.0-beta6. The images have been aligned with a program made by DualAlign called i2k Align 2.1.5.

The expected contrast pattern, i.e. the generation of stray field by the domain walls at the apices invoking MFE contrast, was not observed. There are several possible causes to account for this negative result. For example, even with the use of the alignment software it can be seen that there exists alignment errors typified by the ‘embossed’ appearance of the wires (the bright and dark edges). This is caused by the fact that confocal microscopy is a scanning technique where there exists time for drift to occur *between* line scans creating non-linear distortions in the final image that the alignment software cannot accommodate. Although these distortions do not normally cause issue with regular confocal microscopy use, they are detrimental when performing difference imaging. Another issue is that the confocal microscope is very near the spatial resolution limit for these structures as defined primarily by the 63× oil immersion objective lens. The final issue that can affect difference imaging quality is noise. The amount of noise in these images can be reduced via averaging. This is achieved by scanning a line n times and averaging those line scans together. However, this can incur the same drift penalty as has been previously described.

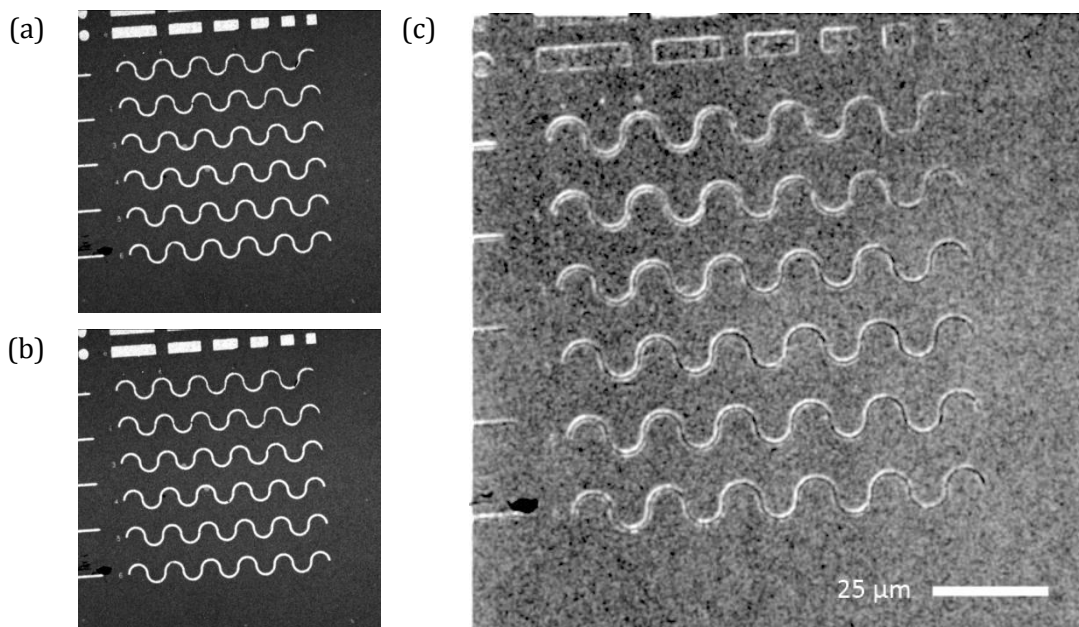


Figure 6.35: Confocal micrographs of a tetracene thin film thermally evaporated on top of Ni-Fe nanostructures. Presented areas measure $133.6 \times 133.6 \mu\text{m}$. (a) Sample is saturated in the $+x$ direction. (b) Sample is saturated in the $+y$ direction. (c) Difference image of micrographs (a) and (b).

A second attempt at detecting MFE contrast in the serpentine wires was made (figure 6.36). The wires shown in figures 6.36a-b were saturated in the same manner as is described for figures 6.35a-b. The attempt was performed at a higher magnification compared to the previous attempt in order to resolve the wire surfaces with greater clarity. This approach incurs the disadvantage that comparison with a large number of wire apices is sacrificed. The creation of the difference image, seen in figure 6.36c appears to have been successful as no misalignment artefacts are observed. The contrast within the wires shows appreciable variation, however, compared to the contrast variation on the substrate and, more importantly, it does not occur periodically as one would expect for MFE contrast of domain walls. Therefore it is suggested that, here also, no contrast is generated by fluorescent MFE. The contrast variation that is observed is mostly likely caused by the diagonal streaks in both precursor images. These streaks are believed to have been caused by damage to the sample prior to measurement.

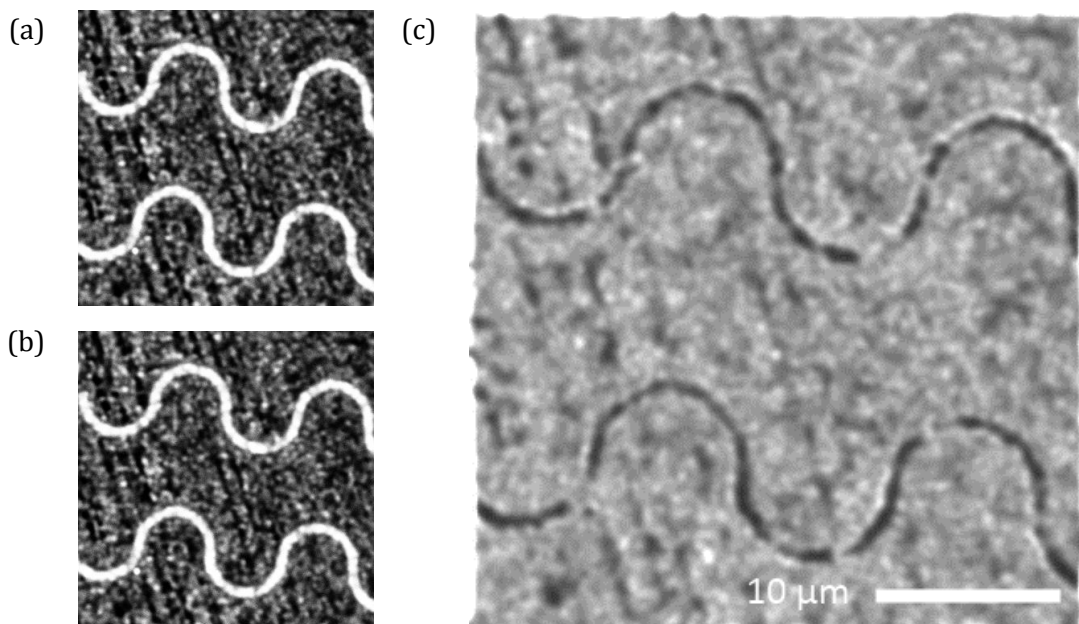


Figure 6.36: Confocal micrographs of a tetracene thin film thermally evaporated on top of Ni-Fe nanostructures. Presented areas measure $33.4 \times 33.4 \mu\text{m}$. (a) Sample is saturated in the $+x$ direction. (b) Sample is saturated in the $+y$ direction. (c) Difference image of micrographs (a) and (b).

Figure 6.37 contains three confocal micrographs of the ring structures where micrograph (a) has been saturated in the $+x$ direction and then removed, forming a horizontal pair of domain walls whilst micrograph (b) has been saturated in the $+y$ direction and then removed, forming a

vertical pair of domain walls. It is expected that the resulting difference image of these micrographs should form a contrast pattern similar to the idealised form illustrated in figure 6.38. As with figure 6.35c it can be seen that no MFE contrast has appeared in figure 6.37c. In fact, it can be seen that the image alignment software has had to perform non-trivial transformations in order to get the two images to align as evidenced by the barrel distortion in figure 6.36c suggesting small amounts of drift may have occurred during the scan.

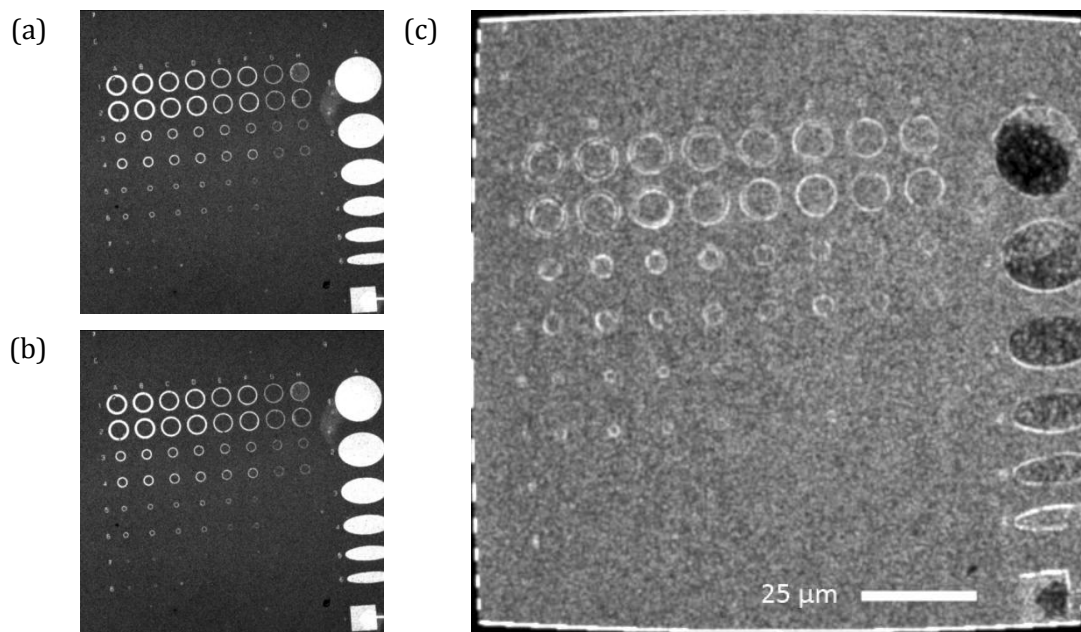


Figure 6.37: Confocal micrographs of a tetracene thin film thermally evaporated on top of Ni-Fe nanostructures. Presented areas measure $133.6 \times 133.6 \mu\text{m}$. (a) Sample is saturated in the $+x$ direction. (b) Sample is saturated in the $+y$ direction. (c) Difference image of micrographs (a) and (b).

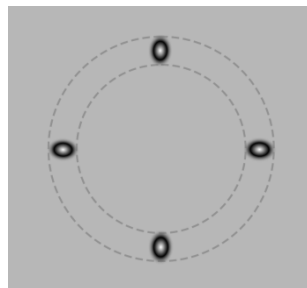


Figure 6.38: Illustration of the idealised MFE contrast pattern in a ring nanostructure resulting from the difference between two precursor images where in one the structure is saturated in the x direction and allowed to relax forming a pair of domain walls and the another image where the structure is saturated in the y direction and allowed to relax forming an orthogonal pair of domain walls.

Figure 6.39 contains three confocal micrographs of the elliptical structures where figure 6.39a has been saturated in the +x direction and removed, forming a multi-domain structure whilst figure 6.39b has been saturated in the +y direction and held, forming a uniform region of magnetisation. The image contrast has been modified so that the Ni-Fe structures' contrast intensity is optimally scaled for storage in the 12-bit depth TIFF image. This results in the regions surrounding the structures to appear black. Figure 6.39c reveals the result of the image difference operation. Here, appreciable variation in the ellipse contrast can be seen, however, this does not appear to take the form of regular domain structure. Instead the pattern of contrast appears speckled suggesting that this variation may, in fact, be caused by either variation in tetracene grain orientation as discussed for figure 6.33, detector shot noise, or a combination of the two.

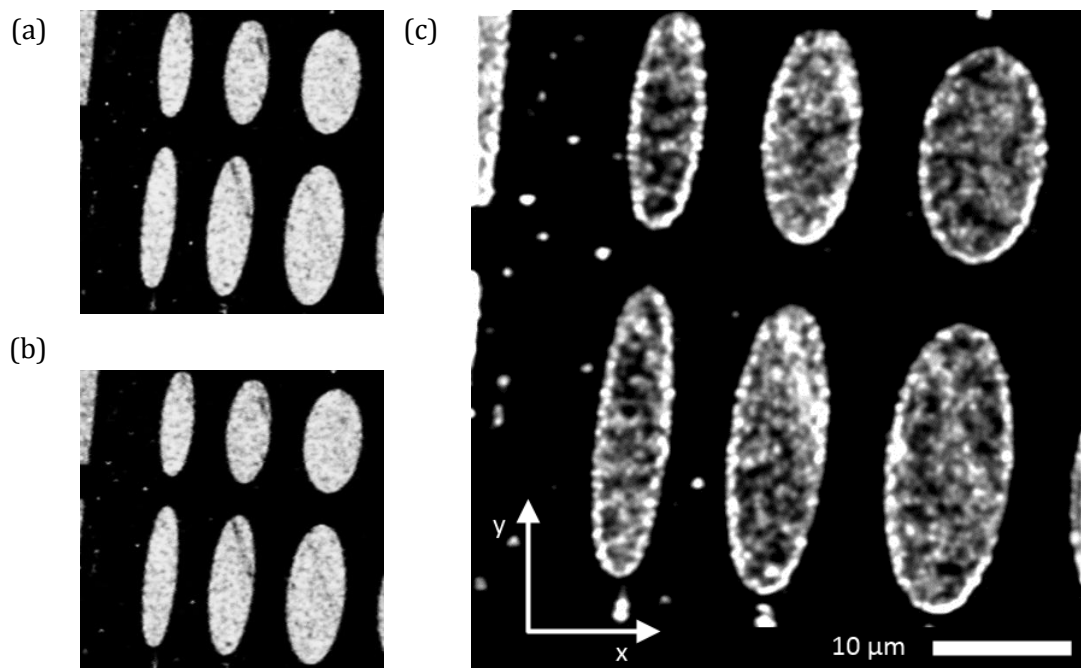


Figure 6.39: Confocal micrographs of a tetracene thin film thermally evaporated on top of Ni-Fe nanostructures. Presented areas measure $44.5 \times 44.5 \mu\text{m}$. (a) Sample is saturated in the +x direction. (b) Sample is saturated in the +y direction. (c) Difference image of micrographs (a) and (b).

As there has been no clear evidence of MFE contrast in the figures presented in this section several potential solutions are proposed which may increase the prospect of visualising MFE contrast at microscopic length-scales. The first of these include using wide-field fluorescence

microscopy in order to image the whole of the structures simultaneously resulting in the elimination of distortions within each precursor image. This would aid the image alignment process. The second potential solution would be to use a different MFE organic thin film material, such as TPD:BBOT:PMMA. This material has the advantage that it does not form a grain microstructure, but instead produces smooth uniform thin films due to the PMMA polymer acting as the host matrix for the TPD and BBOT molecules. This would remove, or at the very least, significantly minimise topographical contribution compared to the thin film grain structure observed with tetracene. A third potential solution could be to fabricate larger magnetic structures so that the microscope isn't operating near the spatial resolution limit. The difficulty with this approach is that the magnetisation configuration within the structures may become less predictable as multi-domain configurations become energetically preferred at larger length-scales. A fourth potential solution may be found via the fabrication of magnetic thin films that possess large out-of-plane anisotropy, such as magnetic garnets [9], forming large stray fields and regular magnetisation patterns that exist on length-scales compatible with confocal microscopy and wide-field fluorescence microscopy. A final potential solution may be to use the stimulated emission depletion microscopy (STED) technique (discussed in §2.6.2) to access a spatial resolution regime exceeding the resolution limitations of confocal microscopy. This should allow the capture of high resolution micrographs capable of generating high quality difference images.

6.5 Macroscopic Regime

In this section results from the magnetic field effect photography experiment (described in §4.3) will be presented. It will be shown that as the experimental system and associated procedures underwent incremental development with time so too did the experimental results.

The first set of images, shown in figure 6.40, reveals an approximately square wafer of silicon mounted upright in a sliding-arm lens holder (see figure 4.17). A tetracene thin film, approximately 80 nm in thickness, was deposited onto the silicon wafer. Positioned centrally

behind the wafer (in figure 6.40a) is an upright toroidal NdFeB permanent magnet that is magnetised out-of-plane. Figure 6.40b shows the same scene with the magnet removed from behind the wafer. By comparing these two images it should be possible to amplify any differences occurring due to the magnet whilst attenuating anything that remains the same between the images. Figure 6.40c is the result of dividing figure 6.40a by 6.40b. The image has undergone contrast enhancement as well as Gaussian blurring in order to reveal the fact that the toroidal magnet's effects can be seen in the film via the appearance of a thin, dark ring occupying the majority of the wafer. This is the first proof to suggest that the *magnetic field effect* can be used to create images of magnetic contrast.

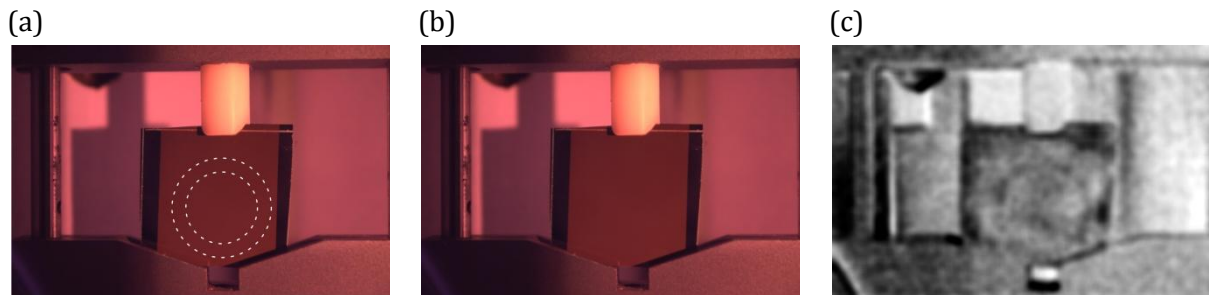


Figure 6.40: Fluorescence photographs of the tetracene thin film thermally evaporated onto a cut silicon wafer. Photograph durations equal 30 seconds with the ISO set to 1600. (a) In this photograph a toroidal NdFeB permanent magnet has been placed behind the silicon wafer (as indicated). (b) The magnet was then removed before taking this photograph. (c) The resulting division image of micrographs (a) and (b) reveals the magnet's stray field pattern captured by the fluorescent MFE of tetracene.

Based on the results obtained in figure 6.40 a second attempt was undertaken. This time the duration of the precursor photographs was extended from the camera's maximum exposure time of 30 seconds to 300 seconds by putting the camera into 'bulb-mode' and using a manual shutter release cable. For the same exposure levels this allowed a reduction of the camera's ISO setting from 1600 to 100 – effectively increasing the signal-to-noise ratio by reducing amplifier gain. Figures 6.41a&b show the tetracene film with and without the toroidal magnet behind the wafer, respectively. Figure 6.41c shows the difference image created from subtracting figure 6.41a from 6.41b with additional contrast enhancement and Gaussian blur. The contrast pattern is immediately apparent and is much stronger compared to what was achieved in figure 6.40c.

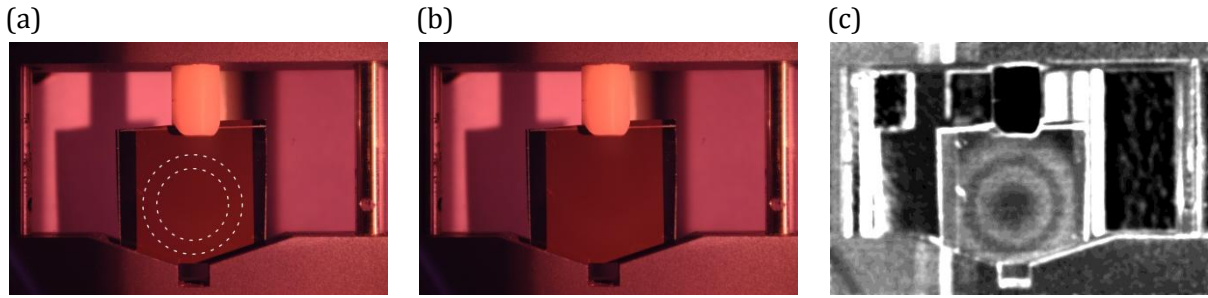


Figure 6.41: Fluorescence photographs of the tetracene thin film thermally evaporated onto a cut silicon wafer. Photograph durations equal five minutes with the ISO set to 100. (a) In this photograph a toroidal NdFeB permanent magnet has been placed behind the silicon wafer (as indicated). (b) The magnet was then removed before taking photograph. (c) The resulting difference image of micrographs (a) and (b) reveals the magnet's stray field pattern captured by the fluorescent MFE of tetracene.

To test the versatility of the technique another magnet geometry, consisting of two cubic NdFeB permanent magnets, was introduced to the experimental setup with their dipolar axis aligned parallel to the plane of the wafer. Figures 6.42a&b show the tetracene film with and without the cubic magnets behind the wafer, respectively. The precursor photographs were captured with the ISO setting set to 100 whilst exposure times of eight minutes each were found to deliver appropriate exposure levels. Figure 6.42c shows the difference image created from subtracting figure 6.42a from 6.42b with additional contrast enhancement and Gaussian blur. The contrast pattern reveals two lobes of bright contrast possibly with darker features existing inside the lobes. As has been assumed up until now, both north and south poles exhibit the same level of contrast making their identification impossible in this current setup.

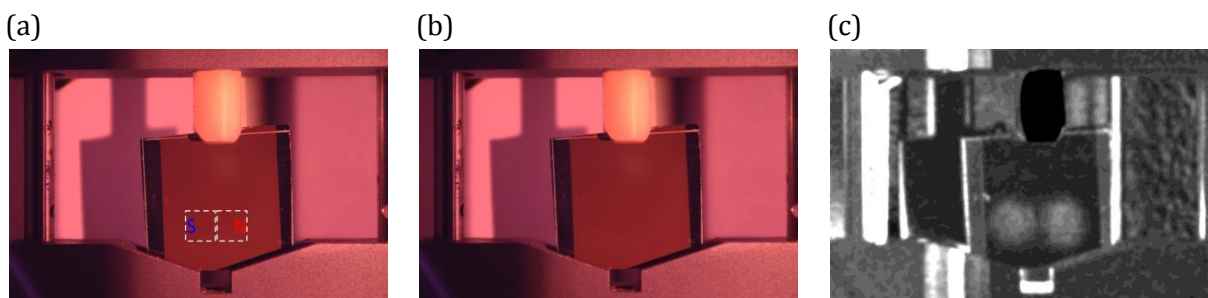


Figure 6.42: Fluorescence photographs of the tetracene thin film thermally evaporated onto a cut silicon wafer. Photograph durations equal eight minutes with the ISO set to 100. (a) In this photograph two cubic NdFeB permanent magnets were connected together and placed behind the silicon wafer (as indicated). (b) The magnets were then removed before taking this photograph. (c) The resulting difference image of micrographs (a) and (b) reveals the magnet's stray field pattern captured by the fluorescent MFE of tetracene.

Another attempt at imaging the tetracene MFE contrast generated from the magnetic stray field of the two NdFeB cubes was undertaken. A fresh thin film of tetracene was evaporated onto the silicon wafer at the same thickness as the previous sample. This effort was undertaken as it was believed the current sample had degraded due to photobleaching. This was indicated by the persistent need to keep increasing the exposure durations. The difference image generated from two five minute exposure photographs can be seen in figure 6.43. By using a fresh sample an impressive amount of image contrast has been revealed compared to the previous attempt. Examples include a dark band surrounding the main contrast pattern and a pair of bright rings inside each lobe. The former contrast feature is similar to the bands seen in figure 6.25 where they represented magnetic stray field magnitudes corresponding with the negative region of tetracene's MFE profile (0-50 mT; see figure 5.9 in §5.3).

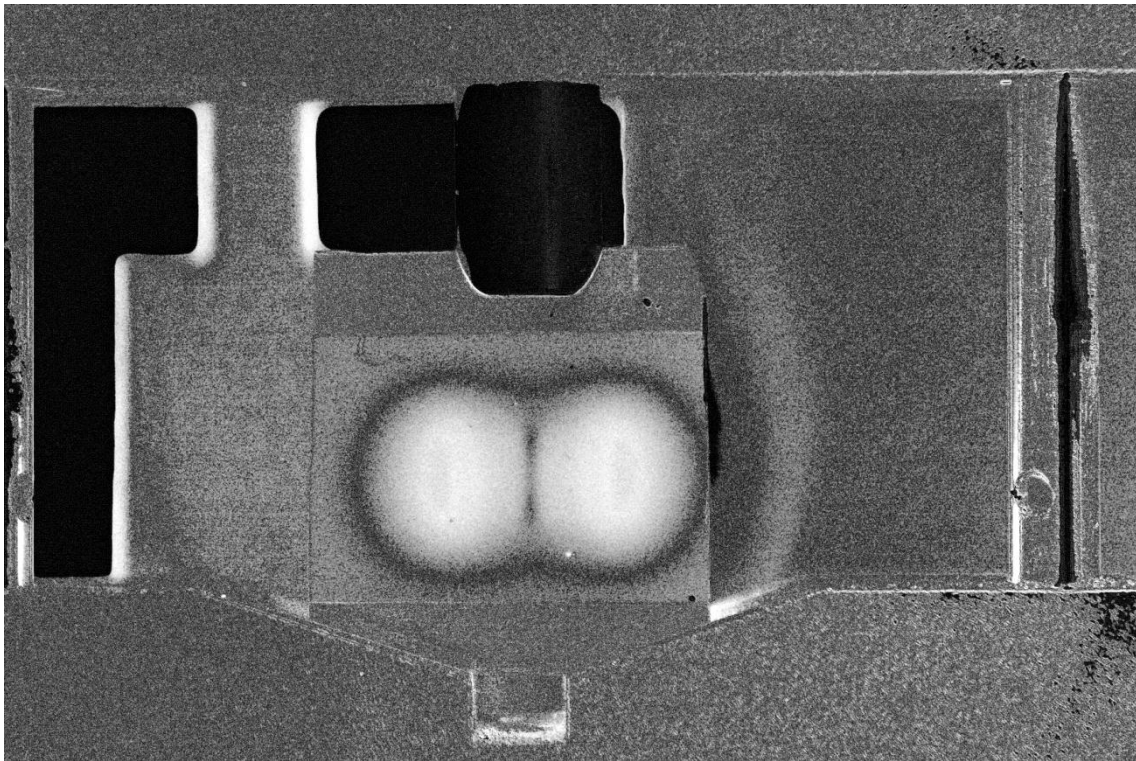


Figure 6.43: Difference image resulting from two fluorescence photographs of the tetracene thin film thermally evaporated onto a cut silicon wafer. Photograph durations equal five minutes with the ISO set to 100. The difference image reveals exquisite detail in the magnet's stray field pattern captured by the fluorescent MFE of tetracene.

A line profile plot of figure 6.43 was taken along the central horizontal axis of the MFE pattern and is shown in figure 6.44. Figure 6.44a depicts the image area that was sampled for the line profile plot; figure 6.44b shows the line profile plot of normalised intensity as a function of distance in pixels. Figure 6.44c shows the same line profile plot except that the intensity has been converted to estimated tetracene MFE magnitude based on the assumption that the intensities in figure 6.44b at 0 and 300 pixels distance represent 0% MFE and the minimum intensity plotted represents the -2% MFE seen in polycrystalline MFE of tetracene (see figure 5.9). It can be seen that in figure 6.44c the estimated MFE, when scaled based on the previously stated assumptions, exceeds the 6.5% MFE of tetracene as measured in figure 5.9. This discrepancy could be the result of the magnetic field generated by the magnets exceeding the 300 mT measuring limit of the HF-MFE system.

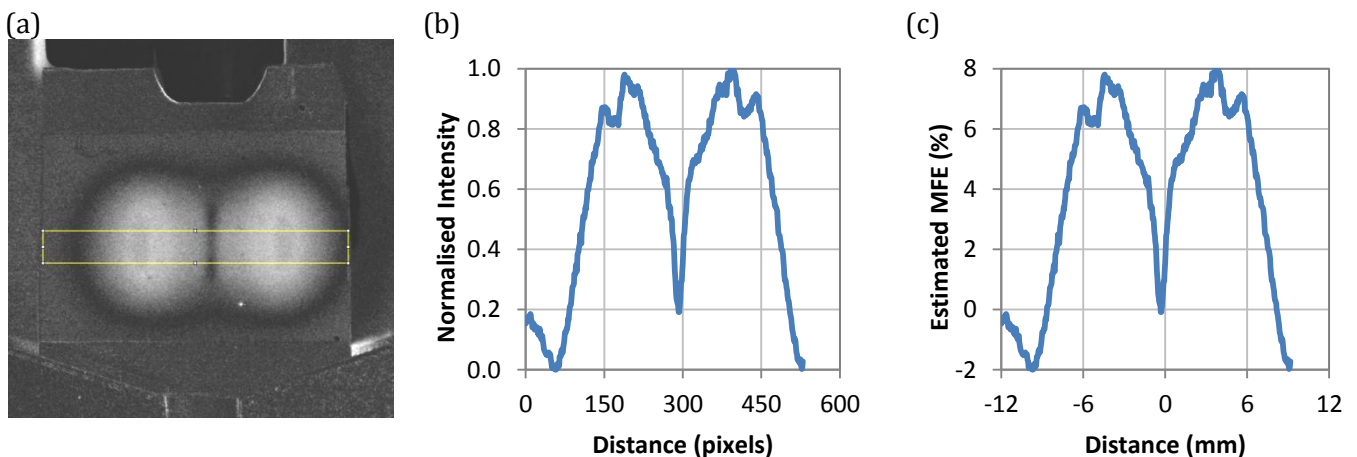


Figure 6.44: Line profile plot of the MFE photograph shown in figure 6.43. (a) Depiction of the image area sampled for the line profile plot. (b) The line profile plot represented as normalised intensity as a function of distance in pixels. (c) Conversion of the line profile plot shown in (b) where the MFE magnitude and distance has been estimated.

At this point the MagCam system, a two-dimensional Hall sensor array used for measuring macroscopic magnetic stray field (described in §3.10), was used to accurately measure the stray field distribution from the two cubic NdFeB permanent magnets. The results of this measurement can be seen in figure 6.45a-b. These measurement plots are identical except that the range of (a) has been scaled to ± 20 mT whilst the range of (b) has been scaled to ± 500 mT,

respectively. This is done intentionally to reveal details only visible at each respective range. The outline of the magnets has been overlaid in each sub-figure. Figure 6.43 has been modified with false colour and has been included in figure 6.45 as sub-figure (c) in order to allow direct comparison with the MagCam plots. A scale bar has been included for (c), based on tetracene's MFE profile, but should only be considered an approximation and is for guidance only.

In figure 6.45a it can be seen that whilst the two main lobes are saturated with respect to the scale bar (i.e. > 20 mT) there exists other features with a magnitude < 20 mT and of opposite polarity. These features can also be seen in figure 6.45c and represent the boundary between the magnets. In figure 6.45b the maximum stray field magnitudes have been marked on the scale bar as $\approx \pm 250$ mT and their locations correspond with the ends of the joined magnets. In figure 6.45c these same positions correspond with a region of increased brightness.

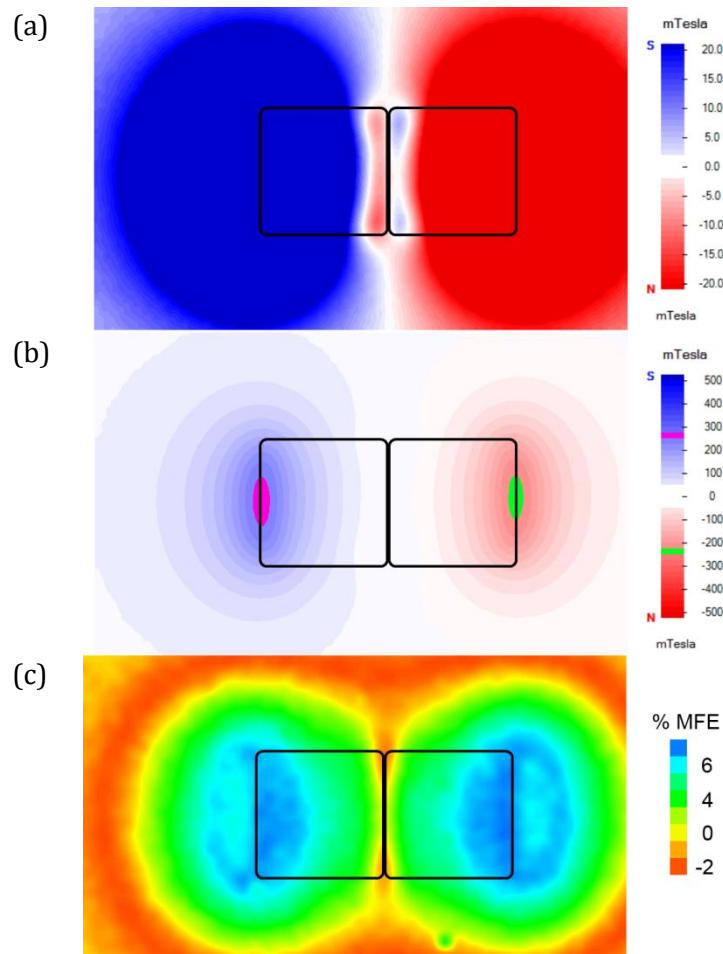


Figure 6.45: (a) MagCam plot of magnetic field magnitude with the two cube magnet outlines overlaid. Blue represents magnetic field from the magnet's south pole whilst red represents field from the magnet's north pole. This plot is scaled to ± 20 mT revealing fine detail whilst (b) is scaled to ± 500 mT to accommodate the entire field range. (c) False colour image of the MFE fluorescence photograph from figure 6.43 with the two cube magnet outlines overlaid. The MagCam plot and the MFE fluorescence photograph have been spatially scaled relative to one another.

6.6 Magnetic Polarity Detection via Optical Polarisation Analysis

One of the issues faced in the previous sections was the inability to differentiate magnetic field of opposing polarity. In §4.2.5 and §4.3 two methods were described that allows an attempt to be made to measure asymmetries in the magnetic field effect consistent with detection of opposing magnetic polarity. In this section results will be presented from each method together with an analysis of the results.

The first experiment, described in §4.2.5, involved using the HF-MFE system with additional polarisation optics on the emission side to collect any circular polarisation emission from a

tetracene thin film and analyse it with a linear polariser aligned either $\pm 45^\circ$ with respect to the $\lambda/4$ wave plate. Three measurements were taken with one in the -45° orientation and two in the $+45^\circ$ orientation to ensure that any differences measured are due to a dependence on the analyser angle. Figure 6.46 contains the results of this experiment. It can be seen that when scaled to view the whole MFE up to 300 mT the plot reveals no obvious differences in MFE intensity in either orientation. Figure 6.47 plots the same data seen in figure 6.46, but only for the data measured above 200 mT, allowing the relative line positions to be seen. It can be seen that each $+45^\circ$ line exists both above and below the -45° orientation suggesting that there is no magnetic polarity-sensitive circular dichroism being observed in the fluorescent emission. This negative result could be due to the geometrical configuration of the experiment setup; i.e. due to the fact that the magnetic field is perpendicular to the fluorescence emission may limit any predicted effect.

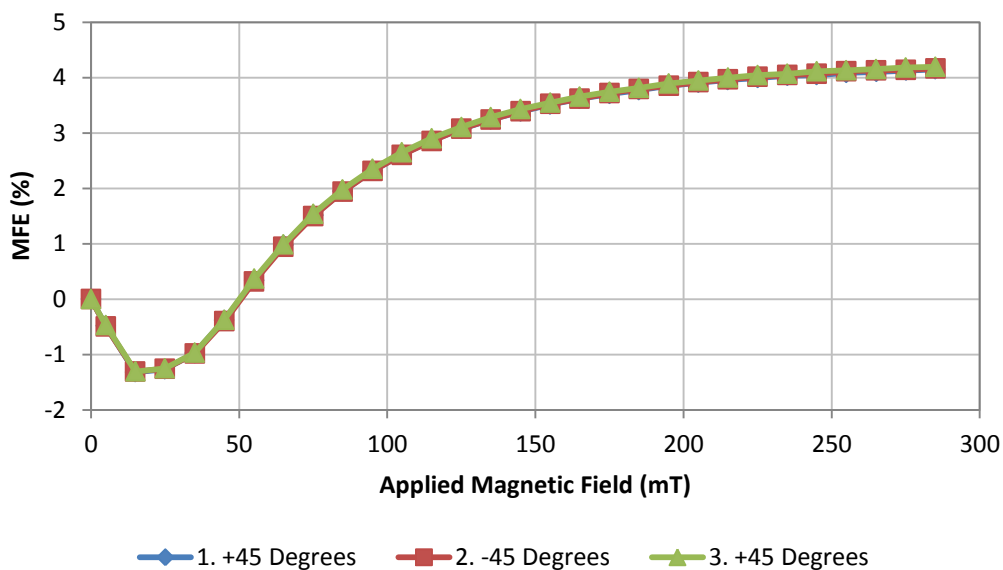


Figure 6.46: Polarisation analysis results from the HF-MFE system using a tetracene powder sample.

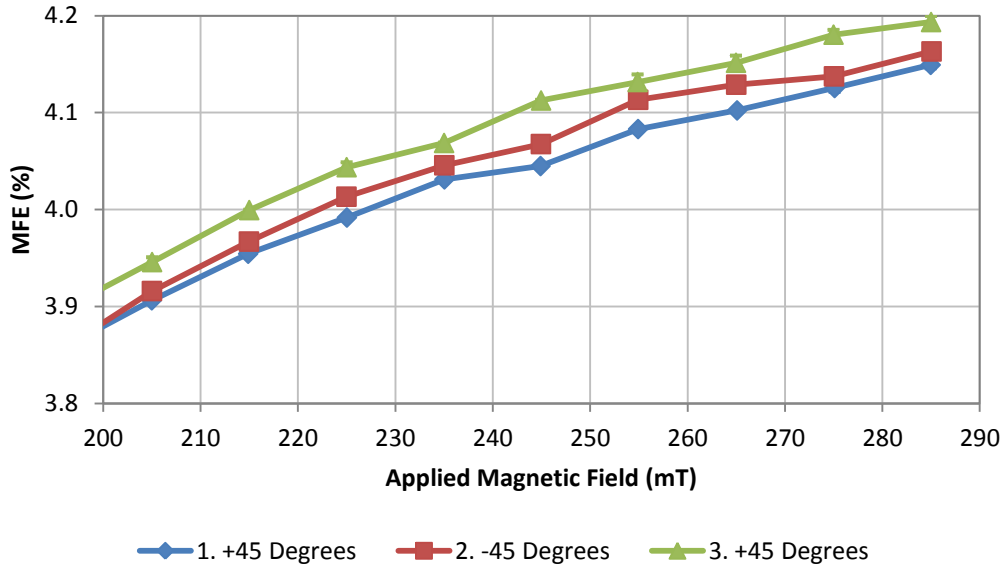


Figure 6.47: Zoomed-in version of the data from figure 6.46 showing the relative positions of each data series.

The second experiment, described in §4.3, made use of the fluorescent magnetic field effect photography system in an attempt to measure magnetic polarity-sensitive circular dichroism. As described in §4.3 polarisation optics were used in both the excitation and emission side of the setup. In the first set of results the excitation $\lambda/4$ wave plate was aligned $+45^\circ$ with respect to the excitation linear polariser with these alignments maintained throughout the first set of results. This was chosen in order to convert the LED emission into circularly polarised light of a particular handedness. The excitation linear polariser and the slow axis of the emission $\lambda/4$ wave plate were maintained at 0° throughout every measurement. The independent variable that was manipulated was the linear polariser angle on the emission side of the setup. This was varied from $+70^\circ$ to -90° to observe circularly polarised emission from the sample, especially of each handedness at $+45^\circ$ and -45° .

Figure 6.48 contains the first set of results. It can be seen that as the analyser angle is increased from 0° the left lobe begins to fade in brightness relative to the right lobe. At the $+45^\circ$ orientation (figure 6.48b) the measured contrast asymmetry between the lobes maximises to $\approx 15\%$. As the angle approaches $+70^\circ$ both lobes darken, however the right lobe can still be seen.

The same is true if the analyser is decreased from 0° down to -90° . Indeed at the -45° orientation (figure 6.48d) the contrast asymmetry between the lobes maximises at $\approx 12\%$.

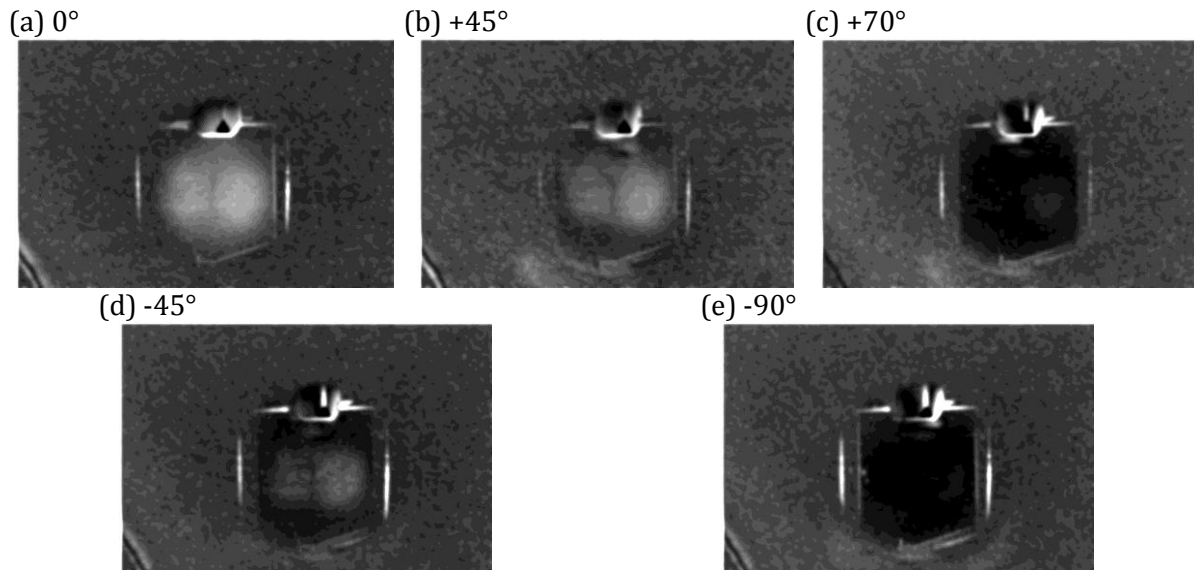


Figure 6.48: First set of fluorescence difference photographs of the tetracene thin film sample as a function of analyser angle.

In the second set of results the excitation $\lambda/4$ wave plate was aligned -45° with respect to the excitation linear polariser with these alignments maintained throughout the second set of results. This was chosen in order to convert the LED emission into circularly polarised light of the opposite handedness with respect to the first set of results. The independent variable that was manipulated was the linear polariser angle on the emission side of the setup. The excitation linear polariser and the slow axis of the emission $\lambda/4$ wave plate were maintained at 0° throughout every measurement. Figure 6.49 contains the second set of images. It can be seen that as the analyser angle is increased from 0° the right lobe begins to fade in brightness relative to the left lobe. At the $+45^\circ$ orientation (figure 6.49b) the measured contrast asymmetry between the lobes $\approx 4\%$. As the angle approaches 90° both lobes darken until they completely disappear. The same is true if the analyser decreased from 0° down to -90° . Indeed at the -45° orientation (figure 6.49d) the contrast asymmetry between the lobes $\approx 5\%$.

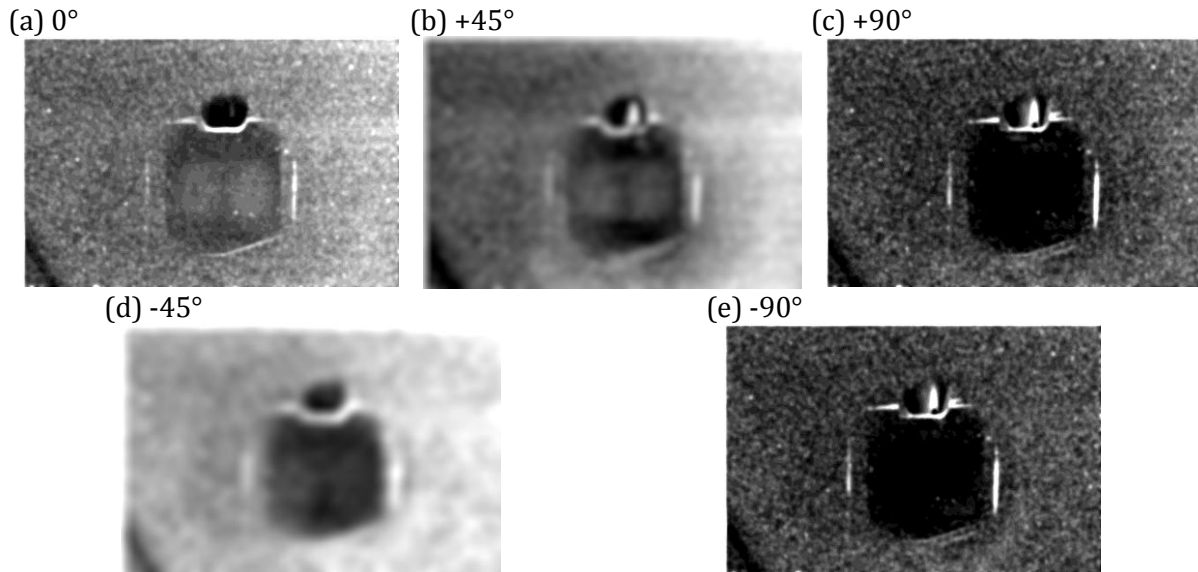


Figure 6.49: Second set of fluorescence difference photographs of the tetracene thin film sample as a function of analyser angle. Figures (b) and (d) have additional Gaussian blurring purely acting as a visual aid.

It is concluded from the two sets of results of the second experiment that magnetic polarity-sensitive circular dichroism can be detected using the fluorescent magnetic field effect observed in tetracene. It appears that the underlying mechanism of the observed lobe brightness asymmetry is likely due to selective absorption of the circularly polarised excitation light by the tetracene thin film in the presence of a magnetic field; otherwise known as magnetic circular dichroism. This is concluded by the fact that the only variable change occurring between the two sets of measurements is that of the excitation quarter-wave plate is being rotated from $+45^\circ$ to -45° causing the handedness of the circularly polarised light to switch and the observed lobe brightness asymmetry to invert.

What complicates this interpretation, however, is observation of contrast variation which is dependent on emission analyser angle. As all of the photographs shown in figures 6.48-49 are difference images taken against a reference image (magnet removed, analyser set to 0°) the dark contrast observed in figures 6.48c&e and figure 6.49c&e suggests that little to nothing has altered between exposures. However, the magnets have been removed meaning a difference image should show the MFE contrast associated with that change. Therefore, rotation of the analyser to $\pm 90^\circ$ must be blocking the fluorescence from the MFE lobes from reaching the camera. One possible reason for this would be if circular polarisation of one handedness was

being emitted from the sample and was been converted to linearly polarised light by the quarter-wave plate. However, to cause the fluorescence to be maximally blocked from the camera's perspective the analyser would have to be at $\pm 45^\circ$ with respect to the quarter-wave plate. In this case, however, maximal blocking is occurring at $\pm 90^\circ$ instead. The only other likely explanation is if the fluorescence emission is unpolarised, which would be unaltered when transmitted through the quarter-wave plate. Upon incidence with the analyser it would become linearly polarised. Now, if the camera lens contains a polariser and it was oriented at 0° this would cause the incident polarised light to be blocked. Although this explanation appears to satisfy all observations it does not explain why the lobe contrast should appear to be strongest when the analyser is at $\pm 45^\circ$.

In summary, further work needs to be performed in order to confirm the exact mechanism of the fluorescent MFE magnetic polarity sensitivity. A likely future experimental design should aim to separate the excitation and emission optics whilst measuring their responses independently.

6.7 Conclusion

This chapter investigated using the magnetic field effect exhibited in the photoluminescence of certain organic molecules to create images of magnetic field from various bulk and nanostructured thin film magnets. An experimental photoluminescent magnetic field effect photography system was used in an attempt to capture MFE images of macroscopic magnetic structures via a tetracene thin film. This experiment was successful with two different structures having been observed. This represents the first ever magnetic field effect image of a magnetic structure.

Confocal microscopy was used to observe magnetic nanostructures coated with a thin film of either TPD:BBOT:PMMA or polycrystalline tetracene. It was hoped that this technique would allow the first MFE micrographs to be observed; however, for various reasons this did not occur

even when employing the difference imaging technique to enhance magnetic contrast. Further work is needed based on the suggestions discussed.

An experiment with the aim to observe magnetic polarity-detection via magnetic circular dichroism was attempted. This experiment comprised of two parts: the first used the HF-MFE system whilst the second used the fluorescence MFE photography system. The first experiment did not yield conclusive results whilst the second experiment successfully measured magnetic polarity-sensitive circular dichroism using the fluorescent magnetic field effect. However, further work is needed to improve the results and achieve consistency between both experiments.

Micromagnetic simulations were undertaken and combined with experimental results to establish the likely appearance of potential MFE micrographs of magnetic nanostructures. This exercise was undertaken for three different structures using two experimentally measured MFE profiles.

Finally, several magnetic contrast detection techniques were presented and discussed. It was found that M-TXM can provide high-resolution micrographs, but that the technique can suffer from non-magnetic contrast contributions such as X-ray beam drift complicating the image difference process. This technique allowed the structure of the magnetic vortex walls present in a ring nanostructure to be revealed in detail. Results from the magnetic force microscopy technique were presented and discussed revealing that MFM can deliver high-resolution, high-contrast micrographs, but can suffer from tip-sample perturbations, long measurement times and contrast patterns that are difficult to interpret due to the indirect method of magnetisation detection. This technique allowed the determination of the appropriate external magnetic field required to nucleate magnetic domain walls in the serpentine wire structures. MOKE magnetometry was used in a time-resolved study to acquire magnetic hysteresis loops of several ring structures and allow the likely magnetisation configurations to be determined.

MOKE also allowed the appropriate external magnetic fields required to create these configurations to be determined.

6.8 References

- [1] T. Shinjo, *et al.*, "Magnetic vortex core observation in circular dots of permalloy," *Science*, vol. 289, pp. 930-932, Aug 2000.
- [2] A. Wachowiak, *et al.*, "Direct observation of internal spin structure of magnetic vortex cores," *Science*, vol. 298, pp. 577-580, Oct 2002.
- [3] T. Uhlig, *et al.*, "Shifting and pinning of a magnetic vortex core in a permalloy dot by a magnetic field," *Physical Review Letters*, vol. 95, Dec 2005.
- [4] T. J. Hayward, *et al.*, "Exquisitely balanced thermal sensitivity of the stochastic switching process in macroscopic ferromagnetic ring elements," *Physical Review B*, vol. 72, Nov 2005.
- [5] S. Ladak, *et al.*, "Direct observation of magnetic monopole defects in an artificial spin-ice system," *Nature Physics*, vol. 6, pp. 359-363, May 2010.
- [6] NIST. (2006, 15/09/2013). *The Object Oriented MicroMagnetic Framework (OOMMF) project at ITL/NIST*. Available: <http://math.nist.gov/oommf/>
- [7] K. Mitsuzuka, *et al.*, "Magnetic vortices in single crystalline Fe-V disks with four folds magnetic anisotropy," *Applied Physics Letters*, vol. 100, May 2012.
- [8] S. McVitie, *et al.*, "Quantitative imaging of magnetic domain walls in thin films using Lorentz and magnetic force microscopies," *Journal of Applied Physics*, vol. 90, pp. 5220-5227, Nov 2001.
- [9] A. Hubert and R. Schafer, *Magnetic domains: the analysis of magnetic microstructures*: Springer, 1998.
- [10] K. J. Kirk, *et al.*, "Switching of nanoscale magnetic elements," *Applied Physics Letters*, vol. 75, pp. 3683-3685, Dec 1999.
- [11] E. C. Stoner and E. P. Wohlfarth, "A Mechanism of Magnetic Hysteresis in Heterogeneous Alloys," *Philosophical Transactions of the Royal Society of London Series a-Mathematical and Physical Sciences*, vol. 240, pp. 599-642, 1948.

- [12] K. M. Seemann, *et al.*, "Disentangling the Physical Contributions to the Electrical Resistance in Magnetic Domain Walls: A Multiscale Study," *Physical Review Letters*, vol. 108, Feb 2012.
- [13] R. Hertel and H. Kronmuller, "Micromagnetic simulation of the domain structure of a flat rectangular permalloy prism," *Journal of Applied Physics*, vol. 85, pp. 6190-6192, Apr 1999.
- [14] B. R. Masters, *Confocal Microscopy and Multiphoton Excitation Microscopy: The Genesis of Live Cell Imaging*: SPIE Press, 2006.
- [15] F. Cicoira, *et al.*, "Correlation between morphology and field-effect-transistor mobility in tetracene thin films," *Advanced Functional Materials*, vol. 15, pp. 375-380, Mar 2005.

7 Muon Spin Resonance Spectroscopy

7.1 Introduction

In the last few years there has been considerable growth in the use of organic semiconductors (OSC) in many sectors of technology from consumer electronics where organic light-emitting diode (OLED) displays are beginning to dominate the consumer market [1, 2], to power generation where organic solar cells are being touted as the next generation of solar cell technology due to their potential low production costs and versatility [3]. Although much is known about these materials there still exists a limited understanding in some of the more fundamental properties such as electronic transport mechanisms and spin dynamics. As OSCs are being incorporated into increasingly sophisticated technologies (e.g. spintronic devices [4, 5]), where it is required that the materials behave in a highly predictable manner, understanding of the fundamental properties of these materials is seen as critical to the successful development of these technologies.

The current methods of investigating electronic transport and spin dynamics in organic semiconductors include femtosecond optical spectroscopy, magnetoresistance (MR) measurements [6, 7], and time-of-flight (TOF) electron mobility measurements [8, 9]. The first of these techniques is extremely successful in the characterisation of inorganic semiconductors, however, it is practically useless in measuring OSCs due to the techniques reliance on the spin-orbit interaction (which is weak in OSCs) [5]. The second technique requires the creation of spin-valve devices in order to characterise the OSC. The ferromagnetic electrodes used in these devices, however, make it difficult to identify which components contribute to the measured properties leading to discrepancies in reported spin coherence time of OSCs, for example [10, 11]. It is also not known what influence the electrodes and their interfaces have on the intrinsic transport properties within the OSC layer. So although these techniques have provided a great

deal of information they cannot provide a complete description of electronic spin transport in OSCs.

In this chapter it will be shown how the muon spin resonance spectroscopy technique (μ SR) can be used as a local matter probe to successfully characterise the electronic transport properties of the organic semiconducting materials poly(3-hexylthiophene-2,5-diyl), P3HT, and poly(3-hexylselenophene-2,5-diyl), P3HS. All work presented was performed at the ISIS Neutron and Muon Source research facility at Harwell Oxford, Didcot, Oxfordshire, UK.

7.2 Theory

7.2.1 Muon Production

The muon is an elementary particle belonging to the lepton family therefore possessing a spin of $\frac{1}{2}$. Its mass is $105.6 \text{ MeV}/c^2$ which is approximately $207\times$ the mass of an electron and $0.113\times$ the mass of a proton. In μ SR spectroscopy the matter probe which is exclusively used is the antiparticle of the muon, the positive muon, μ^+ . The positive muon shares the same properties as the regular muon except the charge is positive instead of being negative. The production of a positive muon beam at the ISIS Neutron and Muon Source research facility is described as follows.

The process [12] begins with the production of hydrogen ions, H^+ , from the ion source device which extracts hydrogen ions from a discharge plasma created from molecular hydrogen gas and caesium vapour. These ions are then accelerated and separated into 'bunches' using an RF quadrupole accelerator. From here the ions are further accelerated using a linear accelerator (linac) until they reach an energy of 70 MeV. Upon reaching the end of the linac the ions pass through a 300 nm thick sheet of aluminium oxide foil where the electrons are stripped away leaving a beam composed entirely of protons. The proton beam is then transferred into the 52 metre diameter synchrotron where the multiple bunches of protons accumulate into two main bunches taking position at opposite sides of the synchrotron. At this point the two bunches are

accelerated to 800 MeV over a period of 10,000 revolutions around the synchrotron. Once the target energy has been reached the 4 μC of protons are ‘kicked’ out of the synchrotron as two 100 ns long pulses into the extracted proton beam line and sent to the muon and neutron targets. The muon target, the first target the protons encounter, consists of a 10 mm thick disc of graphite. Collision of the proton beam with the target results in the production of neutrons and pi mesons (pions) (equations 7.1 and 7.2) which decay after a mean lifetime, τ_π , of 26 ns. The pion decay products (equation 7.3) consist of a positive muon and a muon neutrino. After a mean lifetime, τ_μ , of approximately 2.2 μs [13] the muon decays (equation 7.4) into a positron, an electron neutrino and a muon antineutrino.



The muons used for μSR are referred to as “surface muons”. These muons are produced from the decay of pions that have lost all of their momentum from traversing the thickness of the graphite target and have come to rest at the target surface facing away from the incoming proton beam. Under these conditions the muons produced from the decay of pions at rest have a low and narrowly distributed momentum (29.80 MeV/c). Most importantly the surface muons generated in this process are *highly* spin-polarised (> 99%) [14]. The surface muons are emitted with their spin polarisation aligned anti-parallel to the direction of their momentum. The low momentum of surface muons means that they can be implanted into a sample with relative ease.

7.2.2 Muon Implantation

In order to use the surface muons as a matter probe the process [14] of implanting them into the sample of interest needs to be addressed. Muons, which enter the sample with an energy up to 52.8 MeV, undergo three main mechanisms in order to lose sufficient kinetic energy to

become implanted inside the sample. The first stage of energy loss is referred to as ionisation and describes how muons will scatter off electrons, transferring their momentum in the process, causing ionisation within the sample. This first stage reduces the muon's energy to around 2 keV. The second stage of energy loss is referred to as thermalisation. This is where muons are able to electrostatically capture electrons forming an exotic atomic species known as 'muonium'. Muonium is comparable to atomic hydrogen, consisting of one positively charged species and one negatively charged species. Although a muon is able to capture an electron it still has excess kinetic energy and will cyclically capture and release electrons until it has completely thermalised with a residual kinetic energy of a few hundred electronvolts. The final stage of muon implantation is the 'collision' stage. This stage involves muonium colliding both elastically and inelastically with native atomic and molecular species coming to rest within the sample where it can bond with the host molecule.

All of these processes describing the muon reaching its ground state occur within approximately one nanosecond, which is very fast compared to the muon lifetime. This leaves plenty of time for observations to be made. Also it is important to note that the initial spin-polarisation of the muon does not get affected by these implantation processes as they are primarily electrostatic in nature; only when the muon has reached a stable ground state does the local environment begin to influence its spin causing precession and/or relaxation.

7.2.3 Muon Decay

As discussed previously the muon has a mean lifetime of 2.2 μs . After this time the muon will undergo beta decay and emit a positron, an electron neutrino and a muon antineutrino (as described by equation 7.4). The key to the μSR technique is that due to parity violation of the weak interaction the instantaneous polarisation of the decaying muon can be detected via the anisotropy of the positron decay emission. Upon decay of an individual muon the probability of the positron being emitted at an angle θ relative to the instantaneous spin orientation of the muon is expressed as [15]:

$$p(\theta) = 1 + a \cos \theta \quad \text{Equation 7.5}$$

where a is the asymmetry parameter which is a function of positron energy. For a high asymmetry, $a = 1$ (represented by the red line in figure 7.1), the positron energy is highest whilst for the lowest positron energies, a can be negative [16]. For most μ SR instruments the average positron energy gives $a \approx \frac{1}{3}$ (represented by the blue line in figure 7.1) and means that the forward emission probability is approximately twice that of the backward emission probability. As the muon spin begins to be influenced by the local environment of the sample and/or an applied magnetic field the angular distribution plot should be considered to be 'locked' relative to the orientation of the muon spin.

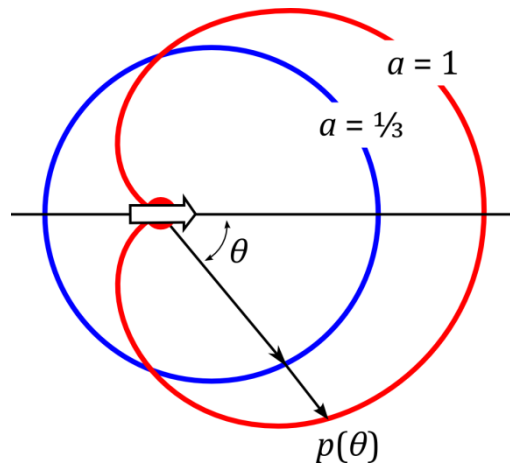


Figure 7.1: Polar diagram of the angular distribution of beta decay emission where a is the asymmetry parameter. Adapted from [15].

7.2.4 Data Acquisition

Once the muon has decayed the aptly named 'forward' and 'backward' detectors, each comprised of a ring of scintillators coupled to photomultiplier tubes (PMTs) via light guides, are able to detect the emitted positron from scintillation produced by the positron striking the scintillator. Figure 7.2 illustrates the typical configuration of a muon spectrometer whereby the muon beam enters through the centre of the backward detector and implants into the sample that is mounted centrally.

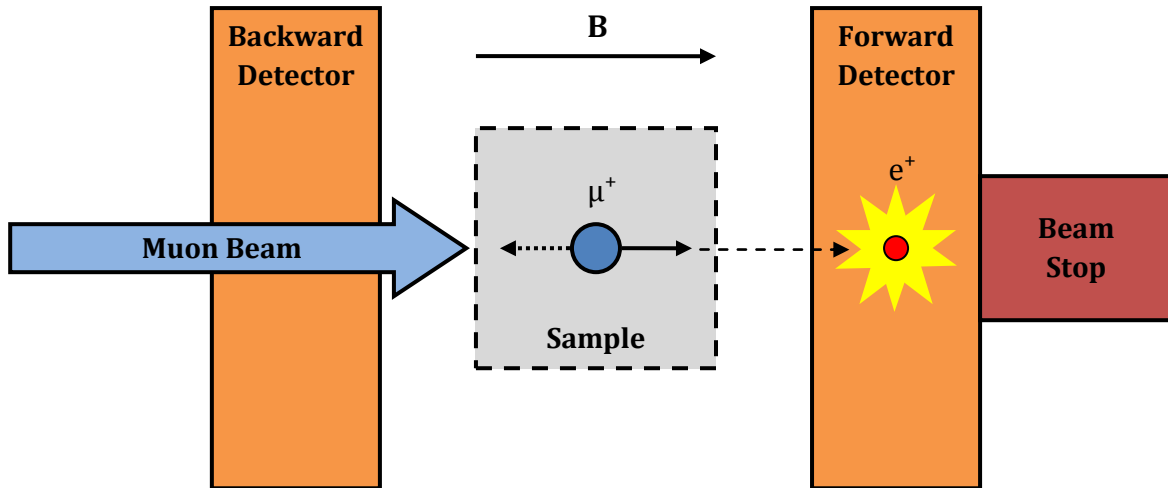


Figure 7.2: Illustration of a typical muon spectrometer instrument configuration. In this illustration a large magnetic field is applied longitudinally with respect to the muon beam axis. This causes the muon spin to rotate from its original orientation (dotted arrow) and align parallel with the applied magnetic field (solid arrow). Upon decay of the muon the positron is most likely to be emitted along the direction of the muon's final spin orientation.

With a pulsed muon source (as per this work) large bunches of muons are implanted into the sample effectively simultaneously. At this point the experimental clock is started. Each detection event is timed with respect to the arrival of the respective muon bunch and as each detector is actually composed of a ring of detectors multiple detections can occur simultaneously. This process is repeated until enough events have been detected such that there is statistical confidence in the measurement.

The time-evolution of the muon spin ensemble is monitored by calculating the difference in count rate between the detectors as a function of time and dividing that by the total count rate in order to normalise with respect to the time-dependent decay of the population of muons. This asymmetry can be written as [17]:

$$A(t) = \frac{N_F - \alpha N_B}{N_F + \alpha N_B} \quad \text{Equation 7.6}$$

where N_F and N_B are the number of events detected at the forward and backward detectors, respectively, whilst α is an empirical constant representing the intrinsic asymmetry between the forward and backward detector count rates. This asymmetry results from differences

between efficiencies of the detectors and can include extrinsic factors such as sample misalignment, etc.

7.2.5 Avoided Level Crossings

One of the main experimental results obtained from performing μ SR longitudinal magnetic field measurements is an avoided level crossing (ALC) resonance as illustrated in figure 7.3. This is where the muon Zeeman splitting is tuned with a magnetic field to match the combined Zeeman and quadrupolar splitting of a neighbouring spin system. The peaks measured represent a spin flip resonance of the muon ensemble implanted within the material. Resonances are caused by an interaction of the muon spin with another particle such as a captured electron or nearby atomic nucleus. Multiple resonances can be observed in one scan with each resonance representing a unique interaction with the muon ensemble.

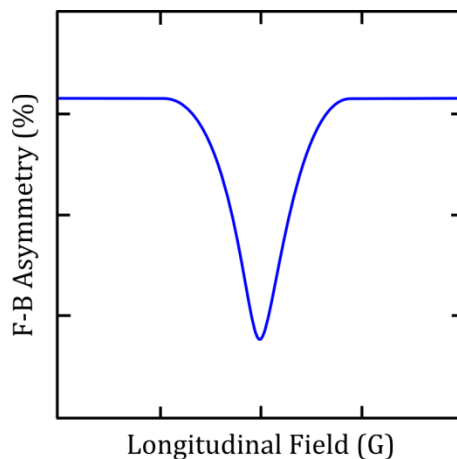


Figure 7.3: Illustration of a typical ALC resonance peak using the muon spin resonance technique with an applied longitudinal field.

In the case of isotropic muonium (a two-spin system consisting of a muon and an electron) the system has four energy levels in two states: singlet and triplet (where the three triplet energy levels are degenerate). Under the application of a magnetic field this degeneracy is lifted via the Zeeman effect (figure 7.4a). At a magnetic field of 16.4 T one of the triplet levels crosses with the singlet level forming a level crossing (see inset in figure 7.4b). Now, by introducing nuclear spins a hyperfine interaction (HFI) is introduced causing a mixing of states. In this scenario the

levels no longer cross, but instead, avoid each other. This is referred to as an *avoided* level crossing. As a magnetic field approaches the ALC so-called ‘Rabi’ oscillations begin to occur in the time-resolved measurements representing spin-flip resonance between the two energy levels. In the time-integrated measurements these oscillations are not visible but instead a resonance is observed in the form of a reduction in the polarisation of the muon ensemble.

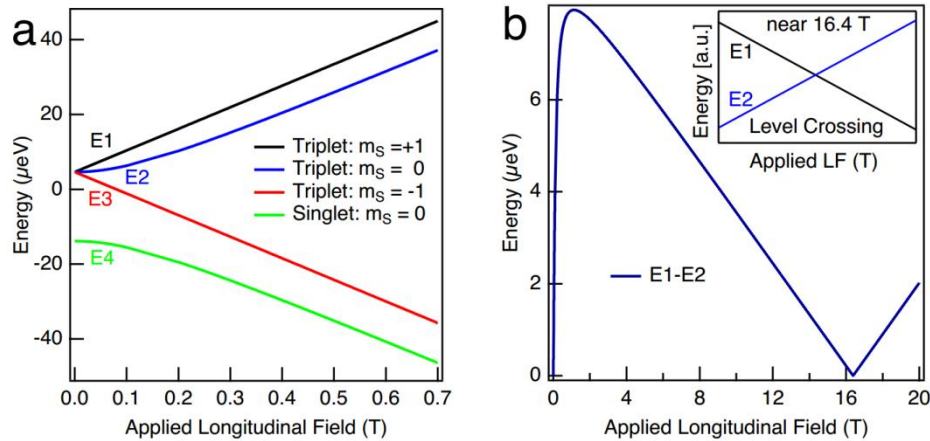


Figure 7.4: Illustration of a typical ALC resonance peak using the muon spin resonance technique with an applied longitudinal field.

Overall three types of ALC resonances exist (see figure 7.5).

1. The first is the $\Delta 0$ and is a muon-nuclear spin flip-flop transition. It is caused by coupling of the isotropic muon hyperfine coupling (HFC) to the nuclear HFC, mediated by the electron.
2. The second type of ALC resonance is the $\Delta 1$ and is a muon-electron spin flip resonance caused by the dipolar components of the HFI.
3. The third type of ALC resonance is the $\Delta 2$ and is a muon-nuclear spin flip-flip transition.

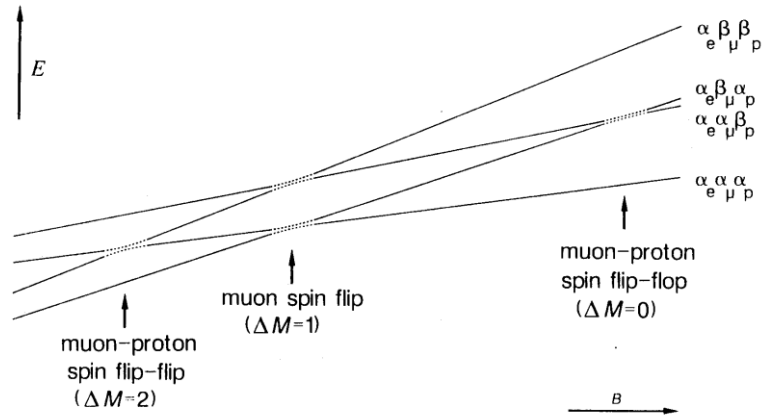


Figure 7.5: Illustration of the energy landscape as a function of applied field. Shown are the three possible types of ALC resonance observed in μ SR spectroscopy.

As this research is focussed on determining the electronic transport properties in OSCs the second type of resonance, $\Delta 1$, will be the only ALC resonance type studied.

By modelling ALC resonances using quantum mechanical density matrix methods [18] it is possible to build up a theoretical picture of the electron spin dynamics and transport properties in OSCs.

7.3 Experimental Details

The muon experiments occurred at the ISIS Neutron and Muon Source research facility maintained by the Science & Technology Facilities Council in Oxfordshire, UK. ISIS consists of two large experimental halls, referred to as target stations, which house over 40 instruments. Target Station 1, where the μ SR instruments are located, produces a typical muon beam current of $6.0 \mu\text{A}$ at a pulse frequency of 40 Hz. The muon target at ISIS consumes 2-3% of the proton beam [12] with the rest reserved for neutron science. The research presented in this chapter occurred exclusively on the high field muon spectrometer and derived from four separate beamline experiments totalling 23 days or 552 hours of measurements. All experimental work was performed in collaboration with research scientists Dr Maureen Willis, Dr Nicola Morley, Dr Laura Nuccio, Dr Alan Drew, and beamline scientists Dr Mark Telling, Dr Francis Pratt and Dr James Lord.

7.3.1 High Field Muon Spectrometer

The high field muon spectrometer (HIFI) is the newest addition to the muon facility at ISIS having been installed in 2009 (see figure 7.6). The spectrometer consists of a ± 5 Tesla superconducting magnet that can operate a sustained magnetic field applied longitudinally with respect to the incoming muon beam. The magnet is cooled by a closed-cycle helium refrigerator which recycles the helium minimising waste. HIFI is also equipped with a magnet capable of applying transverse fields up to 15 mT. The instrument incorporates two sets of 32 scintillators arranged in circular disc arrays to detect positron emissions at the forward and backward positions of the instrument. HIFI offers a diverse range of sample environments with various cryostats and furnaces available.

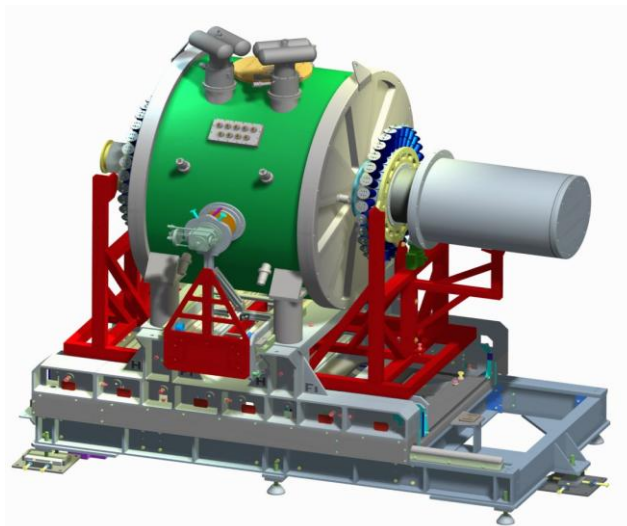


Figure 7.6: 3D rendering of the HIFI spectrometer.

Copyright © 2013 Science and Technology Facilities Council.

The typical event rate on HIFI is in the region of 40-45 million events (MEv) per hour with a default temporal resolution of 16 ns and a maximum time window of 32 μ s [19].

7.3.2 Sample Preparation

Two types of organic semiconductors were studied: P3HT and P3HS (see table 7.1). Three morphologies of P3HT were measured in total with two used in the as-bought state from Sigma Aldrich Corporation. These three morphologies are described as follows:

- 179.0 mg of as-bought regio-regular P3HT (where the repeating unit of the polymer adopts the same orientation throughout the polymer).
- 219.7 mg of as-bought regio-random P3HT (where the repeating unit of the polymer adopts a random arrangement throughout the polymer).
- 373.1 mg of recrystallised regio-regular P3HT (where the as-bought regio-regular P3HT has been further crystallised via dissolution into chloroform and precipitated back out via controlled evaporation of the solvent).

The final sample measured was 87.4 mg of regio-regular P3HS which was produced courtesy of Dr Martin Heeney from Imperial College London.

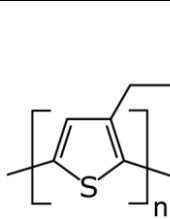
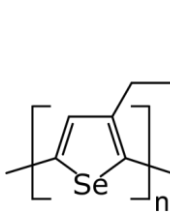
Short Name	IUPAC Name	Chemical Formula	Skeletal Formula
P3HT	Poly(3-hexylthiophene-2,5-diyl)	$(C_{10}H_{14}S)_n$	
P3HS	poly(3-hexylselenophene-2,5-diyl)	$(C_{10}H_{14}Se)_n$	

Table 7.1: Organic semiconductors used in this research.

Samples were individually mounted in high-purity silver packets measuring 20 × 30 mm with a thickness of 25 μm and suspended in an aluminium frame. Silver is used as the packaging medium as it has very little effect on the muons inducing neither precession nor relaxation of

the muon spin ensemble. Sometimes a ‘degrader’ is added to the packet (usually an extra layer or two of silver foil) in order to decelerate the muons sufficiently to implant them in the sample. The aluminium frame was when secured to the end of the cryostat arm and inserted into the centre of the spectrometer (see figure 7.7). The spectrometer was then pumped down to an ultra high vacuum.

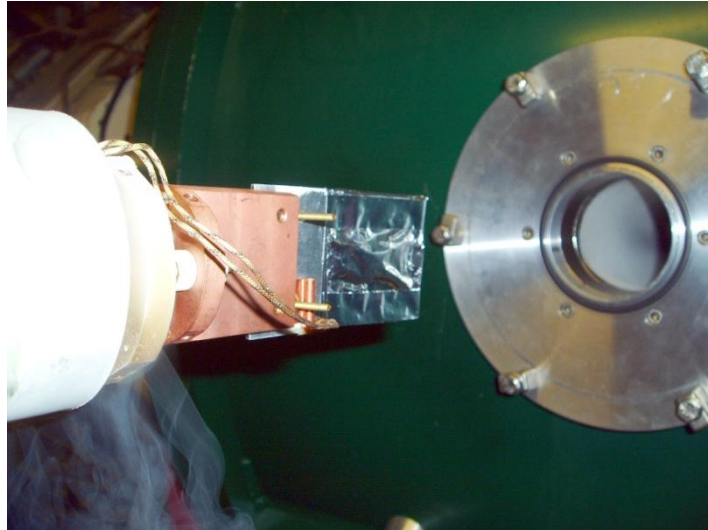


Figure 7.7: Photograph of a silver-packaged sample mounted on the cryostat arm prior to being loaded into the HIFI spectrometer.

7.3.3 Instrument Calibration

At the beginning of every scan set a transverse field measurement is made. This consists of applying a static 20 G transverse magnetic field to the sample whilst allowing the system to reach an event count of 5 million (taking < 7 minutes at an average event rate of 40-45 MEV). The event counts from the individual forward and backward detectors, plotted as a function of time, are shown in figure 7.8. From this measurement it can be seen that an oscillation in the event counts with time has formed. This represents the precession of the muon spin ensemble in the applied field.

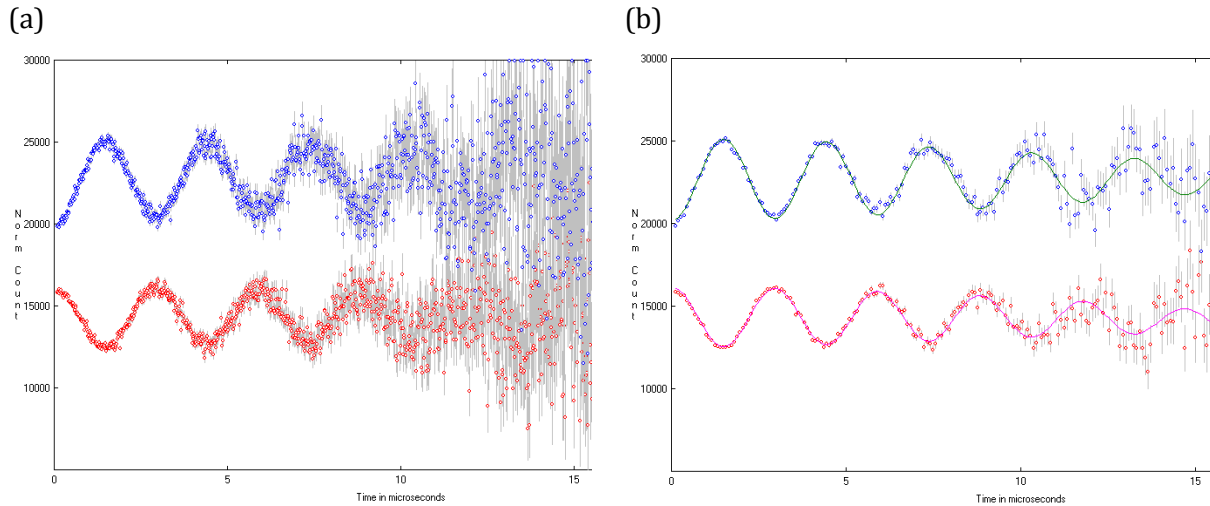


Figure 7.8: (a) Plot of the forward (blue) and backward (red) event detections under the application of a static transverse magnetic field of 20 G against time. The applied field causes the muon spins to precess resulting in an oscillation of the positron detection events with time. (b) The same data as shown in (a) is shown here, however, the data has been averaged and a fit function has been applied in order to calculate α .

This procedure is performed every time a new sample is loaded and at the beginning of a new temperature scan. The reasoning is twofold. Firstly, the appearance of the oscillation indicates the muons are being implanted into the sample and provides confirmation that the sample has been mounted correctly. Should this not be the case a degrader can be added and the measurement can be repeated. Secondly, this procedure, when combined with function fitting (figure 7.8b), allows the instrument asymmetry parameter, α , to be found. It is important that α is determined as it can significantly affect the asymmetry magnitude which would make it difficult to compare different scan sets.

7.3.4 Data Processing

Data processing and analysis was performed in the Windows Muon Data Analysis (WiMDA) package [20]. Each muon spin resonance scan occurred in the longitudinal field mode with 5 MEV statistics per field. The scan range was typically from 5000 G to 13000 G (0.5 – 1.3 T) whilst the field steps were 200 G (20 mT). This range was chosen as the ALC resonance was predicted to appear within this interval. This range would also be large enough to collect data points assumed to be attributed to the background allowing background subtraction to occur.

Once the longitudinal field scan has completed each asymmetry value is calculated and plotted as a function of applied field (see figure 7.9a). After all of the asymmetry values have been plotted a background is determined based on a reference calibration chart of the field-dependent background drift for the instrument. This process involves fitting a 3rd or 4th order polynomial function to the ‘tails’ of each resonance and subtracting it from the whole data set. This produces a normalised ALC resonance plot (shown in figure 7.9b).

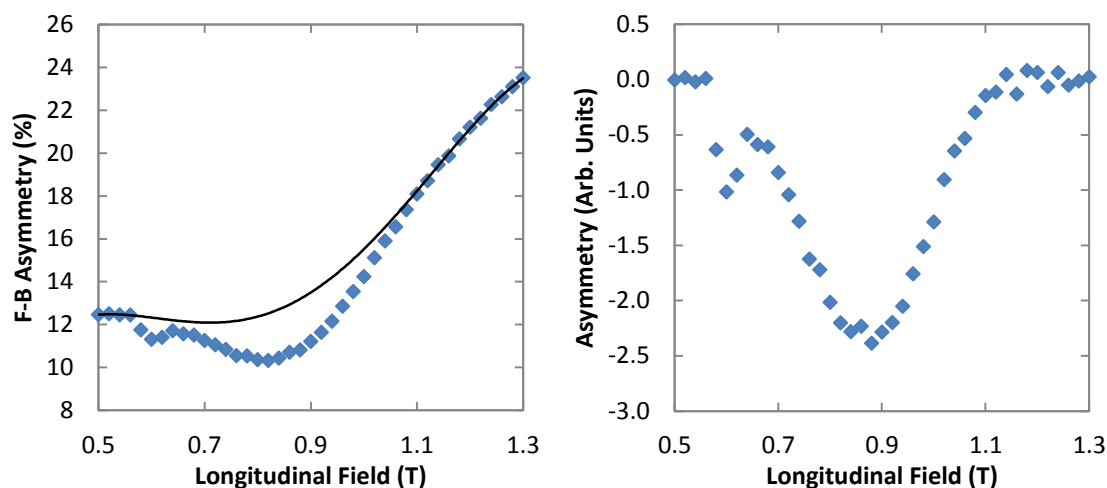


Figure 7.9: Demonstration of how the instrumental background drift is removed from the time-integrated data. (a) A low-order polynomial function is fitted to the regions of the data considered to form the background. (b) The background fit function is subtracted from the entire data set and normalised revealing the true form of the resonance peak.

7.4 Experimental Results

The first sample measured was the as-bought regio-regular P3HT. In this morphology the repeating unit of the polymer adopts a regular orientation along the chain. The time-integrated μ SR longitudinal field data is shown in figure 7.10. These data are plotted as normalised asymmetry as a function of applied magnetic field and temperature. It can be seen that the room temperature scan (300 K) produces the largest resonance centred around 8000 G (0.8 T). As the temperature is reduced to 10 K the resonance collapses in amplitude by around 67% with a slight shifting in peak position. This collapse is attributed to a relaxation of the muon spin ensemble and has been seen in similarly-structured small organic molecules also measured

using μ SR by Schulz, et al. [21]. They concluded that the muon spin relaxation was caused by thermally-activated electron spin relaxation (eSR) via the spin-orbit interaction. However, the relative magnitude of the collapse seen here appears to exceed the limits of this explanation.

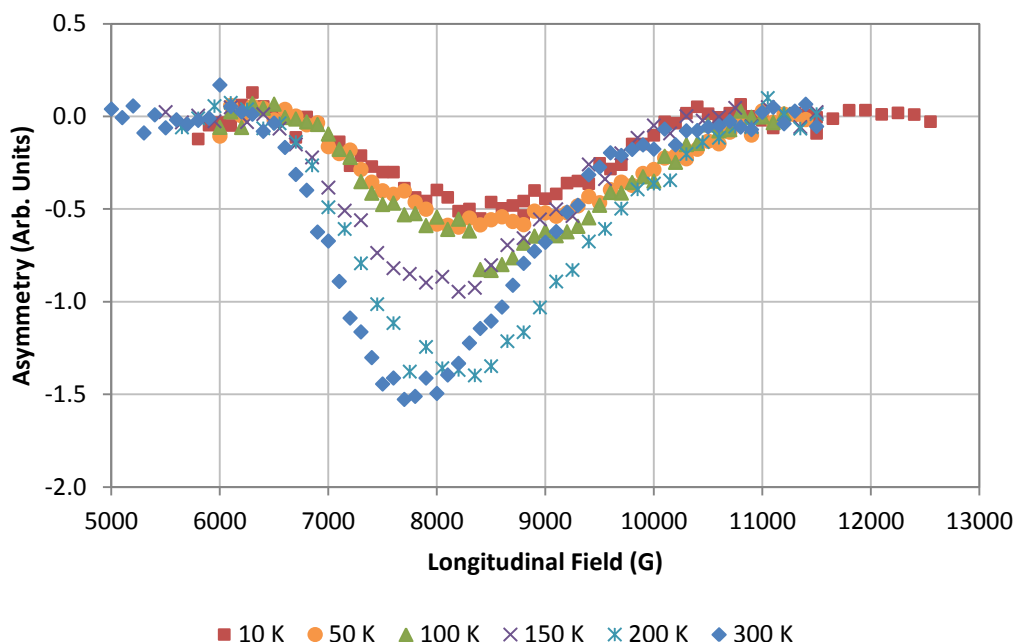


Figure 7.10: Muon spin resonance measurement of as-bought regio-regular P3HT as a function of longitudinally applied magnetic field and temperature.

To investigate what could be causing the dramatic collapse in the muon ALC resonance other morphologies of P3HT were investigated. The next sample to be measured was the regio-random form of P3HT. In this morphology the repeating unit of the polymer adopts a random arrangement throughout the polymer. This is in contrast to the regio-regular form of the polymer where the repeating unit adopts the same orientation throughout the polymer. This latter configuration enhances the crystallinity of the polymer. Figure 7.11 contains the time-integrated μ SR longitudinal field data from that measurement. Due to time constraints on the beam-line only two full temperature scans were made with one at 300 K and the other at 10 K (a larger set of temperature scans were made at the ALC peak magnetic field and are shown in figure 7.16). It can be seen that peak position for both resonances is slightly shifted from regio-regular P3HT to 8700 G. There also appears to be a second smaller ALC resonance at 6000 G. It can be seen that upon cooling to 10 K the ALC resonance has reduced in amplitude by 33%. This

temperature-dependent ALC reduction is much smaller than the collapse seen in figure 7.10 and can be accounted for by the eSR theory.

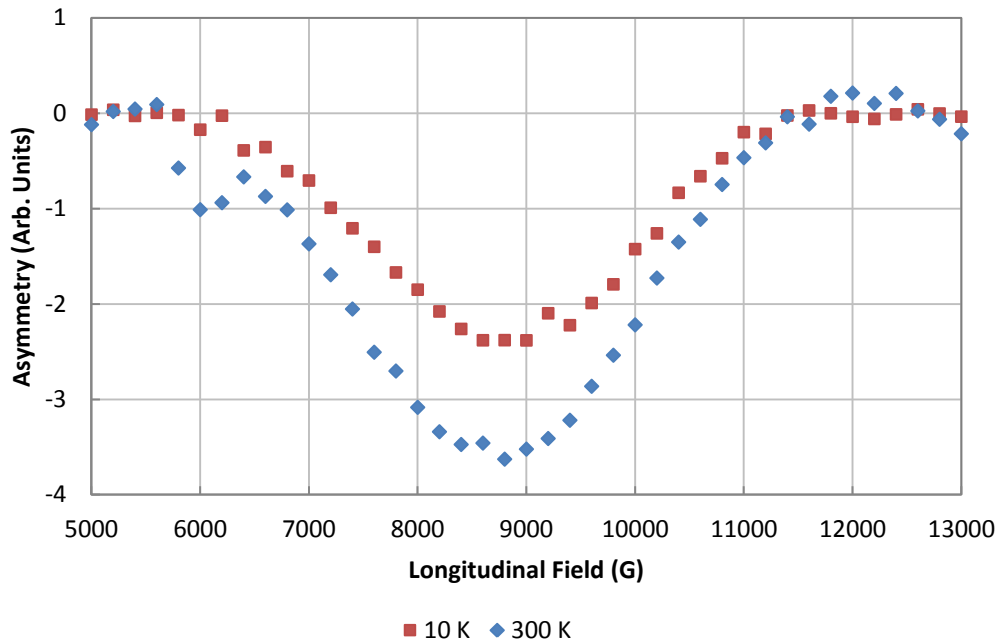


Figure 7.11: Time-integrated muon spin resonance experimental data of regio-random P3HT as a function of longitudinally applied magnetic field and temperature.

By utilising a computer program (called ‘Quantum’ [18]) that simulates the evolution of muon spins interacting with nearby nuclei and/or electrons, using a quantum mechanical density matrix method, simulations were performed in order to model the ALC resonance data presented in figure 7.11. The system was configured to include two interacting spins: a muon and an electron. Atomic nuclei were not incorporated into the model as their impact was found to be negligible. Monte-Carlo averaging was used in order to account for the powder morphology of the sample. The main parameters for the simulations can be found in table 7.2.

Parameter	Description	Effect on ALC	ALC @ 10 K	ALC @ 300 K
A (MHz)	Hyperfine coupling constants between the electron and the muon	Position	240	240
D (MHz)		Width	40	40
E (MHz)		Skewness	41	41
eSR (μs^{-1})	Electron spin relaxation	Amplitude	0.02	0.30
Monte-Carlo Steps	Powder averaging	Asymmetry Precision	5000	5000

Table 7.2: Modelling parameters used in the ‘Quantum’ program for the simulation of the ALC resonances of as-bought regio-random P3HT.

Figure 7.12 contains the results of the simulation overlaid on top of the experimental results from figure 7.11. The experimental results have been scaled onto the polarisation axis belonging to the simulation results. Specifically, the 10 K experimental data has been scaled to match the $eSR = 0.02$ simulated ALC resonance curve as electron spin relaxation is a thermally activated phenomenon therefore eSR is considered to be minimal at 10 K. The rest of the experimental data has had the same scaling factor applied to it.

There exists good agreement between the experimental results and the simulation results. It should be noted that the 6000 G ALC was purposefully excluded from the simulation in order to simplify the calculation. From these results it has been determined that the electron spin relaxation rate, which has induced the relaxation of the muon spin, equals $0.02 \mu\text{s}^{-1}$ at 10 K and increases to $0.3 \mu\text{s}^{-1}$ at room temperature.

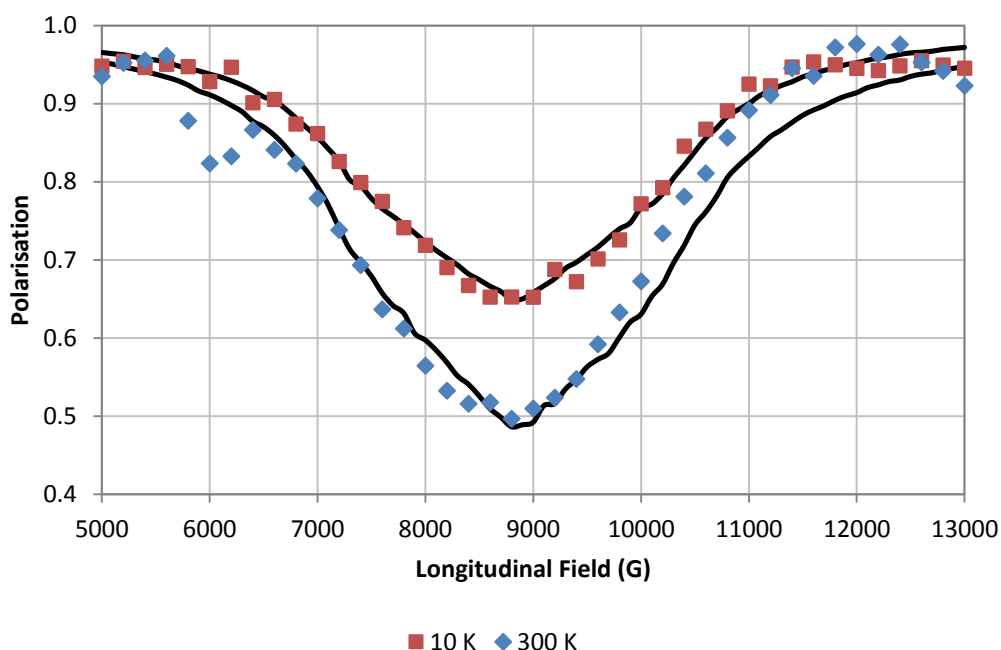


Figure 7.12: Time-integrated muon spin resonance experimental data (squares and diamonds) of regio-random P3HT as a function of longitudinally applied magnetic field and temperature. Modelling of these data is shown as solid black lines.

At this stage it would seem that the morphology of the polymer plays an important role in the collapse of the muon ALC resonance induced via electron spin relaxation. It was therefore decided to investigate the effect of increased polymer crystallinity. The next sample investigated

was the recrystallised form of the as-bought regio-regular P3HT sample. Figure 7.13 contains the time-integrated μ SR longitudinal field data from that measurement. Six temperature scans were performed from 300 K down to 10 K. As with the μ SR data for the as-bought regio-regular P3HT sample (figure 7.10) it can be seen that the ALC resonance is positioned at approximately 8000 G. It can also be seen that as the sample is cooled to 10 K the ALC resonance collapses by approximately 75% - slightly more than what was observed in as-bought regio-regular P3HT. It is suggested that the increase in crystallinity resulting from the recrystallisation process has enhanced the magnitude of the ALC collapse beyond what can be accounted for by eSR.

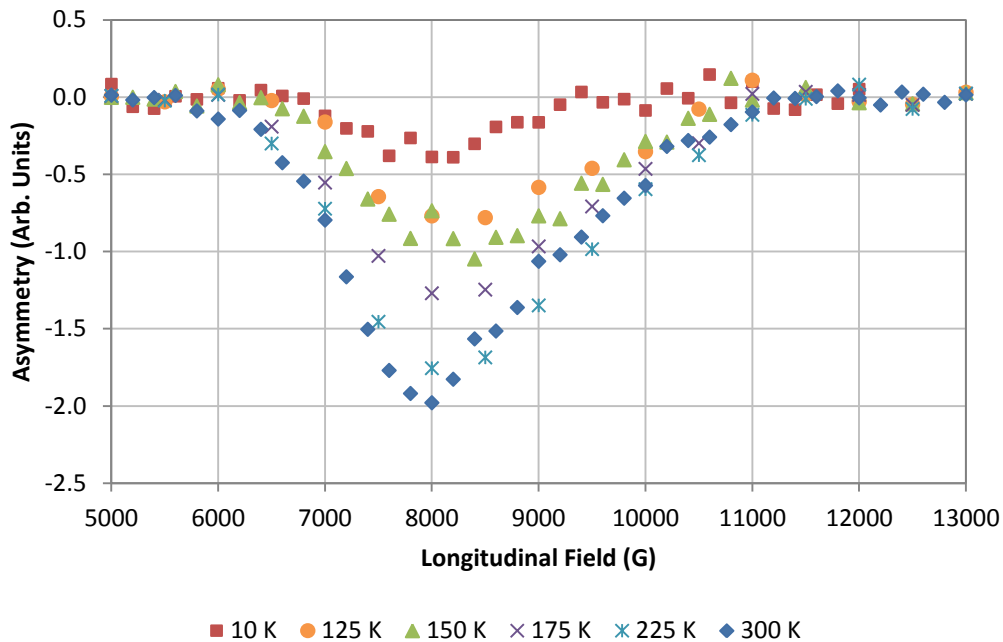


Figure 7.13: Time-integrated muon spin resonance experimental data of recrystallised regio-regular P3HT as a function of longitudinally applied magnetic field and temperature.

In order to substantiate the last statement an attempt to simulate the experimentally determined ALC resonance data was made for the data presented in figure 7.13. The simulations were performed in exactly the same manner as described for the last set of simulations. In total six ALC resonances were simulated with the electron spin relaxation (eSR) rate being the only parameter to be varied. The rest of the parameters used are listed in table 7.3 whilst the simulation results themselves are shown in figure 7.14.

Parameter	Value
A (MHz)	219
D (MHz)	20
E (MHz)	24
eSR (μs^{-1})	0.00 – 10.00
Monte-Carlo Steps	5000

Table 7.3: Modelling parameters used in the 'Quantum' program for the simulation of the ALC resonances of recrystallised regio-regular P3HT.

Just like in the last simulation the experimental results have been scaled onto the polarisation axis belonging to the simulation results. It can be seen that this scaling process has resulted in the 300 K ALC resonance extending below zero polarisation. This is unrealistic and is evidence that the ALC collapse observed for this sample must be induced by some mechanism other than electron spin relaxation. Several other simulated resonance curves have been plotted to indicate the increasingly unrealistic eSR rate required to fit the observed data. For example, for as-bought regio-random P3HT an eSR rate of 0.3 was sufficient to account for the 300 K ALC.

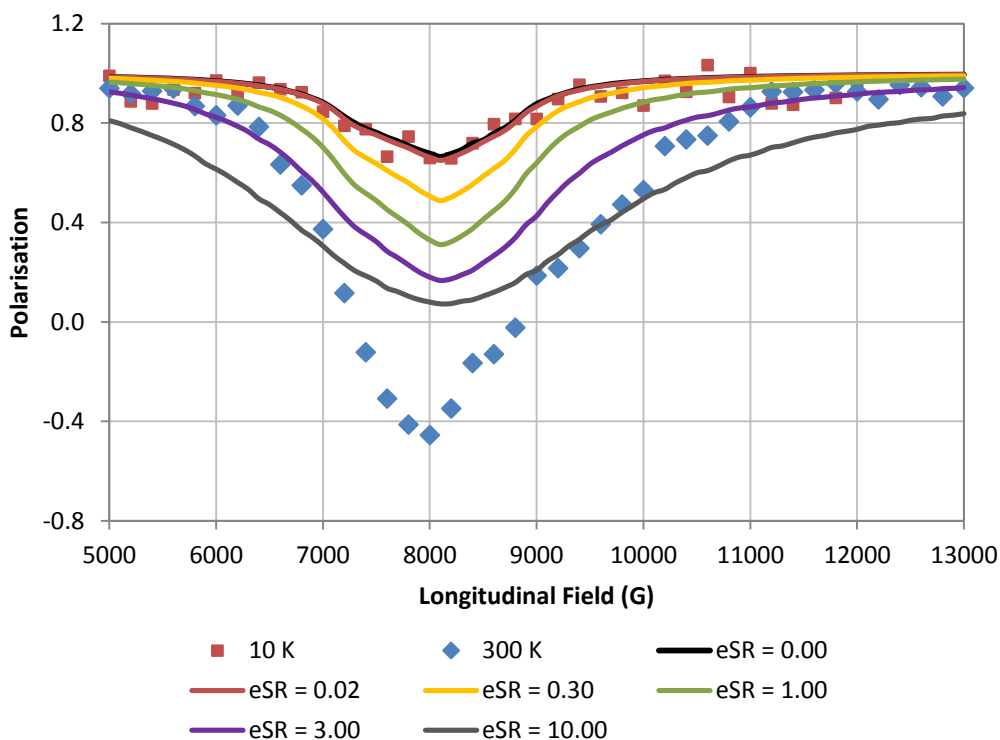


Figure 7.14: Time-integrated muon spin resonance experimental data (squares and diamonds) of recrystallised regio-regular P3HT as a function of longitudinally applied magnetic field and temperature. Only the 10 K and 300 K experimental data has been shown. Modelling of these data is shown as solid coloured lines.

As a final stage to the investigation a sample composed of regio-regular P3HS was measured by μ SR in order to assess the effect of increased spin-orbit coupling due to the heavy-atom effect (§2.4.6). This molecule differs from P3HT by the substitution of sulfur for selenium in the heterocyclic ring structure of the polymer. If eSR is inducing muon spin relaxation then the effect of the atomic substitution is predicted to result in an increase in the magnitude of the ALC collapse as the spin-orbit interaction has been implicated in the mediation of the effect. Figure 7.15 contains the time-integrated μ SR longitudinal field data from that measurement. Six temperature scans were performed from 300 K down to 10 K. It can be seen that the effect of the S-Se substitution has resulted in a shifting of the ALC position to 6000 G (from 8000 G for P3HT). This shift has been theoretically reproduced via ab-initio calculations and is shown in figure 7.16 courtesy of Dr Francis Pratt. Regio-regular P3HS also displays the ALC collapse with temperature that has been demonstrated in regio-regular P3HT. The magnitude of the collapse is approximately 80%, which is the largest collapse measured in this class of polymers.

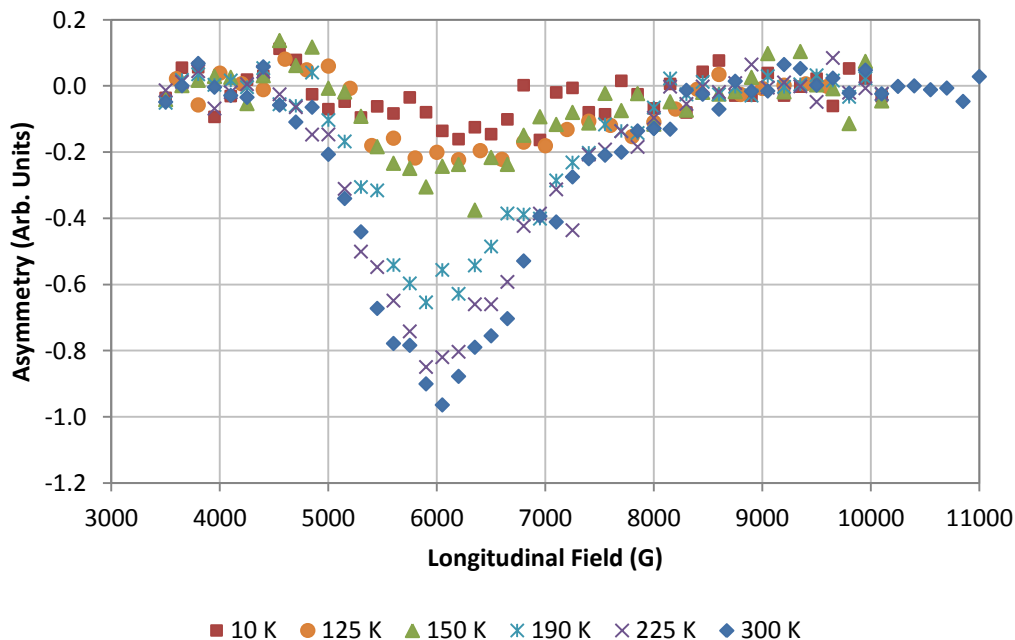


Figure 7.15: Time-integrated muon spin resonance experimental data of regio-regular P3HS as a function of longitudinally applied magnetic field and temperature.

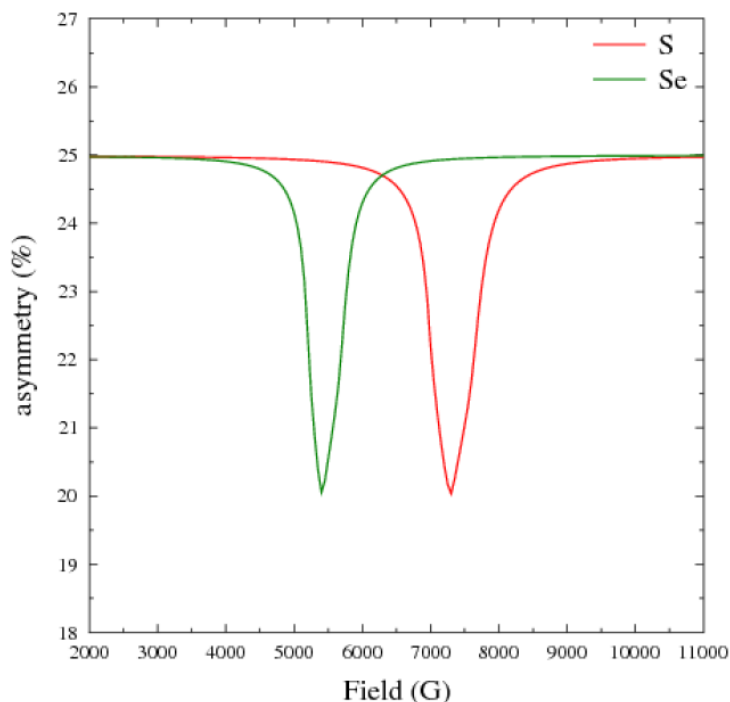


Figure 7.16: Ab-initio simulations of ALC resonances for P3HS (green curve) and P3HT (red curve). A peak separation of 2000 G is observed in the simulation results and correlating well with the experimentally observed ALC resonances (figures 7.13 & 7.15). Courtesy of Dr Francis Pratt.

A summary of the ALC collapses is presented in figure 7.17 where the amplitude of the ALC resonance peaks is plotted as a function of temperature relative to the 300 K peak amplitude. Additional asymmetry measurements were made for regio-random P3HT at nine temperatures. From this figure it is obvious that the regio-regularity of the polymer is critical to observing a large reduction in ALC magnitude with decreasing temperature. The effect of recrystallising the regio-regular P3HT has resulted in an increase in the temperature transition of the collapse by approximately 25 K. The material with the highest transition temperature and lowest overall ALC resonance magnitude is regio-regular P3HS.

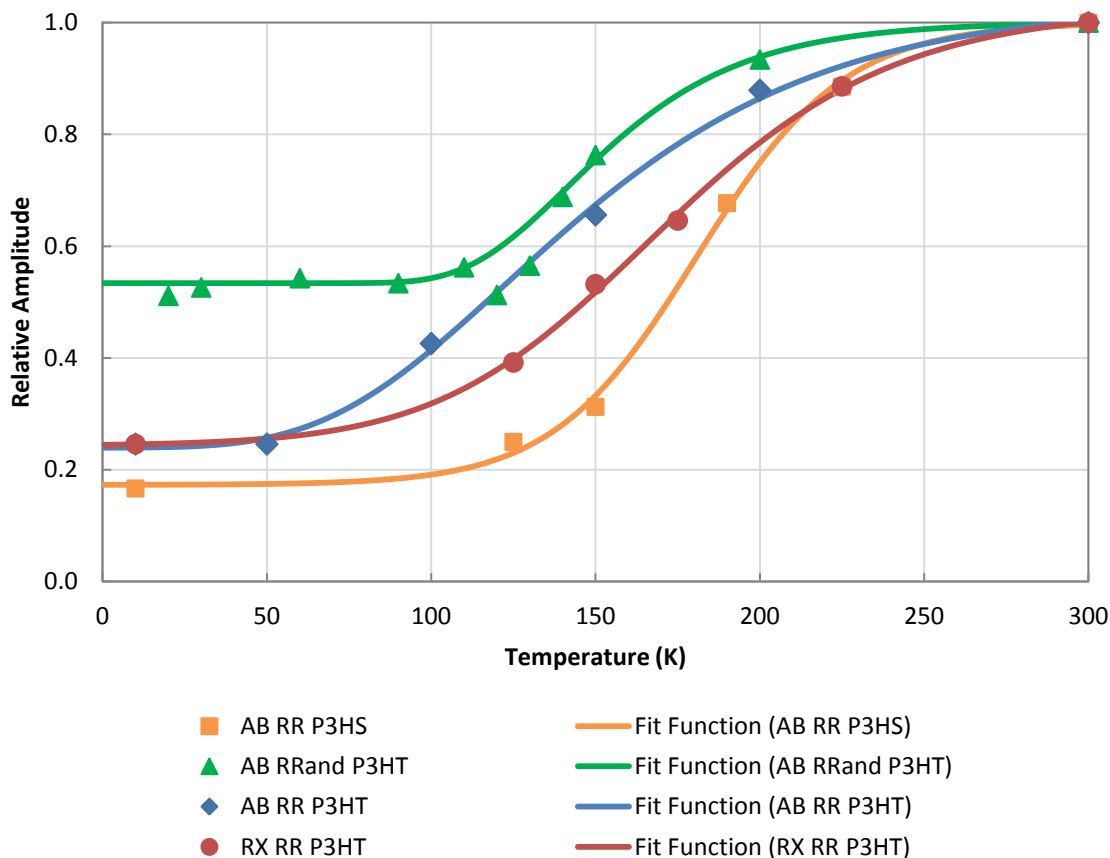


Figure 7.17: Comparative plot of normalised ALC resonance maximum amplitudes of as-bought regio-regular P3HS (yellow diamonds), as-bought regio-random P3HT (green triangles), as-bought regio-regular P3HT (red squares) and recrystallised regio-regular P3HT (blue circles) with temperature. The data has been fitted with sigmoid regression curves.

Collectively, these results suggest that a delocalisation of the conduction electrons is occurring within these organic semiconducting polymers when cooled to low temperatures. This results in a transition from an electronic hopping conduction mechanism at high temperature to the formation of a conduction band leading to electronic band transport at low temperature. If one recalls it was suggested that it is the relaxation of the electron spin that induces the relaxation of the muon spin causing the observed ALC resonance. Therefore if the electrons begin delocalising then there is a reduced probability of muon spin relaxation induced by the electrons due to reduced muon-electron interaction. This hypothesis is supported by the fact that the collapse of the muon ALC resonance is not seen in regio-random P3HT but is seen in all three of the regio-regular polymers measured. It is also not seen in the structurally related organic oligomers [21] suggesting that the increased length of the molecular chain offered by

the polymers enables the electronic wavefunction to extend sufficiently to form a conduction band – but only if the polymer chain is sufficiently ordered.

7.5 Conclusion

Muon spin resonance spectroscopy was undertaken to characterise the electronic transport properties of the organic semiconducting materials poly(3-hexylthiophene-2,5-diyl), P3HT, and poly(3-hexylselenophene-2,5-diyl), P3HS at the ISIS muon and neutron source, Oxfordshire, UK. It was found that both P3HT and P3HS exhibit electron spin relaxation. It was also discovered that a transition in the electronic transport properties occurs as a function of temperature due to delocalisation of the conduction electrons at low temperature. Moreover, this electronic transport transition was found to be dependent on the semiconductor morphology where a high degree of crystallinity was seen to assist the temperature-dependent delocalisation process.

7.6 References

- [1] G. Overton. (2013, 11/10/2013). *Flexible OLED market to rise 334% to nearly \$100M in 2014*. Available: <http://www.laserfocusworld.com/articles/2013/08/flexible-oled-market-to-rise-334-to-nearly-100m-in-2014.html>
- [2] V. Jakhanwal. (2009, 11/10/2013). *OLED Shipments for Primary Cell-Phone Displays to Rise Eightfold by 2015*. Available: <http://www.isuppli.com/display-materials-and-systems/news/pages/oled-shipments-for-primary-cell-phonedisplays-to-rise-two-hundred-fold-by-2015.aspx>
- [3] Z. Shahan. (2012, 11/10/2013). *Organic Photovoltaics Market to Grow 1300% by 2022*. Available: <http://cleantechnica.com/2012/05/16/organic-photovoltaics-market-to-grow-1300-by-2022/>
- [4] S. A. Wolf, *et al.*, "Spintronics: A spin-based electronics vision for the future," *Science*, vol. 294, pp. 1488-1495, Nov 2001.
- [5] S. Sanvito, "Spintronics goes plastic," *Nature Materials*, vol. 6, pp. 803-804, Nov 2007.
- [6] B. Hu and Y. Wu, "Tuning magnetoresistance between positive and negative values in organic semiconductors," *Nature Materials*, vol. 6, pp. 985-991, Dec 2007.

- [7] V. N. Prigodin, *et al.*, "Anomalous room temperature magnetoresistance in organic semiconductors," *Synthetic Metals*, vol. 156, pp. 757-761, May 2006.
- [8] A. M. Ballantyne, *et al.*, "TOF mobility measurements in pristine films of P3HT: control of hole injection and influence of film thickness," in *Organic Photovoltaics VII*. vol. 6334, Z. H. Kafafi and P. A. Lane, Eds., ed Bellingham: Spie-Int Soc Optical Engineering, 2006, pp. U21-U31.
- [9] R. Dost, *et al.*, "Time-of-flight mobility measurements in organic field-effect transistors," *Journal of Applied Physics*, vol. 104, Oct 2008.
- [10] M. Cinchetti, *et al.*, "Determination of spin injection and transport in a ferromagnet/organic semiconductor heterojunction by two-photon photoemission," *Nature Materials*, vol. 8, pp. 115-119, Feb 2009.
- [11] V. Dediu, *et al.*, "Room temperature spin polarized injection in organic semiconductor," *Solid State Communications*, vol. 122, pp. 181-184, 2002.
- [12] ISIS. (2013, 08/10/2013). *How ISIS works - in depth*. Available: <http://www.isis.stfc.ac.uk/about-isis/how-isis-works---in-depth4371.html>
- [13] National Physical Laboratory. (2013, 07/10/2013). *Kaye & Laby - Table of Physical & Chemical Constants - Subatomic particles*. Available: [http://www.kayelaby.npl.co.uk/atomic and nuclear physics/4 8/4 8 4.html](http://www.kayelaby.npl.co.uk/atomic%20and%20nuclear%20physics/4%208/4%208%204.html)
- [14] K. Nagamine, *Introductory Muon Science*: Cambridge University Press, 2003.
- [15] S. F. J. Cox. (1994, 19/10/2013). Introduction to uSR: What, How, Where? Available: <http://www.isis.stfc.ac.uk/groups/muons/muon-training-school/2005-introduction-cox-review7904.pdf>
- [16] S. F. J. Cox, "Implanted Muon Studies In Condensed Matter Science," *Journal of Physics C-Solid State Physics*, vol. 20, pp. 3187-3319, Aug 1987.
- [17] A. J. Steele, "Quantum Magnetism Probed With Muon-Spin Relaxation," University of Oxford, 2011.
- [18] J. S. Lord, "Computer simulation of muon spin evolution," *Physica B-Condensed Matter*, vol. 374, pp. 472-474, Mar 2006.
- [19] ISIS. (2013, 16/10/2013). *Hifi technical information*. Available: <http://www.isis.stfc.ac.uk/instruments/hifi/technical/hifi-technical-information2994.html>

- [20] F. Pratt. (2013, 16/10/2013). *WiMDA Home Page*. Available: <http://shadow.nd.rl.ac.uk/wimda/>
- [21] L. Schulz, *et al.*, "Importance of intramolecular electron spin relaxation in small molecule semiconductors," *Physical Review B*, vol. 84, Aug 2011.